1-1-2016

Dielectric Anomalies Of Both Chiral And Achiral Nematogens Near The Isotropic To Mesogenic Phase Transition

Garrett Justin Godfrey
Wayne State University,

Recommended Citation
Godfrey, Garrett Justin, "Dielectric Anomalies Of Both Chiral And Achiral Nematogens Near The Isotropic To Mesogenic Phase Transition" (2016). *Wayne State University Dissertations*. 1533.
https://digitalcommons.wayne.edu/oa_dissertations/1533

DIELECTRIC ANOMALIES OF BOTH CHIRAL AND ACHIRAL NEMATOGENS NEAR THE ISOTROPIC TO MESOGENIC PHASE TRANSITION

by

GARRETT J. GODFREY

DISSERTATION

Submitted to the Graduate School

of Wayne State University,

Detroit, Michigan

in partial fulfillment of the requirements

for the degree of

DOCTOR OF PHILOSOPHY

2016

MAJOR: PHYSICS

Approved By:

____
Advisor Date

____

____

____

DEDICATION

To my wife, Minjung.

ACKNOWLEDGEMENTS

The work of this dissertation was made possible by the assistance of many people.

I would like to express my appreciation to my advisor Dr. Paul Keyes for the opportunity to work with him. His in-depth understanding, guidance, and support have encouraged me to the end of this project.

I would also to thank my Ph.D. committee members Professors Claudio Verani from the Department of Chemistry, Peter Hoffman and Ashis Mukhopadhyay from the Department of Physics and Astronomy, as well as my past committee member, the late Professor Gavin Lawes. Professor Lawes provided access to equipment necessary to perform dielectric measurements; we also had many discussions concerning the interpretation of dielectric results helped further my understanding of dielectric measurements.

Appreciation especially is due to Dr. Ratna Naik. She helped me obtain my first research experience as an undergraduate. Her guidance and advice from my undergraduate through graduate years have been indispensable.

I would also like to extend my appreciation to Professors Claude Pruneau, Sean Gavin, and Gil Paz with whom I had discussions on problems that I encountered in non-linear curve fitting.

A special thank you is in order to Dr. Gholam-Abbas Nazri. The many conversations we had concerning relaxation phenomena from a chemist point of view enriched my learning process.

And appreciation is due to colleagues, both past and present, for our discussions in physics, research, and curve fitting: Dr. Ambish Dixit, Dr. Rajesh Regmi, Dr. Akila Kumarasiri, Dr. Vera Loggins, Dr. Khadije Bazzi, Dr.Indermeet Kholi, Dr. Essa Mayyas, Dr. Rupam Mukherjee, Dr. Kulwinder Dhindsa, Dr. Humeshkar Nemala, Dr. Mackenzie Smith, Ehab Hamdy, Edward Kramkowski, Christopher Yaldo and Joydeep Roy.

TABLE OF CONTENTS

LIST OF TABLES

LIST OF FIGURES

CHAPTER 1 AN INTRODUCTION TO ORDER

The macroscopic orientational order parameter, chirality, and dielectric permittivity are of primary interest to this dissertation. In this chapter, I start with an introduction to molecular order, the most common liquid crystalline phases, and those phases that are relevant to this dissertation. Both the microscopic and macroscopic orientational order parameters will then be discussed. Finally, the Landau free energy expansion will be explained along with Pierre de Gennes' application of it to nematic order.

1.1 Molecular Order and Liquid Crystalline Phases

At the introductory level, it is taught that there are three phases of matter: solid, liquid, and vapor [1-3]. While this is a useful starting point, it is an incomplete picture. There are substances that have many more phases.

There is a class of molecules called liquid crystals. Upon melting from the crystalline solid toward the isotropic liquid, there exists a continuum of phases. Liquid crystals are liquid in that they are nearly incompressible fluids. However, when observed with cross-polarized microscopy, they exhibit patterns reminiscent of solid crystals. These phases are also referred to as mesophases.

A more complete picture views each mesophase as having some degree of long-range positional order as well as orientational order. The orientational order can be described by a director $\hat{n}$. The director defines the average orientation of the long molecular axis. Upon melting, degrees of order are gradually lost. Figure 1.1 illustrates an example of this loss of order upon increasing the temperature.

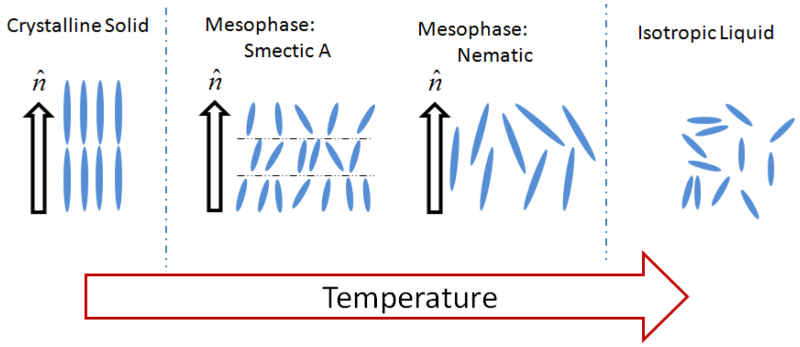

Figure 1.1: An example phase sequence.

The degrees of order are, moving from left to right:
- Crystalline Solid: Three dimensions of positional order plus orientational order
- Smectic A: One dimension of positional order (that is, a one-dimensional crystal) plus orientational order within each layer.
- Nematic: No positional order, only orientational order. The average orientation can be defined with respect to the director $\hat{n}$.
- Isotropic Liquid: Neither long range positional nor orientational order.

1.1.1 Common types of Mesophases: Achiral Nematics and Smectics

Mesophases are generally classified as either lyotropic (having an explicit dependence on concentration) or thermotropic (having an explicit dependence on temperature). The scope of this dissertation is on thermotropic liquid crystals. Thermotropic mesophases can be further divided into three broad categories: columnar (C), smectic (S), and nematic (N). The columnar phases arise when the constituent molecules have a disc-like geometry and form columned structures. In contrast, the samples under investigation are geometrically rod-like and have a rigid core. The smectic phases are layered structures with positional order in one direction and orientational order throughout. The nematic phase has only orientational order. A description of nematic and smectic phases can be seen in Figure 1.1. Figure 1.2 gives two examples of liquid crystals with nematic ordering. Although smectic phases are present in some of my samples, the focus of this dissertation is primarily on nematics.

(a) Hexyl-cyano-biphenyl (6CB)

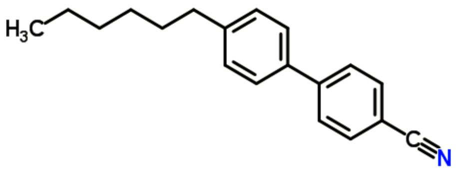

(b) Octyl-cyano-biphenyl (8CB)

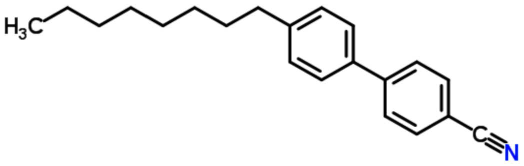

Figure 1.2: Examples of achiral nematic (N) liquid crystals. These chemical structure images are taken from the Royal Society of Chemistry's online database [4, 5].

Although both 6CB and 8CB are from the same *n*CB series, 6CB has only a nematic phase while 8CB has both a nematic and a smectic A phase [4]. The image of 8CB was reformatted to display horizontally [5].

1.1.2 Chiral Phases: Cholesteric and Blue Phases

Molecules can be chiral (i.e., they lack mirror symmetry). When chirality is present in a nematic system, the director $\hat{n}$ is helically distorted resulting in a non-uniform alignment. The periodicity of this rotation around the helical axis is called the pitch. These are generally referred to as chiral nematics (N*). Traditionally chiral nematics are referred to as cholesterics (CH) because the first ones discovered were cholesteryl esters. A schematic of the chiral nematic phase is seen in Figure 1.3. Example cholesteric molecules are seen in Figure 1.4.

In the limit of small pitch, high chirality, the tendency to twist becomes greater. This leads to the formation of a double twist structure that has a lower free energy than a single twist structure. At high chirality, the helical axis no longer is restricted to follow a precession about a single axis [3]. The helical precession is simultaneously allowed in all directions perpendicular to the director [3, 6]. This can result in three additional phases appearing between the chiral nematic and isotropic phases. These three phases are called blue phase I (BPI), II (BPII), and III (BPIII). They were named for what was at first observed as predominately blue platelets that form and are seen under reflected light [7].

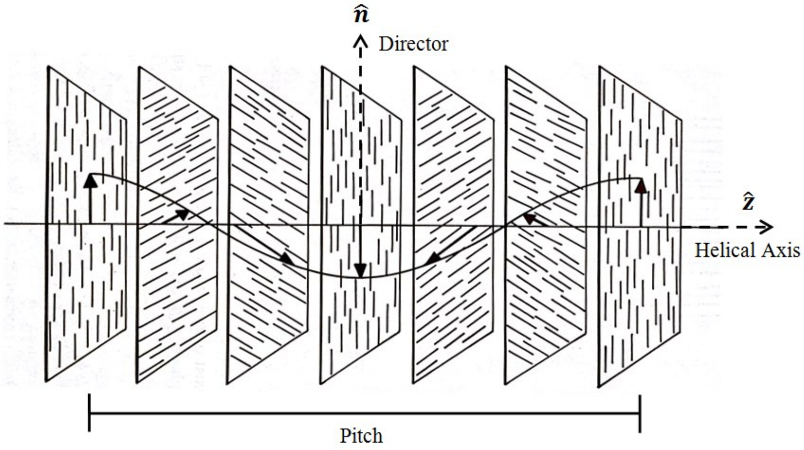

Figure 1.3: Schematic of the cholesteric (i.e., Chiral Nematic) phase from Chandrasekhar [8].

Each vertical plane is schematic of the direction $\hat{n}$ of the molecules at given location along the helical axis $\hat{z}$. The orientation director $\hat{n}$ rotates around the helical axis $\hat{z}$. The pitch p of the rotation is along the helical axis $\hat{z}$.

All three blue phases are optically isotropic. The lower temperature blue phases I and II are cubic in structure. Blue phase III is amorphous [3, 9].

The first materials studied that exhibit blue phases had blue-phase temperature ranges as narrow as a tenth of a degree [10-13]. Modern materials and mixtures can have blue phase temperature widths from 10 K to 60 K [14]. In order to verify that blue phases are thermodynamically distinct, heat capacity measurements are taken. The heat capacity measurements for blue phases I, II, and III for two chiral nematic liquid crystals are shown in Figure 1.5. Figure 1.5a shows a narrow BPIII range. Figure 1.5b shows a wide BPIII range.

(a) Cholesteryl chloride (CC)	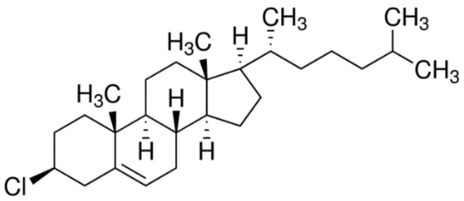
(b) Cholesteryl nonanoate (CN)	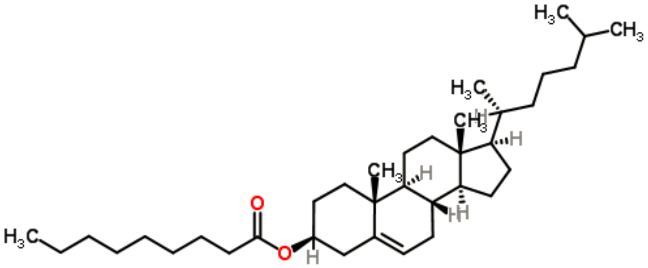
(c) Cholesteryl oleyl carbonate (COC)	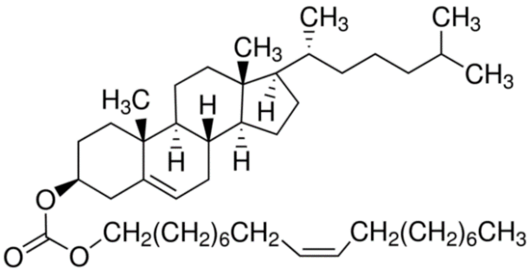
(d) (S-(+)4-(2'-methylbutyl)phenyl 4'-n-octylbiphenyl-4-carboxylate (CE8)	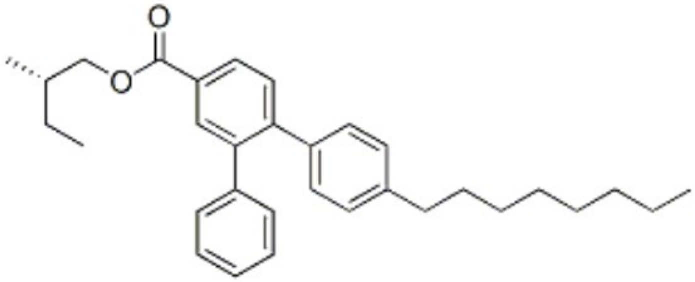

Figure 1.4: Examples of chiral nematic (N*) liquid crystals. The chemical structure images are taken from the both Sigma-Aldrich and the Royal Society of Chemistry's online databases [15-18].

The first N* materials were cholesteryl esters; because of this, chiral nematic molecules are interchangeably referred to as cholesterics. Examples a, b, and c are cholesteryl esters [15-17]. Example (d) is a cholesteric that is not a cholesteryl ester [18].

(a) Cholesteryl nonanoate measurements from Thoen et. al. [13]. It has blue phases that are only a few tenths of a degree wide [13]. Its chemical structure can be seen in Figure 1.4.

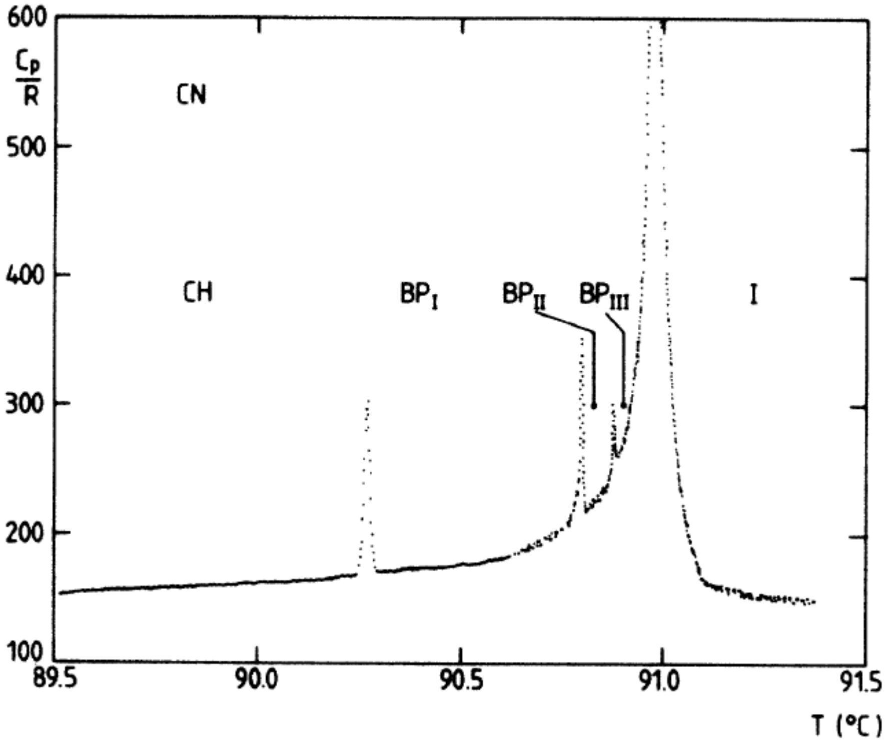

(b) A mixture of CE8 and CdSe, a non-liquid cyrstalline nano-particle, measurements from Karatairi et. al. [14]. The temperature range for blue phase III can be up to 10 K, and blue phase II is not present [14]. Its chemical structure is seen in Figure 1.4.

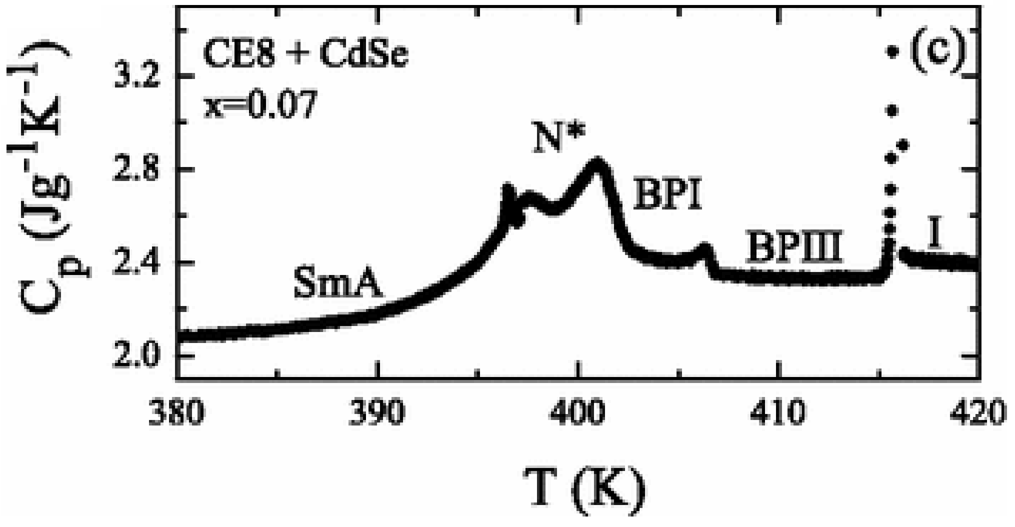

Figure 1.5: Thermodynamic distinction of the blue phases using Adiabatic Scanning Calorimetry from two other groups [13, 14]. A distinct peak is seen at each phase transition.

1.2 Describing Nematic Order

As already mentioned in Section 1.1, a given phase is characterized by the degree of positional and orientational order of each constituent molecule relative to another. The extent of both types of order for each phase is quantified by what is referred to as an order parameter. Once quantified, this parameter is used in a free energy expression to determine the thermodynamic properties of a substance. Traditionally, this parameter is required to be zero in a purely disordered, isotropic state and non-zero in an anisotropic state.

Furthermore, the degree of short range order is dependent on a correlation length. The following equation describes the temperature dependence of a typical correlation length near a critical temperature T^*.

$$\xi = \xi_0 \sqrt{\frac{T^*}{T-T^*}} \tag{1.1}$$

The parameter ξ_0, called the bare correlation length, is about the size of a molecule.

1.2.1 Orientational Order: The Microscopic Approach

In the nematic phase, only orientational order exists. In Figure 1.1 for the nematic phase, each molecule is modeled as a rigid rod. An angle θ_i is defined between each ith molecule's long axis and the overall director axis $\hat{n}$. With this model, the constituent molecules are not expected to distinguish between θ_i and $\theta_i + \pi$. For this reason, the second Legendre polynomial has traditionally been used as the microscopic order parameter S noted in Equation 1.2 below. It is insensitive to a π rotation and is zero when the distribution of $\theta_i{}'$ is completely random – that is, isotropic:

$$S = \langle \frac{3}{2} cos^2\theta - \frac{1}{2} \rangle. \tag{1.2}$$

Grandjean used this definition in 1917 when he applied the formalism of the theory of magnetism to anisotropic liquids [19]. Tsvetkov also utilized this definition in his 1942 paper which discussed anisotropic liquid phases [20].

Subsequent microscopic mean field theories were developed around this order parameter [21]. In these theories, the constituent molecules were treated as simple, rigid rods. Maier and Saupe considered the primary intermolecular interaction to be attractive dispersion forces while Onsager took the opposite approach of the primary interaction being repulsive [21]. However, these theories suffered from the oversimplification of both the geometry of each molecule and the intermolecular interactions between each molecule. Fluctuations were also not taken into account [3]. This leads to only a qualitative understanding of the characteristics of a given mesophase. While these models predicted transitions, the quantitative results were not always accurate.

Defining the order parameter with respect to a distribution of molecular angles as in Equation 1.2 is impractical to measure, since real nematic liquid crystals are not rigid rods. Since liquid crystals tend to have long hydrocarbon chains, every carbon-carbon pair would have to be defined by its own angle of alignment. This would lead to each individual molecule having its own internal distribution of angles while being a part of a broader distribution of angles for the entire sample.

1.2.2 Orientational Order: The Macroscopic Approach

Under some conditions, a phenomenological approach that is independent of molecular details is preferred. An approach developed around quantitatively describing macroscopic phenomena is more practical than finding a distribution of molecular angles. Light scattering, heat capacity, dielectric permittivity, and magnetic susceptibility are examples of bulk phenomena that can be calculated from such an approach. The following subsections examine a free energy expansion using a macroscopic order parameter.

1.2.2.1 The Macroscopic Order Parameter and the Landau Free Energy Expansion

L.D. Landau first proposed a mean-field model for phase transitions in which a thermodynamic potential Φ (such as the free energy) is expressed as a power series of a macroscopic order parameter η [22]. This parameter η must be sensitive to the degree of order and symmetry of a phase:

$$\Phi = \Phi_0 + \alpha\eta^1 + A\,\eta^2 + B\eta^3 + C\eta^4 + O(\eta^5). \tag{1.3}$$

The explicit dependence of Φ on thermodynamic quantities such as temperature and pressure is contained within the coefficients α, A, B, C, etc. Typically, α, B, and C are constants while A is taken to be a linear function of temperature such that $A = A_0(T - T_c)$, where T_c is the critical temperature [22].

There are only two conditions placed on the order parameter η. First, all powers of η in the expansion of Equation 1.3 must be rotationally invariant scalars. Second, all terms allowed by symmetry must be included.

The order parameter η could be a scaler, vector, or a second rank tensor. If η were a scalar (such as a density modulation), then any power of η is allowed due to any power being rotationally invariant and already a scalar. If η were a vector, however, (such as a magnetization M_α), then only even powers of η would be allowed resulting in a free energy symmetric about the origin. It is not possible to construct a rotationally invariant scalar from an odd power of a vector. Lastly, if η were a second rank tensor (such as magnetic susceptibility $\chi^m_{\alpha\beta}$, or electric susceptibility $\chi^e_{\alpha\beta}$), then all powers of η would be allowed. The first order rotationally invariant term would be simply the trace of the tensor. The second order rotationally invariant term would be the inner product of the tensor with itself followed by taking the trace, and so on.

1.2.2.2 The Free Energy Expansion Applied to Nematic Liquid Crystals: P. G. de Gennes

Pierre de Gennes applied Landau's theory to nematic liquid crystals. He chose the anisotropic part $Q_{\alpha\beta}$ of the full dielectric permittivity tensor $\varepsilon_{\alpha\beta}$ as the nematic order parameter. The choice of the tensor order parameter was such that it was symmetric, traceless and vanished in the isotropic phase. From this choice, the parameter $Q_{\alpha\beta}$ was found by subtracting out any isotropic contribution $\bar{\varepsilon}\,\delta_{\alpha\beta}$ from $\varepsilon_{\alpha\beta}$,

$$Q_{\alpha\beta} = \varepsilon_{\alpha\beta} - \frac{1}{3}\bar{\varepsilon}\,\delta_{\alpha\beta}. \qquad (1.4)$$

Here, $\delta_{\alpha\beta}$ represents the identity matrix. Equation 1.4 defines $Q_{\alpha\beta}$ such that it vanishes in the isotropic phase.

The resultant free energy expression would be given as,

$$F = \tfrac{1}{2}A\, Q_{\alpha\beta}Q_{\beta\alpha} - \tfrac{1}{3}B\, Q_{\alpha\beta}Q_{\beta\gamma}Q_{\gamma\alpha} + \tfrac{1}{4}C\, (Q_{\alpha\beta}Q_{\beta\alpha})^2. \qquad (1.5)$$

Due to de Gennes' additional requirement that the isotropic contribution be subtracted out, the linear term is absent in the free energy expansion.

1.2.2.3 Vector versus Tensor Order Parameter

It is instructive to consider the consequences between a free energy with and without a cubic term. If the order parameter η were a vector M_α, there would be no odd powers of M_α, as no rotationally invariant scalar could be made. Equation 1.3 rewritten for this case would be,

$$F = \frac{1}{2}A_0(T - T_c)\, M_\alpha M_\alpha + \frac{1}{4}C(M_\alpha M_\alpha)^2. \qquad (1.6)$$

The transition temperature T_c marks the boundary between two phases. Equation 1.6 could also represent the free energy expansion for a tensor in which the coefficient of the third order term is zero. Again, Equation 1.5 represents the free energy expansion for a tensor order parameter in which the linear term is zero and the third order term is non-zero. The Equations 1.5 and 1.6 will be plotted in Figure 1.6.

A symmetric free energy in which no odd powers in η are present leads to a continuous, second order transition. At a second order phase transition the first derivatives of the free energy are continuous [21].

An asymmetric free energy in which there is at least a cubic term leads to a first order phase transition. That is, a discontinuity in one of the first derivatives of the free energy appears. This includes discontinuities in the entropy and the order parameter. In the case of a nematic liquid crystal, the transition from isotropic liquid is weakly first order [21].

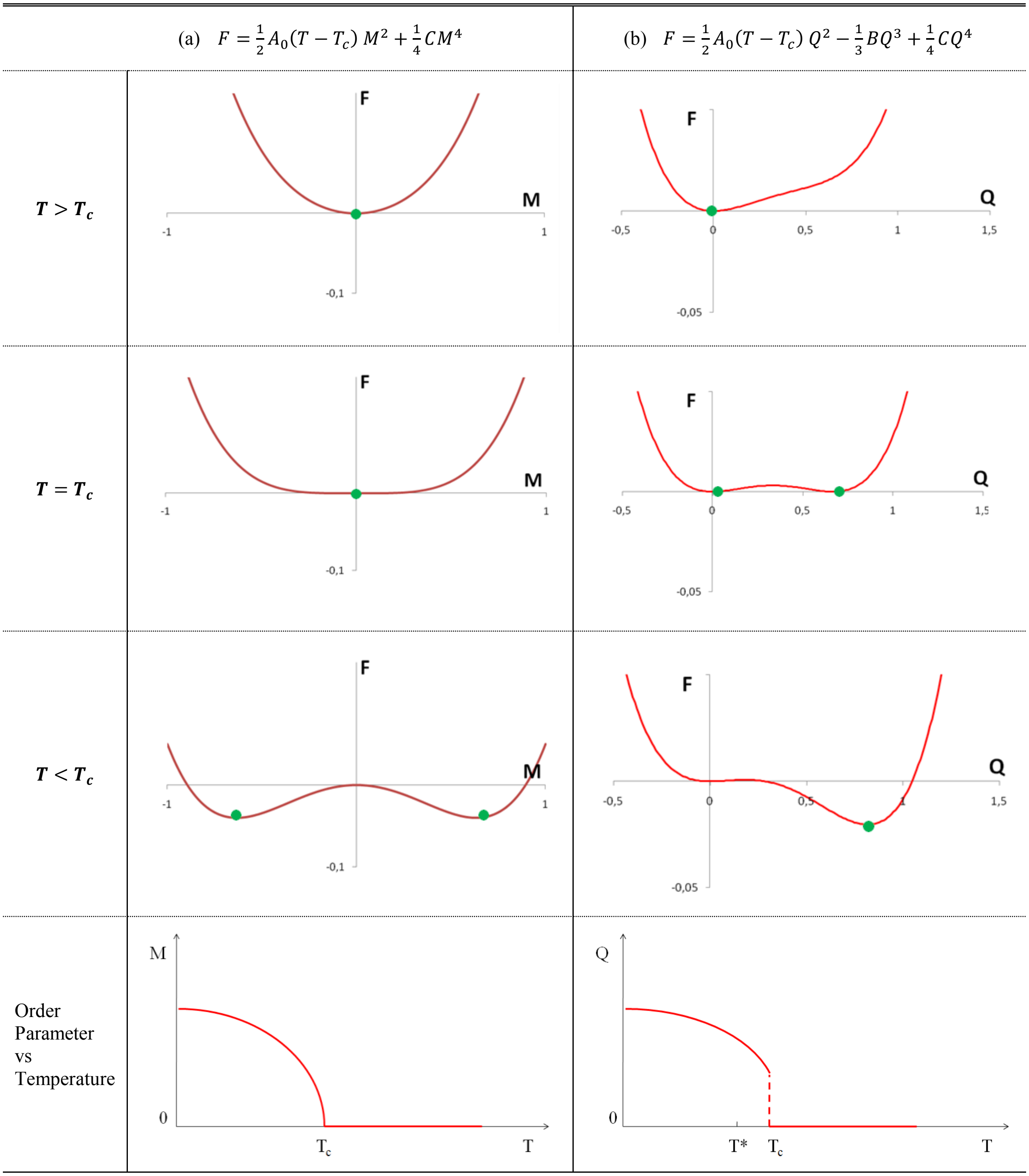

Figure 1.6: The free energy expansion for simulated data.

(a) A symmetric free energy leads to a continuous, 2nd order phase transition.
(b) An asymmetric free energy with no linear term leads to a discontinuous, 1st order phase transition.

1.3 Goals of This Dissertation

Liquid crystals are model systems for studying phase transitions. The varying degrees of positional and orientational order that exist lead to interesting behaviors. When chirality is present, unexpected phases such as the cubic blue phases I and II or the amorphous blue phase III may show up. Furthermore, where bulk behavior is concerned, it is more practical to use a macroscopic order parameter and to utilize the Landau-de Genne free energy expansion as a predictive tool. This tool will be used in the upcoming sections to generalize the order parameter as well as to study the high chirality limit where blue phases appear.

This dissertation has two goals. The first goal is to show a model that generalizes the order parameter to the full dielectric permittivity tensor $\varepsilon_{\alpha\beta}$. The nematic order parameter $Q_{\alpha\beta}$ will retain its properties as defined above, but now its fluctuations will be allowed to couple with the isotropic part. This results in describing pretransitional anomalies that show up in published dielectric data. The dielectric pretransitional anomalies are not currently predicted by theory.

The second goal of this dissertation is to look at this pretransitional effect for chiral nematic systems. Few dielectric studies have been done on the isotropic to cholesteric phase transition. Only one has looked at the effect of varying chirality [23]. In addition to what we usually call the isotropic phase, there are additional isotropic phases called the blue phases. The dielectric response of a variable chiral system is studied through mixtures of two oppositely handed chiral nematic molecules. By varying the chirality, blue phases can be studied from where they dominate to where they disappear in the low chirality limit.

CHAPTER 2 DIELECTRIC THEORY AND A GENERALIZED NEMATIC ORDER PARAMETER

The relative dielectric permittivity $\varepsilon_{\alpha\beta}$ contains the macroscopic order parameter $Q_{\alpha\beta}$. The theories behind the frequency and thermal dependence of $\varepsilon_{\alpha\beta}$ are needed to understand the results of this dissertation. The theory behind the dielectric permittivity's frequency response is well established and will be discussed in Section 2.2. The thermal response for the isotropic to nematic phase transition, however, is not well described by current theory. It will be understood from the context of a generalization of the macroscopic order parameter in Section 2.3. The end of this chapter will show the full dielectric permittivity $\varepsilon_{\alpha\beta}$ as the generalized order parameter.

2.1 Orientational Order and Electric Polarization

When materials, such as liquid crystals, are exposed to an externally applied field E_β, the medium responds by polarizing. A quantity called the relative dielectric permittivity tensor $\varepsilon_{\alpha\beta}$ is used to measure this polarization.

Irrespective of the frequency (whether it is a low frequency AC field, a DC field, or a beam of light), the field inside the material is expressed by a displacement field D_α. The induced polarization of the molecules is expressed by the electric polarization density P_α. The displacement field is the sum of the electric polarization density P_α and the inner product of the identity matrix $\delta_{\alpha\beta}$ with the applied electric field E_β multiplied by the constant permittivity of free space ε_0:

$$D_\alpha = \varepsilon_0 \delta_{\alpha\beta} E_\beta + P_\alpha. \tag{2.1}$$

The polarization density P_α is modeled as the inner product of the applied field E_β with a material property $\chi_{\alpha\beta}$ multiplied by the constant permittivity of free space ε_0. The term $\chi_{\alpha\beta}$ is called the electric susceptibility tensor:

$$P_\alpha = \varepsilon_0 \chi_{\alpha\beta} E_\beta. \tag{2.2}$$

The electric polarization density P_α can be attributed to two main mechanisms: the charge displacement of individual charges and the orientational polarization of already present dipoles [24-27]. Charge displacement is a fast process (measured around infrared, visible, or ultraviolet frequencies). For polar molecules (which this dissertation deals with), the slower orientational polarization dominates at lower frequencies.

When E_β is an applied AC field, the response of a mechanism is counteracted by viscous forces. For a given mechanism, there is a characteristic (i.e., relaxation) frequency f_r. At f_r, the polarization field is out of phase with the applied field by 90°. Also, at f_r, the amount of energy from E_β that is absorbed and then converted into heat is maximum [24, 26]. Above f_r, viscous forces begin to dominate.

If $\chi_{\alpha\beta}$ is measured at a frequency $\frac{\omega}{2\pi} \ll f_r$ (where ω is the angular frequency), then the mechanism under investigation fully contributes to the electric polarization density P_α. If $\chi_{\alpha\beta}$ is measured at a frequency $\frac{\omega}{2\pi} \approx f_r$, then the mechanism under investigation is inhibited by viscous forces. If $\chi_{\alpha\beta}$ is measured at a frequency $\frac{\omega}{2\pi} \gg f_r$, then the mechanism under investigation contributes nothing to the measured polarization density P_α due to the molecules being unable to follow the field [25, 26].

2.2 The Frequency Dependence of the Dielectric Permittivity

Dielectric permittivity is the macroscopic orientational order parameter. The relative dielectric permittivity is a function of both frequency and temperature. In this section, the frequency dependence of $\varepsilon_{\alpha\beta}$ is explored. The dispersion relationships to be used are presented. In Section 2.3, the temperature dependence of $\varepsilon_{\alpha\beta}$ at a constant frequency is of interest to describe how the order of a sample evolves from one phase to the next.

Equations 2.1 and 2.2 are the starting points to understanding permittivity. To begin, Equation 2.2 is substituted into Equation 2.1 to give a direct relationship between an applied field E_β and the materials response D_α:

$$D_\alpha = \varepsilon_0(\delta_{\alpha\beta} + \chi_{\alpha\beta})E_\beta. \tag{2.3a}$$

From Equation 2.3a, the relative dielectric permittivity tensor is defined as the sum of the identity matrix and the electric susceptibility tensor:

$$\varepsilon_{\alpha\beta} = \delta_{\alpha\beta} + \chi_{\alpha\beta}. \tag{2.3b}$$

After an applied AC field $E_\beta(t) = E_{\beta 0}e^{i\omega t}$ is turned on at time $t = 0$, it takes time for the field $D_\alpha(t)$ inside the material to reach a steady state equilibrium. The way in which a steady state is achieved and the transient effects fade away is called the decay function $\nu_{\alpha\beta}(t)$ with a characteristic relaxation time τ. The decay function $\nu_{\alpha\beta}(t)$ can be either for a single relaxation process or for a distribution of processes. The relaxation frequency f_r mentioned in Section 2.1 is related to this time constant by $\tau = (2\pi f_r)^{-1}$. Superposition can be applied to find the value of $D_\alpha(t)$ for all previous instances that $E_\beta(t)$ was applied including transient effects [24, 26]. Equation 2.4a then 2.4b shows this integral form:

$$\mathrm{D}_\alpha(t) = \varepsilon_0\left(\varepsilon_{\alpha\beta}^{\infty}E_\beta(t) + \int_0^\infty du\, \nu_{\alpha\beta}(u)E_\beta(t-u)\right). \tag{2.4a}$$

Equation 2.4a leads to a Fourier transform into the frequency domain where the relative dielectric permittivity $\varepsilon_{\alpha\beta}(\omega)$ is a complex quantity that can be broken into a real and an imaginary part [24]:

$$\varepsilon_{\alpha\beta}(\omega) = \varepsilon_{\alpha\beta}^{\infty} + \int_0^\infty du\, \nu_{\alpha\beta}(u)e^{-i\omega u}, \tag{2.4b}$$

$$\varepsilon_{\alpha\beta}(\omega) = \varepsilon'_{\alpha\beta} - i\varepsilon''_{\alpha\beta}. \tag{2.4c}$$

The constant parameter $\varepsilon_{\alpha\beta}^{\infty}$ in Equation 2.4b is the instantaneous, high frequency contribution to the permittivity. In Equation 2.4c, the real part $\varepsilon'_{\alpha\beta}$ is the relative dielectric strength. The imaginary part $\varepsilon''_{\alpha\beta}$ is the dielectric loss. By convention, Equation 2.4c is written with a negative sign to ensure that $\varepsilon''_{\alpha\beta}$ is a positive quantity. The reasoning will be evident after breaking Equation 2.6e into real and imaginary parts.

The following subsections discuss the types of relaxation. The simplest model is Debye relaxation. The two slightly more complicated models are the Cole-Cole and Cole-Davidson relaxation processes. The most complicated and empirically determined model is the Havriliak-Negami model. Section 2.2 will conclude with low frequency contributions and how they are accounted for.

2.2.1 Debye Relaxation

Peter Debye proposed a model in which a single relaxation process is assumed and the molecule is spherical [28, 29]. The decay function $\nu_{\alpha\beta}(t)$ in Equations 2.4a and 2.4b is assumed to be exponential with the characteristic time τ:

$$\nu_{\alpha\beta}(t) = \nu_{\alpha\beta}^{0} e^{\frac{-t}{\tau}}. \tag{2.5}$$

The relaxation time can be related to various properties such as the modulus of rigidity or the viscosity [24]. Substituting Equation 2.5 into Equation 2.4b gives the Debye relaxation equation,

$$\varepsilon_{\alpha\beta}(\omega) = \varepsilon_{\alpha\beta}^{\infty} + \frac{\tau\nu_{\alpha\beta}^{0}}{1+i\omega\tau}. \tag{2.6a}$$

The constant $\tau\nu_{\alpha\beta}^{0}$ comes from carrying out the integration in Equation 2.4b with Equation 2.5.

The magnitude of the decay function $\nu_{\alpha\beta}^{0}$ from Equation 2.5 can be found by looking at the polarization density $P_{\alpha}(t)$ from Equation 2.2 and its time derivative $P_{\alpha,t}(t)$. The polarization eventually approaches a steady state value P_{α}^{static} with a steady state susceptibility $\chi_{\alpha\beta}(0) = \chi_{\alpha\beta}^{0}$:

$$P_{\alpha}^{static} = \varepsilon_{0}\chi_{\alpha\beta}^{0}E_{\beta}. \tag{2.6b}$$

For an overdamped system perturbed from equilibrium, the system will tend to relax at a rate of $1/\tau$. For a Debye process, the time derivative $P_{\alpha,t}$ of the polarization density is proportional to the deviation of polarization density P_α from the steady state value P_α^{static}, as seen in Equation 2.6c:

$$P_{\alpha,t} = \frac{P_\alpha^{static} - P_\alpha}{\tau}. \tag{2.6c}$$

The magnitude of the decay function $\nu_{\alpha\beta}^0$ is $\frac{\chi_{\alpha\beta}^0}{\tau}$. The time derivative is replaced with $i\omega$. A dispersion relation identical in form to Equation 2.6a is found by substituting the functional forms of Equations 2.2 and 2.6b into Equation 2.6c,

$$\chi_{\alpha\beta}(\omega) = \Delta\chi_{\alpha\beta}^0. \tag{2.6d}$$

Equations 2.6a and 2.6d are the same for a single relaxation process of spherical molecules that relax exponentially to a steady state:

$$\varepsilon_{\alpha\beta}(\omega) = \varepsilon_{\alpha\beta}^\infty + \frac{\Delta\chi_{\alpha\beta}^0}{1+i\omega\tau}. \tag{2.6e}$$

The real and imaginary parts $\varepsilon'_{\alpha\beta}$ and $\varepsilon''_{\alpha\beta}$ of the Debye relaxation (Equation 2.6e) can be separated. I will follow the form of Equation 2.4c above, $\varepsilon_{\alpha\beta}(\omega) = \varepsilon'_{\alpha\beta} - i\varepsilon''_{\alpha\beta}$:

$$\varepsilon'_{\alpha\beta}(\omega) = \varepsilon_{\alpha\beta}^\infty + \frac{\Delta\chi_{\alpha\beta}^0}{1+(\omega\tau)^2}, \tag{2.7a}$$

$$\varepsilon''_{\alpha\beta}(\omega) = \frac{\Delta\chi_{\alpha\beta}^0\omega\tau}{1+(\omega\tau)^2}. \tag{2.7b}$$

Cole and Cole observed that, when plotting Debye's dispersion relations $\varepsilon'_{\alpha\beta}(\omega)$ and $\varepsilon''_{\alpha\beta}(\omega)$ in the complex plane, a semicircle with radius $\frac{\Delta\chi_{\alpha\beta}^0}{2}$ is formed [29]. By plotting $\varepsilon''_{\alpha\beta}(\omega)$ versus $\varepsilon'_{\alpha\beta}(\omega)$, the explicit frequency dependence is factored out. This can be seen by adding the squares of Equations 2.7a and 2.7b:

$$\left(\varepsilon'_{\alpha\beta}-\left(\varepsilon^{\infty}_{\alpha\beta}+\frac{\Delta\chi^{0}_{\alpha\beta}}{2}\right)\right)^{2}+\left(\varepsilon''_{\alpha\beta}\right)^{2}=\left(\frac{\Delta\chi^{0}_{\alpha\beta}}{1+(\omega\tau)^{2}}-\frac{\Delta\chi^{0}_{\alpha\beta}}{2}\right)^{2}+\left(\frac{\Delta\chi^{0}_{\alpha\beta}\omega\tau}{1+(\omega\tau)^{2}}\right)^{2}, \tag{2.8a}$$

$$\left(\varepsilon'_{\alpha\beta}-\left(\varepsilon^{\infty}_{\alpha\beta}+\frac{\Delta\chi^{0}_{\alpha\beta}}{2}\right)\right)^{2}+\left(\varepsilon''_{\alpha\beta}\right)^{2}=\left(\frac{\Delta\chi^{0}_{\alpha\beta}}{2}\right)^{2}. \tag{2.8b}$$

In Equation 2.8b, the explicit frequency dependence is cancelled out from Equation 2.8a. Equation 2.8b is the equation of a circle with radius $\frac{\Delta\chi^{0}_{\alpha\beta}}{2}$ shifted to the right by $\varepsilon^{\infty}_{\alpha\beta}+\frac{\Delta\chi^{0}_{\alpha\beta}}{2}$. For Debye relaxation, the parameter $\Delta\chi^{0}_{\alpha\beta}$ is the diameter of this semicircle.

2.2.2 Cole-Cole Relaxation

Not all relaxation phenomena follow Debye relaxation. In their 1941 publication, Kenneth Cole and Robert Cole observed that some relaxation behaviors appeared as shifted semicircles [30]. An empirical modification to Debye's relaxation (Equation 2.6e) has an additional exponent on the term $i\omega\tau$,

$$\varepsilon_{\alpha\beta}(\omega)=\varepsilon^{\infty}_{\alpha\beta}+\frac{\Delta\chi^{0}_{\alpha\beta}}{1+(i\omega\tau)^{\alpha}}. \tag{2.9}$$

The real and imaginary parts of Equations 2.7a and 2.8b become:

$$\varepsilon'_{\alpha\beta}(\omega)=\varepsilon^{\infty}_{\alpha\beta}+\frac{\Delta\chi^{0}_{\alpha\beta}\left(1+(\omega\tau)^{\alpha}cos\left(\frac{\pi}{2}\alpha\right)\right)}{1+(\omega\tau)^{2\alpha}+2(\omega\tau)^{\alpha}cos\left(\frac{\pi}{2}\alpha\right)}, \tag{2.10a}$$

$$\varepsilon''_{\alpha\beta}(\omega)=\frac{\Delta\chi^{0}_{\alpha\beta}\left((\omega\tau)^{\alpha}sin\left(\frac{\pi}{2}\alpha\right)\right)}{1+(\omega\tau)^{2\alpha}+2(\omega\tau)^{\alpha}cos\left(\frac{\pi}{2}\alpha\right)}. \tag{2.10b}$$

Just as Debye relaxation in the complex plane shows a semicircle, it was found that the depressed semicircles were circles shifted downward on the imaginary axis $\varepsilon''_{\alpha\beta}$. Going through the same process of eliminating $\omega\tau$ and plotting $\varepsilon''_{\alpha\beta}$ vs $\varepsilon'_{\alpha\beta}$ gives the equation of a circle shifted to the right along the real axis by $\left(\varepsilon^{\infty}_{\alpha\beta}+\frac{\Delta\chi^{0}_{\alpha\beta}}{2}\right)$ and down on the imaginary axis b:

$$\left(\varepsilon'_{\alpha\beta}(\omega) - \left(\varepsilon^{\infty}_{\alpha\beta} + \frac{\Delta\chi^{0}_{\alpha\beta}}{2}\right)\right)^{2} + \left(\varepsilon''_{\alpha\beta}(\omega) + b\right)^{2} = (R)^{2}. \tag{2.11}$$

The shift downward is,

$$b = \frac{\Delta\chi^{0}_{\alpha\beta}}{2} tan\left(\frac{\pi}{2}(1-\alpha)\right). \tag{2.12a}$$

The diameter of the circle increases from the Debye case to,

$$R = \frac{\Delta\chi^{0}_{\alpha\beta}}{2\, sin\left(\frac{\pi}{2}\alpha\right)}. \tag{2.12b}$$

The parameter $\Delta\chi^{0}_{\alpha\beta}$ now describes the width of the arc of the circle that begins and ends at $\varepsilon''_{\alpha\beta}$=0. The angle $\frac{\pi}{2}(1-\alpha)$ is from the real axis rotated downward. For both the Debye and Cole-Cole cases, $\Delta\chi^{0}_{\alpha\beta}$ can be called the dielectric strength. Cole-Cole relaxation reduces to Debye relaxation when $\alpha = 1$.

Figure 2.1 shows the cases in which Equation 2.10a and 2.10b are plotted versus frequency. Part (a) of Figure 2.1 shows Equation 2.11 plotted. A simulated relaxation frequency f_r of either 5 kHz or 100 kHz is chosen. As will be seen in Chapter 5, a typical relaxation frequency in the isotropic phase was greater than 100 kHz.

(a) A Cole-Cole Plot: ε'' vs ε'

- The leftmost data points correspond to 1 MHz
- The rightmost data points correspond to 20 Hz

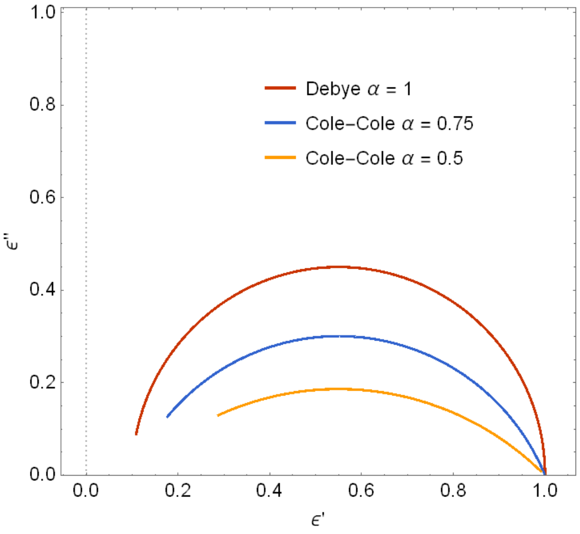

(b) Relative Permittivity: ε' versus frequency.

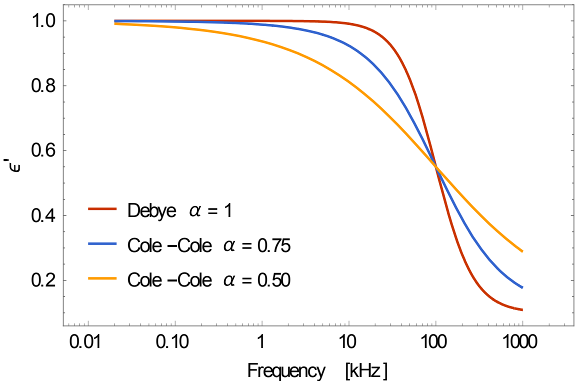

(c) Dielectric Loss: ε'' versus frequency.

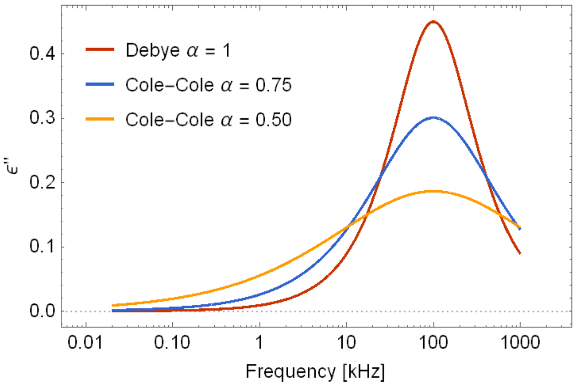

Figure 2.1: Cole-Cole Plot and the frequency dependence at difference values for α for simulated data.

Equations 2.10a and 2.10b are plotted with simulated data as functions of frequency. The data are simulated for $\varepsilon_{\alpha\beta}$ generated over 20 Hz to 1 MHz (the measuring capability of the apparatus).
For all curves:

- $\varepsilon_{\infty} = 0.1$
- $\Delta\chi^{0}_{\alpha\beta} = 0.9$
- $f_r = 100$ kHz.

2.2.3 Two Additional Types of Relaxation: Cole-Davidson and Havriliak-Negami

There exist two additional empirical modifications to Debye's relaxation model that are worthy to note but will not be used in this dissertation. R. H. Cole and Davidson proposed that the entire denominator be raised to an exponent β [31, 32]:

$$\varepsilon_{\alpha\beta}(\omega) = \varepsilon_{\alpha\beta}^{\infty} + \frac{\Delta\chi_{\alpha\beta}^{0}}{(1+i\omega\tau)^{\beta}}. \tag{2.12}$$

This equation leads to an asymmetric curve in the complex plane. At frequencies below the relaxation frequency f_r (the rightmost data for ε'' plotted versus ε'), the curve follows a semicircle. Above f_r, the relationship between the imaginary part $\varepsilon_{\alpha\beta}''$ and real part $\varepsilon_{\alpha\beta}'$ becomes more linear and less of a circular arc. The main limitation in using this model is that, in order to distinguish a Cole-Cole mechanism with two dielectric peaks immediately adjacent to one another from a Cole-Davidson mechanism, a sufficient amount of high frequency data (i.e., $\frac{\omega}{2\pi} \gg f_r$) must be collected.

The second empirical modification is the Havriliak-Negami relaxation. This model combines Equations 2.9 and 2.12 [33]:

$$\varepsilon_{\alpha\beta}(\omega) = \varepsilon_{\alpha\beta}^{\infty} + \frac{\Delta\chi_{\alpha\beta}^{0}}{(1+(i\omega\tau)^{\alpha})^{\beta}}. \tag{2.13}$$

This model was applied mostly to large polymers such as polyvinyl acetal and polyvinyl chloroacetate. The Havriliak-Negami relaxation requires a sufficient measured frequency range on both sides of the relaxation frequency f_r in order to distinguish between a single skewed peak and two adjacent peaks. As seen in Figure 2.2, it is difficult to distinguish between the case of part (a) (where there are two relaxation peaks with $\alpha < 1$ and $\beta = 1$) and the case of a single relaxation process in part (b). The molecules under investigation are relatively small compared to polymers. For this dissertation, parameter β is fixed at one due to a low density of data collected.

(a) Cole-Cole Relaxation

- Parameter α is noted on the Plots
- Fixed Parameter $\beta = 1$

Double peak

Left Peak

- $\varepsilon_\infty = 0.1$
- $\Delta\chi^0_{\alpha\beta} = 0.25$
- $f_f = 100$ kHz

Right Peak

- $\varepsilon_\infty = 0.35$
- $\Delta\chi^0_{\alpha\beta} = 0.65$
- $f_r = 5$ kHz

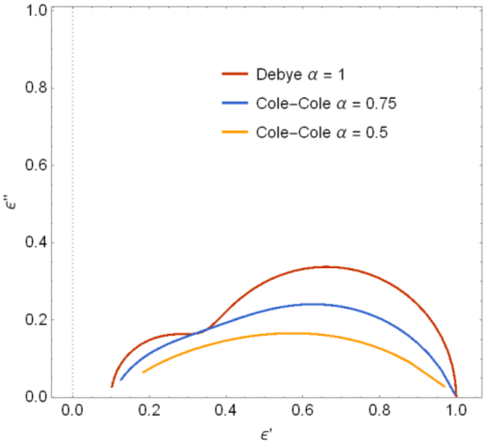

(b) Havriliak-Negami Relaxation.

- Fixed Parameter $\beta = 0.5$

Single peak

- $\varepsilon_\infty = 0.1$
- $\Delta\chi^0_{\alpha\beta} = 0.90$
- $f_r = 100$ kHz

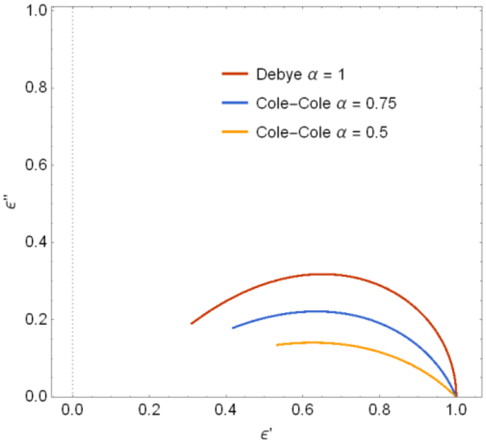

(c) Havriliak-Negami Relaxation.

- Fixed Parameter $\beta = 0.5$ for both peaks

Double peak

Left Peak

- $\varepsilon_\infty = 0.1$
- $\Delta\chi^0_{\alpha\beta} = 0.25$
- $f_r = 100$ kHz

Right Peak

- $\varepsilon_\infty = 0.35$
- $\Delta\chi^0_{\alpha\beta} = 0.65$
- $f_r = 5$ kHz.

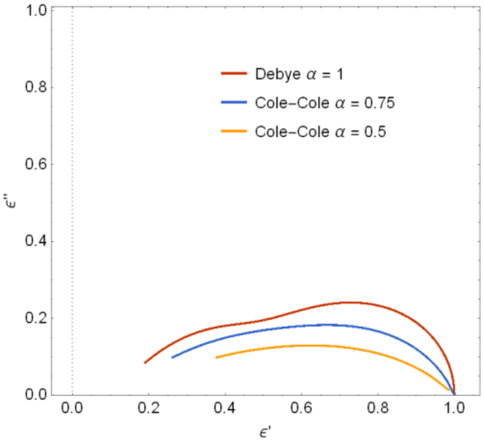

Figure 2.2: Cole-Cole plot of simulated data comparing the relaxation types.

The data are simulated for $\varepsilon_{\alpha\beta}$ generated from 20 Hz to 1 MHz (the measuring capability of the apparatus). Part (a) shows the case of Cole-Cole relaxation with two relaxation peaks. Part (b) shows a single relaxation peak for Havriliak-Negami relaxation. Part (c) shows a double relaxation peak for Havriliak-Negami relaxation. Cole-Davidson is shown where $\beta < 1$ and $\alpha = 1$.

2.2.4 Low-Frequency Contributions

There are three types of undesirable contributions to dielectric measurements at low frequencies: Ionic impurities, electrode polarization, and internal interfacial polarization (Maxwell-Wagner-Sillars polarization).

Ionic impurities are commonly present and only contribute to the measurement of the imaginary part of the relative dielectric permittivity $\varepsilon''_{\alpha\beta}$. It can be modeled as another relaxation process with a relaxation frequency that peaks below 1 Hz [25, 26]. However, actual measurements rarely go to the peak frequency. The asymptotic function used to describe it is:

$$\varepsilon_{\alpha\beta}^{ionic} = \frac{\sigma_{\alpha\beta}^{DC}}{i\varepsilon_0\omega}, \tag{2.14}$$

where the DC conductivity $\sigma_{\alpha\beta}^{DC}$ represents the ionic contributions.

For electrode polarization, the ions move within the field toward the electrodes then build up on the plates. This can contribute to both the real and imaginary parts of $\varepsilon_{\alpha\beta}(\omega)$. Its behavior is like a Debye relaxation mechanism [25, 26].

Lastly, the internal interfacial polarization occurs when the motion of migrating charges is impeded. This occurs in mixtures when electrically conducting regions are separated and prevented from being in contact with each other by non-conducting regions [34]. It also behaves similar to a Debye relaxation mechanism. For measurements ranging between 10 Hz and 10 MHz, only a tail can be seen, much like that for ionic impurities in Equation 2.14 [25]. However, it also has a contribution to the real part of the dielectric permittivity $\varepsilon_{\alpha\beta}(\omega)$ that increases $\varepsilon'_{\alpha\beta}$ at low frequencies [34]. Its behavior can be modeled with a $\frac{1}{\omega}$ function.

In some of the liquid crystal literature, Equation 2.14 is empirically modified and low frequency behavior is accounted for with an exponent *n* on the frequency,

$$\varepsilon_{\alpha\beta}^{lowfrequency} = \frac{\sigma_{\alpha\beta}^{0}}{i\varepsilon_0 \omega^n}, \qquad (2.15)$$

where “*n*” is a fitting parameter to account for various low frequency processes [26, 28, 35, 36].

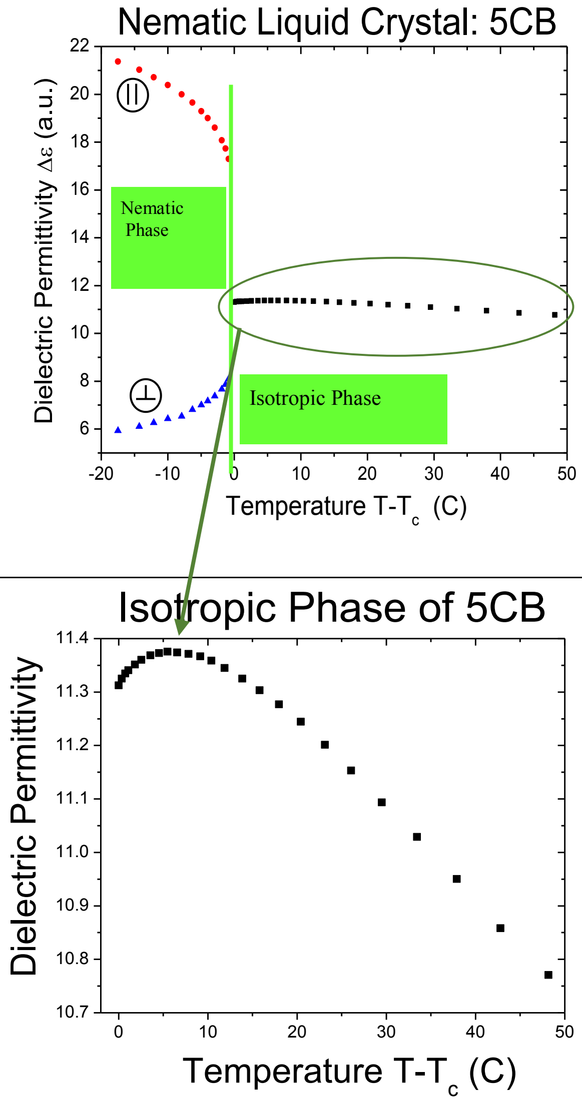

(a) Full Range of Data for 5CB

(b) Zoomed in to the Isotropic Phase

Figure 2.3: Both the isotropic and nematic phases of pentyl-cyano-biphenyl (5CB). Data from Thoen et. al. [37].

2.3 Temperature Dependence: Generalizing the Nematic Order Parameter

2.3.1 Motivation

The isotropic to nematic transition is weakly first order. This leads to short-range order effects having non-negligible contributions to various physical phenomena near the transition temperature [3]. The contributions are dependent upon a correlation length, as expressed in Equation 1.1. As the transition temperature is approached, the correlation length increases. This should lead to various pretransitional behaviors. The phenomenological approach of de Gennes, presented in Chapter 1, predicts several pretransitional effects of which two examples are discussed.

First, de Gennes predicted magnetic birefringence in the isotropic phase for nematic liquid crystals (LC). Nematics are easily aligned by both magnetic and electric fields, making them optically birefringent in the isotropic phase. When either an electric field E_β or a magnetic field H_β is applied, Equation 1.5 would have an additional term $Q_{\alpha\beta}E_\alpha E_\beta$ (or $\chi_{\alpha\beta}H_\alpha H_\beta$). Birefringence is predicted by minimizing the lowest-order terms in the free energy density of Equation 1.5 with the electric (or magnetic) field contributions added [3].

Second, in light scattering experiments, as the transition temperature T_c is approached, the intensity increases as $(T - T^*)^{-1}$. As the asymptotic critical temperature is approached, the correlation length becomes increasingly non-negligible [3]. Likewise, in heat capacity experiments, as ξ increases near the transition temperature, the heat capacity also anomalously increases.

While recent experiments show pretransitional dielectric effects on the isotropic side of the isotropic to nematic phase transition, de Gennes theory does not predict pretransitional dielectric effects on the isotropic side near the isotropic to nematic phase transition [37-46]. In Figure 2.3a, birefringent behavior is observed in the nematic phase as expected. When plotted on the same scale as the N phase, the isotropic phase appears almost linear. However, when the isotropic side is looked at more closely in Figure 2.3b, small but distinct pretransitional behavior in the form of deviations from linearity is observed [37].

2.3.2 A Generalized Nematic Order Parameter

Although $Q_{\alpha\beta}$ is a good choice for an order parameter, the rationale of subtracting out the isotropic part needs to be justified. Additionally, in field theory, all terms allowed by symmetry must be included. As can be seen from the Landau-de Gennes theory being applied to the smectic A-nematic transition, coupling is important to describe pretransitional behavior (i.e., ordering of one phase extending into another phase) [8].

A minimal modification to the Landau-de Gennes order parameter is to include all terms encapsulated in the full dielectric permittivity tensor $\varepsilon_{\alpha\beta}$ (contrary to Equation 1.14) and then to properly account for fluctuations in the free energy expansion [47]:

$$\varepsilon_{\alpha\beta} = Q_{\alpha\beta} + \frac{1}{3}\bar{\varepsilon}\,\delta_{\alpha\beta}. \tag{2.16}$$

The order parameter $Q_{\alpha\beta}$ retains its original definition as the anisotropic contribution to the generalized order parameter in Equation 2.16. The average of $Q_{\alpha\beta}$ would still be on average zero in the isotropic phase. However, fluctuations in $Q_{\alpha\beta}$ can now properly couple to the isotropic part $\bar{\varepsilon}\,\delta_{\alpha\beta}$.

For the more general order parameter in Equation 2.16, the form of the free energy expansion would be similar to Equation 1.5. However, instead of expanding in powers of a traceless tensor $Q_{\alpha\beta}$, the expansion would be in terms of the total permittivity $\varepsilon_{\alpha\beta}$ which has a non-zero trace. Since a Landau type expansion allows for all rotationally invariant scalars to be included, higher order terms of the trace itself would be included. Moreover, as in the de Gennes model, a gradient term $F_{gradient}$ is needed to account for fluctuations of the anisotropic part $Q_{\alpha\beta}$. With Equation 1.5 relabeled as $F_{anisotropic}$, we have a general free energy expression with four parts:

$$F_{general} = F_{anisotropic} + F_{isotropic} + F_{coupling} + F_{gradient}. \qquad (2.17)$$

Although the original order parameter $Q_{\alpha\beta}$ is zero on average in the isotropic phase, its square is not. Gradient terms are still present. To lowest order, the gradient term is expressed as,

$$F_{gradient} = \tfrac{1}{2} L Q_{\alpha\beta,\gamma} Q_{\beta\alpha,\gamma}. \qquad (2.18)$$

As with any expansion, it is important to consider the minimal number of terms needed to adequately describe the system. If the minimal expansion does not describe the experimental data, higher order terms can then be reincorporated. Before proceeding, this new free energy can be made more manageable and simplified in the isotropic phase through reasonable approximations. First, for $F_{isotropic}$, it is conceivable that the cubic and fourth power terms in $\bar{\varepsilon}$ describe important phenomena; however, they will be neglected for this research since deviations from $\langle\bar{\varepsilon}\rangle$ are not expected to vary too much from the higher temperature background value $\bar{\varepsilon}_{BG}$. Therefore, only second order terms in $\bar{\varepsilon}$ will be kept, as this allows for coupling. Second, for $F_{anisotropic}$ and $F_{coupling}$ in Equation 2.17, fluctuations about $Q_{\alpha\beta}$ are expected to be quadratic in the isotropic phase. Only up to second order in $Q_{\alpha\beta}$ is kept. Third, for fitting, it is useful to break up the isotropic term $\bar{\varepsilon}$ into two additive parts as seen in Equation 2.19. The first term is a temperature dependent background $\bar{\varepsilon}_{BG}$ describing the high temperature behavior in the absence of a phase transition while the second term is any deviation $\Delta\bar{\varepsilon}$ from that background as the isotropic to nematic transition is approached:

$$\bar{\varepsilon} = \bar{\varepsilon}_{BG} + \Delta\bar{\varepsilon}. \qquad (2.19)$$

Taking these approximations into account leads to the free energy expression in Equation 2.20a:

$$F_{General}^{Approx.} = \tfrac{1}{2} A_{eff} Q_{\alpha\beta} Q_{\beta\alpha} + h \Delta\bar{\varepsilon} Q_{\alpha\beta} Q_{\beta\alpha} + \tfrac{1}{2}\mu^{-1}(\Delta\bar{\varepsilon})^2 + \tfrac{1}{2} L Q_{\alpha\beta,\gamma} Q_{\beta\alpha,\gamma}. \qquad (2.20a)$$

The coefficients h and μ are combinations of the coefficients and $A_{eff}(T) = A - 2h\bar{\varepsilon} + g\bar{\varepsilon}^2$. The term h in Equation 2.20a describes the curvature seen in Figure 2.3b. All data studied in this dissertation have negative, downward curvature. As will be more evident later on in this dissertation, it is convenient to define downward curvature as having a positive h. For this, Equation 2.20a has the second term as $+h\Delta\bar{\varepsilon}Q_{\alpha\beta}Q_{\beta\alpha}$ to account for the negative curvature.

Now that the free energy is in a more manageable form, it is minimized with respect to deviations $\Delta\bar{\varepsilon}$:

$$\frac{\partial F_{general}}{\partial \Delta\bar{\varepsilon}} = hQ_{\alpha\beta}Q_{\beta\alpha} + \mu^{-1}\Delta\bar{\varepsilon} = 0,$$

$$\Delta\bar{\varepsilon} = -h\mu Q_{\alpha\beta}Q_{\beta\alpha}. \tag{2.20b}$$

By allowing for $Q_{\alpha\beta}$ to couple with the isotropic term, a prediction is made in Equation 2.20b for pretransitional behavior in the dielectric permittivity. To the lowest order, the variation in permittivity $\Delta\bar{\varepsilon}$ turns out to be directly proportional to $Q_{\alpha\beta}Q_{\beta\alpha}$, the square of the anisotropic part of the order parameter. Combining Equations 2.20a and 2.20b gives the following lowest order form for the free energy:

$$F_{General}^{Approx.} = \tfrac{1}{2}A_{eff}Q_{\alpha\beta}Q_{\beta\alpha} - \tfrac{1}{2}\mu h^2\left(Q_{\alpha\beta}Q_{\beta\alpha}\right)^2 + \tfrac{1}{2}LQ_{\alpha\beta,\gamma}Q_{\beta\alpha,\gamma}. \tag{2.21}$$

Fluctuations about $Q_{\alpha\beta}$ are expected to be small in the isotropic phase, so it is justifiable to neglect the quartic term in $Q_{\alpha\beta}$. While Equation 2.21 is re-expressed in terms of the original anisotropic component, quadratic fluctuations in $Q_{\alpha\beta}$ in the isotropic phase are now properly accounted for.

The fluctuations of $\langle Q_{\alpha\beta}Q_{\beta\alpha}\rangle$ remain to be calculated from Equation 2.21. It is convenient to convert to reciprocal q-space and then average. The nematic order parameter $Q_{\alpha\beta}$ has five independent modes that are the same in the isotropic phase. Expanding over all five fluctuation modes in Fourier space, the quadratic term is

$$\langle Q_{\alpha\beta} Q_{\beta\alpha} \rangle = \Sigma_{\vec{q}} \langle \tilde{Q}_{\alpha\beta}(\vec{q}) \tilde{Q}^{*}_{\beta\alpha}(\vec{q}) \rangle. \tag{2.22}$$

The average of the gradient term $Q_{\alpha\beta,\gamma} Q_{\beta\alpha,\gamma}$ is

$$\langle Q_{\alpha\beta,\gamma} Q_{\beta\alpha,\gamma} \rangle = \Sigma_{\vec{q}}\, q^2 \langle \tilde{Q}_{\alpha\beta}(\vec{q}) \tilde{Q}^{*}_{\beta\alpha}(\vec{q}) \rangle. \tag{2.23}$$

The expression for the free energy density in Fourier space for a single term in q may then be expressed as

$$\mathcal{F}_{general,q} = \tfrac{1}{2}\left(A_{eff} + Lq^2\right) \langle \tilde{Q}_{\alpha\beta}(\vec{q}) \tilde{Q}^{*}_{\beta\alpha}(\vec{q}) \rangle. \tag{2.24}$$

The equipartition theorem may now be invoked. Each term in q in Equation 2.24 is set equal to $\frac{1}{2} k_b T$:

$$\mathcal{F}_{general,q} = \tfrac{1}{2} k_b T = \tfrac{1}{2}\left(A_{eff} + Lq^2\right) \langle \tilde{Q}_{\alpha\beta}(\vec{q}) \tilde{Q}^{*}_{\beta\alpha}(\vec{q}) \rangle. \tag{2.25}$$

After rearranging Equation 2.25, the average $\langle Q_{\alpha\beta} Q_{\beta\alpha} \rangle$ is found by integrating over Fourier space to the maximum wave-vector q_{max}:

$$\langle Q_{\alpha\beta} Q_{\beta\alpha} \rangle = \Sigma_{\vec{q}} \langle \tilde{Q}_{\alpha\beta}(\vec{q}) \tilde{Q}^{*}_{\beta\alpha}(\vec{q}) \rangle = \frac{5 k_b T 4\pi}{(2\pi)^3} \int_0^{q_{max}} dq \, \frac{q^2}{A_{eff} + Lq^2}. \tag{2.26}$$

After integrating, $\langle Q_{\alpha\beta} Q_{\beta\alpha} \rangle$ is found to be

$$\langle Q_{\alpha\beta} Q_{\beta\alpha} \rangle = \frac{5 k_b T}{2\pi^2} \left(\frac{q_{max}}{L} \right) \left[1 - \left(\sqrt{\frac{L}{A_{eff}}}\, q_{max} \right)^{-1} arctan \left(\sqrt{\frac{L}{A_{eff}}}\, q_{max} \right) \right]. \tag{2.27}$$

The factor of five in Equation 2.27 comes from all five modes of $Q_{\alpha\beta}$ having the same average in the isotropic phase. The term $\sqrt{\frac{L}{A_{eff}}}$ is the temperature dependent correlation length ξ mentioned in Equation 1.1. Combining Equations 2.19 and 2.20b with the result of Equation 2.27 results in

$$\bar{\varepsilon} = \bar{\varepsilon}_{BG} - h\mu \frac{5 k_b T^{*} q_{max}}{2\pi^2 L} \frac{T}{T^{*}} \left[1 - \left(q_{max} \xi_0 \sqrt{\frac{T^{*}}{T - T^{*}}} \right)^{-1} arctan \left(q_{max} \xi_0 \sqrt{\frac{T^{*}}{T - T^{*}}} \right) \right]. \tag{2.28}$$

The term $\bar{\varepsilon}_{BG}$ is the isotropic background value. The background is not predicted by this theory; only the deviation from the background is predicted. The high temperature data in Figure

2.3b (that is, furthest from the transition) reveals that a background that is linear in temperature is sufficient for many samples. However, a higher order temperature dependence may be needed in some cases.

Note that the above theory is developed for just achiral nematic liquid crystals. Second order fluctuations about the isotropic and anisotropic components of the generalized order parameter $\varepsilon_{\alpha\beta}$ are included. There are five fluctuation modes accounted for in this derivation.

2.4 Summary

With the generalized order parameter, the temperature dependent pretransitional anomalies such as those in Figure 2.2 can now be characterized. Although the current derivation does not include any term for chirality, it can be applied to chiral results to see where the theory needs additional terms to account for chirality.

Back to the first goal of this dissertation, the result from Equation 2.28 will be used in Chapter 4 to fit and compare published data. Good agreement is found.

The relative dielectric permittivity tensor $\varepsilon_{\alpha\beta}$ has useful information concerning the orientational order parameter. Moreover, both the isotropic and anisotropic parts must be included in the free energy expansion in order to properly allow for fluctuations of $Q_{\alpha\beta}$ to couple with the isotropic part.

The analysis of the frequency dependence of $\varepsilon_{\alpha\beta}$ is a well-established framework. For isothermal results in which the frequency was swept, this will be used to understand the relaxation phenomena of my samples.

CHAPTER 3 EXPERIMENTAL SETUP AND METHODS

This dissertation has two general themes: to apply the generalized nematic order parameter to published dielectric data, and to investigate the dielectric behavior of cholesteric phases including the emergence of blue phases in the high chirality limit. The dielectric permittivity is central to both of these themes.

First, a discussion is needed on how the dielectric permittivity is measured as a function of both frequency and temperature. While frequency control is an embedded function in the Agilent 4284A LCR meter used in my investigation, the temperature control was a more involved effort and will be discussed in detail.

Second, the data acquisition algorithm will be described. As will be discussed in the first part, the dielectric permittivity has both a frequency and a temperature dependence to measure. Each of these require different approaches.

Third, the measurements are of mixtures of two molecules. Each mixture represents a different chirality. This serves as a chirality scale.

Fourth, with dielectric measurements, each phase may give a distinct curve. However, for additional verification of what phase a particular dielectric signature represents, optical cross-polarized microscopy is utilized.

Lastly, non-linear curve fitting is necessary. The order parameter has been generalized to allow for a description of pre-transitional behavior. Also, the frequency response data will be fitted according to Cole-Cole’s relaxation model. The results from Chapter 2 need to be expressed in a form that is more easily used for testing the model.

3.1 Experimental Measurement of the Complex Dielectric Permittivity

3.1.1 Circuit Model

In order to easily apply an AC electric field E_β, a material needs to be sandwiched between two electrodes. This by definition is a capacitor. The simplest capacitor to construct is a parallel plate capacitor in which the field lines of E_β are uniform. The capacitance of such a capacitor is given by the function,

$$C_{material} = \varepsilon_0 \varepsilon' \frac{A}{d}, \qquad (3.1a)$$

where ε_0 is the constant permittivity of free space, ε' is the relative dielectric permittivity characterizing the material, A is the area of the portion of the electrode in contact with the sample given by $A = wh$ from Figure 3.1a, and the electrode separation d.

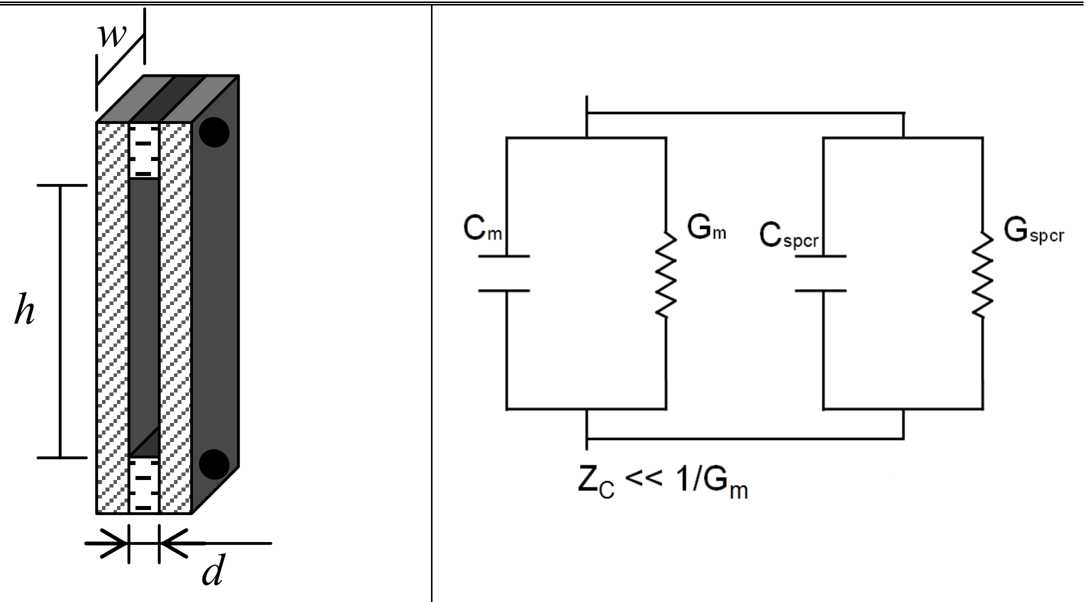

(a) Parallel plate capacitor with spacers

(b) Circuit model for a parallel plate capacitor with spacers

Figure 3.1: A parallel plate capacitor of width *w*, height *h*, and separation *d*.

The white objects with horizontal dashed lines are spacers (that is, dielectric materials separating the metal electrodes). The area of the spacers need to be accounted for.

When the capacitor is filled, its ability to store energy goes up by a factor ε'. The capacitance of only air is called the open cell capacitance C_0:

$$C_0 = \varepsilon_0 \frac{A}{d}. \tag{3.1b}$$

The impedance of a capacitor is given by,

$$Z_C = \frac{1}{i\omega C}, \tag{3.1c}$$

where ω is the applied angular frequency. If the material is not perfectly insulating, then it will also have a conductance G (i.e., inverse resistance Z_G). Analogous to Equation 3.1a, conductance can be related to a material property σ, conductivity,

$$G_{material} = \sigma \frac{A}{d}. \tag{3.1d}$$

As shown in Figure 3.1b, the conductance G is modeled as being in parallel with the corresponding capacitance. The capacitor plates are usually separated by a spacer made of an insulating or dielectric material such as Teflon. Between the electrodes, the Teflon spacers are also modeled as a capacitor in parallel with a conductance G. Figure 3.1b and Equation 3.1c lead to a set of equations for the total impedance Z of the parallel plate capacitor cell for two states: the filled cell state, and the unfilled open cell state. The open cell impedance is given by,

$$\left(Z_{opencell}\right)^{-1} = G_{opencell} + i\omega\left(C_{opencell}\right), \tag{3.2a}$$

$$\left(Z_{opencell}\right)^{-1} = G_0 + G_{spacers} + i\omega\left(C_0 + C_{spacers}\right). \tag{3.2b}$$

The filled cell impedance can likewise be expressed as,

$$\left(Z_{filled}\right)^{-1} = G_{filled} + i\omega\left(C_{filled}\right), \tag{3.3a}$$

$$\left(Z_{filled}\right)^{-1} = G_{material} + G_{spacers} + i\omega\left(C_{material} + C_{spacers}\right). \tag{3.3b}$$

Subtracting Equation 3.2b from Equation 3.3b eliminates the need to measure and calculate the spacers' conductance and capacitance:

$$\left(Z_{filled}\right)^{-1}-\left(Z_{opencell}\right)^{-1}=G_{material}-G_0+i\omega(C_{material}-C_0). \qquad (3.4)$$

Using Equations 3.1a, 3.1b, 3.2a and 3.3a, the measured values of *C* and *G* can be related to the desired material values of *C* and *G*,

$$C_{material}=C_{filled}-C_{opencell}-C_0, \qquad (3.5a)$$

$$G_{material}=G_{filled}-G_{opencell}-G_0, \qquad (3.5b)$$

where C_0 and G_0 are the capacitance and conductance of air, respectively. The conductance of the air G_0 is zero. Taking into account Equations 3.1a and 3.1b in Equation 3.5a gives,

$$\varepsilon'=\frac{C_{filled}-C_{opencell}}{\varepsilon_0\frac{A}{d}}-1, \qquad (3.6a)$$

which is the real part to the relative permittivity discussed in Chapter 2, specifically from Equation 2.4c. Similarly, taking into account Equations 3.1b, 3.1d, and 3.5b,

$$\frac{\sigma}{i\varepsilon_0\omega}=\frac{G_{filled}-G_{opencell}}{\varepsilon_0\frac{A}{d}}. \qquad (3.6b)$$

The term $\frac{\sigma}{\varepsilon_0\omega}$ is called the imaginary part of the relative dielectric permittivity, ε'' (i.e., the dielectric loss). Adding Equations 3.6a and 3.6b together gives an equation identical to Equation 2.4c:

$$\varepsilon(\omega,T)=\varepsilon' - i\,\frac{\sigma}{\varepsilon_0\omega}. \qquad (3.7)$$

This is an expression for the complex dielectric permittivity that can be calculated from any measurement performed at a given angular frequency *ω* and temperature *T*.

3.1.2 Setup, Sample Containment, Frequency, Capacitance, and Conductance

A parallel plate capacitor was constructed. Figure 3.2 is a schematic of the capacitor and sample containment cell setup. The capacitor was submerged into a glass cuvette containing the sample and then placed into an aluminum oven with a temperature control element. Figure 3.3 shows a photograph of the setup capacitor submerged into the filled cuvette.

The shape of the capacitor was determined by the available glass cuvettes. Glass was chosen over the acrylic cuvettes as they were robust over the temperatures measured and did not react with the samples. Also, submerging the capacitor into the liquid sample ensured that the space between the plates was completely filled with no leakage. The setup was connected to an Agilent 4284A LCR meter in order to apply an AC field E_β at an angular frequency ω and to measure both capacitance and conductance. Note that the nylon screws pierced the Teflon spacer area and the brass electrodes. This allowed for a sturdy assembly. The temperature control will be discussed in more detail shortly.

The LCR meter had the option for the output to be expressed as either impedance with a phase shift or capacitance with conductance. Both cases were equivalent and used the model from Figure 3.1b in which a capacitor is in parallel with a resistor (called "Parallel Mode" on the meter). The capacitance and conductance were chosen as the recorded output. The real and imaginary parts of the complex relative permittivity were more intuitively related to the capacitance and conductance. Each measurement was time averaged over 990 ms.

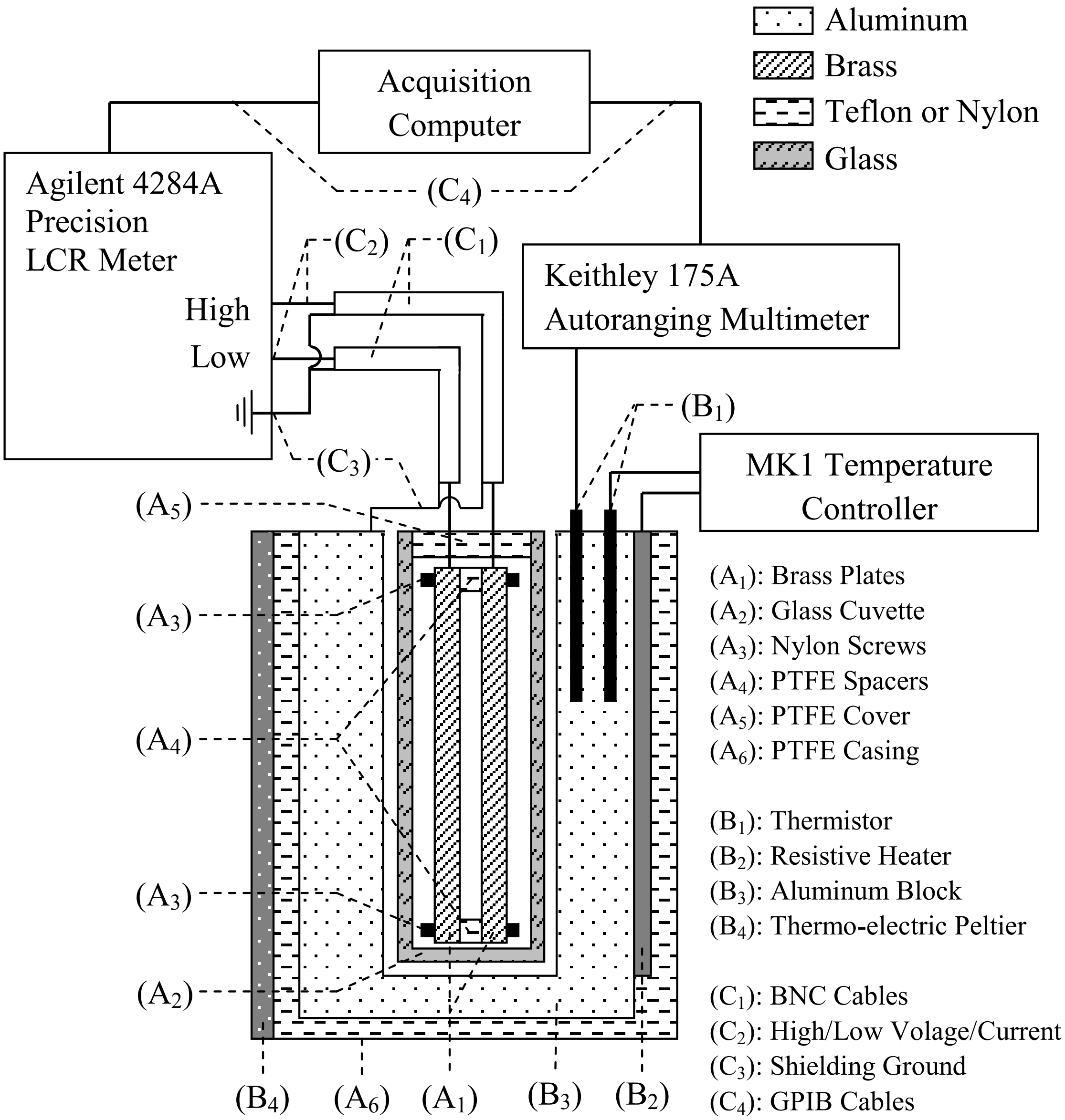

Figure 3.2: The schematic of my experimental setup and oven.

Two things are not included in this schematic but should be noted: between the peltier thermoelectric and PTFE casing is a thin sheet of copper covering all but the top of the setup. Excluding the side with the peltier as well as the top, all sides were further insulated to allow for better thermal control.

(a) Without Insulation

(b) With Insulation

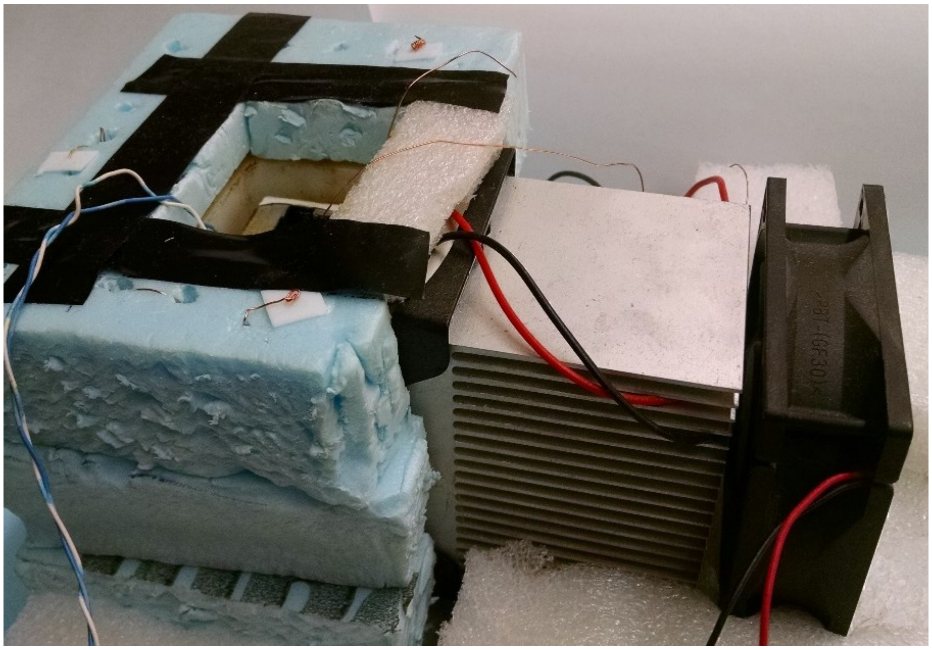

Figure 3.3: A photograph of the experimental setup and oven without the capacitor.

The aluminum casing for the cuvette can be seen in the upper left hand corner. It has the resistive heater affixed directly onto it. Surrounding that is a PTFE casing. Surrounding that is a copper sheet. In the center of the pictures a black and red wire are seen on top connecting to the peltier device. Between the fan on the far right and the peltier device in the middle is a CPU heat sink to help draw away heat. In part (b), foam insulation can be seen around the copper plate on the left to help regulate temperature.

Figure 3.4: A picture of the capacitor submerged into the cuvette prior to placing into the oven.

The PTFE tape was used to seal the setup so as to protect the sample from the air as well as to provide a flexible cap to prevent the sample from leaking out in the event the cuvette was moved relative to the plates. A BNC wire was exposed from the BNC cable, embedded into each plate and then soldered in place.

3.1.3 Controlling and Measuring Temperature

The temperature was controlled by a separate computer and thermistor. The temperature was passively recorded by the acquisition computer with a second thermistor.

A thin copper sheet further enclosed the four side walls and bottom of the setup around the PTFE casing referred to in Figures 3.2 and 3.3. Thermal conductivity between the copper sheet and casing was enhanced with a layer of *Arctic Silver 5 Thermal Compound* in between – this compound is commonly used between the heat sink of a CPU (central processing unit) and the CPU itself. The heat sink and fan were reclaimed from a defunct motherboard. This setting was adapted for thermal regulation here. From Figure 3.3, the top side was left open to allow for wires to pass through and was mostly covered for each experiment with insulating foam. The bottom side and three sides were covered with insulating foam. The side with the thermoelectric Peltier device (opposite to the heater) had the cooling side adhered to the copper sheet with the thermal compound. A CPU heat sink fixture was screwed into the PTFE casing and affixed such that the hot side of the thermo-electric Peltier device made good mechanical contact with it. A CPU fan was attached to the outside of the heat sink to facilitate drawing the heat produced by the Peltier away.

From Figure 3.2, there are two thermistors (B_2) inserted into adjacent holes that were bored into the aluminum block. One was connected to the MK1 temperature control computer. The temperature given by the MK1 system was used as reference. The second thermistor was connected to a Keithley 175A multimeter which was connected to the acquisition computer. The temperature was measured in units of resistance. The resistance was calibrated prior to each experiment to the temperature given by the MK1 temperature control system.

3.1.4 Recording Frequency, Effective Temperature, Capacitance, and Conductance

The data were recorded on the acquisition computer using the program LabVIEW. This allowed for a partially automated measurement in which the frequency was actively controlled while the temperature was passively recorded. The data were recorded in four columns: frequency, temperature in units of resistance, capacitance, and conductance. From the Agilent 8284A Precision LCR meter, the frequency f, capacitance C, and conductance G were recorded. From the Keithley 175A Autoranging Multimeter, the effective temperature was recorded as resistance. This resistance was calibrated to the temperature of the separately controlled MK1 temperature controller. The MK1 temperature controlling computer was not controlled by the acquisition computer due to technical difficulties.

3.2 Measurement Procedure

3.2.1 Capacitor Assembly

Prior to each measurement, the setup was disassembled, cleaned, and reassembled. The thickness of both plates at both the top and bottom portions was measured. When the plates and spacers were assembled and fixed into place by the nylon screws, the thicknesses of both the top and bottom portions were again measured. This thickness minus the thickness of the individual plates gave the spacing. Prior to reassembly, the PTFE spacers were measured to be just under 0.39 mm with calipers. The screws were adjusted so that this spacing was as close to 0.38 mm as possible to ensure the setup was in good mechanical contact. The results of these measurements averaged over every experiment are seen in Table 3.1.

Table 3.1: The dimensions of the capacitor.

Prior to each material studied, the capacitor was taken apart, cleaned, and reassembled. Due to this method, it was determined that re-measuring the setup each time would serve as a diagnostic tool in the event problems were encountered. With that said, there were two calibrations. After July 2013, one of the spacers was lost and needed to be replaced.

(a) Pre July 2013 setup measurements

Total Area A_{total} (mm^2)	379.7 ± 0.2
Spacer Area$A_{spacers}$ (mm^2)	108.4 ± 0.6
Open Cell Area A_0 (mm^2)	271.3 ± 0.7
Plate Spacing d (mm)	0.375 ± 0.004

(b) Post July 2013 setup measurements

Total Area A_{total} (mm^2)	379.7 ± 0.2
Spacer Area $A_{spacers}$ (mm^2)	103.0 ± 0.2
Open Cell Area A_0 (mm^2)	276.7 ± 0.3
Plate Spacing d (mm)	0.383 ± 0.008

3.2.2 Scenario 1: Constant Temperature, Sweep Frequency

The experiment involved two scenarios. The first scenario was to obtain the frequency dependence. The frequency was swept from 20 Hz to 1 MHz while the temperature was held constant. Each frequency sweep took about 36 minutes. Each frequency was sampled for 30 seconds at one second intervals. The hard disk drive used had a 0.2 second delay in recording each measurement (that is, the LabVIEW program was setup to write every measurement to the file as opposed to memory; this served as a precaution toward power failures, but inherently slowed down the acquisition computer. This lag was measured to be 0.2 seconds per write). The measured capacitance and conductance were time averaged. Upon changing the frequency, the system was programmed to allow for a 10-second pause prior to recording the next frequency; this allowed sufficient time to avoid transient effects due to switching. The setup had a five decade recording capability. From preliminary tests, ten frequencies per decade appeared to be a reasonable resolution data; the capacitance and conductance were measured for 47 frequencies. The frequency sweeps would terminate automatically.

The temperature had to be manually changed to the next temperature. To ensure the experiment was working properly, the acquisition computer displayed the acquired data in real-time as a function of time. Prior to beginning the subsequent frequency sweep, I waited for the temperature, capacitance, and conductance to be constant as a function of time at 10 kHz.

3.2.3 Scenario 2: Ramp Temperature, Constant Frequency

For the second scenario, the frequency was held constant. The temperature was cycled at 0.2 °C/min from around 15 °C below the expected mesophase-isotropic transition and to around 25 °C into the isotropic phase. At both the lowest and highest temperatures measured, the temperature was held constant for about 50 to 60 minutes. A typical heating and cooling cycle took eight hours. At least three temperature cycles were recorded per frequency. At a given frequency, the system would continue cycling until stopped manually.

To ensure the experiment was going well, the acquisition computer displayed the acquired data in real-time. At the upper and lower temperatures, the capacitance and conductance were monitored to ensure they were constant over the hour mentioned in the previous paragraph. During this time, the frequency was manually changed when testing the thermal response at a low and high frequency.

3.2.4 The Open-Cell Measurement

Prior to each sample measurement, the parallel plate capacitor setup was disassembled and cleaned. After reassembling, the physical dimensions of the setup were re-measured. Scenario 2 was then performed at 10 kHz (the desired frequency for the samples) to test repeatability over multiple temperature cycles between 25 °C and 100 °C.

Scenario 1, the frequency response of the setup, was then measured and recorded over six discrete temperatures ranging between 30 °C and 80 °C, the planned measurement range for the samples. The open-cell capacitance C_{opc} and conductance G_{opc} were recorded as functions of temperature and frequency. The temperature dependences of C_{opc} and G_{opc}were fitted to a third order polynomial per frequency so as to compare to the filled cell temperature sweep data.

3.2.5 The Filled-Cell Measurement

After sufficiently characterizing the open cell, the capacitor was dipped into a cuvette of the liquid crystal sample. This was done slowly to allow air bubbles to diffuse out. The cuvette and capacitor together were sealed by PTFE tape. Scenario 2 was then carried out both to ensure that the system was working (i.e., continuous change from one temperature to the next, constant capacitance and conductance at constant temperature) and to obtain an initial estimate of the mesophase-to-isotropic phase transition.

Scenario 1 was then carried out. Based on the initial high temperature phase transition, the discrete temperatures were chosen such that at least two were in the isotropic phase, at least four were below and near the isotropic transition, and at least one was near the lowest temperature to be measured.

Scenario 2 was then carried out again. Two frequencies were chosen: 10 kHz and 100 kHz. The temperature was cycled for three to four times for each frequency. At minimum, multiple cycles served as a test of system repeatability.

3.3 Chirality Scale and Samples

The blue phases, which are isotropic, appear in the high chirality limit. An easy way to vary the chirality is to prepare various mixtures of two compounds that are of opposite chirality. Two molecules were chosen because of their previous use in light scattering experiments: cholesteryl oleyl carbonate (COC, left handed) and cholesteryl chloride (CC, right handed). The chemical structure of each of these can be seen in Figures 1.4a and 1.4b. Cholesteryl chloride has a strong longitudinal dipole, while COC does not. Cholesteryl oleyl carbonate has the advantage that it is highly chiral and easy to handle near room temperature with a blue phase III to isotropic phase transition around 39 °C.

Both cholesteryl chloride and cholesteryl oleyl carbonate have monotropic phase transitions. This means that the phase sequences are different on heating versus cooling. Cholesteryl chloride goes from crystal to isotropic on heating. However, on cooling it goes from isotropic to blue phases I and II followed by cholesteric on cooling. Cholesteryl oleyl carbonate transitions from smectic A to cholesteric to isotropic on heating. On cooling from the isotropic phase, COC transitions to blue phases III, II, and I followed by cholesteric then smectic A at the lowest temperatures.

The cholesteryl oleyl carbonate rich mixtures were more stable than the cholesteryl chloride rich mixtures. From cross-polarized microscopy observations, the cholesteryl oleyl carbonate rich mixtures did not spontaneously crystallize between their isotropic-mesophase transitions and room temperature. Observed with cross-polarized microscopy, cholesteryl chloride is a crystal from room temperature through 98 °C. After melting, the sample is cooled. On cooling, cholesteryl chloride stays an isotropic liquid down to 71.5 °C. At 71.5 °C a green, speckled blue phase appears and persists down to 70.3 °C. The N* phase forms below that. On further cooling, the N* phase persists until 60 °C. Between 60 °C and 55 °C, N* can exist. However, if the temperature is held too long (anywhere between a few minutes and a couple of hours), the sample spontaneously crystallizes. Once this happens, it has to be heated back up to 98 °C. The heating and cooling cycles are repeatable for cross-polarized microscopy observations.

For dielectric measurements, the heating and cooling cycles at constant frequency were not repeatable for cholesteryl chloride. With an applied field, heating and cooling from a crystal to isotropic apparently placed too much stress on cholesteryl chloride. It eventually broke down chemically after one to two cycles. This resulted in a sticky, viscous, brown goo forming, beyond which the sample was destroyed. The cholesteryl chloride rich mixtures (above 70% cholesteryl chloride) followed this same pattern of breaking down after one or two heating and cooling cycles.

Since the blue phases are of primary interest, it is reasonable to focus on the mixtures that are of high enough chirality to exhibit a blue phase. For these mixtures, the BPs are not seen above 35% cholesteryl chloride. Out of curiosity, up through 60% cholesteryl chloride was successfully measured. Beyond that, the above mentioned problem occurred.

As mentioned in Table 3.1, two different permittivity conversion calibrations were used. The pre-July 2013 measurements were for the following percent mixtures of cholesteryl chloride with cholesteryl oleyl carbonate: 0%, 3%, 6%, 12%, 20%, 30%, and 40%. The post-August 2013 measurements were a premeasurement of the 0% mixture for comparison followed by 1.5%, 16%, 25%, 35%, 45%, 50%, 55%, and 60%.

3.4 Data Processing, Curve Fitting, Analysis

3.4.1 Own Data

The data acquired, mentioned in Section 3.2, were imported into MATLAB. An in-house script was developed to convert the raw data into relevant quantities: resistance of thermistor to temperature, capacitance to the real part of the relative dielectric permittivity, and conductance to the imaginary part of the relative dielectric permittivity. The results were then plotted and saved in various formats for further analysis. Excel and OriginLab were then used for collating the resulting plots.

The frequency dependent data were exported into Mathematica for non-linear curve fitting. The Havriliak-Negami and Cole-Cole equations (Equations 2.9, 2.11, and 2.13) were used for modeling the data. The equation for fitting was expressed as,

$$\varepsilon = \varepsilon_\infty + \frac{\Delta\chi_0}{\left(1+\left(i\frac{\omega}{2\pi f_r}\right)^{\alpha}\right)^{\beta}} + i\,\frac{S}{\omega^N}, \qquad (3.8)$$

where ε_∞ is the high frequency permittivity, $\Delta\chi_0$ is the real-axis width of the dispersion arc, f_r is the linear relaxation frequency, α is the shift in the dielectric loss, β is the amount of linearity in the high frequency data, S is an effective DC conductivity, and N is a fitting parameter for quantifying low frequency contributions to the dispersion. For the results shown in Chapter 5, parameter β was fixed at a value of one due to limited high frequency data.

Excel, Mathematica, and Origin are used extensively for the remainder of the temperature dependent analysis.

3.4.2 General Nematic Order Parameter: Data from Other Groups

Low frequency, dielectric data were acquired in two ways: directly from the author as is the case for the Leuven group [28, 37], and from the published plots in papers as is the case for the Warsaw group [38-46]. All of these data were for the temperature dependence at constant frequency for liquid crystals. Of the 22 data sets looked at, 15 were samples that have a nematic-isotropic phase transition. Six of the data sets have a smectic-isotropic phase transition. One data set has a chiral nematic to isotropic phase transition.

For the Warsaw group [38-46], the data were extracted from figures in published papers using a program called *WinDig*. The graphs were saved as picture files and loaded into *WinDig*. Using the graph axes as reference, *WinDig* allows for a calibration to be used in order to extract and save numerical information.

Both groups obtained data for the *n*CB homologue series, where *n* is length of the carbon chain attached to the rigid cyano-biphenyl (CB) group. This allows for a comparison of the resultant fitting parameters as a function of both carbon chain length *n* and frequency as the Rzoska group obtained their data at a different frequency from that of Thoen et al. Rzoska et. al. also obtained data for various other compounds such as the *n*OCB series (6, 7, and 8OCB). The *n*OCB homologue series is like *n*CB except that an oxygen atom separates the carbon chain from the CB core. This provides another useful comparison.

All of the above mentioned data exhibit pretransitional curvature in the isotropic phase as the lower temperature mesophase is approached. The aim of Equation 2.28 is to be a model that adequately describes this pretransitional dielectric behavior. The need for this is motivated by

Figure 2.2. While it is possible to apply this general approach to the nematic side of the transition, it is desired to first test the validity of Equation 2.28 in the isotropic phase.

TableCurve was used for initial curve fitting. The results were then repeated in MATLAB and Mathematica. Each program has advantages. The goodness of fits is assessed by χ^2 versus each fitting parameter per program. The standard error (i.e., the uncertainty in each fitting parameter calculated from the non-linear least squares routine using the best fit χ^2 parameter) is useful obtaining error bars on the fitting parameters. However, its calculation is a bit trickier since the data do not have included error bars. The uncertainty in each data point is estimated by both the least significant figure in the data as well as the spread over an entire data set. The spread in a given data set will be discussed in Chapter 4.

The non-linear fitting routines use chi-square as a way of estimating the parameter values as well as calculating the standard errors. In particular, the programs are setup to use the Levenburg-Marquardt method. Chi-square is defined as,

$$\chi^2 = \sum_i^N \left(\frac{\bar{\varepsilon}-y_i}{\sigma_i}\right)^2. \tag{3.9}$$

The fitting function is represented by $\bar{\varepsilon}$. The ith data points are represented by y_i. The index N represents the number of data points, and σ_i is the estimated uncertainty per data point. For five fitting parameters A, B, C, D, and E, the estimated values are obtained by minimizing χ^2, which results in a system of equations.

In addition to χ^2, it is informative to know what the standard errors are. Mathematica computes the estimated standard errors using the correlation matrix. For five parameters, this would be a five-by-five matrix in which the square root of the diagonal elements return the standard errors.

For each fit, a method called range shrinking will be used. This involves deleting *m* data points in order from the highest temperature data and seeing how that changes the fit, including χ^2 and the estimated standard errors. In order to compare each fit of different number of data points, χ^2 must be normalized by the number of degrees of freedom of the fit ν:

$$\nu = N - m - k. \tag{3.10}$$

The integer *N* is the number of data points, *m* the number of data points subtracted, and *k* the number of fitting parameters. This normalized quantity is the reduced chi-square,

$$\chi_\nu^2 = \frac{\chi^2}{\nu}. \tag{3.11}$$

3.5 Summary

The setup and procedure have been discussed in detail as well as how to measure the complex dielectric permittivity. The dielectric permittivity is key to both themes of this dissertation. The first theme is to test the generalized order parameter, Equation 2.28, on published data. The second theme is to experimentally investigate the dielectric behavior of cholesteric phases as chirality is varied. The second theme also will look at emergence of blue phases between the cholesteric and isotropic phases in the high chirality limit.

Non-linear curve fitting is necessary for both the frequency response equations as well as for the generalized nematic fluctuation equation. The fitting parameters will be compared. Moreover, the equation from the general nematic order parameter may be applied to chiral data. Strictly speaking, Equation 2.28 is applicable in the zero-chirality. It would be interesting to see at what point it breaks down for higher chirality.

CHAPTER 4 THE GENERALIZED NEMATIC ORDER PARAMETER APPLIED

In Chapter 2, the theory for a more general nematic order parameter was discussed. This was needed in order to describe the anomalous dielectric curvature seen near the isotropic to nematic phase transition. The resultant model of this theory, Equation 2.28, will now be applied to dielectric data obtained from other research groups [28, 37-46]. The model's ability to analytically describe the relevant data is studied.

The goal of this chapter is to find a robust fitting approach that applies to the available data sets [28, 37-46]. A typical sample (6CB from Thoen et. al. [28, 37]) will be used as a framework to discuss the results of various fitting approaches. The data for the typical sample are shown in Figure 4.1. Mentioned in Figure 4.1, for this chapter, a subscript index m will be used on fitting parameters when the full function is used. A subscript index μ will be used when an expansion is taken. A subscript index N will be used to refer to the entire temperature range of data available.

Sections 4.1 and 4.2 of this chapter are prologue for this chapter. Section 4.1 will begin with a recap of the equation of this theory. Equation 2.28 will be expressed in a way that is amenable to curve fitting. Fitting difficulties in the form of absurd results were experienced in the fitting of the full function. The initial approaches to overcome these difficulties and results of fitting the theory to example data are presented.

Section 4.2 attempts to understand the relationships among the fitting parameters by taking a series expansion of this theory. Three possible expansions are found to be reasonable for consideration with each having four parameters of identical definition. All three expansions are fitted to example data with their parameter estimates compared and shown.

Section 4.3 is the heart of this chapter. Using the relationships found from the series expansion, the full function is transformed into a hierarchical model that uses the form of the full function, Equation 2.28. The hierarchical model accounts for the parameter estimates as well as the relationships found from a series expansion.

Using the robust hierarchical model, Section 4.4 will end this chapter with the best parameter results for all samples investigated. These include those examined by the Leuven group who systematically obtained dielectric measurements for the *n*CB series under similar conditions at 1 kHz [28, 37]. The carbon chain length *n* ranged from five to twelve. The Warsaw group has a diverse selection of samples measured under various conditions and frequencies [38-46].

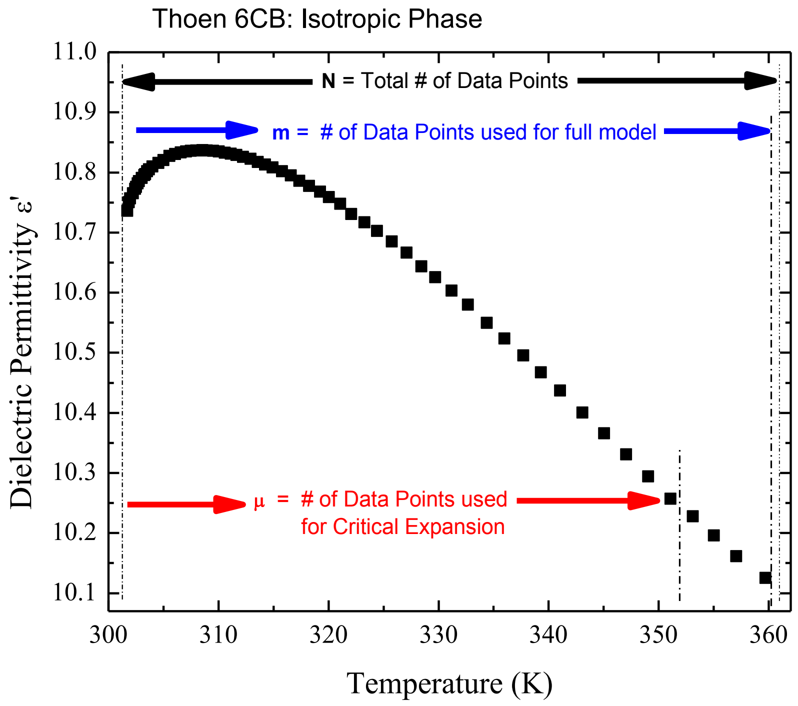

Figure 4.1: Isotropic data for a typical sample. The data set is of 6CB from the Leuven group, which represents two thirds of the data sets studied [28, 37].

The use of the indices *m* and μ are to distinguish between the two types of fits performed in this chapter:

- Black Horizontal Arrows: *N*: The total number of data points for a given sample.
- Blue Horizontal Arrows: *m*: The initial approach to analyzing the model (Equation 2.28) was to truncate the higher temperature side of the data. This is referred to as range shrinking. The number of data points leftover is *m*.
- Red Horizontal Arrows: μ: A series expansion is taken of the model discussed. Since a series expansion may not necessarily describe the entire range of temperature data, the higher temperature side of the data may need to be truncated or range-shrunk. The number of data points leftover is μ.

Additionally, as will be evident in this chapter, typical is with respect to the reduced chi-square χ_ν^2 vs D plots. Two-thirds of the data sets had a double minimum; one-third had a single minimum.

4.1 The Model and Results: Full Function

Prior to delving into finding a solution to the difficulties encountered in the fitting process, some background is needed. This section will first focus on only the full function. The section will then end with a discussion of the initial attempts to resolve apparently absurd results. These results will show a few of the difficulties encountered. However, the results will also show that there is an underlying pattern to these difficulties. Section 4.2 discusses the underlying patterns. Table 4.1 at the end of Section 4.1 shows the numerical fitting results for selected fits.

The model is given by Equation 2.28:

$$\bar{\varepsilon} = \bar{\varepsilon}_{BG} - h\mu \frac{5k_b q_{max}}{2\pi^2 L} T \left[1 - \left(q_{max}\xi_0\sqrt{\frac{T^*}{T-T^*}}\right)^{-1} arctan\left(q_{max}\xi_0\sqrt{\frac{T^*}{T-T^*}}\right)\right].$$

Equation 2.28 describes the pretransitional curvature that appears on the isotropic side of the nematic-isotropic phase transition. Typical data are seen in Figure 4.1. As mentioned in Chapter 2, the model is composed of two parts: the background $\bar{\varepsilon}_{BG}$ and the pretransitional curvature $\Delta\bar{\varepsilon}$.

4.1.1 The Fitting Parameters

In order to simplify the discussion Equation 2.28 is written in a more compact form. The first step is to define the reduced temperature x:

$$x = \frac{T-T^*}{T^*}. \tag{4.1a}$$

The reduced temperature is a dimensionless quantity that conveniently shows the relative temperature dependence with respect to the critical temperature T^*. The critical temperature T^* is the theoretical absolute temperature where the correlation length ξ would diverge in the absence of a phase transition. A typical data set has a reduced temperature range Δx of around 0.30. In Figure 4.1, this corresponds to an absolute temperature range of about 60 K.

It has been reported for the *n*-cyano-biphenyl series (referred to as *n*CB in this chapter) that T^* is expected to be no more than 2 K below the isotropic to nematic phase clearing temperature T_C [48]. The clearing temperature is the temperature at which the phase transition happens. The value of T_C is approximated by the lowest temperature data point in the isotropic phase which in this dissertation will be called T_{IM}. The subscript *IM* stands for isotropic-mesogenic, since more than one isotropic to mesogenic phase transition is discussed in this dissertation.

4.1.1.1 Fitting Parameters: The Background

The background $\bar{\varepsilon}_{BG}$ in the isotropic phase is not predicted by this generalized theory. The functional form of $\bar{\varepsilon}_{BG}$ needs to be estimated. By inspection of typical data seen in Figure 4.1, the highest temperature range of data (between 335 K to 360 K) can be fitted with a low order polynomial of order no more than two:

$$\bar{\varepsilon}_{initial\ background} = f_{BG}x^2 - Ax + B. \tag{4.1b}$$

The way chosen to justify either the exclusion or inclusion of f_{BG} is to fit the highest data points. For typical data seen in Figure 4.1, the highest temperature range of data (325 K to 360 K) are used to estimate the functional form of the background. Figure 4.2 shows the fitting parameter results for the cases of $f_{BG} = 0$ and f_{BG} as a free parameter for typical data. For completeness, the background ranges that were fit were from four to sixty-four data points. The total number of data points were 64. The value of four is the lowest number of data points allowed by least-squares regression for a three-parameter (quadratic polynomial) model in order to estimate the standard errors as well as other regression statistics.

In Figure 4.2, the abscissa is the number of data points used that counted from the highest temperature data point (see Figure 4.1 for reference). The quadratic coefficient in Figure 4.2a does not become constant over any range of background. The slope and intercept terms (Figure

4.2, parts (b) and (c), respectively) vary significantly more for the quadratic fit than for the linear fit. By inspection of Figure 4.1, a linear fit to the background ranges (that is, up to a range of 30 K) is reasonable. Figure 4.2, parts (b) and (c) confirm that the linear fit is indeed relatively constant for the 20 highest temperature data points (that is, up to a 30 K temperature range).

For typical data, the inclusion of $f_{BG}x^2$ in fitting the highest temperature data points (see Figure 4.2) does not show any range for which the quadratic fits parameters become constant over any range of data points (that is, temperature ranges). The inclusion of $f_{BG}x^2$ in the fitting process gives an extra degree of freedom that leads to further complications. For this dissertation, $\bar{\varepsilon}_{BG}$ is modeled as a two parameter linear function of reduced temperature x:

$$\bar{\varepsilon}_{BG} = -Ax + B. \tag{4.1c}$$

The slope is expressed with a negative sign as all data sets fitted at the high temperature side have negative slopes. Parameter B is the value of the background permittivity at the critical temperature T^* (that is, when the reduced temperature x is zero).

(a) Quadratic coefficient f_{BG}

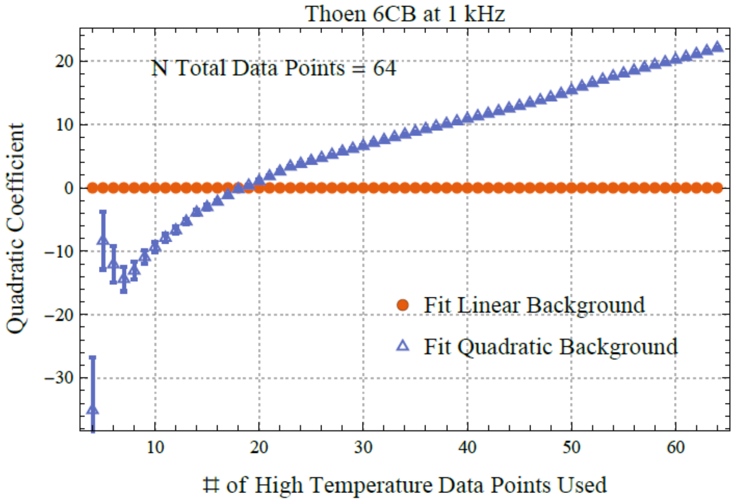

(b) Slope coefficient A. A flat line is desireable.

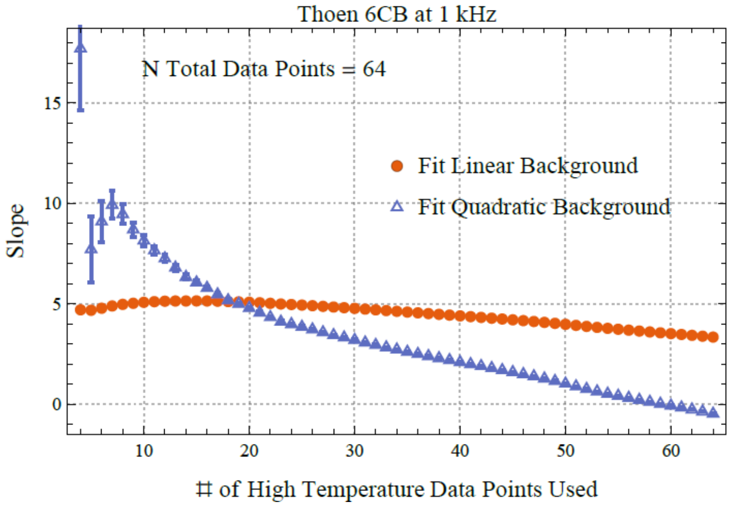

(c) Intercept B

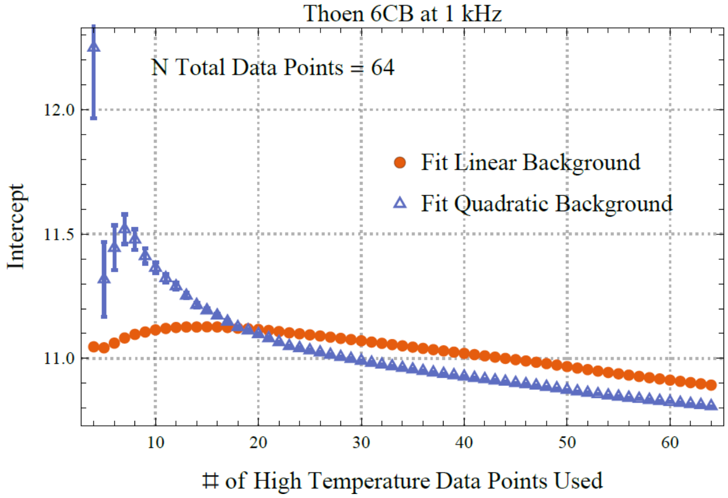

Figure 4.2: Estimating the background of 6CB from Thoen et. al.

4.1.1.2 Fitting Parameters: The Pretransitional Curvature

The pretransitional curvature can be defined with respect to two fitting parameters: C and D. The magnitude of the pretransitional curvature comprises multiple coefficients from the free energy expansion in Chapter 2. These will be made into a single fitting parameter:

$$C = h\mu \frac{5k_b q_{max}}{2\pi^2 L} T^*. \tag{4.1d}$$

Recall that in Equation 2.21 the coefficient h is defined to be a positive quantity for downward curvature. Likewise, C is positive for downward curvature as the other parameters in Equation 4.1d are always positive. All fitted data studied in this dissertation have a downward pretransitional curvature.

Since the cutoff wave vector q_{max} and the bare correlation length ξ_0 appear as a products in Equation 2.28, the product is made into a single, dimensionless fitting parameter D:

$$D = q_{max}\xi_0. \tag{4.1e}$$

Both the cutoff wavelength q_{max} and the bare correlation length ξ_0 are inherently positive quantities. The estimate of D is reported in the literature to be between 0.25 and 1 [48]. The Debye estimate of D, found by looking at a Wigner-Seitz cell in reciprocal space, is near a value of five.

The resultant fitting equation is, in terms of the reduced temperature x,

$$\bar{\varepsilon}_{full} = -A\mathrm{x} + B - C(1+x)\left[1 - \frac{\sqrt{x}}{D} arctan\left(\frac{D}{\sqrt{x}}\right)\right]. \tag{4.2}$$

Equation 4.2 will be referred to as $\bar{\varepsilon}_{full}$, the full function or the full model. The full function is a five parameter model: A, B, C, D, and T^*. Section 4.2 will show how these parameters are interrelated.

(a) All parameters $A, B, C, D,$ and T^* free. The initial D is set to less than or equal to 1. $\boldsymbol{\chi^2_{\upsilon,m} = 18.6}$

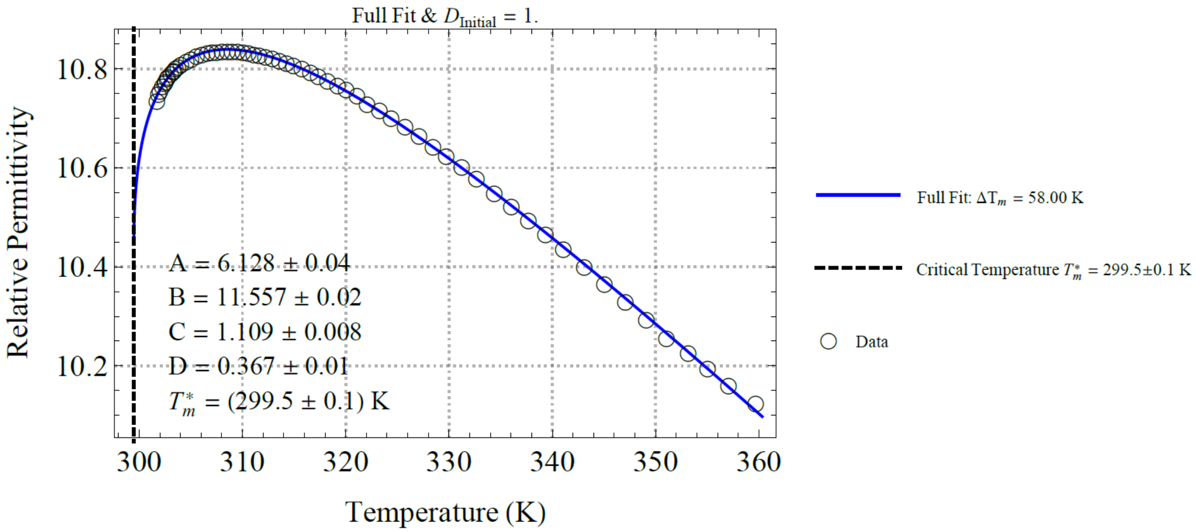

(b) All parameters A, B, C, D, and T^* free. The initial D is set to greater than 1. $\boldsymbol{\chi^2_{\upsilon,m} = 17.9}$

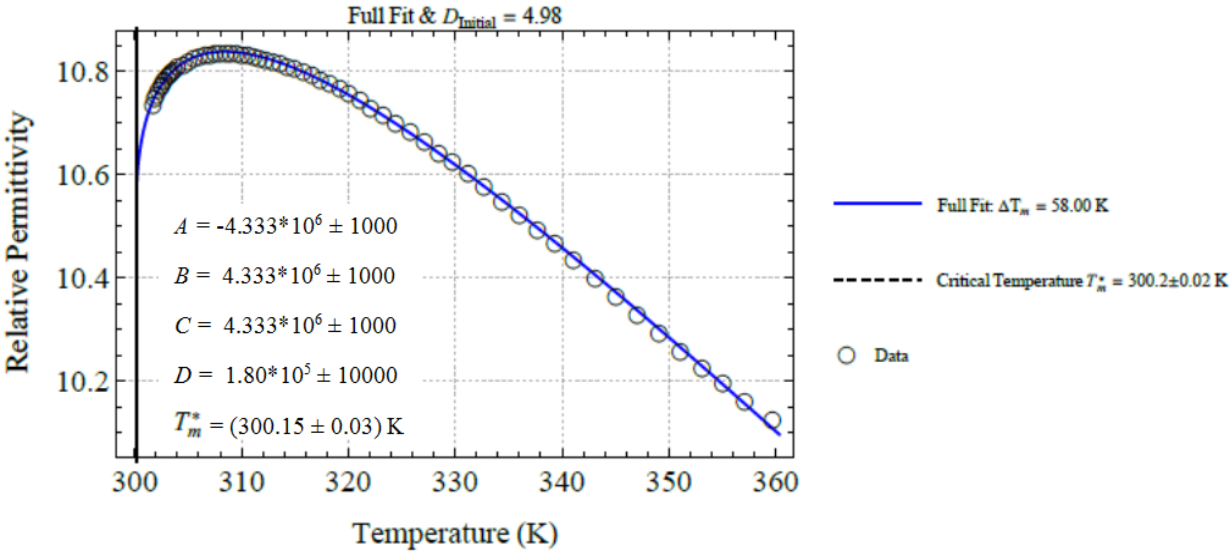

Figure 4.3: Fitting of the full function to typical data. The 6CB data from Thoen et. al. are used [37].

The only conditions separating the fit results of part (a) from part (b) are the initial conditions for the fitting parameters. The fitting routine was especially sensitive to whether the initial value of D were less than or greater than 1. For parts (a) and (b), the function fits the data well. The standard errors for the parameters in both cases are less than 1%.
Using only the reduced chi-square $\chi^2_{\upsilon,m}$ as a test of the goodness of fit would select part (b) as the better fit. However, part (b) has the most absurd values for the magnitudes.

4.1.2 Fitting Approaches and Results

Figure 4.3 reveals two problems in fitting the full function $\bar{\varepsilon}_{full}$. First, for typical data (about two-thirds of the data sets analyzed), two sets of results are obtained depending on the initial conditions. In Figure 4.3a, when the initial conditions corresponding to a D that is less than one, reasonable results with reasonable fitting error estimates are obtained. In Figure 4.3b, when the initial condition for D is greater than one, the fitting routine seems to run amok, reporting unphysical estimates with relatively small percent standard errors. Secondly, the fit results in Figure 4.3b have the lower reduced chi-square $\chi^2_{v,m}$. The other third of the data sets analyzed had a problem with the value of D always going to a value of one along with parameters B, C, and D having large infinite standard errors. The following three approaches reveals insight into these problems.

First, seen in Figure 4.3, all parameters are allowed to be free and the initial conditions are explored. For clarity, an index m will be used on T^* (or any other parameter such as χ^2_v, A, B, C, or D) to emphasize that T^*_m is an estimate of T^* using $\bar{\varepsilon}_{full}$.

Second, parameters D and T^* are held constant at discrete values, since $\bar{\varepsilon}_{full}$ has a nonlinear dependence on these two parameters. The same approach of fixing T^* to a literature value will be used in Section 4.2. The paper by Zink et. Al. Report the literature value only for the *n*CB series. For clarity, this fixed T^* will be referred as T^*_{Zink}.

Third, a technique called range shrinking is used. Index m also refers to T^*_m (and the other fitting parameters) being allowed to estimate of T^* on range shrinking.

4.1.2.1 Approach 1: All Parameters Free

The model was first fit to the data such that all five parameters were free. Figure 4.3 shows that the model fits the data well. However, also seen in Figure 4.3 is that the parameter estimates are ambiguous for typical data. The fitting results in applying Equation 4.2 to the 6CB data were dependent on the initial conditions.

4.1.2.2 Approach 2: Holding Parameters *D* and *T** Constant

The full model $\bar{\varepsilon}_{full}$ is linear in parameters A, B, and C. However $\bar{\varepsilon}_{full}$ has a complicated dependence on both parameters D and T^*. It was hoped that manually varying D and or fixing T^* to a literature value may reveal the underlying issue that leads to the ambiguous results shown in Figure 4.3. Note that, in Figures 4.4b and 4.4c, the standard errors are reasonable when D is fixed.

The first part of this approach is to manually vary parameter D at discrete values in Equation 4.2 while the remaining parameters are free in the fitting process. The resultant lowest reduced chi-square plot χ_v^2 versus D reveals two general categories among the 22 data-sets fitted: $D = 1$ is a minimum and $D = 1$ is a maximum. About one-third of the fitted data sets had a minimum at D equal to one. In this case, the reported standard errors for parameters B, C, and D were unphysical. Unphysical here refers to the standard errors being well above double the parameter estimates. The remaining two-thirds of the data sets had a maximum χ_v^2 at D equal to one with local minima on either side. The typical data set used, *n*-6-*n*-cyano-biphenyl (shown in Figure 4.1), falls into the second category. Figure 4.4a shows the lowest χ_v^2 as parameter D is manually varied. In χ_v^2-space, a maximum lies at $D = 1$ for typical data.

The second part of this approach is again to manually vary D with the addition of fixing parameter T^* to a literature reported value [48]. Fixing parameter T^* has the same two general categories mentioned in the plot of χ_v^2 versus D. However, in this case, a little over half of the cases have a minimum at $D = 1$. A little under half of the data sets have a maximum χ_v^2 at $D = 1$ with minima on either side. The typical data set used, 6CB, falls into the second category again, where $D = 1$ is a maximum.

D fixed and T^* free	*D* and T^* both fixed

(a) Goodness of fit as the reduced χ^2_ν versus parameter *D*.

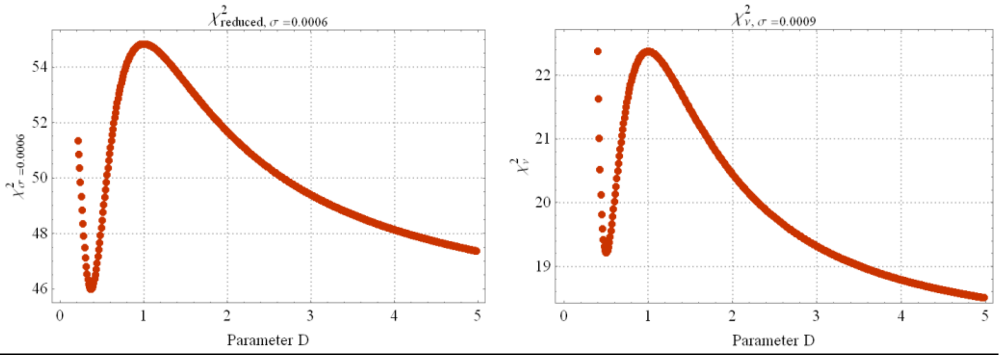

(b) A fit with the initial condition $D < 1$

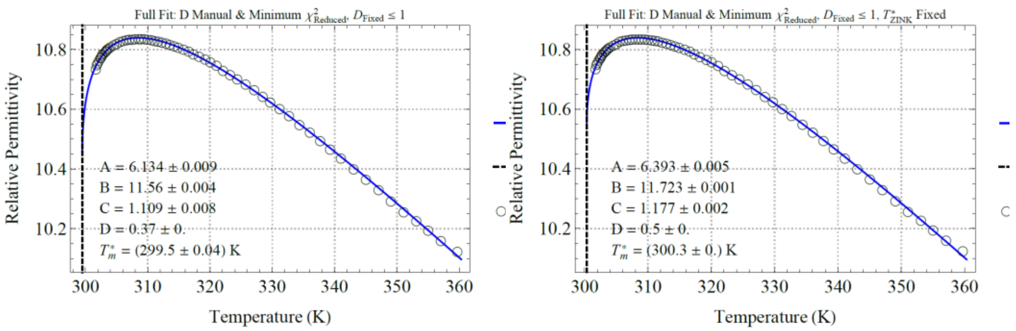

(c) A fit with the initial condition $D > 1$

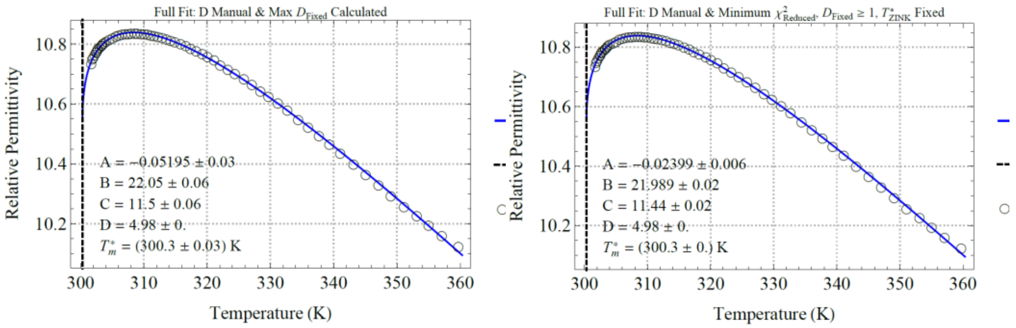

Figure 4.4: A fit of Equation 4.2 to typical data with *D* manually varied.

Parts (b) and (c) correspond to the two minima seen in part (a).

Figure 4.4 shows the results of fitting the full function with parameter *D* manually varied. Part (a) reveals that for typical data the plot of χ^2_ν versus D has a peak at $D = 1$. Figure 4.4b is a plot of the minimum at $D < 1$. Figure 4.4c shows the case of D as $A \rightarrow 0$ (that is, as D increases). It is clear that, while the function fits the data quite well, the parameter estimates are ambiguous.

As D increases above 1, the background slope A decreases until it changes sign. For all samples studied, when D is manually varied, zero slope is reached near $D = 5$, the Debye value. This corresponds to a constant background $\bar{\varepsilon}_{BG} = B$. However, a value of D near the Debye value did not result in a lowest χ_v^2 fit. Table 4.1b at the end of Section 4.1 shows the results of fitting the full function to typical data with parameter D manually varied.

4.1.2.3 Approach 3: Range Shrinking

In the study of phase transitions, range shrinking is a method used to test a model's temperature range of applicability ΔT_m (or a corresponding reduced temperature range Δx_m). Figure 4.1 is a plot of typical data. The total number of data points is N. Range shrinking sequentially removes $N - m$ data points from the highest temperature side of the plot. No data are range shrunk on the lowest temperature side of the plot. The number of data points m that remain are used in fitting the data over the corresponding ΔT_m. The index m is counted from the phase transition clearing temperature (that is the lowest temperature data point T_{IM} in the isotropic phase). In this chapter, index m identifies range shrinking when the full function $\bar{\varepsilon}_{full}$ is fit to data.

Caution must be taken when removing data from the fitting process and then reporting the results. In order to assess the choice of temperature range ΔT_m to report, two metrics are used: the reduced chi-square χ_v^2 plotted against ΔT_m, and the single deletion variance test which is the normalized variance of a fit plotted versus the absolute temperature. If range shrinking is an applicable tool then the corresponding fitting parameters should stay constant irrespective of the temperature range beyond a certain shrinkage of data.

4.1.2.4 Range Shrinking Using $\chi^2{}_v$

The reduced-chi square χ_v^2 versus ΔT_m is the first metric used with each temperature range ΔT_m. The resultant goodness of fit χ_v^2 is seen in Figure 4.5a for each range ΔT_m. Each range corresponds to the removal of $N - m$ data points. Chapter 3 introduced the reduced chi-square χ_v^2 as the chi-square χ^2 divided by the number of degrees of freedom υ (see Equations 3.10 and 3.11). When either the number of data points or model parameters are varied, the number of degrees of freedom change. In order to directly compare the goodness of various fits with different degrees of freedom d, normalization is required. The number of degrees of freedom serves as a normalization factor of χ^2 for data sets with different υ.

Figure 4.5a shows the results of ranging shrinking using Equation 4.2 to fit the typical data. The χ_v^2 significantly drops over the removal of the highest 10 K of data (the furthest four data points on the right). While the model fits the data well over all temperature ranges, a steep drop in χ_v^2 indicates that the parameter estimates are not very stable when the highest 10 K of data are included. After dropping the highest four data points, the χ_v^2 roughly levels out versus ΔT_m. This indicates that the parameter estimates upon further range shrinking may be more stable after removing the aforementioned data points.

The removal of just four data points, in the case of 6CB, results in the ambiguous double minimum with reasonable standard errors from Figure 4.4a, turning into a single minimum χ_v^2 fit corresponding to $D = 1$ with large standard errors. The plot of parameter D versus ΔT_m is seen in Figure 4.5b (for the cases of two minima, only one is shown for all parameter plots). Comparing Figure 4.4a to Figure 4.5c shows this change in number of minima.

Figure 4.5 shows the remainder of the fitting parameters A, B, C, and T^*, each plotted versus ΔT_m. For each parameter, the results are smoother for the case of $m < N - 4$ and vary much less than the case of m going to N. It is seen that χ_v^2 is a good metric for justifying the removal of a few high temperature data points.

Typical data (two-thirds of all data sets studied), in χ_v^2 space, the parameter set corresponding to $D = 1$ always shows up as a local maximum (see Figure 4.3a as an example). The two minima are centered around $D = 1$. Upon sufficient range shrinking ΔT_m, a single χ_v^2 minimum emerges corresponding to a parameter set with $D = 1$ with large standard errors. Chosen typical fits based on using χ_v^2 can be viewed numerically in Table 4.1 at the end of Section 4.1.

The other third of data sets return a single minimum χ_v^2 set of parameters corresponding to $D = 1$ with large standard errors. In these cases, either range shrinking has no effect or the opposite scenario happens to that of the typical data. That is, a double minimum emerges in χ_v^2 space centered around a maximum χ_v^2 at $D = 1$ upon sufficient range shrinking. However, when D is allowed to be a free parameter with range shrinking, it returns unphysical standard errors.

Note that the critical temperature T^* was held constant at a literature value to see if it would resolve various problems seen. This is seen in the right most column of Figures 4.5 and 4.6. Holding T^* constant did not resolve the problems seen in Figure 4.4a with a double minimum in χ_v^2. Upon sufficient range shrinking, holding T^* fixed also did not resolve the problem with large standard errors seen in Figures 4.5b, 4.6b, and 4.6c.

T^* as a free parameter	T^* fixed

(a) The reduced chi-square χ_{υ}^{2} vs ΔT_m.

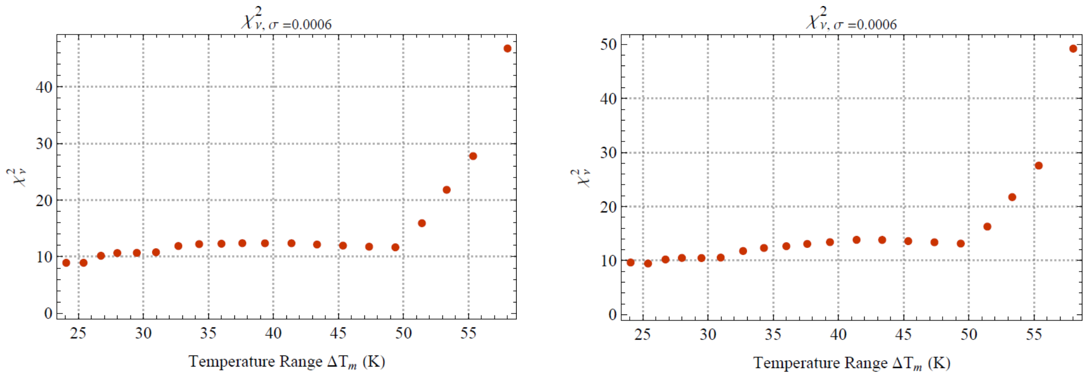

(b) Parameter D vs ΔT_m.

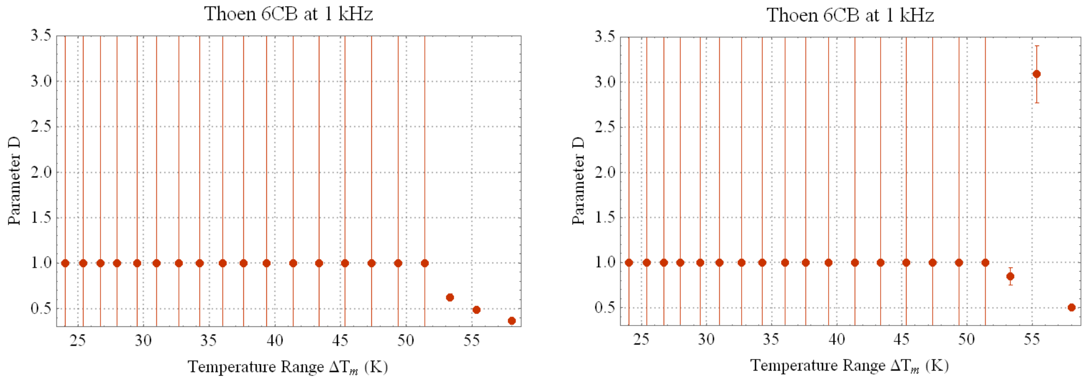

(c) After range shrinking $\Delta T_{m=4}$, the reduced chi-square χ_{υ}^{2} vs D upon deletion of four data points.

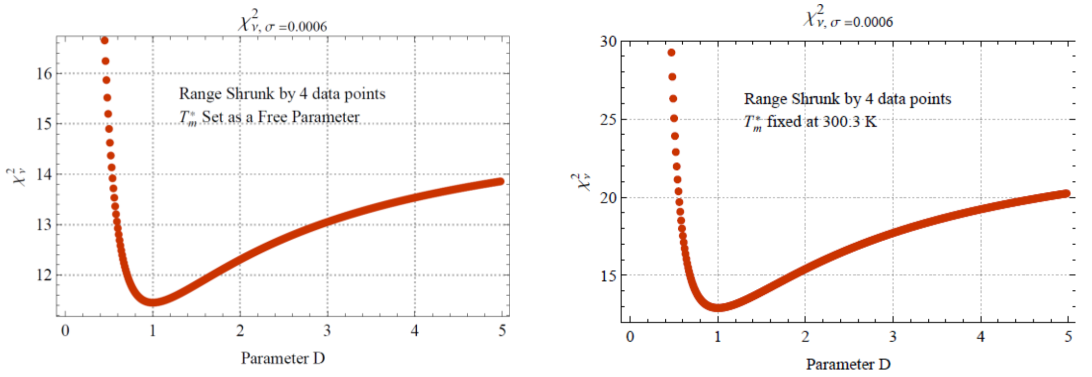

Figure 4.5: A justification for removing the highest four data points.

- The vertical stripes in parts (a) and (b) are error bars.
- Reduced Chi-square versus Range shrinking shows that red chi-sqr stabilizes after removing first four data points
- Parameter D versus range shirnking shows that D changes over the first four data points, but after that constant value for remainder of smaller ranges
- Reduced Chi-square versus D for four data points subtracted. This is in striking contrast to Figure 4.4a.

	T* as a free parameters	T* fixed
(a) A vs ΔT_m	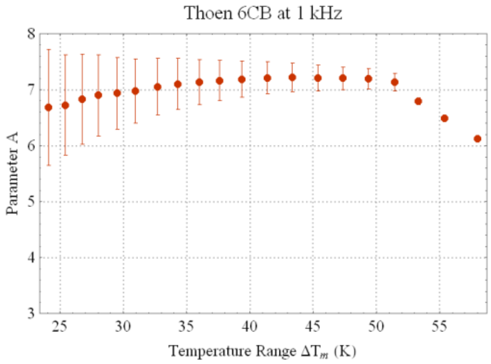	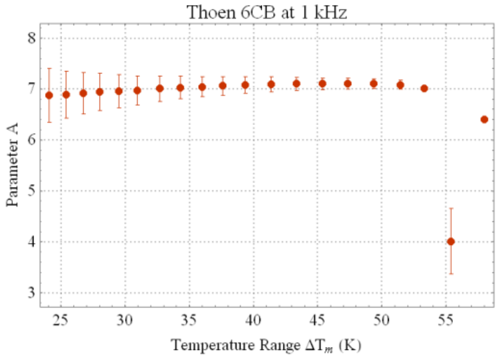
(b) B vs ΔT_m	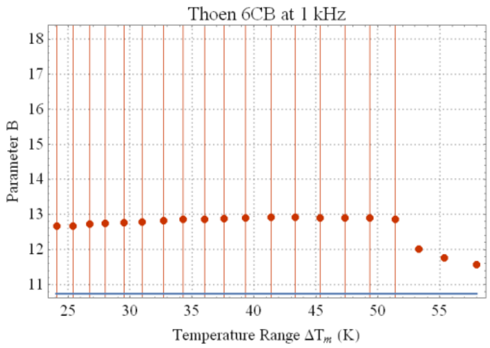	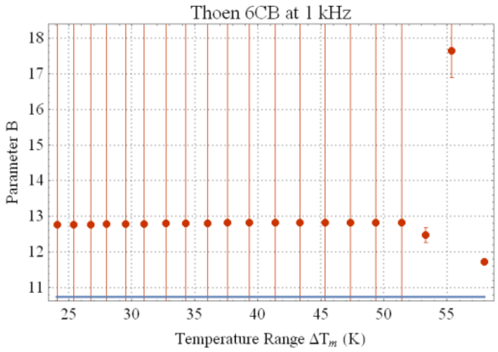
(c) C vs ΔT_m	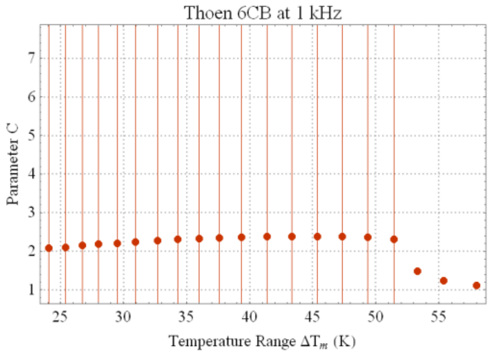	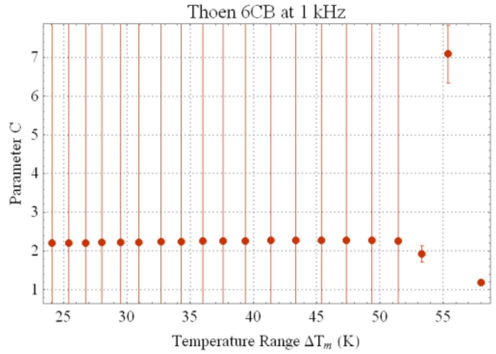
(d) T_m^* vs ΔT_m	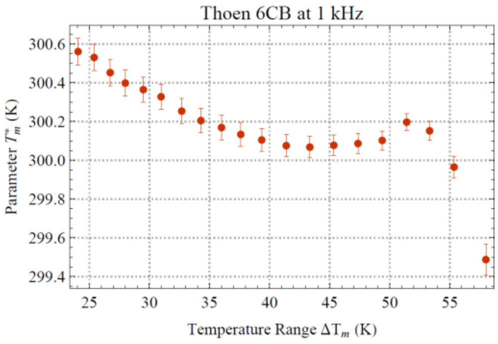	Fixed at $T_m^* = 300.3$ K The literature value $\Delta T_N^* = 1.37$ K below the transition temperature T_{IM} [48].

Figure 4.6: The parameter estimates on range shrinking for the full function.

- The red stripes in parts (a) through (c) are error bars.
- These are the corresponding parameter plots to Figure 4.5

4.1.2.5 Range Shrinking using Single Deletion Variance

The second metric used in determining the number of data points to truncate from the high temperature side is single deletion variance [49, 50]. This type of test is used to test if any data point has undue influence on the fit. It is expected that the data furthest from the phase transition should have the least influence on the fit. Two single deletion variance plots are shown in Figure 4.7 with the abscissa being the absolute temperature over the whole range of data ΔT_N. Recall from Figure 4.1 that index *N* refers to all data points available for a given data set. Part (a) shows the case where parameters A, B, C, D, and T_m^* are free. Part (b) shows the case where T_m^* is fixed at a literature value and parameters A, B, C, and D are free.

A single deletion variance plot is constructed by first calculating the variance σ_N^2 of a fit for the entire data set N is found by fitting Equation 4.2 to the data. Then $N - 1$ fits are performed in which the *i*th data point is deleted for each fit. The *i*th data point is deleted for each fit, resulting in data sets each of $N - 1$ data points and variance σ_i^2. Each σ_i^2 is a measure of the influence of each individual data point on the entire fit by removing that data point. A single deletion variance plot is the variance σ_i^2 of the fit for the *i*th data point that was deleted versus the corresponding temperature. If each data point contributes equally to a fit, then the plot should be a horizontal line. The dotted lines in Figure 4.7 correspond to the mean of all σ_i^2 plus or minus one standard deviation from that mean. Focusing our attention to only the high temperature side, at minimum the highest data point can be filtered out of the fitting process. The next three highest temperature data points do not significantly affect the fit compared to the mean. The fifth through ninth data points from the left do seem to affect the fit more. Based on Figure 4.6, it seems that a reasonable range to shrink the data by would be for $4 \leq (N - m) \leq 9$ data points. While the χ_v^2 versus ΔT_m

plot places a lower limit to the number of data that can be justifiably deleted, the single deletion variance plot places an upper limit to the number of data points that can be justifiably deleted.

(a)
A, B, C, D, and T^*.

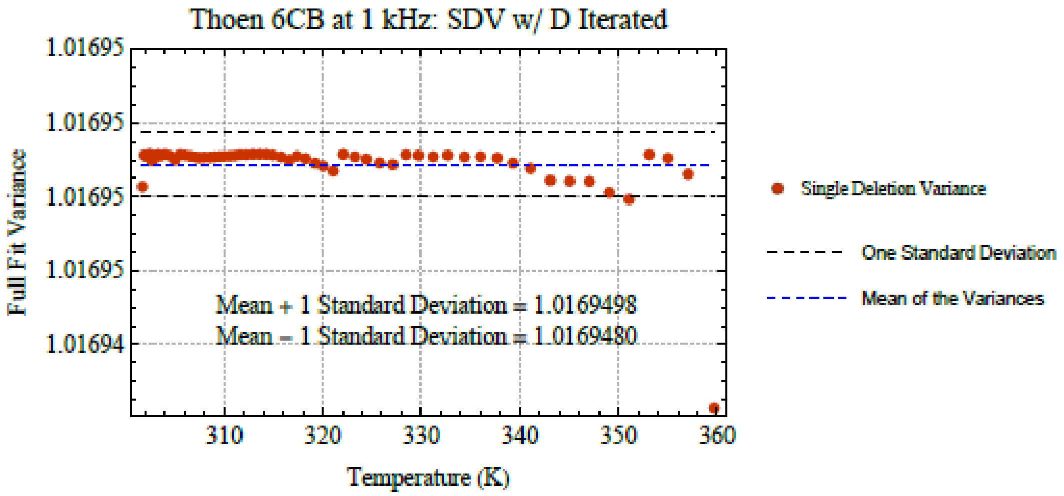

(b)
A, B, C, D, T^* fixed at literature value.

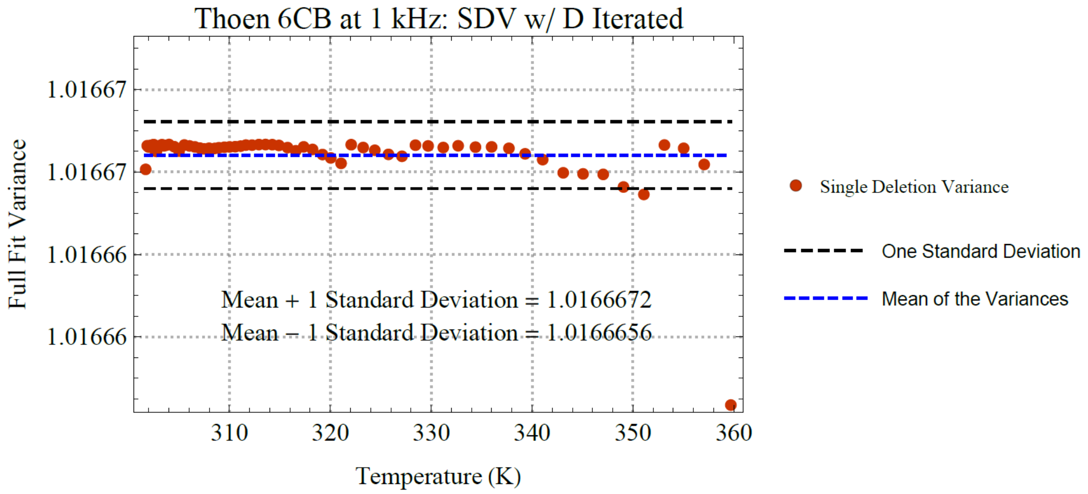

Figure 4.7: The single deletion variance plots (SDV) for the full fit.

4.1.3 Another Use of Single Deletion Variance: Uncertainty for Each Data Point

It is now appropriate to mention what goes into estimating the standard errors for all fitting parameters that are returned by the fitting routine. The weights $\frac{1}{\sigma_j^2}$ for each data set are neither known nor given in the papers. The estimate of σ_j is vital for reporting reasonable estimates of the standard errors for the fitting parameters from the fitting routine. The reduced chi-square χ_{υ}^{2} is central to the fitting routine. A consistent method needs to be used for estimating σ_j for all data sets studied.

Without information concerning the uncertainty in each data point ε_j, a first approximation of σ_j is that for all j the data points are equally weighted: $\sigma_{error} = \sigma_j$. A rewrite of Equation 3.11 gives,

$$\chi_{\upsilon}^{2} = \frac{1}{\upsilon\, \sigma_{error}^{2}} \sum_{j}^{N} \left(\varepsilon_{model} - \varepsilon_j\right)^{2}.$$

Toward the end of this chapter, a table will show the estimated σ_{error} for each data set fitted.

A second approximation of σ_j is that σ_j should be no more accurate than the order of the last decimal of data reported. The last decimal is explicitly given for only eight of the data sets in which the numerical tables were directly obtained [37, 51]. For 6CB, this would give an estimate of $\sigma_j \geq 0.0001$. However, strictly speaking, such an estimate of σ_j cannot be used for remaining fourteen data sets as these data sets were obtained graphically and the level of precision in the analysis can only be assumed at best [38-46].

Thirdly, σ_j relies on the reduced chi-square χ_{υ}^{2} (defined by Equation 3.11). For a perfect fit, χ_{υ}^{2} should be equal to one. However, it is unreasonable to expect the model from Equation 4.2 to perfectly fit all data sets analyzed. Equation 4.2 is developed for the isotropic to achiral nematic phase transition, of which 15 data sets fit that description [28, 37-41, 43, 45, 46, 51, 52]. One data set has an isotropic to chiral nematic phase transition [44]. The remaining six data sets have an isotropic to smectic phase transition [37, 41, 42]. Both chiral nematic order and smectic order have a nematic component to their order parameters. Chiral nematic ordering has an additional order parameter to account for the pitch of the chirality. Smectic ordering has an additional order parameter to account for layering by way of a periodic density function. Equation 2.28 does not account for these additional order parameters.

The single deletion variance plot is independent of the estimated σ_j. The single deletion variance plot, Figure 4.7, is composed of the variances σ_i^2 corresponding to the removal of permittivity data point ε_i at a given temperature T_i. How the removal of each data point ε_i affects the fit is now used as an approximation for the weight $\frac{1}{\sigma_j^2}$ of each data point.

In order to reduce any bias and to have a consistent method for estimating weights, the above three guidelines will be used. The error σ_{error} (or weight $\frac{1}{\sigma_{error}^2}$) will be estimated by first taking the mean σ_{mean}^2 of the variances σ_i^2 and then relating the square of σ_{error},

$$\sigma_{error}^2 = \sqrt{\frac{1}{N-1}\sum_i^N(\sigma_i^2 - \sigma_{mean}^2)^2}. \tag{4.3}$$

In all data sets studied, σ_{error} from Equation 4.3 was either the same as or one order of magnitude larger than the last reported decimal place per permittivity measurement ε_j. The aforementioned approximation scheme for σ_{error} is suitable for the purposes of this dissertation. See Table 4.6 at the end of this chapter for the estimated average σ_{error} for all data sets investigated. This allows for a meaningful lower limit approximation to the standard errors.

Table 4.1: Selected parameter results for fitting Equation 4.2 to the 6CB sample data.

Fit Method	Selection Criterion for m §	m	ΔT_m (K)	T^* (K)	A	B	C	D	$\chi^2_{v,m}$
(a) All Parameters Free:									
$D_{Initial} \ll 1$	m = N	64	58.0	299.5 $\pm$ 0.1	6.13 $\pm$ 0.04	11.56 $\pm$ 0.02	1.109 $\pm$ 0.008	0.37 $\pm$ 0.01	18.6
$D_{Initial} \geq 1$	m = N	64	58.0	300.15 $\pm$ 0.03	-4.333×10^6 $\pm$ 1000	4.333×10^6 $\pm$ 1000	4.333×10^6 $\pm$ 1000	1.80×10^5 $\pm$ 10000	17.9
$D_{Initial} \ll 1$	m = N	64	58.0	[[300.33]]	6.39 $\pm$ 0.03	11.72 $\pm$ 0.02	1.18 $\pm$ 0.02	0.50 $\pm$ 0.01	19.5
$D_{Initial} \geq 1$	m = N	64	58.0	[[300.33]]	-3.9194×10^6 $\pm$ 100	3.9194×10^6 $\pm$ 400	2.2260×10^6 $\pm$ 300	1.6780×10^5 $\pm$ 300	18.0
(b) *D* Manually Varied:									
$\chi^2_{v\,min}$ & $D \ll 1$	All Data	64	58.0	299.51 $\pm$ 0.04	6.134 $\pm$ 0.009	11.560 $\pm$ 0.004	1.109 $\pm$ 0.008	[0.370]	18.3
$D = 1$	All Data	64	58.0	300.56 $\pm$ 0.03	6.893 $\pm$ 0.01	12.707 $\pm$ 0.009	2.13 $\pm$ 0.01	[1.00]	21.8
$D \gg 1$	All Data	64	58.0	300.30 $\pm$ 0.03	-0.05 $\pm$ 0.03	22.05 $\pm$ 0.06	11.50 $\pm$ 0.06	[4.98]	18.8
$D \ll 1$	All Data	64	58.0	[[300.33]]	6.393 $\pm$ 0.005	11.723 $\pm$ 0.001	1.177 $\pm$ 0.002	[0.500]	19.2
$D = 1$	All Data	64	58.0	[[300.33]]	6.964 $\pm$ 0.006	12.773 $\pm$ 0.003	2.213 $\pm$ 0.004	[1.00]	22.4
$\chi^2_{v\,min}$ & $D \gg 1$	All Data	64	58.0	[[300.33]]	-0.024 $\pm$ 0.006	21.99 $\pm$ 0.02	11.44 $\pm$ 0.02	[4.98]	18.5
(c) Range Shrinking:									
Fit based on:	All Data	64	58.0	299.49 $\pm$ 0.1	6.13 $\pm$ 0.04	11.56 $\pm$ 0.02	1.109 $\pm$ 0.008	0.367 $\pm$ 0.01	18.6
Fit based on:	χ^2_v	60	49.4	300.10 $\pm$ 0.08	7.2 $\pm$ 0.3	12.90 $\pm$ 8000	2.36 $\pm$ 8000	1.0000 $\pm$ 3000	4.63
Fit based on:	χ^2_v	58	45.3	300.08 $\pm$ 0.09	7.2 $\pm$ 0.4	12.91 $\pm$ 500	2.37 $\pm$ 500	1.0000 $\pm$ 200	4.75
Fit based on:	Lowest χ^2_v	45	24.1	300.56 $\pm$ 0.1	7 $\pm$ 2	12.66 $\pm$ 8000	2.08 $\pm$ 8000	1.0000 $\pm$ 4000	3.54
Fit based on:	SDV	55	39.3	300.10 $\pm$ 0.1	7.2 $\pm$ 0.5	12.90 $\pm$ 10000	2.36 $\pm$ 10000	1.0000 $\pm$ 6000	4.91
Fit based on:	All Data	64	58.0	[[300.33]]	6.40 $\pm$ 0.03	11.73 $\pm$ 0.02	1.18 $\pm$ 0.02	0.50 $\pm$ 0.01	19.5
Fit based on:	χ^2_v	60	49.4	[[300.33]]	7.1 $\pm$ 0.2	12.82 $\pm$ 700	2.27 $\pm$ 700	0.9999 $\pm$ 300	5.22
Fit based on:	χ^2_v	58	45.3	[[300.33]]	7.1 $\pm$ 0.2	12.82 $\pm$ 1000	2.27 $\pm$ 1000	0.9999 $\pm$ 600	5.40
Fit based on:	Lowest χ^2_v	45	24.1	[[300.33]]	6.9 $\pm$ 0.8	12.76 $\pm$ 300	2.20 $\pm$ 300	1.0014 $\pm$ 200	3.83
Fit based on:	SDV	55	39.3	[[300.33]]	7.1 $\pm$ 0.3	12.81 $\pm$ 400	2.26 $\pm$ 400	0.9996 $\pm$ 200	5.32

§: the number of fitting points
[ ]: fixed value based on the reduced chi-square χ^2_v plot
[[ ]]: fixed, literature from Zink et. al. [48]
SDV: Single Deletion Variance

4.2 The Model: A Series Expansion of the Full Function

Section 4.1 served as an introduction to the difficulties in obtaining single valued, unambiguous fitting parameter estimates with reasonable standard errors. Section 4.1 also hinted at $\bar{\varepsilon}_{full}$ having a dependence on D that confuses the fitting routine. Because of this, it is useful to find an equivalent model that is simpler and reveals relationships among the fitting parameters in $\bar{\varepsilon}_{full}$, Equation 4.2. Series expansions are such a tool. For an expansion, all powers in the reduced temperature x that are reasonable to include are shown. An argument will be constructed so as to consider the minimal number of terms needed to adequately describe the data.

By using a series expansion, this section reveals four important aspects of Equation 4.2 that make direct fitting difficult. First, both $\bar{\varepsilon}_{BG}$ and $\Delta\bar{\varepsilon}$ have constant contributions. Second, both $\bar{\varepsilon}_{BG}$ and $\Delta\bar{\varepsilon}$ have contributions to the linear coefficient of x. Third, if $\bar{\varepsilon}_{BG}$ is expanded to x^2, then both $\bar{\varepsilon}_{BG}$ and $\Delta\bar{\varepsilon}$ have contributions to the quadratic coefficient of x^2. Fourth, the expansion of Equation 4.2 reveals that the $D = 1$ extremum is inherent to the function itself and not necessarily to the physics. Table 4.2 at the end of Section 4.2 shows the numerical fitting results for selected fits.

4.2.1 The Fitting Parameters

A series expansion $\bar{\varepsilon}_{II}$ of Equation 4.2 is taken about the argument $\frac{D}{\sqrt{x}}$ of the arctangent being large. Only to second order in the reduced temperature is kept, as higher order terms are negligible and contribute no new information to the argument. The subscript "II" denotes that terms up to second order in the reduced temperature x are included:

$$\bar{\varepsilon}_{II} = -\left(A + \frac{C}{D}\left(D + \frac{1}{D}\right)\right)x + (B - C) + \frac{\pi}{2}\frac{C}{D}\left(x^{\frac{1}{2}} + x^{\frac{3}{2}}\right) + \frac{C}{D}\left(\frac{1}{3D^3} - \frac{1}{D}\right)x^2. \tag{4.4a}$$

The reduced temperature range near the transition is commonly referred to as the critical region.

In order to simplify the discussion for the critical expansion in Equation 4.4a, the coefficients of each power of x will be labelled. The critical slope will be referred to as α:

$$\alpha = A + \frac{C}{D}\left(D + \frac{1}{D}\right). \tag{4.4b}$$

There are two competing phenomena accounted for by the total slope α: the background A and the part due to the pretransitional effect. The dependence of α on D in Equation 4.4b will be referred to as g,

$$g = \left(D + \frac{1}{\mathrm{D}}\right). \tag{4.4c}$$

The critical intercept will be referred to as β:

$$\beta = B - C. \tag{4.4d}$$

Parameter β is the value of the permittivity $\bar{\varepsilon}$ in Equation 4.2 at the critical temperature T^*.

Both the $x^{\frac{1}{2}}$ and $x^{\frac{3}{2}}$ terms have the the ratio of C to D as a common coefficient. The coefficient $\frac{\pi}{2}$ will be left as is. The ratio of C to D will be refered to as γ:

$$\gamma = \frac{C}{D}. \tag{4.4e}$$

Parameter γ will be factored out of the quadratic term. This leaves the coefficients of x^2 as γ times *f*, where,

$$f = \frac{1}{3D^3} - \frac{1}{D}. \tag{4.4f}$$

As with contribution g, parameter *f* is left as only a function of all positive *D*.

Parameter γ is ubiquitous in the expansion. For this reason it is factored out. When γ is factored out (this includes in α, f, and higher order terms in x), functions of D appear that have extrema at $D = 1$. It is known that when standard errors are unphysically large, a model is either misspecified or stuck in a false minimum due to highly correlated parameters [53]. The results seen in Section 4.1 show that the fitting routine is stuck at a false minimum centered around extrema at $D = 1$. The series expansion in Equation 4.3a further reveals that the parameters are highly correlated. Figure 4.8 shows the minima of the slope contribution g and quadratic coefficient f plotted versus D.

For the purpose of fitting, Equation 4.4a is rewritten in terms of the critical parameters α, β, γ, and f:

$$\bar{\varepsilon}_{II} = -\alpha x + \beta + \frac{\pi}{2}\gamma\left(x^{\frac{1}{2}} + x^{\frac{3}{2}}\right) + \gamma f x^2. \tag{4.5a}$$

Equation 4.4a will be referred to as the second order critical expansion $\bar{\varepsilon}_{II}$. Equation 4.5a is a five parameter model: α, β, γ, f, and T^*.

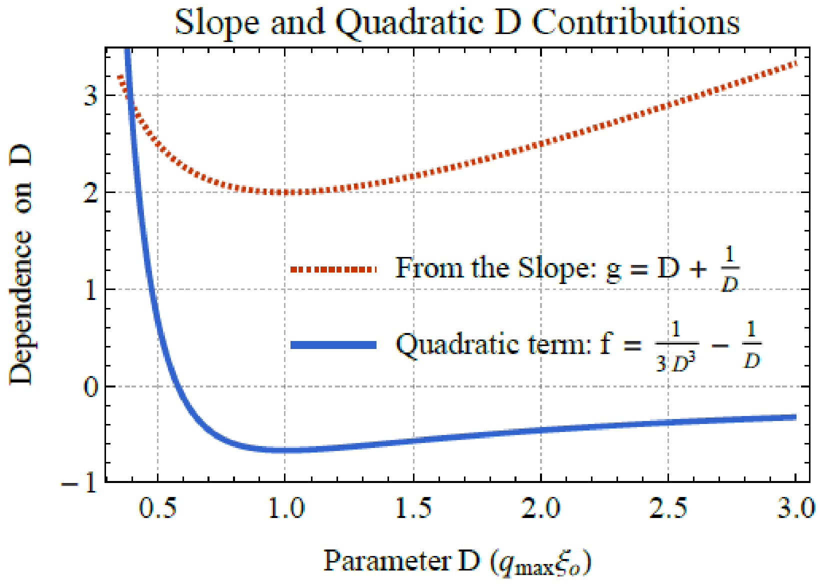

Figure 4.8: Plotting the D dependence of critical parameters g and f. For both, the common coefficient γ is factored out.

The critical slope α has a dependence on D shown by the dotted red curve. The quadratic coefficient f has a dependence on D shown by the solid blue curve. Four values of D are of interest:

- $D \leq 0.393$: f dominates the linear contribution g. Contribution f can dominate the background slope A as well as the singularities $x^{\frac{1}{2}}$ and $x^{\frac{3}{2}}$. This does not seem physical for small x, since the leading singularity is $x^{\frac{1}{2}}$.
- $D < 0.577$: f is positive and can be appreciable.
- $D \geq 0.577$: f is zero at 0.577 and then remains small and negative for all larger D. Contribution g dominates for all larger values of D.
- $D = 1$: Both f and g are at their global minimum. Contribution f cannot be less than $-\frac{2}{3}$. Contribution g cannot be less than 2.

4.2.2 Three Choices for the Expansion

I aim to show that it is justified to leave out the quadratic term from the fitting process and that the expansion to $x^{\frac{3}{2}}$ is sufficient for reliably fitting the critical expansion to data. In order to do this, the influence of each nonlinear terms $x^{\frac{1}{2}}$, $x^{\frac{3}{2}}$, and x^2 on the fitting process must be compared. This results in three possible series expansions to fit to the data with: the second order expansion $\bar{\varepsilon}_{II}$, the removal of x^2 from $\bar{\varepsilon}_{II}$, and the removal of both x^2 and $x^{\frac{3}{2}}$ from $\bar{\varepsilon}_{II}$. For reduced temperatures below 0.30, the dominating singularly of the pretransitional curvature is $\frac{\pi}{2}\gamma\left(x^{\frac{1}{2}}\right)$.

The first additional equation removes the quadratic contribution $\gamma f x^2$ from the fitting process resulting in,

$$\bar{\varepsilon}_{3/2} = -\alpha x + \beta + \frac{\pi}{2}\gamma\left(x^{\frac{1}{2}} + x^{\frac{3}{2}}\right). \qquad (4.5b)$$

Equation 4.5b will be referred to as $\bar{\varepsilon}_{3/2}$, the three-halves critical expansion in the reduced temperature x. Figure 4.8 has shown that when $D > 0.577$, f is required to be small and negative. The ratio is taken of $\gamma f x^2$ to $\frac{\pi}{2}\gamma\left(x^{\frac{1}{2}}\right)$ for a typical allowed value of f (that is, half of the data sets fitted with $\bar{\varepsilon}_{II}$ had allowed values of f that ranged between $-\frac{2}{3}$ and $+1$). The relative contribution of the quadratic term is less than 0.5% at $x = 0.05$ and less than 10% at $x = 0.3$.

The next term to investigate through elimination is $\frac{\pi}{2}\gamma x^{\frac{3}{2}}$. Relative to the dominating root term, the three-halves term is 5% at $x = 0.05$ and 30% at $x = 0.3$. If the three-halves term can be neglected in the fitting process then the resultant equation is,

$$\bar{\varepsilon}_{I} = -\alpha x + \beta + \frac{\pi}{2}\gamma\left(x^{\frac{1}{2}}\right). \qquad (4.5c)$$

Equation 4.5c will be referred to as the first order critical expansion $\bar{\varepsilon}_I$ where the subscript I denotes the highest order term in the reduced temperature that is to the first power. The ratio of

$\frac{\pi}{2}\gamma x^{\frac{3}{2}}$ to $\frac{\pi}{2}\gamma x^{\frac{1}{2}}$ hints that $x^{\frac{3}{2}}$ is needed over the range of reduced temperatures for the data fitted. The first order expansion $\bar{\varepsilon}_I$ is still investigated as it contains the lowest order singularity $x^{\frac{1}{2}}$. One of the papers by Rzoska et. al. used an empirical equation that has the same form as Equation 4.5c but with the power of the non-linear term left as a free fitting parameter [40]. In that equation, the nonlinear term's exponent came out to one-half, within a margin of error [40]. As seen in this section, the expansion of Equation 4.2 gives an exponent of exactly one-half plus an additional term with an exponent of three-halves.

Unlike expansion $\bar{\varepsilon}_{II}$ as well as $\bar{\varepsilon}_{full}$, both $\bar{\varepsilon}_I$ and $\bar{\varepsilon}_{3/2}$ are four parameter models: α, β, γ, and T^*. This means that the parameters of a four parameter model cannot be used in isolation to find the parameters of a five parameter model such as $\bar{\varepsilon}_{full}$. Fit results from applying Equations 4.5b and 4.5c are in Tables 4.2a and 4.2b at the end of this section.

4.2.3 Fitting Methods and Results

The fit results for the series expansions $\bar{\varepsilon}_I$, $\bar{\varepsilon}_{3/2}$, and $\bar{\varepsilon}_{II}$ are all compared for typical data in Table 4.2 at the end of Section 4.2. The chosen fit results (see the column "Selection Criterion" in Figure 4.2) are based on range shrinking that was discussed in Section 4.1. All three expansions fit the data well with reasonable, single valued parameter estimates as well as with reaosnable standard errors. However, only parameters β and T^*agree well across fitting Equations $\bar{\varepsilon}_I$, $\bar{\varepsilon}_{3/2}$, and $\bar{\varepsilon}_{II}$.

Just as in Section 4.1 for the full function, both range shrinking and fixing T^* were used as methods. The index used for range shrinking the critical expansions $\bar{\varepsilon}_I$, $\bar{\varepsilon}_{3/2}$, and $\bar{\varepsilon}_{II}$ will be referred to as μ. The difference $N - \mu$ is the number of data points removed from the typical data set. The distinction between m and μ will be important for the heirarchical model proposed in

Section 4.3. Parts (a), (b), and (c) of Figure 4.7 show the reduced chi-square and single deletion variance plots. As with the full model $\bar{\varepsilon}_{full}$, these are used to identify a reasonable number of data points $N-\mu$ to delete based on range shrinking.

4.2.3.1 Results from Fitting the Second Order Expansion

Figures 4.9 and 4.10 show the χ_ν^2 and parameter estimates over range shrinking ΔT_μ from fitting the second order expansion $\bar{\varepsilon}_{II}$ to typical data. Figure 4.11 shows the single deletion variance plots versus absolute temperature T. Table 4.2c at the end of Section 4.2 shows the numerical results for typical data fitted by $\bar{\varepsilon}_{II}$.

Under range shrinking ΔT_μ, χ_ν^2 in Figure 4.9a drops significantly over the removal of the first four data points under both cases of T^* as a free and fixed parameter. The corresponding parameters T^*, α, β, γ, and f (see Figures 4.9b and 4.10 parts (a) through (d), respectively in the left column) also show this trend when T^* is a free parameter. When T^* is fixed, parameters α, β, γ, and f do not change significantly compared to when T^* is a free parameter (see Figures 4.10 parts (a) through (d) in the left column). Beyond four data points, it is not clear if the drop in χ_ν^2 from a value of 4 to 2 is statistically significant for the case of T^* free. For this, Table 4.2 shows a reasonable range of selected fits for range shrinking for $(N-\mu) \leq 8$.

The following argument for exclusion of the quadratic term $\gamma f x^2$ will partially follow the same argument made for the quadratic background coefficient f_{BG} discussed in Section 4.1 and shown in Figure 4.2. In addition to the range shrinking argument, the functional form of f seen in Figure 4.8 is taken into account. The behavior of the function under both cases of T^* as a free and fixed parameter is considered.

First, in Figure 4.10d with T^* free, parameter f is increasingly negative on decreasing ΔT_μ and spans a wide range. Similar to the case of f_{BG} in Figure 4.2a, f does not level out. When T^* is fixed for $(N-\mu) \geq 4$ parameter f is better constrained.

Second, Figure 4.8 revealed that for f has a minimum at a value of $-\frac{2}{3}$. On range shrinking by four data points and more, all values of f in Figure 4.10d are too negative given that f_{BG} is probably near zero (as defined in in Equation 4.1b and shown in Figure 4.2a). Half of the data sets that were fitted with $\bar{\varepsilon}_{II}$ on range shrinking ΔT_μ had estimates for f that were less than the minimum value of $-\frac{2}{3}$ irrespective of fixing T^*. The other half of the data sets had a typical value of f that varied between $-\frac{2}{3}$ and $+1$.

The single deletion variance plot seen in Figure 4.11 reveals how each data point contributes to the fit of $\bar{\varepsilon}_{II}$. Ideally, the deleted variances should follow a horizontal line or at least randomly vary around the average of the variances (seen by the center, horizontal blue short dashed line, where the black horizontal lines represent one standard deviation from that average).

In both cases of T^* free and fixed, it is seen that the highest temperature data point unduly affects the fit over the other data points. The model by Equation 4.2 aims to describe the pretransitional curvature at the lowest data points. Given a sufficient temperature range, the highest temperature data points should not affect the fit. Based on Figure 4.11, it is justifieable to range shrink by at least the highest temperature data point.

When T^* is a free parameter (Figure 4.11a), the first data point also seems to greatly affect the fit. However, this should be expected, as the determination of T^* is sensitive to the purpose of the model which is to characterize the pretransitional curvature. Note that in Figure 4.11b, when

T^* is fixed, the lowest temperature data points do not affect the fit as much and have more of a random contribution.

	T^* is a free parameter	T^* is fixed at literature value
(a) χ_ν^2 vs ΔT_μ	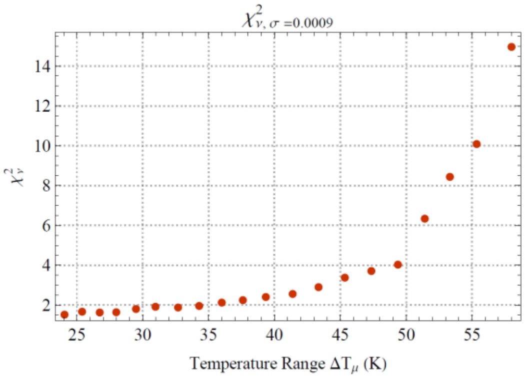	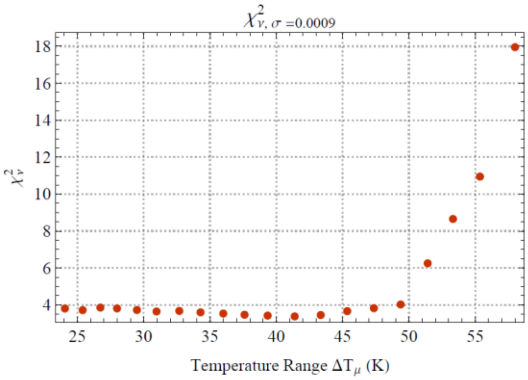
(b) T^* vs ΔT_μ	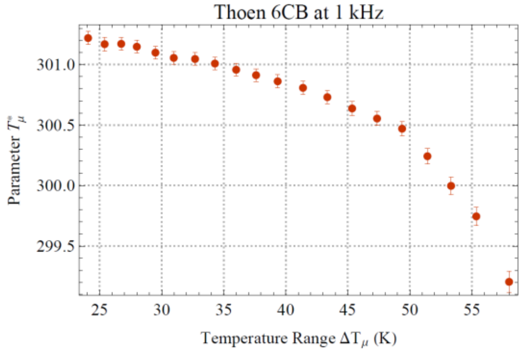	Fixed at $T_\mu^* = 300.3$ K. The literature value $\Delta T_\mu^* = 1.37$ K below the transition temperature T_{IM} [48].

Figure 4.9: Second order expansion goodness of fit and critical temperature.

<table>
<tr><th></th><th>T^* is a free parameter</th><th>T^* is fixed at literature value</th></tr>
<tr><td>(a)
α vs ΔT_μ</td><td>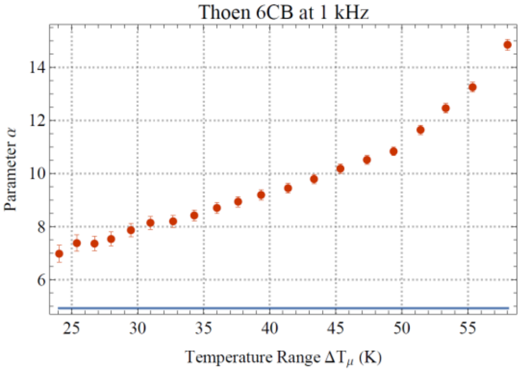
</td><td>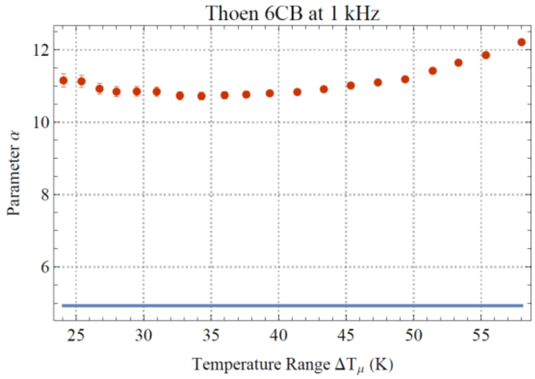
</td></tr>
<tr><td>(b)
β vs ΔT_μ</td><td>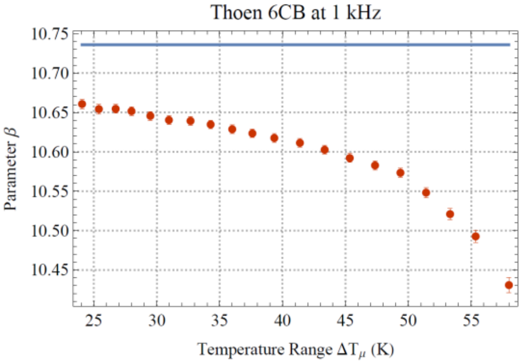
</td><td>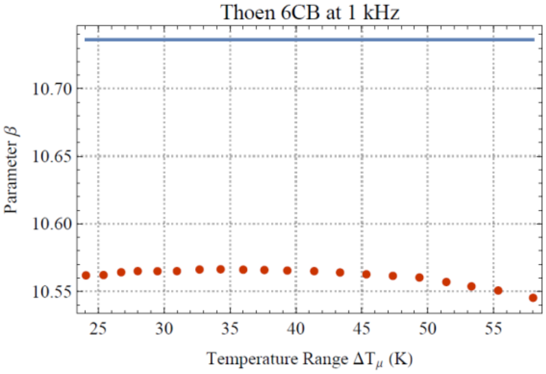
</td></tr>
<tr><td>(c)
γ vs ΔT_μ</td><td>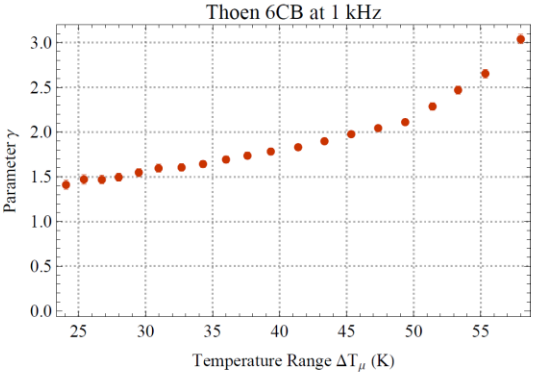
</td><td>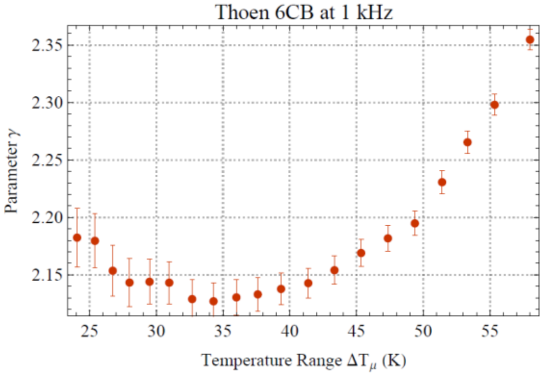
</td></tr>
<tr><td>(d)
f vs ΔT_μ</td><td>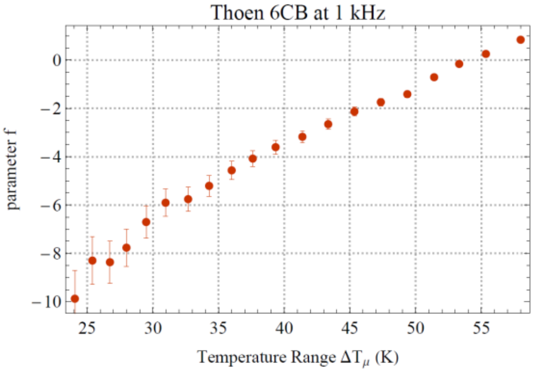
</td><td>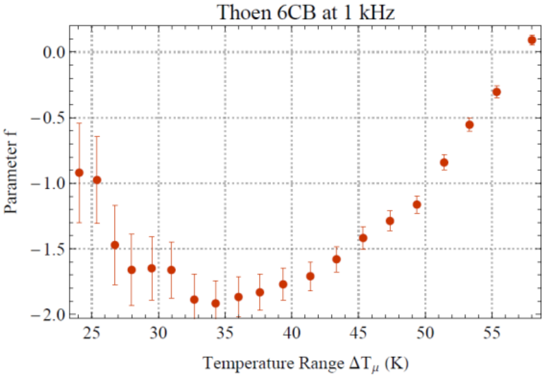
</td></tr>
</table>

Figure 4.10: Second order Expansion fitting parameters. The blue, horizontal lines represent values from the raw data.

(a)
T^* free

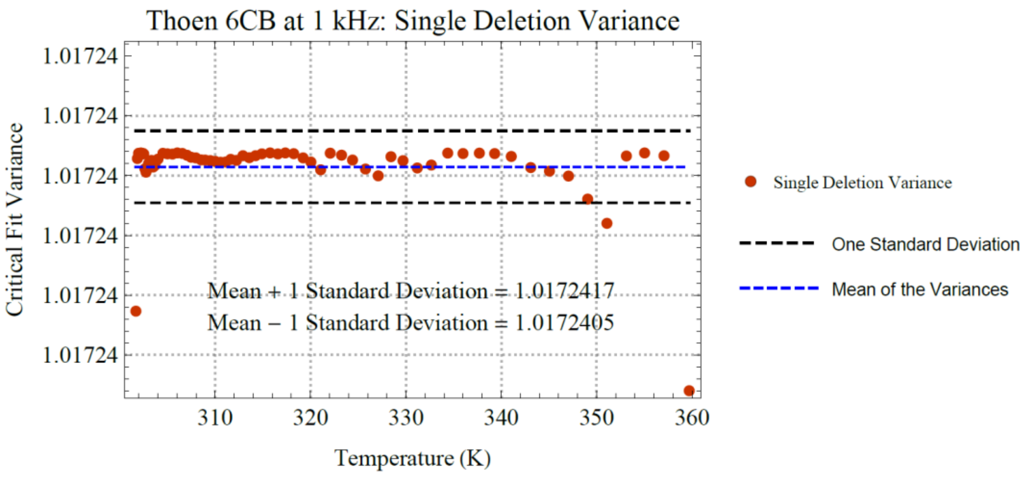

(b)
T^* fixed

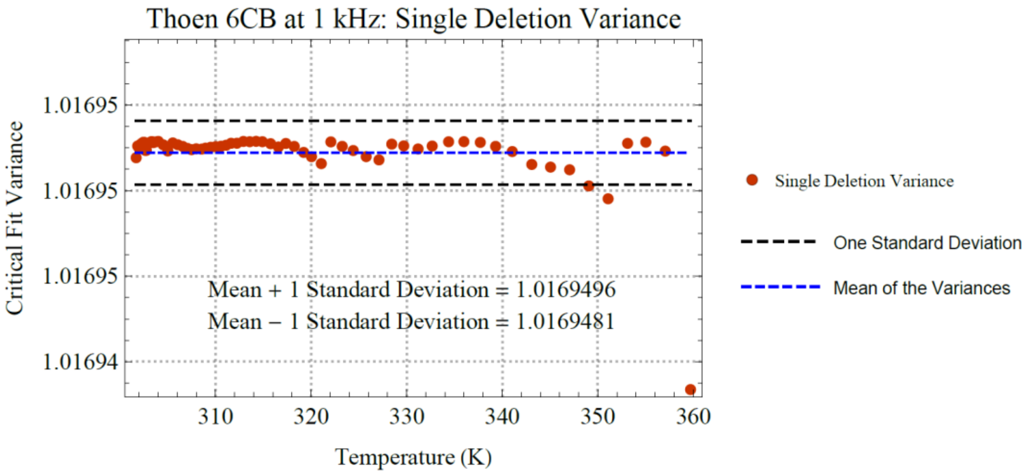

Figure 4.11: Second order expansion single deletion variance plot.

4.2.3.2 Results from Fitting the Three-Halves Order Expansion

Figures 4.12 and 4.13 show the χ_ν^2 and parameter estimates over range shrinking ΔT_μ from fitting the three-halves order expansion $\bar{\varepsilon}_{3/2}$. Figure 4.14 shows the single deletion variance plots versus absolute temperature T. Table 4.2b at the end of Section 4.2 shows the numerical results for typical data fitted by $\bar{\varepsilon}_{3/2}$.

Under range shrinking ΔT_μ, χ_ν^2 in Figure 4.12a drops significantly over the removal of the four highest temperature data points when T^* is a free parameter. The χ_ν^2 is weakly constant for

$4 \leq (N - \mu) < 12$. However, when T^* is fixed, the choice of range shrinking ΔT_μ based on χ_ν^2 is only clear to the highest temperature data point. For fixed T^*, the the χ_ν^2 plot appreciably decreases on decreasing ΔT_μ.

The corresponding parameter plots of T^*, α, and γ (see Figures 4.12b and 4.13 parts (a) through (c)) have a smaller spread in parameter estimates compared to $\bar{\varepsilon}_{II}$. Parameter β is well determined for fitting both $\bar{\varepsilon}_{3/2}$ and $\bar{\varepsilon}_{II}$ over range shrinking ΔT_μ. Additionally, unlike the parameter estimates for $\bar{\varepsilon}_{II}$, the parameter estimates for $\bar{\varepsilon}_{3/2}$ follow a non-monotonic trend versus ΔT_μ which allows for a better approximation of T^*, α, β, and γ.

Figure 4.13c shows the parameter γ versus range shrinking ΔT_μ. The fit of $\bar{\varepsilon}_{3/2}$ gives a better estimate for γ than $\bar{\varepsilon}_{II}$ (see in Figure 4.10c). The estimates using $\bar{\varepsilon}_{3/2}$ are better in that, for range shrinking beyond four data points, the rate of change in γ per ΔT_μ is even less than for $\bar{\varepsilon}_{II}$. As before, when T* is held constant, γ is more narrowly constrained.

The single deletion variance plots seen in Figure 4.14 reveal how each data point contributes to the fit of $\bar{\varepsilon}_{3/2}$ to typical data. Ideally, the deleted variances should follow a horizontal line or at least randomly vary around the average of the variances (seen by the center, horizontal blue short dashed line, where the black horizontal lines represent one standard deviation from that average).

The single deletion variance plots for $\bar{\varepsilon}_{3/2}$ have an important distinction from $\bar{\varepsilon}_{II}$ (see Figure 4.11). The lower temperature data points for both cases of T^* free (Figure 4.14a) and fixed (Figure 4.14b) are more similar than the Figures 4.11a and 4.11b. The Figures 4.14 a and b also do not unduly contribute to the fit for the low temperature data points. Unduly, here, refers to the low temperature variance points lying within one standard deviation of the avarance variance from Figure 4.14.

In both cases of T^* free and fixed, it is seen that the highest temperature data point unduly affect the fit over the other data points. The model by Equation 4.2 aims to describe the pretransitional curvature at the lowest data points. Given a sufficient temperature range, the highest temperature data points should not affect the fit. Most of the variances lie within one sigma of the average variance in Figure 4.14. Based on Figure 4.14, it is justifieable to range shrink by at least the highest temperature data point, which lies well beyond five sigma from the average variance.

	T* as a free parameter	T* fixed at literature value
(a) χ_v^2 vs ΔT_μ	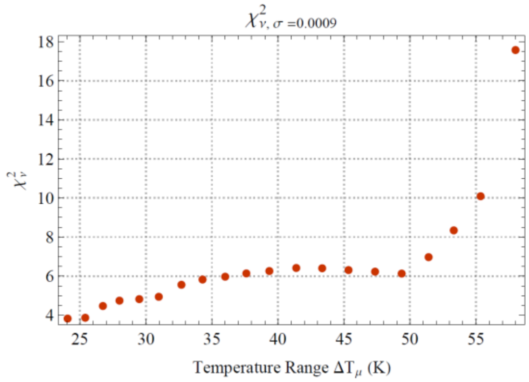	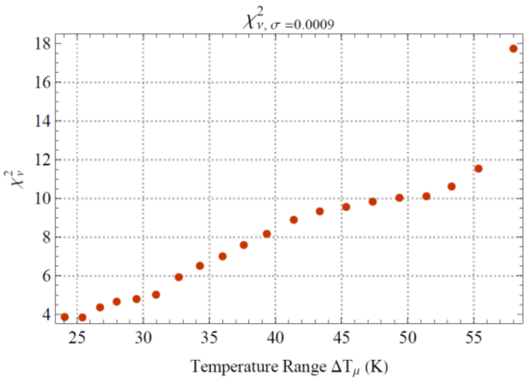
(b) T vs ΔT_μ	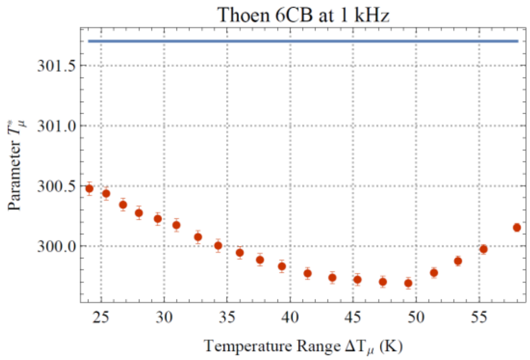	Fixed at $T_\mu^* = 300.3$ K. The literature value $\Delta T_\mu^* = 1.37$ K below the transition temperature T_{IM} [48].

Figure 4.12: Three-halves expansion goodness of fit and critical temperature.

T^* is a free parameter | T^* is fixed at literature value

(a)
α vs ΔT_μ

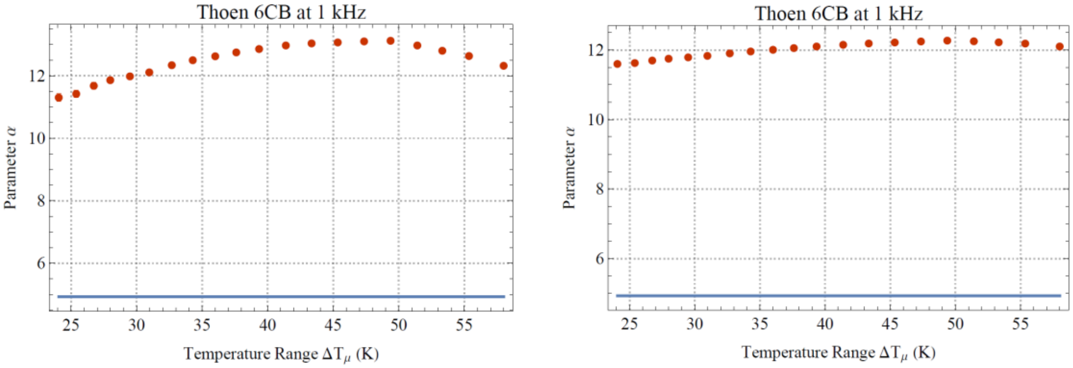

(b)
β vs ΔT_μ

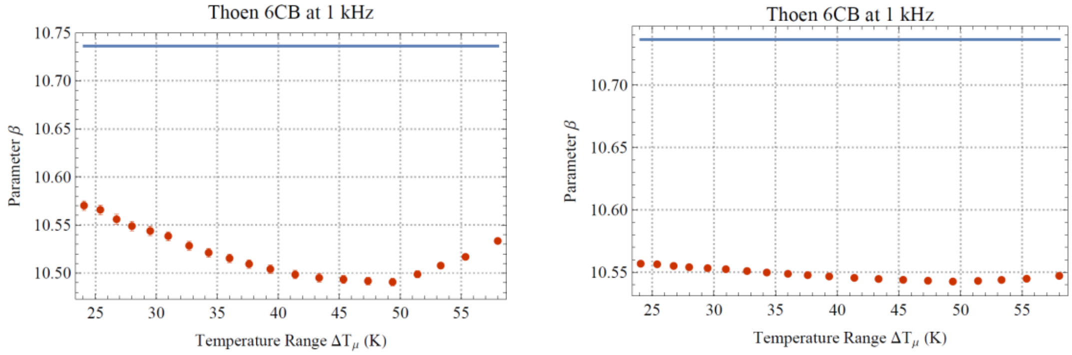

(c)
γ vs ΔT_μ

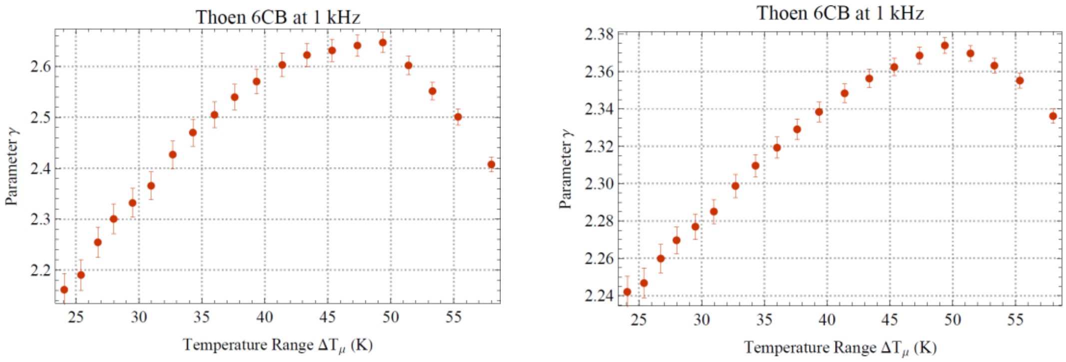

Figure 4.13: Three-halves order expansion fitting parameter results

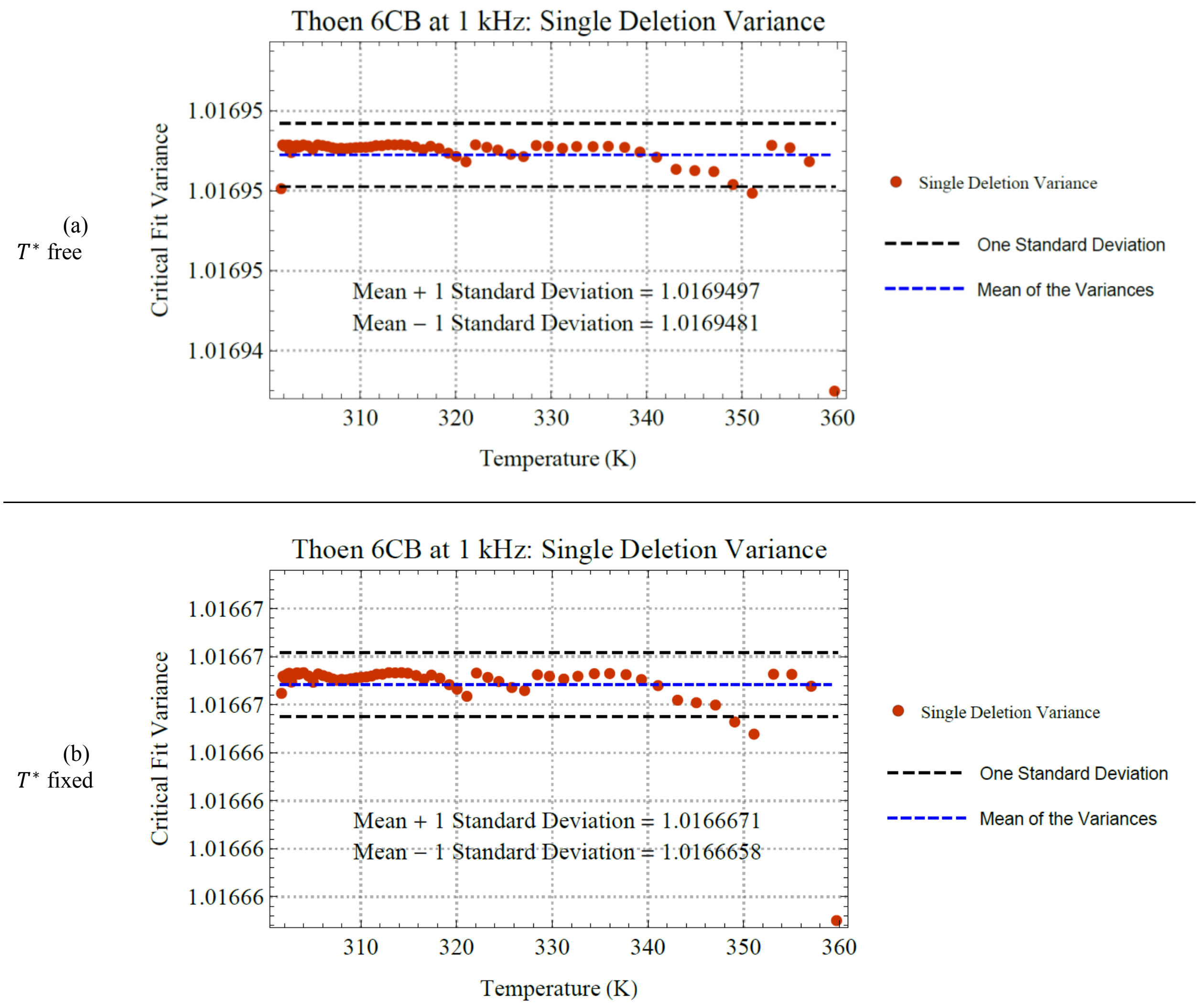

Figure 4.14: Three-halves order expansion single deletion variance plots.

4.2.3.3 Results from Fitting the First Order Expansion

Figures 4.15 and 4.16 show the χ_ν^2 and parameter estimates over range shrinking ΔT_μ from fitting the first order expansion $\bar{\varepsilon}_I$ to typical data. Figure 4.17 shows the single deletion variance plots versus absolute temperature T. Table 4.2a at the end of Section 4.2 shows the numerical results for typical data fitted by $\bar{\varepsilon}_I$. As with the previous two expansions, there is a significant drop in χ_{ν}^{2} over range shrinking by up to four data points. The χ_{ν}^{2} is relatively constant for $(N-\mu) > 4$ for both cases of T^{*} when fixed and free.

The corresponding parameter estimates T^{*}, α, β, and γ are seen in Figures 4.15b and 4.16 parts (a) through (c), respectively. The spread in the parameter estimates for the $4 < (N-\mu) < 12$ is quite small. The following is a comparison of the spread in parameter estimates for the range of $4 < (N-\mu) < 12$ when T^{*} is a free parameter. This range is chosen because $\bar{\varepsilon}_{3/2}$ has a relatively constant χ_{ν}^{2}. For fits $\bar{\varepsilon}_{I}$, $\bar{\varepsilon}_{3/2}$, and $\bar{\varepsilon}_{II}$, parameter α respectively had a spread of 0.1, 0.5, and 2.5. Parameter β respectively had a spread of 0.02, 0.04, and 0.07. Parameter γ respectively had a spread of 0.01, 0.17, and 0.5. Parameter T^{*} respectively had a spread of 0.02, 0.3, and 0.5.

Under range shrinking, the fits for $\bar{\varepsilon}_{I}$ and $\bar{\varepsilon}_{3/2}$ have no obvious advantage over each other. However, the fit for the spread in the parameter estimates for $\bar{\varepsilon}_{I}$ and $\bar{\varepsilon}_{3/2}$ are more similar than $\bar{\varepsilon}_{II}$. The parameter estimate values, however, are not all in agreement. Parameters T^{*} and β are in good agreement among the three expansions. Parameters α and γ are not in good agreement among $\bar{\varepsilon}_{I}$, $\bar{\varepsilon}_{3/2}$, and $\bar{\varepsilon}_{II}$.

The single deletion variance plots seen in Figure 4.17 are similar to the case of the three-halves order expansion in Figure 4.14. Most of the deleted variances are within one standard deviation of the average. Just as in the case of $\bar{\varepsilon}_{3/2}$ and $\bar{\varepsilon}_{II}$, the highest temperature data point has a single deletion variance that is unduly affecting the fit for both a fixed and free T^{*}. It is justified to range shrink by at least the highest temperature data point based on Figure 4.17.

<table>
<tr><th></th><th>T* is a free parameter</th><th>T* is fixed</th></tr>
<tr><td>(a)
χ_ν^2 vs ΔT_μ</td><td>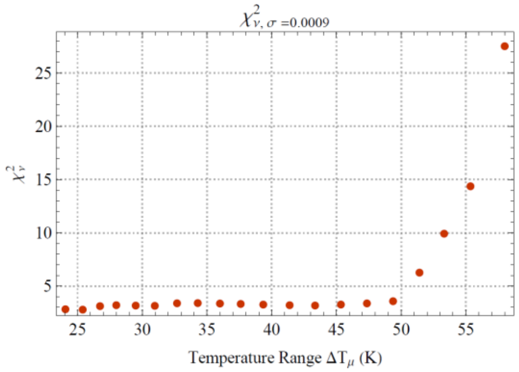
</td><td>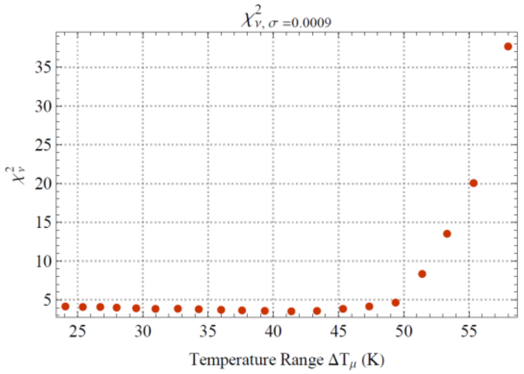
</td></tr>
<tr><td>(b)
T^* vs ΔT_μ</td><td>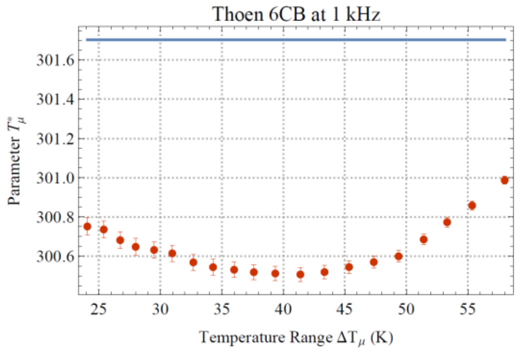
</td><td>Fixed at $T_\mu^* = 300.3$ K.
The literature value $\Delta T_\mu^* = 1.37$ K below the transition temperature T_{IM} [48].</td></tr>
</table>

Figure 4.15: First order expansion goodness of fit and critical temperature.

	T^* is a free parameter	T^* is fixed
(a) α vs ΔT_μ	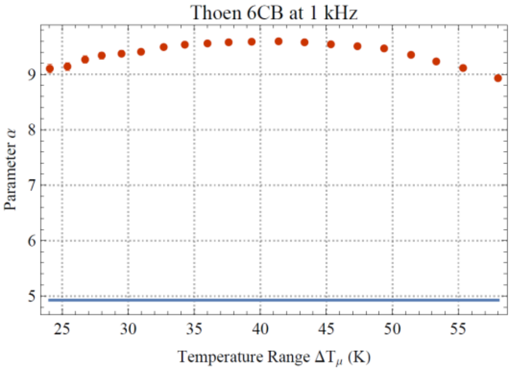	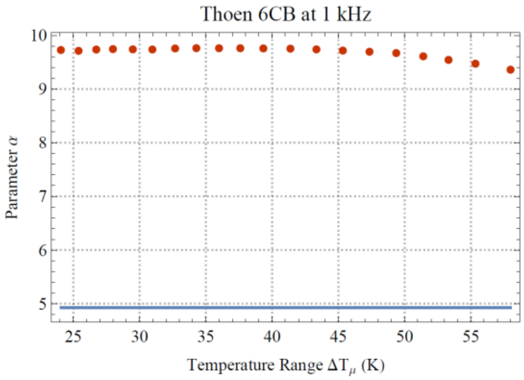
(b) β vs ΔT_μ	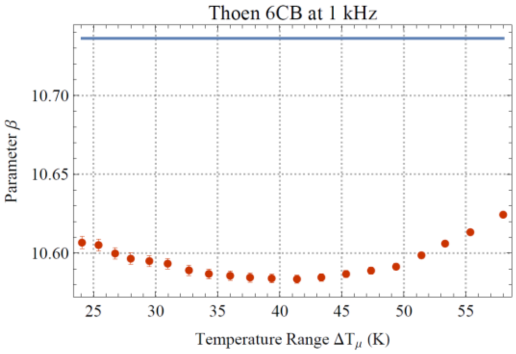	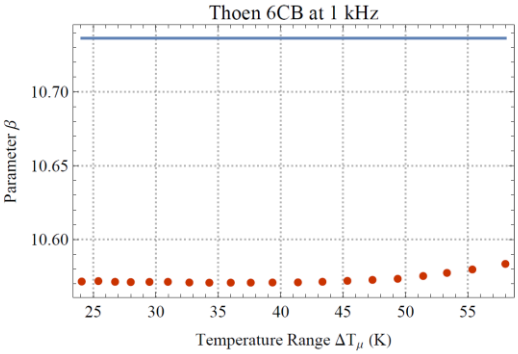
(c) γ vs ΔT_μ	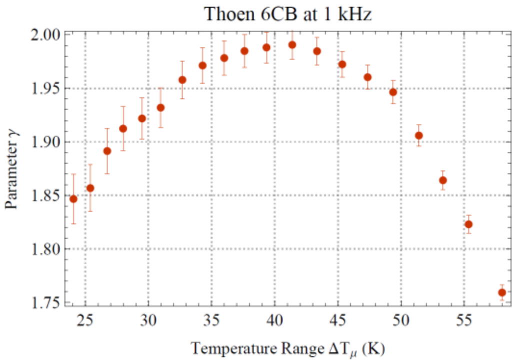	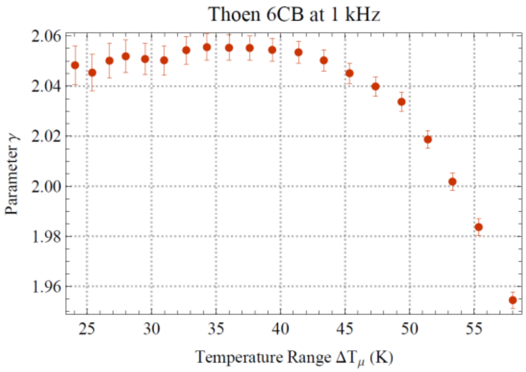

Figure 4.16: First order Expansion fitting parameter results.

(a)
T^* free

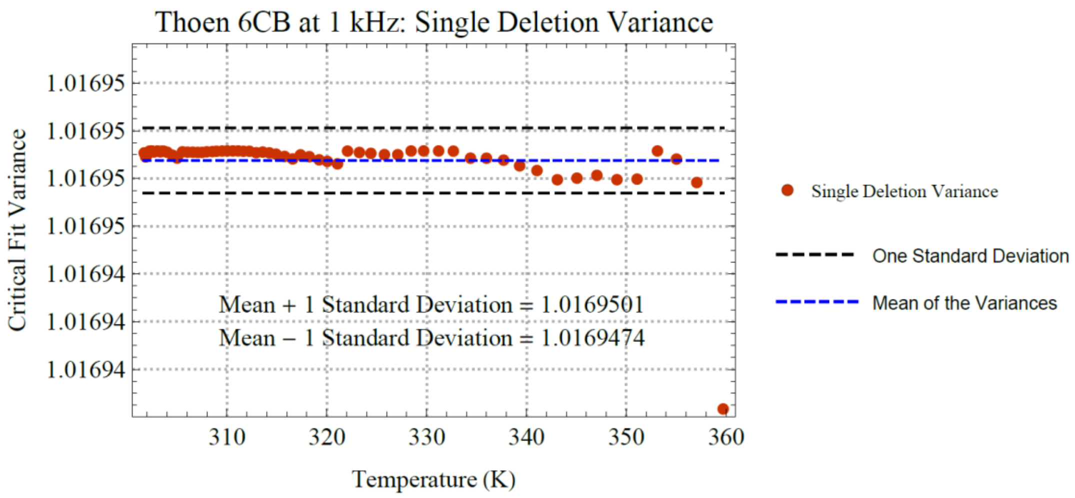

(b)
T^* fixed

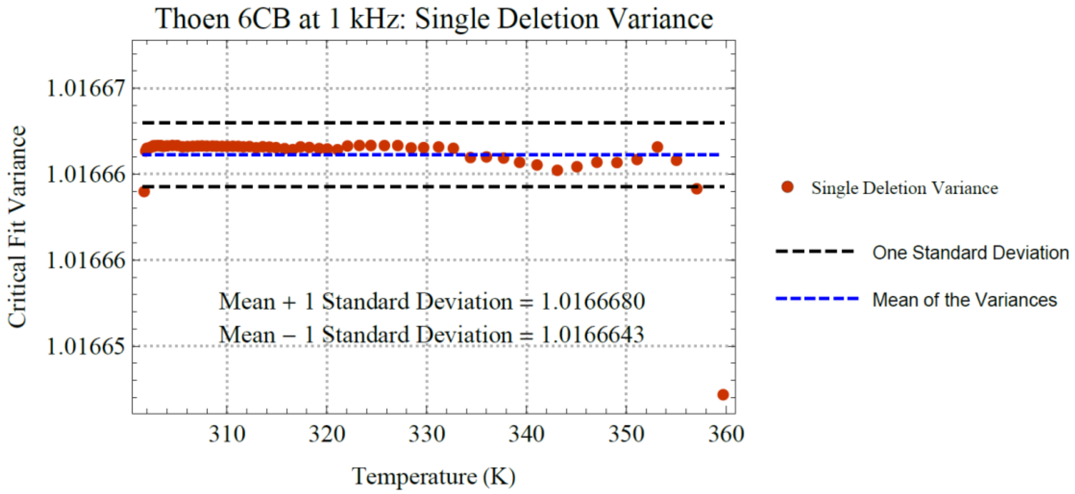

Figure 4.17: First order expansion single deletion variance plots.

4.2.4 Recap of the Expansion Fits

Figures 4.10, 4.13, and 4.16 show that all three expansions return reasonably determined parameter estimates for T^*, α, β and γ over range shrinking. However, parameter f from the second order expansion $\bar{\varepsilon}_{II}$ (see Figure 4.10) changes by over an order magnitude for range shrinking. The fit of $\bar{\varepsilon}_{II}$ is not stable over range shrinking. This leaves the expansions $\bar{\varepsilon}_{I}$ and $\bar{\varepsilon}_{3/2}$ as reasonable choices.

Table 4.2: Fitting parameter results using expansion Equations 4.4a, b, and c applied to the 6CB sample data.

Selection Criterion for μ §	μ	ΔT_μ (K)	T^* (K)	α	β	γ	f	$\chi^2_{\upsilon,\mathrm{m}}$
(a) $\bar{\varepsilon}_I$, Range Shrinking								
All Data	64	58.0	300.99 ± 0.02	8.93 ± 0.02	10.624 ± 0.001	1.759 ± 0.007	-	27.5
χ^2_υ	60	49. 4	300.60 ± 0.03	9.47 ± 0.03	10.591 ± 0.002	1.95 ± 0.01	-	3.58
χ^2_υ	56	41.4	300.51 ± 0.04	9.60 ± 0.04	10.584 ± 0.003	1.99 ± 0.01	-	3.21
SDV	53	36.0	300.53 ± 0.04	9.56 ± 0.04	10.586 ± 0.003	1.98 ± 0.02	-	3.36
All Data	64	58.0	[[300.33]]	9.36 ± 0.01	10.5835 ± 0.0005	1.955 ± 0.003	-	37.7
χ^2_υ	60	49. 4	[[300.33]]	9.67 ± 0.01	10.5734 ± 0.0006	2.034 ± 0.004	-	4.65
χ^2_υ	56	41.4	[[300.33]]	9.75 ± 0.02	10.5710 ± 0.0007	2.053 ± 0.004	-	3.52
SDV	53	36.0	[[300.33]]	9.76 ± 0.02	10.5708 ± 0.0007	2.055 ± 0.005	-	3.72
(b) $\bar{\varepsilon}_{3/2}$, Range Shrinking								
All Data	64	58.0	300.15 ± 0.03	12.32 ± 0.04	10.533 ± 0.003	2.41 ± 0.01	-	17.6
χ^2_υ	60	49.4	299.69 ± 0.05	13.12 ± 0.06	10.491 ± 0.004	2.65 ± 0.02	-	6.13
χ^2_υ	58	45.3	299.72 ± 0.05	13.07 ± 0.07	10.493 ± 0.004	2.63 ± 0.02	-	6.31
SDV	55	39.3	299.83 ± 0.05	12.86 ± 0.08	10.504 ± 0.004	2.57 ± 0.02	-	6.26
All Data	64	58.0	[[300.33]]	12.10 ± 0.01	10.5472 ± 0.0006	2.336 ± 0.004	-	17.7
χ^2_υ	60	49.4	[[300.33]]	12.27 ± 0.02	10.5426 ± 0.0006	2.374 ± 0.004	-	10.0
χ^2_υ	54	37.6	[[300.33]]	12.06 ± 0.02	10.5477 ± 0.0007	2.329 ± 0.004	-	7.59
SDV	55	39.3	[[300.33]]	12.10 ± 0.02	10.5467 ± 0.0007	2.338 ± 0.005	-	8.17
(c) $\bar{\varepsilon}_{II}$, Range Shrinking								
All Data	64	58.0	299.20 ± 0.09	14.8 ± 0.2	10.431 ± 0.009	3.04 ± 0.05	0.84 ± 0.05	15.0
χ^2_υ	60	49.4	300.47 ± 0.06	10.8 ± 0.2	10.573 ± 0.006	2.11 ± 0.04	-1.4 ± 0.1	4.03
χ^2_υ	61	51.4	300.24 ± 0.07	11.6 ± 0.2	10.548 ± 0.006	2.29 ± 0.04	-0.7 ± 0.1	6.34
SDV	55	39.3	300.86 ± 0.05	9.2 ± 0.2	10.618 ± 0.005	1.78 ± 0.04	-3.6 ± 0.3	2.4
All Data	64	58.0	[[300.33]]	12.21 ± 0.05	10.545 ± 0.001	2.355 ± 0.009	0.09 ± 0.04	18.0
χ^2_υ	60	49.4	[[300.33]]	11.18 ± 0.06	10.560 ± 0.001	2.195 ± 0.01	-1.16 ± 0.07	4.03
χ^2_υ	55	39.3	[[300.33]]	10.80 ± 0.09	10.565 ± 0.001	2.138 ± 0.01	-1.8 ± 0.1	2.43
SDV	55	39.3	[[300.33]]	10.80 ± 0.09	10.565 ± 0.001	2.138 ± 0.01	-1.8 ± 0.1	2.43

§: the number of fitting points
[[ ]]: fixed, literature from Zink et. al. [48]
SDV: Single Deletion Variance

4.3 A Hierarchical Model

This section aims to reveal a workaround to the problems encountered in the fitting process encountered in Sections 4.1 and 4.2. The shortcomings of using either the full function $\bar{\varepsilon}_{full}$ or the critical expansions $\bar{\varepsilon}_{II}$, $\bar{\varepsilon}_{3/2}$, and $\bar{\varepsilon}_{I}$ in isolation were seen in Sections 4.1 and 4.2, respectively. This section will build on the critical expansions $\bar{\varepsilon}_{II}$, $\bar{\varepsilon}_{3/2}$, and $\bar{\varepsilon}_{I}$ so as to achieve a self-consistent, hierarchical model that bypasses these problems. The relationships observed in Equations 4.4a through 4.4f among the parameters of $\bar{\varepsilon}_{full}$ and those of the series expansion will facilatate a multilevel model solution.

Each of the three series expansions $\bar{\varepsilon}_{I}$, $\bar{\varepsilon}_{3/2}$, and $\bar{\varepsilon}_{II}$ were used as separate estimators for parameters α, β, γ, and T^*. This section will show which is the most reliable estimator of those critical parameters and how to use those estimates to obtain reasonable estimates for parameters A, B, and C. Table 4.3 at the end of Section 4.3 shows the numerical fitting results for selected fits to typical data.

4.3.1 Untangling the Parameters: Three Expressions for *D*

As seen in the series expansion of Equation 4.2, parameters *B*, *C*, and *D* of $\bar{\varepsilon}_{full}$ are highly correlated. Either *B*, *C*, or *D* needs to be expressed in terms of the others in order to untangle these parameters and to obtain both reasonable and unambiguous results. Reasonable here refers to both the parameter estimates and the reported standard errors not being unphysically large.

In Section 4.2 it is seen that the critical expansions $\bar{\varepsilon}_{II}$, $\bar{\varepsilon}_{3/2}$, and $\bar{\varepsilon}_{I}$ (that is, Equations 4.5a, 4.5b and 4.5c, respectively) fit the data well and return unambiguous, well determined estimates for parameters α, β, γ, and T^* (see Table 4.2). Although the estimated uncertainty in the parameter estimates of f are reasonably determined from using $\bar{\varepsilon}_{II}$, parameter f does not become constant over range shrinking. For typical data that is range shrunk while using $\bar{\varepsilon}_{II}$, parameter f is not constrained in accordance with Equation 4.4f. Half of the data sets available return values for f that violate Figure 4.8. This happens for half of the data sets available and may not lead to a robust method that is the focus of this chapter.

Parameter D is chosen to be substituted in the full function $\bar{\varepsilon}_{full}$. Figure 4.4 shows that, when parameter D is fixed, the standard errors are reasonble for parameters B and C. However, manually varying D also revealed a false extremum cenetered around $D = 1$ with no resolution to the inifinte standard errors [53]. Figures 4.10b, 4.13b, and 4.16b reveal that parameter β (the difference between B and C) is a well determined quantity irrespective of the fitting model used as well as range shrinking.

All three critical expansions reveal two common relationships for parameter D that serve both as a consistency check and as a way to untangle B, C, and D. From parameter α in Equation 4.4b, D can be related directly to the full function parameters A and C as well as critical parameter α:

$$D = \sqrt{\frac{C}{(\alpha - A) - C}}\,. \tag{4.6a}$$

Note that parameters α, A, C, and D are defined as positive. Call Equation 4.6a a calculated parameter D_1. The second equation for D relies on the ratio of two critical expansion relations, Equations 4.4d and 4.4e:

$$D = \frac{B - \beta}{\gamma}. \tag{4.6b}$$

Call Equation 4.6b D_2. By definition, β and γ are positive. Parameter B is greater than β.

Additionally, $\bar{\varepsilon}_{II}$ has an expression for D that is a cubic equation found from paramter f defined in Equation 4.4f:

$$3fD^3 + 3D^2 = 1. \tag{4.6c}$$

Call the results of Equation 4.6c as D_3. The solution D_3 is multivalued and difficult to solve for analytically. It will only be used as a consistency check with equations D_1 and D_2. As will be seen in Tables 4.3 and 4.4, there are cases in which D_1 and D_2 are not equal.

4.3.2 Untangling the Parameters: the Hierarchical Model

Equations 4.6a and 4.6b reveal that calculated parameters D_1 and D_2 are simultaneously dependent on the parameters from both the full function $\bar{\varepsilon}_{full}$ and the series expansion $\bar{\varepsilon}_{series}$ (that is, $\bar{\varepsilon}_{II}$, $\bar{\varepsilon}_{3/2}$, or $\bar{\varepsilon}_{I}$). In order to find D, both the full function and the series expansion must be fitted to data.

Either D_1 or D_2 can be used as a substitute for D in the full function $\bar{\varepsilon}_{full}$. Parameter D_1 is chosen to substitute D in $\bar{\varepsilon}_{full}$. A physical solution for D should be real, positive, and single valued. Also, based on the definition of γ, it stands to reason that any relationship for parameter D used in the fitting process must involve C. For this, D is substituted with D_1 while D_2 is used as a consistency check. The resultant fitting equation that untangles B, C, and D from each other is,

$$\bar{\varepsilon}_{mod} = -Ax + B - C(1+x)\left[1 - \sqrt{x\left(\frac{C}{(\alpha-A)-C}\right)^{-1}}\, arctan\left(\sqrt{\frac{1}{x}\left(\frac{C}{(\alpha-A)-C}\right)}\right)\right]. \quad (4.7)$$

Equation 4.7 will be referred to as the modified full function, $\bar{\varepsilon}_{mod}$.

Figure 4.18 shows a flowchart that clarifies the proposed heirarchical model. The most robust approach is to first estimate the critical parameters α, β, γ, and T^* by fitting the series expansion $\bar{\varepsilon}_{series}$ (that is, $\bar{\varepsilon}_{II}$, $\bar{\varepsilon}_{3/2}$, or $\bar{\varepsilon}_{I}$) to data for a given temperature range ΔT_μ. The chosen values for parameters α and T^* are then substituted into $\bar{\varepsilon}_{mod}$. Then $\bar{\varepsilon}_{mod}$ is fitted to the data as a three parameter sub-model for a given temperature range ΔT_m. The consistency check is applied,

$$D_1(\alpha_\mu, A_m, C_m) = D_2(B_m, \beta_\mu, \gamma_\mu). \quad (4.8)$$

If the identity in Equation 4.8 is false, then the fit is considered inconsistent and unreasonable. The series expansion to be chosen ($\bar{\varepsilon}_{I}$, $\bar{\varepsilon}_{3/2}$, or $\bar{\varepsilon}_{II}$) will be determined, in part, by Equation 4.8 as well as how well this applies over all 22 data sets investigated.

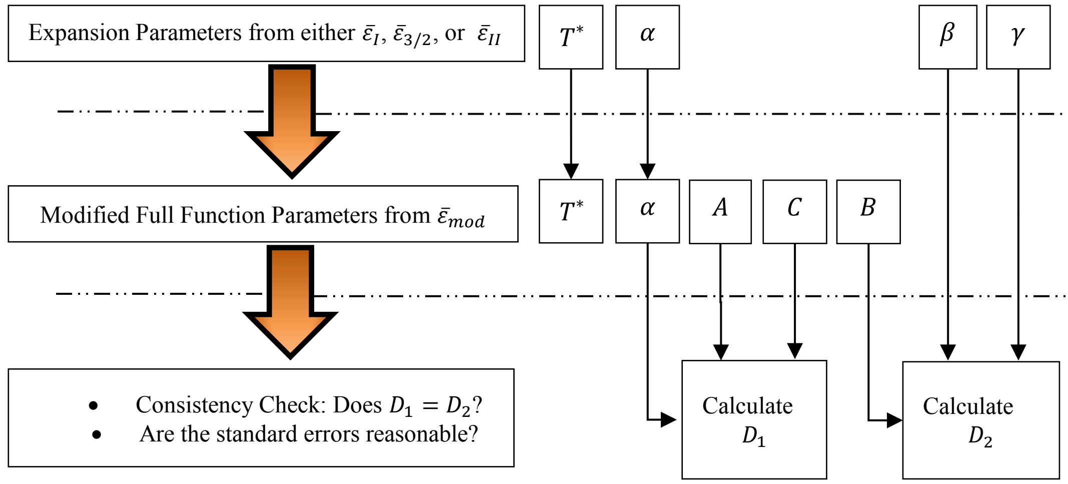

Figure 4.18: Flow chart of the proposed heirarchical fitting process.

Both expressions for *D* (Equations 4.6a and 4.6b) must be equal for a physical solution.

4.3.3 Fitting Methods and Results

As with the full function in Section 4.1 as well as the series expansions in Section 4.2, range shrinking is used. The range ΔT_N is that of the entire temperature range for a given data set. The nature of $\bar{\varepsilon}_{mod}$ involves two temperature ranges, hence two approaches: ΔT_μ and ΔT_m. As with Section 4.1, the index m will refer to range shrinking using $\bar{\varepsilon}_{mod}$. The index μ refers to range shrinking using the series expansions. Both data ranges $N - m$ and $N - \mu$ do not necessarily have to be the same since the critical expansion is an approximation of the full function. The first approach is seen numerically in Table 4.3. In this case, ΔT_m is fixed at ΔT_N while ΔT_μ varies (that is, the results from the critical fits). Second, Table 4.4 shows the case of $\Delta T_m = \Delta T_\mu$, where both are simultaneously range shrunk.

The following subsections individually apply the parameter results α, β, γ, and T_μ^* from $\bar{\varepsilon}_I$, $\bar{\varepsilon}_{3/2}$, and $\bar{\varepsilon}_{II}$ to $\bar{\varepsilon}_{mod}$. The case T_μ^* fixed will not be addressed from this point onward. As seen in Section 4.2, holding T_μ^* fixed did not resolve the problems of D going to one, the other parameter estimates having inordinately large standard errors, and the cases of a double minimum in χ_{ν}^{2}-space.

4.3.3.1 Modified Fit Results from Using the First Order Critical Parameters

Figures 4.19, 4.20, and 4.21 are the main results from using the parameter estimates α, β, γ, and T^* from $\bar{\varepsilon}_I$ followed by plugging those estimates into the modified full fit $\bar{\varepsilon}_{mod}$. The first column of Figures 4.19 and 4.20 show when ΔT_μ is varied and ΔT_m is fixed at ΔT_N. The second column shows the case of both ΔT_μ and when ΔT_m in comparison to Figures 4.5 and 4.6. The numerical results for the chosen fits using $\bar{\varepsilon}_I$ at $m = N$ with μ varied are shown in Table 4.3a. The numerical results for the case of $m = \mu$ are shown in Table 4.4a.

Let column (a) of Figure 4.5a (when $\bar{\varepsilon}_{full}$ was used) be a measure of the order of magnitude of the goodness of fit χ_{υ}^{2}. Figure 4.19a shows that χ_{υ}^{2} from using $\bar{\varepsilon}_{mod}$ is an order of magnitude larger than using $\bar{\varepsilon}_{full}$. This is indicative of the results from $\bar{\varepsilon}_I$ not being appropriate for use with $\bar{\varepsilon}_{mod}$. This happens for all data sets that were fitted.

Figures 4.19c, 4.20a, and 4.20b (compared to Figures 4.5 and 4.6, column (a)) reveal that the problem of unphysical standard errors persists for parameters B, C, and D. Figure 4.20b reveals that D_1 and D_2 disagree. The calculation of D_1 returns a value of one, yet the calculation of D_2 is about 10% lower than D_1. The red and blue veritical lines are error bars. Tables 4.3a and 4.4a show the chosen fits.

	Set $m = N$, μ varies	Set $m = \mu$, m varies with μ
(a) χ_v^2 vs. ΔT_m	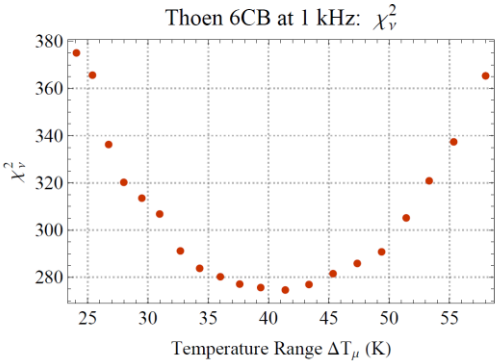	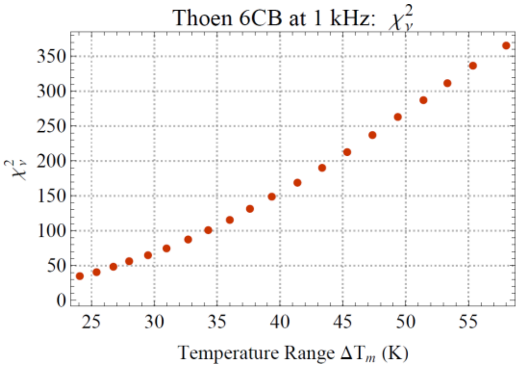
(b) A_m vs. ΔT_m	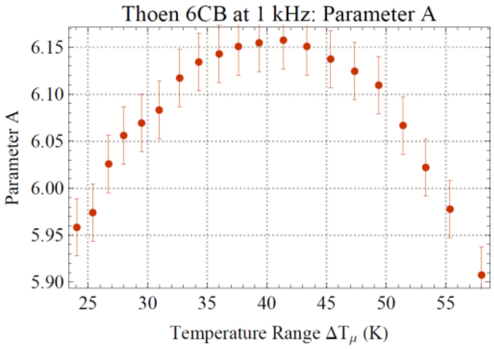	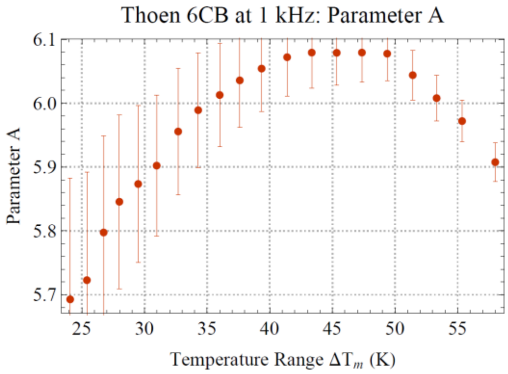
(c) B_m vs. ΔT_m	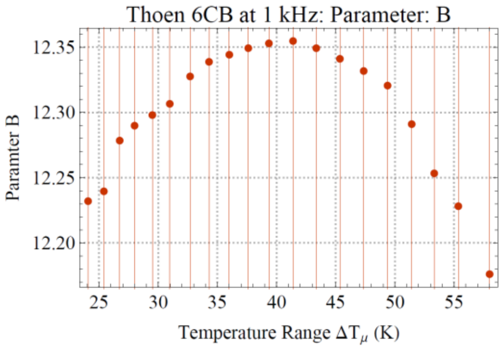	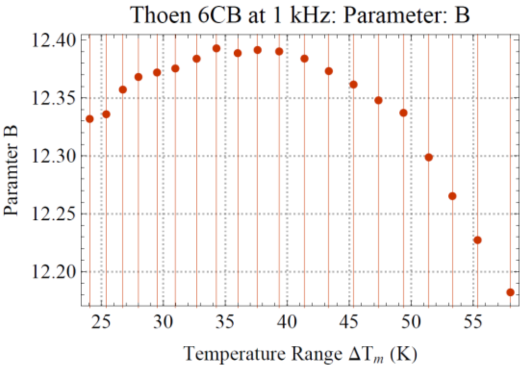

Figure 4.19: Modified full function fitting parameter results using the first order parameter estimates.

	Set $m = N$, μ varies	Set $m = \mu$, m varies with μ
(a) C_m vs. ΔT_m	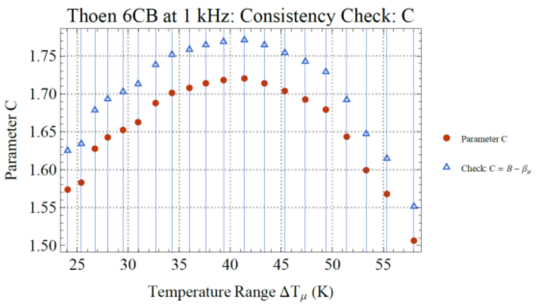	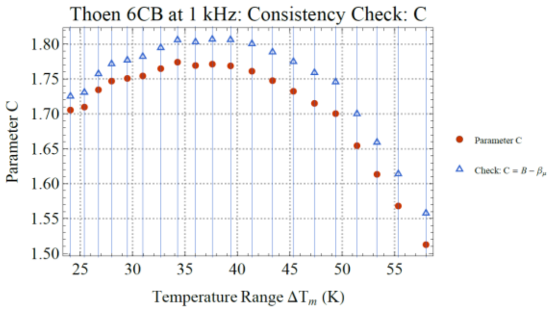
(b) D_m vs. ΔT_m	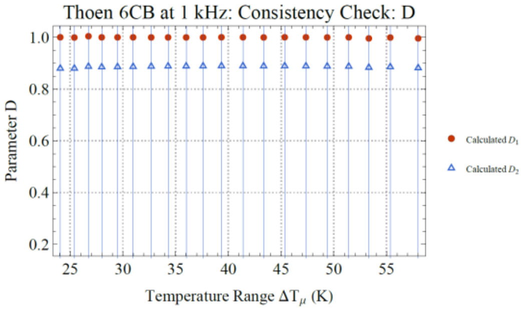	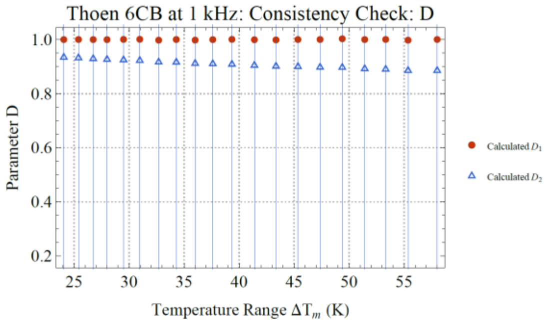

Figure 4.20: Modified full function fitting parameter results using the first order parameter estimates.

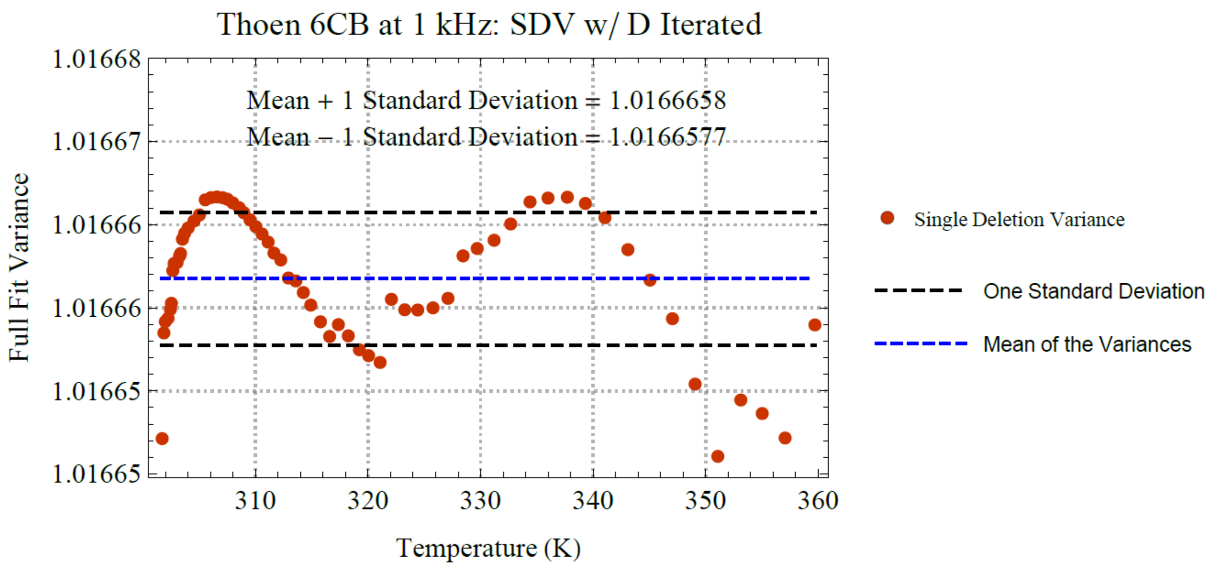

Figure 4.21: Modified full function single deletion variance plot using the first order expansion parameters. For the case of $m = N$.

4.3.3.2 Modified Fit Results from Using the Three-Halves Order Critical Parameters

Figures 4.22, 4.23, and 4.24 are the main results from using the parameter estimates using $\bar{\varepsilon}_{3/2}$ followed by plugging those estimates into the modified full fit $\bar{\varepsilon}_{mod}$. The first column of Figures 4.22 and 4.23 show when ΔT_μ is varied while ΔT_m is fixed at ΔT_N. The second column shows the case when both ΔT_μ and ΔT_m are simultaneously varied. The numerical results for the chosen fits using $\bar{\varepsilon}_{3/2}$ at $m = N$ with μ varied are shown in Table 4.3b. The numerical results for the case of $m = \mu$ are shown in Table 4.4b.

Relative to Figure 4.5a column a, χ_v^2 barely changes in Figure 4.22a column (a), and is about the same order of magnitude as χ_v^2 for the full fit $\bar{\varepsilon}_{full}$. When all of the $\bar{\varepsilon}_{mod}$ fits are not explicitly range shrunk in column (a) (that is, $m = N$, but μ is range shrunk), the parameter estimates are relatively constant with low standard errors versus ΔT_μ. The parameter estimates in column (a) begin to deviate when $\Delta T_{\mu}{\sim}40$ K and below. This shows that the $x^{\frac{3}{2}}$ term in the series expansion is needed in order to properly relate the critical expansion parameters to the full fit parameters (refer to Equations 4.4a through 4.4f).

Recall that the χ_{υ}^{2} over range shrinking for all of the fits in Sections 4.1 and 4.2 (see Figures 4.5a, 4.9a, 4.12a, and 4.15a) reveal that truncating a few data points from the high temperature side is necessary for typical data. This is the reasoning behind the second approach of explicitly range shrinking $\bar{\varepsilon}_{mod}$ such that $m = \mu$. The results are seen in Figure 4.22a column (a), relative to Figures 4.5a and 4.22a, χ_{υ}^{2} is much lower in Figure 4.11b. The parameter estimates in Figures 4.22 and 4.23 vary far less in column (b) than in column (a).

Lastly, the consistency check in Equation 4.8, holds in Figure 4.23b for the calculated parameters D_1 and D_2 over all range shrinking. The standard errors are also reasonable. Column (b), where $m = \mu$, further shows that D_1 as better determined overall range shrinking ΔT_{μ} and ΔT_{m}. All data sets fitted returned reasonable results when $m = \mu$.

	Set $m = N$, μ varies	Set $m = \mu$, m varies with μ
(a) χ_v^2 vs. ΔT_m	Thoen 6CB at 1 kHz: χ_v^2 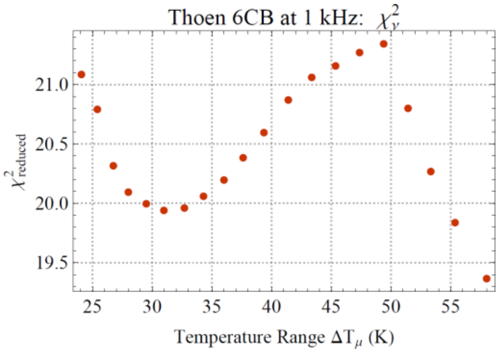	Thoen 6CB at 1 kHz: χ_v^2 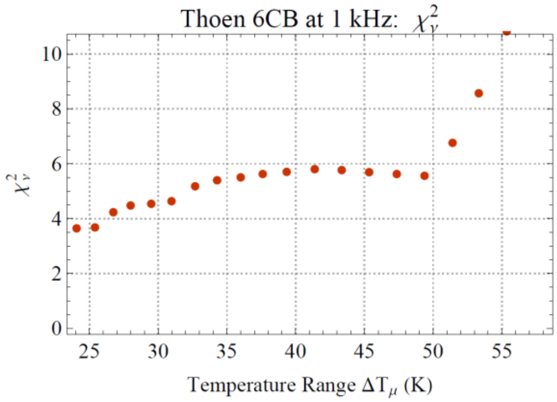
(b) A_m vs. ΔT_m	Thoen 6CB at 1 kHz: Parameter A 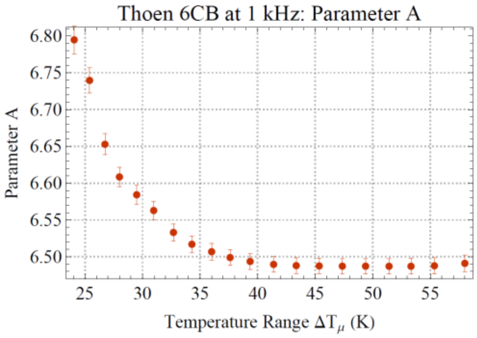	Thoen 6CB at 1 kHz: Parameter A 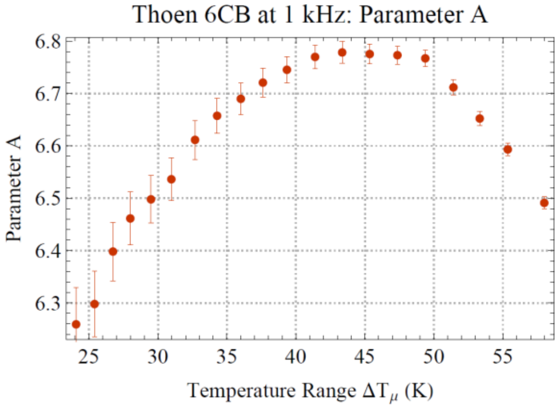
(c) B_m vs. ΔT_m	Thoen 6CB at 1 kHz: Parameter: B 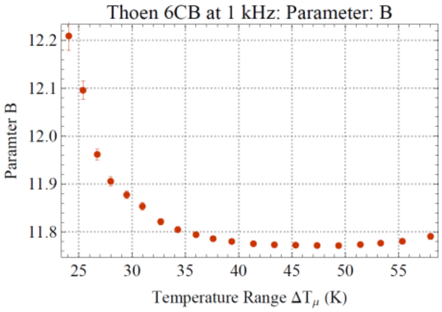	Thoen 6CB at 1 kHz: Parameter: B 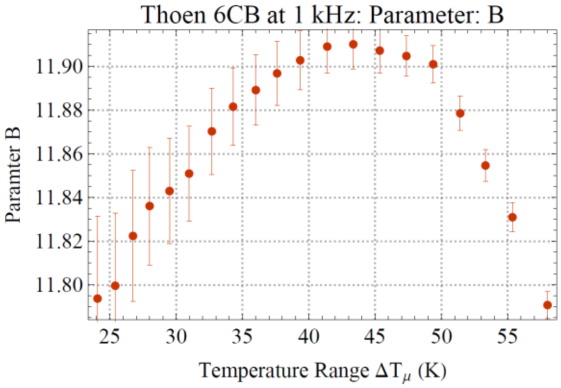

Figure 4.22: Modified full function fitting parameter results using the three-halves order parameters estimates.

	Set $m = N$, μ varies	Set $m = \mu$, m varies with μ
(a) C_m vs. ΔT_m	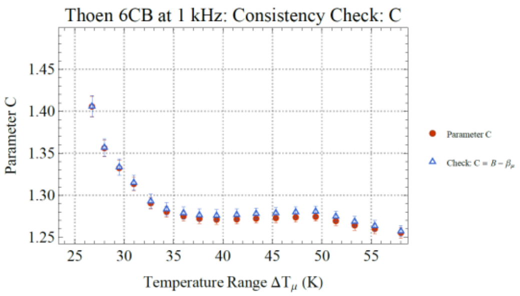	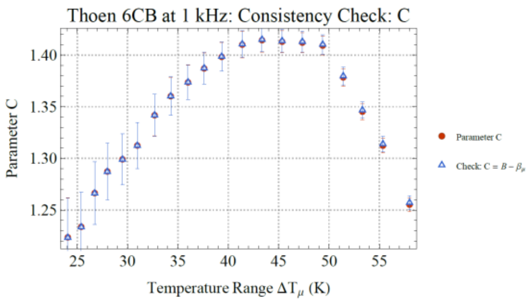
(b) D_m vs. ΔT_m	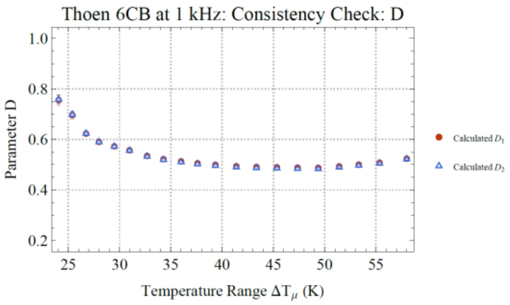	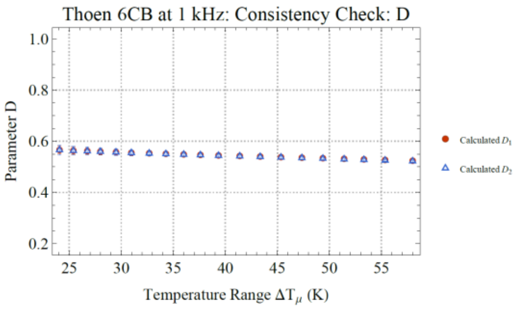

Figure 4.23: Modified full function fitting parameter results using the three-halves order parameters.

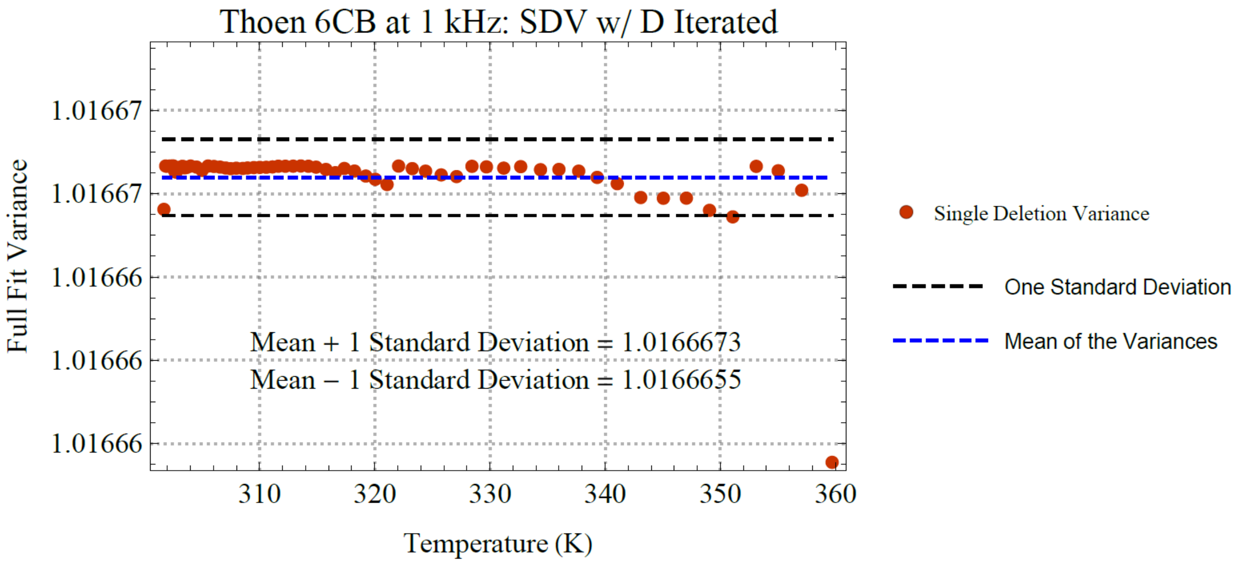

Figure 4.24: Modified full function single deletion variance plot using the three-halves order parameters. For the case of $m = N$.

4.3.3.3 Modified Fit Results from Using the Second Order Critical Parameters

For completeness, the results of using $\bar{\varepsilon}_{II}$ as an estimator for the critical fit parameters are discussed. With the same pattern as Figures 4.19 through 4.24, Figures 4.25, 4.26, and 4.27 show the results for using the parameter estimates from $\bar{\varepsilon}_{II}$. These fits are equally ambiguous as Section 4.3.3.1 where the results for $\bar{\varepsilon}_{I}$ are shown. The chosen numerical fit results using $\bar{\varepsilon}_{II}$ at $m = N$ with μ varied are shown in Table 4.3c. The numerical results for the case of $m = \mu$ are shown in Table 4.4c.

For both methods in Figures 4.25 and 4.26 (that is, column (a) where $m = N$ compared with column (b) where $m = \mu$), χ^2_υ increases by up to two orders of magnitude larger than all of the previous fits when range shrinking beyond six data points. This same pattern is seen via the standard errors in Figure 4.25b, 4.26a, and 4.27b. After range shrinking by four data points, the standard errors become unreasonable.

Figure 4.26b shows the results for the calculated D parameter and the consistency check. Parameters D_1 and D_2 are equal to each over the first four data points of range shrinking. However, the value of D over range shrinking does not remain constant. Beyond four data points of range shrinking (counting from the right to left of the plot), the values of D_1 and D_2 diverge from each other with both returning unreasonable standard errors.

	Set $m = N$, μ varies	Set $m = \mu$, m varies with μ
(a) χ_v^2 vs. ΔT_m	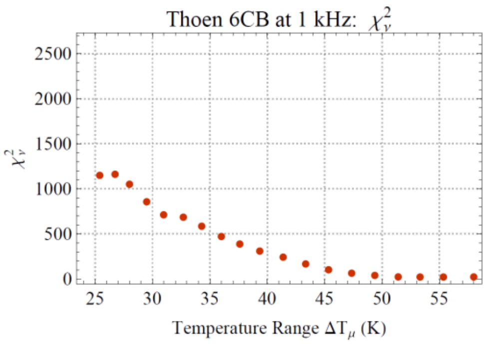 	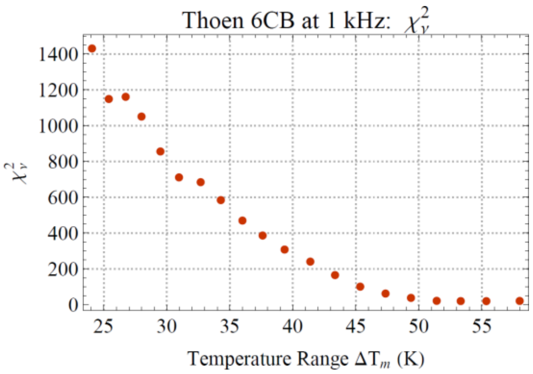
(b) A_m vs. ΔT_m	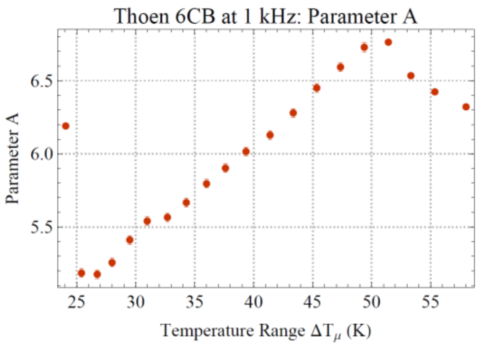 	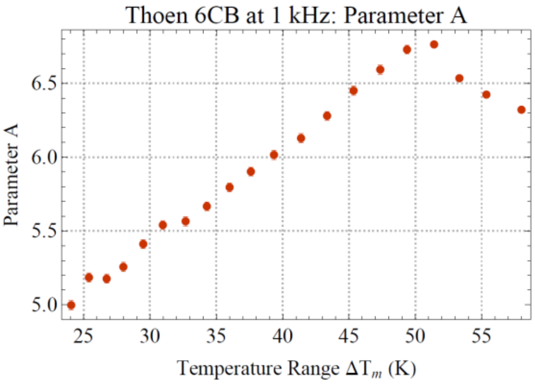
(c) B_m vs. ΔT_m	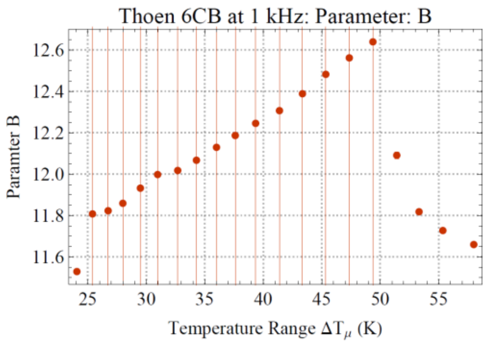 	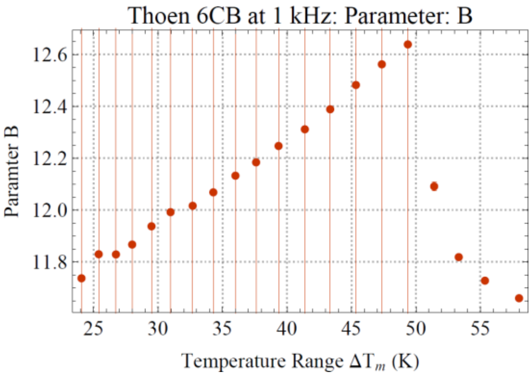

Figure 4.25: Modified full function fitting parameter results using the second order parameter estimates.

	Set $m = N$, μ varies	Set $m = \mu$, m varies with μ
(a) C_m vs. ΔD_m	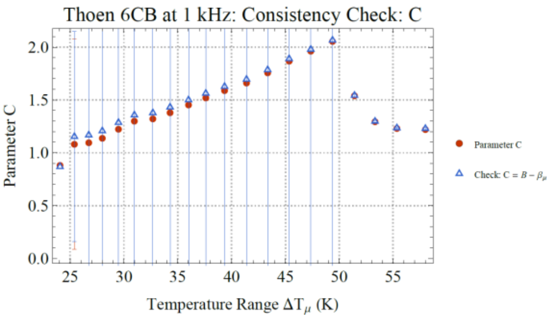	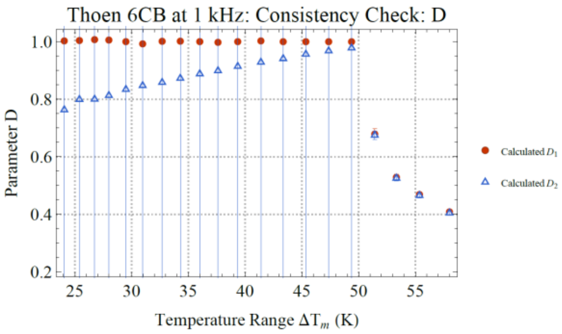
(b) D_m vs. ΔT_m	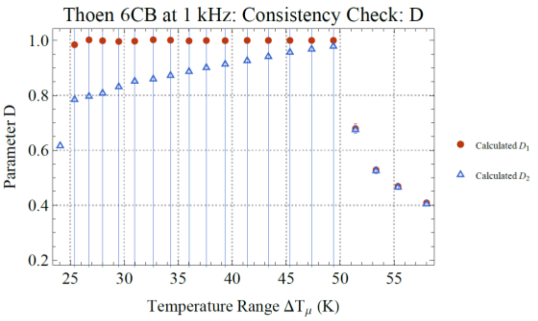	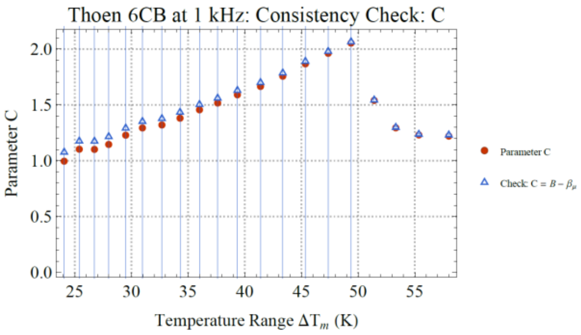

Figure 4.26: Modified full function fitting parameter results using the second order parameters

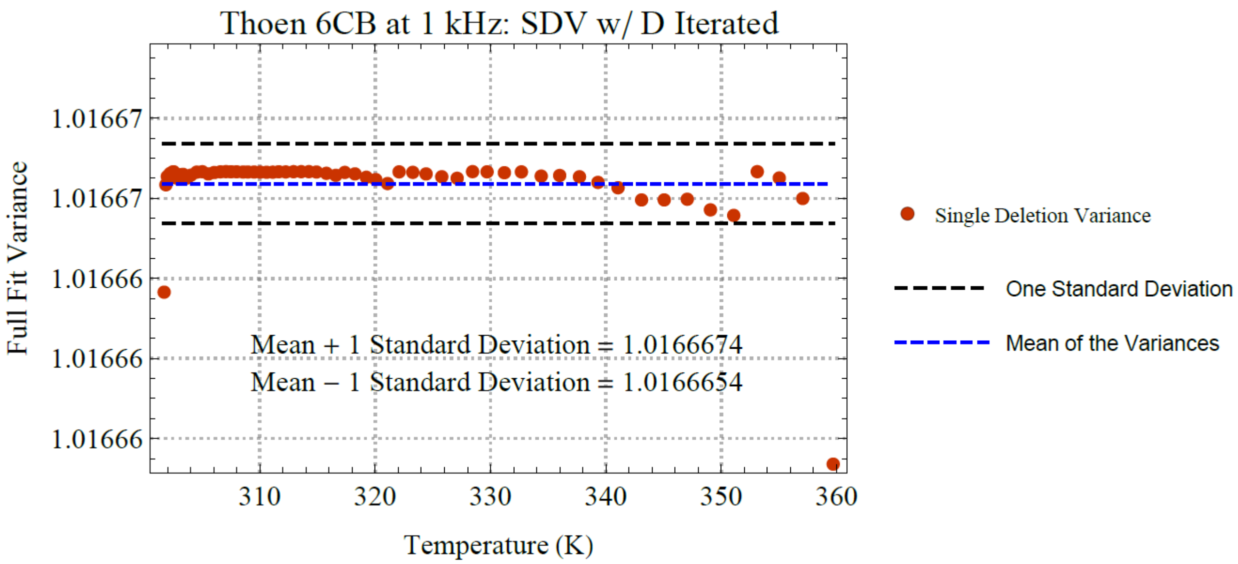

Figure 4.27: Modified full function fitting parameter results using the second order parameter estimates. For the case of $m = N$.

4.3.4 Comparison Summary

It has been shown in Sections 4.3.3.1 and 4.3.3.3 that using both $\bar{\varepsilon}_I$ and $\bar{\varepsilon}_{II}$ with $\bar{\varepsilon}_{mod}$ still does not resolve the problems seen in Section 4.1. When $\bar{\varepsilon}_I$ is used, the fitting routine returns inconsistent D_1 and D_2 values over all of range shrinking ΔT_m. Figure 4.19 reveals that, for this range of temperatures for typical data, χ_v^2 vs ΔT_m does not stabilize at a constant value for any significant range of temperatures and that all values of χ_v^2 are much larger than using $\bar{\varepsilon}_{3/2}$.

When $\bar{\varepsilon}_{II}$ is used, the fitting routine returns D_1 and D_2 values that initially agree with each other for the first few data points. However, over those few data points, D does not go to a constant value. Figure 4.26b reveals that, when range shrinking ΔT_m beyond those few highest data points, the values of D_1 and D_2 diverge with D_1 constant at a value of one with large standard errors. The most telling fault of using $\bar{\varepsilon}_{II}$ is that, from Figure 4.25a, the χ_v^2 is two orders of magnitude larger than using $\bar{\varepsilon}_{3/2}$, and one order of magnitude larger than using $\bar{\varepsilon}_I$.

From Section 4.3.3.2, $\bar{\varepsilon}_{3/2}$ is the best compromise for all data sets studied where ΔT_μ equals ΔT_m. Figure 4.22a reveals a χ_v^2 that barely changes (relative Figures 4.19a and 4.25a). The parameter estimates minimally changes (again relative to the other two cases $\bar{\varepsilon}_I$ and $\bar{\varepsilon}_{II}$). Over the entire range shrinking ΔT_m, the consistency check that D_1 equals D_2 holds. Most importantly, for the case of $\Delta T_\mu = \Delta T_m$ (column (b) of Figure 4.11), D is constant over the entire range shrinking ΔT_m. Paramter D for 6CB is between 0.50 and 0.60. Table 4.3 below shows the results of the heirarchical model when ΔT_m is held fixed at ΔT_N, but ΔT_μ is varied. Table 4.4 shows the results when $\Delta T_\mu = \Delta T_m$. In both cases (that is, Tables 4.3 and 4.4), the $D = 1$ extremum shows up when $\bar{\varepsilon}_I$ and $\bar{\varepsilon}_{II}$ are used with $\bar{\varepsilon}_{mod}$. However, the use of $\bar{\varepsilon}_{3/2}$ does not have that extremum appearing.

Table 4.3: Fitting results using Equations 4.7 applied to the 6CB sample data with $m = N$.

Selection Criterion for m §	μ †	m	T^* (K)	A	B	C	D_1‡	D_2‡‡	$\chi^2_{v,\mathrm{m}}$
(a) Range Shrinking μ: $\bar{\varepsilon}_I$									
All Data	64	64	(300.99 ± 0.02)	5.91 ± 0.03	12.2 ± 4	1.5 ± 4	1.0 ± 3	0.88 ± 2	365
χ_v^2	60	64	(300.60 ± 0.03)	6.11 ± 0.03	12.3 ± 100	1.7 ± 100	1.0 ± 60	0.89 ± 60	291
χ_v^2	56	64	(300.51 ± 0.04)	6.16 ± 0.03	12.4 ± 60	1.7 ± 60	1.0 ± 30	0.89 ± 30	275
SDV	53	64	(300.53 ± 0.04)	6.14 ± 0.03	12.3 ± 100	1.7 ± 100	1.0 ± 70	0.89 ± 60	280
All Data	64	64	[[300.33]]	6.03 ± 0.03	12.3 ± 3	1.7 ± 3	1.0 ± 2	0.89 ± 2	405
χ_v^2	60	64	[[300.33]]	6.17 ± 0.03	12.4 ± 100	1.8 ± 100	1.0 ± 60	0.89 ± 50	297
χ_v^2	56	64	[[300.33]]	6.21 ± 0.03	12.4 ± 10	1.8 ± 10	1.0 ± 7	0.89 ± 6	272
SDV	53	64	[[300.33]]	6.21 ± 0.03	12.4 ± 200	1.8 ± 200	1.0 ± 100	0.89 ± 100	269
(b) Range Shrinking: $\bar{\varepsilon}_{3/2}$									
All Data	64	64	(300.15 ± 0.03)	6.49 ± 0.01	11.791 ± 0.006	1.255 ± 0.006	0.524 ± 0.003	0.522 ± 0.004	19.4
χ_v^2	60	64	(299.69 ± 0.05)	6.49 ± 0.01	11.771 ± 0.005	1.274 ± 0.005	0.488 ± 0.003	0.484 ± 0.004	21.3
χ_v^2	58	64	(299.72 ± 0.05)	6.49 ± 0.01	11.772 ± 0.005	1.273 ± 0.005	0.490 ± 0.003	0.486 ± 0.005	21.2
SDV	55	64	(299.83 ± 0.05)	6.49 ± 0.01	11.780 ± 0.005	1.271 ± 0.006	0.500 ± 0.004	0.496 ± 0.005	20.6
All Data	64	64	[[300.33]]	6.46 ± 0.01	11.774 ± 0.006	1.225 ± 0.006	0.527 ± 0.002	0.525 ± 0.003	19.3
χ_v^2	60	64	[[300.33]]	6.40 ± 0.01	11.726 ± 0.005	1.180 ± 0.006	0.501 ± 0.002	0.498 ± 0.002	19.2
χ_v^2	54	64	[[300.33]]	6.48 ± 0.01	11.789 ± 0.006	1.240 ± 0.007	0.535 ± 0.002	0.533 ± 0.003	19.3
SDV	55	64	[[300.33]]	6.46 ± 0.01	11.774 ± 0.006	1.225 ± 0.006	0.527 ± 0.002	0.525 ± 0.003	19.3
(c) Range Shrinking: $\bar{\varepsilon}_{II}$									
All Data	64	64	(299.20 ± 0.09)	6.321 ± 0.009	11.660 ± 0.003	1.220 ± 0.004	0.409 ± 0.006	0.405 ± 0.008	21.1
χ_v^2	60	64	(300.47 ± 0.06)	6.73 ± 0.03	12.6 ± 70	2.1 ± 70	1.0 ± 40	0.98 ± 40	38.1
χ_v^2	61	64	(300.24 ± 0.07)	6.76 ± 0.02	12.09 ± 0.02	1.54 ± 0.02	0.68 ± 0.01	0.68 ± 0.01	21.6
SDV	55	64	(300.86 ± 0.05)	6.02 ± 0.03	12.2 ± 20	1.6 ± 20	1.0 ± 10	0.91 ± 10	308
All Data	64	64	[[300.33]]	6.42 ± 0.01	11.742 ± 0.006	1.195 ± 0.006	0.510 ± 0.003	0.508 ± 0.003	19.2
χ_v^2	60	64	[[300.33]]	6.87 ± 0.03	12.7 ± 500	2.2 ± 500	1.0 ± 200	0.99 ± 200	26.4
χ_v^2	55	64	[[300.33]]	6.69 ± 0.03	12.6 ± 10	2.1 ± 10	1.0 ± 5	0.97 ± 5	55.1
SDV	55	64	[[300.33]]	6.69 ± 0.03	12.6 ± 10	2.1 ± 10	1.0 ± 5	0.97 ± 5	55.1

§: the number of fitting points
†: the number of fitting points from the critical fit table
‡, ‡‡: calculated values from Equations 4.6a and 4.6b
( ): values taken from the critical fit table
[[ ]]: fixed, literature from Zink et. al. [48]

Table 4.4: Fitting results using Equations 4.7 applied to the 6CB sample data with $m = \mu$.

Selection Criterion for m §	μ †	m	T^* (K)	A	B	C	D_1‡	D_2‡‡	$\chi^2_{\upsilon,m}$
(a) Range Shrinking: $\bar{\varepsilon}_I$									
All Data	64	64	(300.99 ± 0.02)	6.03 ± 0.03	12.2 ± 200	1.5 ± 200	1.0 ± 100	0.89 ± 100	365
χ^2_υ	60	60	(300.60 ± 0.03)	6.08 ± 0.04	12.3 ± 8	1.7 ± 8	1.0 ± 5	0.90 ± 4	263
χ^2_υ	56	56	(300.51 ± 0.04)	6.07 ± 0.06	12.4 ± 40	1.8 ± 40	1.0 ± 20	0.90 ± 20	169
SDV	53	53	(300.53 ± 0.04)	6.01 ± 0.08	12.4 ± 20	1.8 ± 20	1.0 ± 10	0.91 ± 10	115
All Data	64	64	[[300.33]]	6.03 ± 0.03	12.3 ± 4	1.7 ± 4	1.0 ± 2	0.88 ± 2	405
χ^2_υ	60	60	[[300.33]]	6.14 ± 0.04	12.4 ± 4	1.8 ± 4	1.0 ± 2	0.89 ± 2	274
χ^2_υ	56	56	[[300.33]]	6.12 ± 0.06	12.4 ± 20	1.8 ± 20	1.0 ± 9	0.91 ± 8	174
SDV	53	53	[[300.33]]	6.08 ± 0.08	12.4 ± 100	1.8 ± 100	1.0 ± 70	0.91 ± 160	120
(b) Range Shrinking: $\bar{\varepsilon}_{3/2}$									
All Data	64	64	(300.15 ± 0.03)	6.49 ± 0.01	11.791 ± 0.006	1.255 ± 0.006	0.524 ± 0.003	0.522 ± 0.004	19.4
χ^2_υ	60	60	(299.69 ± 0.05)	6.77 ± 0.02	11.901 ± 0.009	1.409 ± 0.009	0.534 ± 0.004	0.533 ± 0.005	5.56
χ^2_υ	58	58	(299.72 ± 0.05)	6.78 ± 0.02	11.907 ± 0.01	1.41 ± 0.01	0.538 ± 0.005	0.537 ± 0.006	5.69
SDV	55	55	(299.83 ± 0.05)	6.75 ± 0.03	11.903 ± 0.01	1.40 ± 0.01	0.545 ± 0.006	0.544 ± 0.008	5.70
All Data	64	64	[[300.33]]	6.46 ± 0.01	11.774 ± 0.006	1.225 ± 0.006	0.527 ± 0.002	0.525 ± 0.003	19.3
χ^2_υ	60	60	[[300.33]]	6.63 ± 0.02	11.837 ± 0.009	1.294 ± 0.009	0.546 ± 0.003	0.545 ± 0.004	8.39
χ^2_υ	54	54	[[300.33]]	6.58 ± 0.03	11.85 ± 0.02	1.30 ± 0.02	0.558 ± 0.005	0.559 ± 0.007	6.82
SDV	55	55	[[300.33]]	6.60 ± 0.03	11.849 ± 0.01	1.30 ± 0.01	0.557 ± 0.005	0.557 ± 0.006	7.25
I Range Shrinking: $\bar{\varepsilon}_{II}$									
All Data	64	64	(299.20 ± 0.09)	6.321 ± 0.009	11.660 ± 0.003	1.220 ± 0.004	0.409 ± 0.006	0.405 ± 0.008	21.1
χ^2_υ	60	60	(300.47 ± 0.06)	6.73 ± 0.03	12.6 ± 100	2.1 ± 100	1.0 ± 70	0.98 ± 70	38.1
χ^2_υ	61	61	(300.24 ± 0.07)	6.76 ± 0.02	12.09 ± 0.02	1.54 ± 0.02	0.68 ± 0.02	0.68 ± 0.01	21.6
SDV	55	55	(300.86 ± 0.05)	6.02 ± 0.03	12.2 ± 100	1.6 ± 100	1.0 ± 80	0.91 ± 70	308
All Data	64	64	[[300.33]]	6.42 ± 0.01	11.742 ± 0.006	1.195 ± 0.006	0.510 ± 0.003	0.508 ± 0.003	19.2
χ^2_υ	60	60	[[300.33]]	6.88 ± 0.04	12.7 ± 900	2.2 ± 900	1.0 ± 400	0.99 ± 400	20.1
χ^2_υ	55	55	[[300.33]]	6.66 ± 0.07	12.6 ± 200	2.1 ± 200	1.0 ± 90	0.97 ± 80	33.3
SDV	55	55	[[300.33]]	6.66 ± 0.07	12.6 ± 200	2.1 ± 200	1.0 ± 90	0.97 ± 80	33.3

§: the number of fitting points
†: the number of fitting points from the critical fit table
‡, ‡‡: calculated values from Equations 4.6a and 4.6b
( ): values taken from the critical fit table
[[ ]]: fixed, literature from Zink et. al. [48]

4.4 General Theme: The Hierarchical Method Applied to All Data Sets

The problems encountered with $\bar{\varepsilon}_{full}$ are resolved by using the method outlined in Section 4.3. The most robust approach to the hierarchical model outlined in Figure 4.18 is to first use the $\bar{\varepsilon}_{3/2}$ expansion to estimate the critical parameters α, β, γ, and T^*. Range shrinking by ΔT_μ is used to ensure that the fit is in a region of parameter stability. The parameter results of α and T^* at a chosen μ are then fed into $\bar{\varepsilon}_{mod}$. The modified full fit is range shrunk by the same amount as $\bar{\varepsilon}_{3/2}$ such that $\Delta T_\mu = \Delta T_m$. Estimates are returned for parameters A, B, and C. The consistency check from Equation 4.8 is then applied by calculating D_1 and D_2. The results for a typical sample are seen in column (b) of both Figures 4.22 and 4.23 along with numerical results in Table 4.4b. The parameter estimates are constant after range shrinking by an amount based on χ_v^2 (see column (b) of Figure 4.22a). The standard errors are reasonable. The SDV plots are also used as a guide in range shrinking; however, their relevance lies within Sections 4.1 and 4.2.

Section 4.4 is organized thusly. First, summary tables are shown with information about each sample, the chosen critical fits for each sample, and the chosen modified fit results for each sample. Second, selected plots are shown and discussed to assess if the results are reasonable.

4.4.1 Summary of Result Tables

The outlined heirarchical model is applied to 22 data sets, obtained from two groups. Fifteen of the data sets have the isotropic to nematic phase transitions for which the theory outlined in Chapter 2 is developed for. Six data sets have smectogenic to isotropic phase transitions, which still have nematic ordering. One of the data sets has an isotroipc to cholesteric transition. As mentioned in Chapter 1, the cholesteric phase is a slightly chiral variant of the nematic phase. Table 4.5 outlines some relevant metadata concerning these data sets.

From critical exponents, Rzoska et. al. used an empirical function to fit their data [40],

$$\bar{\varepsilon}_{Rzoska} = -\alpha x + \beta + \gamma'(x^{\varphi}),$$

where φ came out to be one-half, to within a margin of error, irrespective of the sample. The model discussed in this chapter has an expansion that ends up with a similar form given by Equation 4.5b:

$$\bar{\varepsilon}_{3/2} = -\alpha x + \beta + \frac{\pi}{2}\gamma\left(x^{\frac{1}{2}} + x^{\frac{3}{2}}\right).$$

As shown in Section 4.2 and then through Section 4.3, the $x^{\frac{3}{2}}$ term is necessary in order to obtain a self consistent model given by Equations 4.7 and 4.8. However, the x^2 term seems to overparameterize the model. The chosen critical expansions for all 22 samples are shown in Table 4.6.

A change of variables is made using the critical relationship for parameter D, Equation 4.6a. Prior to fitting $\bar{\varepsilon}_{mod}$, $\bar{\varepsilon}_{3/2}$ gives parameters α, β, γ, and T^*. By using these, $\bar{\varepsilon}_{mod}$ is reduced to fitting only three parameters. The chosen fit results for all samples are seen in Table 4.7.

Figures 4.6 and 4.7 display the magnitudes and uncertainties in a slightly modified format from Sections 4.1 through 4.3: $p_{\pm\,\delta p\,\pm\,\Delta p}$. A given parameter magnitude p represents the chosen value on range shrinking ΔT_μ or ΔT_m. The subscripted δp represents the associated standard error reported by the fitting routine where the fitting routine takes into account σ_{error} reported in the far right column of Table 4.5. The subscripted Δp represents the spread in possible values of a given parameter p on range shrinking. As an example, Table 4.2b shows when T^* is a fixed parameter. Exluding all data used, three sets of fitting results are reported for range shrinking: based on the first most reasonable χ_v^2, based on the second most reasonable χ_v^2, and based on single deletion variance (SDV). The spread looks at the standard deviation of a given parameter estimate over the aforementioned three values.

Table 4.5: Information about each sample and select metadata concerning the corresponding dielectric data sets.

Sample + Frequency	Transition Type From Isotropic	Molar Mass (g/mol)	N	ΔT_N(K)	T_{IM}(K)	$\Delta\varepsilon_N$	ε_{IM}	Estimated Spread in $\bar{\varepsilon}$, σ_{error}‡‡
(a) Thoen nCB Series								
5CB at 1 kHz	N	249.35	32	109	308.57	1.963	11.312	0.003
6CB at 1 kHz	N	263.38	64	58.0	301.70	0.7117	10.7361	0.0009
7CB at 1 kHz	N	277.40	33	92.1	315.79	1.531	9.962	0.002
8CB at 1 kHz	N	291.43	36	89.2	315.02	1.234	9.584	0.001
9CB at 1 kHz	N	305.46	34	56.6	323.27	0.7175	9.0169	0.0005
10CB at 1 kHz	Sm	319.48	39	39.4	324.11	0.4335	8.7485	0.0003
11CB at 1 kHz	Sm	333.51	36	38.2	330.49	0.3850	8.5346	0.0003
12CB at 1 kHz	Sm	347.54	38	58.4	331.61	0.8456	8.1393	0.002
(b) Rzoska nCB Series								
4CB at 100 kHz	N	235.32	78	47.5	290.56	0.5170	11.2230	0.0005
5CB at 10 kHz	N	249.35	51	24.6	308.59	0.1695	10.8883	0.0003
6CB at 10 kHz	N	263.38	48	96.0	302.34	1.973	10.507	0.001
8CB at 100 kHz	N	291.43	42	50.4	313.37	0.5310	10.5600	0.0004
9CB at 10 kHz	N	305.46	40	34.3	323.01	0.3140	10.4680	0.0009
12CB at 10 kHz	Sm	347.54	50	34.9	331.12	0.4019	9.8003	0.0003
(c) Rzoska nOCB Series								
6OCB at 10 kHz	N	279.38	28	21.1	349.30	0.1040	11.5520	0.0005
7OCB at 10 kHz	N	293.40	52	43.6	346.70	0.2070	10.0490	0.0003
8OCB at 10 kHz	N	307.43	53	32.5	352.80	0.2230	10.4410	0.0006
(d) Rzoska: Miscellaneous								
5CN at 10 kHz	N	283.45	40	11.4	325.57	0.09190	8.7992	0.0002
HCPP at 100 kHz	N	355.48	61	44.0	325.00	0.5340	18.2400	0.0006
9BT at 10 kHz	Sm	337.52	22	36.8	339.95	0.2091	6.7536	0.0002
10BT at 10 kHz	Sm	351.55	29	39.2	339.20	0.2849	6.7087	0.0002
5*CB at 1 kHz	Ch	249.35	29	55.7	252.62	1.108	12.790	0.005

‡: Calculated molar mass of materials.

‡‡: Calculated spread in permittivity data ε. The single deletion variance test was used to estimate the average weight for a given data set. Note that this value is, in most cases, an order of magnitude larger than the last decimal. For Thoen et. al., the last decimal was the fourth.

Table 4.6: The chosen critical fit parameter estimates for each sample studied.

Sample + Frequency	μ	ΔT_μ(K)	T^* (K)	α	β	γ	χ_v^2
(a) Thoen nCB Series							
5CB at 1 kHz	23	37.9	305.8 ± 0.4 ± 0.6	14.0 ± 0.6 ± 1	11.02 ± 0.03 ± 0.05	2.7 ± 0.2 ± 0.3	0.322
6CB at 1 kHz	60	49.8	299.69 ± 0.05 ± 0.07	13.12 ± 0.06 ± 0.1	10.491 ± 0.004 ± 0.007	2.65 ± 0.02 ± 0.04	6.13
7CB at 1 kHz	22	38.9	311.1 ± 0.4 ± 2	17.3 ± 0.6 ± 3	9.47 ± 0.04 ± 0.2	3.9 ± 0.2 ± 1	2.04
8CB at 1 kHz	31	59.4	312.54 ± 0.07 ± 0.5	16.7 ± 0.1 ± 1	9.190 ± 0.008 ± 0.06	3.81 ± 0.04 ± 0.4	12.8
9CB at 1 kHz	26	28.0	320.84 ± 0.05 ± 0.1	16.4 ± 0.1 ± 0.3	8.662 ± 0.006 ± 0.01	3.49 ± 0.04 ± 0.08	3.96
10CB at 1 kHz	32	23.2	321.25 ± 0.05 ± 0.06	14.83 ± 0.09 ± 0.1	8.446 ± 0.004 ± 0.006	2.91 ± 0.03 ± 0.03	4.47
11CB at 1 kHz	28	17.3	326.6 ± 0.1 ± 0.2	14.2 ± 0.2 ± 0.3	8.220 ± 0.01 ± 0.01	2.79 ± 0.07 ± 0.09	1.20
12CB at 1 kHz	32	40.3	327.6 ± 0.4 ± 0.07	12.4 ± 0.4 ± 0.09	7.93 ± 0.02 ± 0.004	2.0 ± 0.1 ± 0.03	0.372
(b) Rzoska nCB Series							
4CB at 100 kHz	60	22.6	289.41 ± 0.06 ± 0.3	7.74 ± 0.06 ± 0.4	11.140 ± 0.002 ± 0.01	1.15 ± 0.02 ± 0.1	28.2
5CB at 10 kHz	51	24.7	307.57 ± 0.02 ± 0.05	9.54 ± 0.03 ± 0.2	10.771 ± 0.001 ± 0.005	1.652 ± 0.008 ± 0.04	19.3
6CB at 10 kHz	43	58.4	299.80 ± 0.07 ± 0.2	18.9 ± 0.1 ± 0.4	10.092 ± 0.008 ± 0.03	4.04 ± 0.04 ± 0.1	18.0
8CB at 100 kHz	41	41.1	310.87 ± 0.02 ± 0.1	17.01 ± 0.05 ± 0.3	10.146 ± 0.003 ± 0.02	3.91 ± 0.01 ± 0.1	11.0
9CB at 10 kHz	32	24.2	321.05 ± 0.07 ± 0.02	17.8 ± 0.2 ± 0.07	10.11 ± 0.01 ± 0.003	3.81 ± 0.06 ± 0.02	4.28
12CB at 10 kHz	44	26.8	325.6 ± 0.1 ± 0.6	16.1 ± 0.1 ± 0.8	9.404 ± 0.008 ± 0.05	3.21 ± 0.04 ± 0.3	36.5
(c) Rzoska nOCB Series							
6OCB at 10 kHz	24	13.1	348.17 ± 0.07 ± 0.2	11.1 ± 0.3 ± 1	11.402 ± 0.007 ± 0.03	2.05 ± 0.05 ± 0.2	12.3
7OCB at 10 kHz	52	43.6	345.07 ± 0.02 ± 0.08	11.02 ± 0.03 ± 0.2	9.825 ± 0.001 ± 0.008	2.522 ± 0.008 ± 0.05	38.2
8OCB at 10 kHz	50	23.6	351.21 ± 0.03 ± 0.03	17.0 ± 0.1 ± 0.2	10.137 ± 0.005 ± 0.005	3.65 ± 0.03 ± 0.04	15.9
(d) Rzoska: Miscellaneous							
5CN at 10 kHz	40	11.4	323.83 ± 0.06 ± 0.1	10.7 ± 0.1 ± 0.3	8.698 ± 0.003 ± 0.007	1.38 ± 0.03 ± 0.06	1.18
HCPP at 100 kHz	60	39.7	323.94 ± 0.01 ± 0.05	17.91 ± 0.04 ± 0.3	17.969 ± 0.002 ± 0.009	3.71 ± 0.01 ± 0.06	12.8
9BT at 10 kHz	22	36.8	326.2 ± 0.6 ± 1	9.9 ± 0.3 ± 0.8	6.37 ± 0.02 ± 0.07	2.4 ± 0.1 ± 0.3	15.5
10BT at 10 kHz	29	39.2	329.4 ± 0.3 ± 0.9	9.6 ± 0.1 ± 0.6	6.418 ± 0.009 ± 0.04	2.07 ± 0.04 ± 0.2	8.33
5*CB at 1 kHz	23	43.66	249.3 ± 0.4 ± 0.9	24.0 ± 0.9 ± 3	12.07 ± 0.07 ± 0.2	5.7 ± 0.3 ± 0.9	11.1

Table 4.7: The chosen modified full fit parameter results for each sample studied such that $\Delta T_m = \Delta T_\mu$.

Name and Frequency	A	B	C	D_1‡	D_2‡‡	χ_υ^2
(a) Thoen nCB Series						
5CB at 1 kHz	7.4 ± 0.1 ± 0.4	12.50 ± 0.08 ± 0.1	1.47 ± 0.08 ± 0.2	0.54 ± 0.04 ± 0.01	0.54 ± 0.05 ± 0.01	0.332
6CB at 1 kHz	6.77 ± 0.02 ± 0.02	11.901 ± 0.009 ± 0.003	1.409 ± 0.009 ± 0.007	0.534 ± 0.004 ± 0.005	0.533 ± 0.005 ± 0.006	5.56
7CB at 1 kHz	7.95 ± 0.09 ± 0.4	11.55 ± 0.05 ± 0.2	2.08 ± 0.05 ± 0.4	0.54 ± 0.02 ± 0.02	0.53 ± 0.03 ± 0.02	1.83
8CB at 1 kHz	7.46 ± 0.02 ± 0.3	11.19 ± 0.01 ± 0.08	1.99 ± 0.01 ± 0.1	0.525 ± 0.005 ± 0.02	0.524 ± 0.006 ± 0.02	12.1
9CB at 1 kHz	8.18 ± 0.05 ± 0.2	10.58 ± 0.02 ± 0.06	1.91 ± 0.02 ± 0.07	0.549 ± 0.007 ± 0.008	0.549 ± 0.009 ± 0.008	3.83
10CB at 1 kHz	7.96 ± 0.03 ± 0.06	10.05 ± 0.02 ± 0.02	1.60 ± 0.02 ± 0.03	0.552 ± 0.006 ± 0.002	0.552 ± 0.008 ± 0.003	4.35
11CB at 1 kHz	7.64 ± 0.07 ± 0.2	9.77 ± 0.04 ± 0.05	1.55 ± 0.04 ± 0.06	0.56 ± 0.02 ± 0.004	0.56 ± 0.02 ± 0.004	1.16
12CB at 1 kHz	7.49 ± 0.08 ± 0.06	9.03 ± 0.04 ± 0.02	1.09 ± 0.04 ± 0.03	0.54 ± 0.03 ± 0.006	0.54 ± 0.04 ± 0.006	0.362
(b) Rzoska nCB Series						
4CB at 100 kHz	5.03 ± 0.03 ± 0.2	11.77 ± 0.02 ± 0.05	0.63 ± 0.02 ± 0.07	0.551 ± 0.01 ± 0.008	0.550 ± 0.02 ± 0.008	27.7
5CB at 10 kHz	5.63 ± 0.02 ± 0.09	11.682 ± 0.009 ± 0.02	0.91 ± 0.01 ± 0.02	0.552 ± 0.005 ± 0.002	0.551 ± 0.006 ± 0.002	18.9
6CB at 10 kHz	9.10 ± 0.02 ± 0.03	12.20 ± 0.01 ± 0.008	2.1 ± 0.01 ± 0.03	0.524 ± 0.004 ± 0.009	0.522 ± 0.006 ± 0.009	16.7
8CB at 100 kHz	7.69 ± 0.01 ± 0.06	12.249 ± 0.007 ± 0.008	2.102 ± 0.007 ± 0.02	0.539 ± 0.002 ± 0.007	0.539 ± 0.003 ± 0.007	9.67
9CB at 10 kHz	8.82 ± 0.09 ± 0.03	12.22 ± 0.05 ± 0.009	2.11 ± 0.05 ± 0.01	0.56 ± 0.01 ± 0.002	0.55 ± 0.02 ± 0.003	4.11
12CB at 10 kHz	8.43 ± 0.02 ± 0.2	11.14 ± 0.01 ± 0.1	1.74 ± 0.01 ± 0.1	0.543 ± 0.007 ± 0.002	0.542 ± 0.009 ± 0.002	35.8
(c) Rzoska nOCB Series						
6OCB at 10 kHz	6.4 ± 0.2 ± 0.5	12.6 ± 0.1 ± 0.09	1.2 ± 0.1 ± 0.1	0.58 ± 0.05 ± 0.0009	0.58 ± 0.06 ± 0.0009	11.7
7OCB at 10 kHz	5.01 ± 0.01 ± 0.1	11.193 ± 0.005 ± 0.04	1.368 ± 0.006 ± 0.05	0.543 ± 0.002 ± 0.007	0.543 ± 0.003 ± 0.008	37.9
8OCB at 10 kHz	8.47 ± 0.07 ± 0.05	12.20 ± 0.04 ± 0.01	2.07 ± 0.04 ± 0.02	0.566 ± 0.009 ± 0.005	0.566 ± 0.01 ± 0.005	15.5
(d) Rzoska: Miscellaneous						
5CN at 10 kHz	7.47 ± 0.09 ± 0.2	9.48 ± 0.04 ± 0.03	0.78 ± 0.04 ± 0.04	0.57 ± 0.03 ± 0.005	0.57 ± 0.03 ± 0.005	1.15
HCPP at 100 kHz	9.13 ± 0.02 ± 0.09	20.01 ± 0.01 ± 0.01	2.04 ± 0.01 ± 0.02	0.549 ± 0.003 ± 0.008	0.549 ± 0.004 ± 0.008	12.1
9BT at 10 kHz	4.06 ± 0.02 ± 0.1	7.599 ± 0.009 ± 0.08	1.228 ± 0.009 ± 0.1	0.52 ± 0.02 ± 0.003	0.52 ± 0.02 ± 0.003	15.2
10BT at 10 kHz	4.63 ± 0.01 ± 0.1	7.502 ± 0.006 ± 0.05	1.081 ± 0.006 ± 0.09	0.526 ± 0.009 ± 0.007	0.52 ± 0.01 ± 0.007	8.56
5*CB at 1 kHz	10.2 ± 0.1 ± 0.7	14.99 ± 0.07 ± 0.3	2.91 ± 0.08 ± 0.5	0.52 ± 0.02 ± 0.008	0.52 ± 0.03 ± 0.008	10.5

‡, ‡‡: calculated values from Equations 4.6a and 4.6b

Table 4.8: Miscellaneous comparisons of each sample studied.

Sample + Frequency	ΔT_N(K)	ΔT_μ(K)	Δx_N	Δx_μ	$(T_{IM} - T^*)$ (K)	$(T_{IM} - T^*_{ZINK})$ (K)	$\varepsilon_{Peak} - \varepsilon_{IM}$	$\varepsilon_{Peak} - \beta$
(a) Thoen nCB Series								
5CB at 1 kHz	109	37.9	0.366 ± 0.003	0.133 ± 0.003	2.8 ± 0.7	[[1.40]]	0.063	0.35 ± 0.06
6CB at 1 kHz	58.0	49.8	0.2002 ± 0.0003	0.1715 ± 0.0003	2.01 ± 0.08	[[1.37]]	0.1006	0.346 ± 0.007
7CB at 1 kHz	92.1	38.9	0.311 ± 0.009	0.140 ± 0.007	5 ± 2	[[1.25]]	0.082	0.6 ± 0.2
8CB at 1 kHz	89.2	59.4	0.293 ± 0.002	0.198 ± 0.002	2.5 ± 0.5	[[1.02]]	0.182	0.58 ± 0.06
9CB at 1 kHz	56.6	28.0	0.1841 ± 0.0004	0.0948 ± 0.0004	2.4 ± 0.1	[[1.50]]	0.1307	0.49 ± 0.01
10CB at 1 kHz	39.4	23.2	0.1316 ± 0.0003	0.0810 ± 0.0002	2.87 ± 0.07	[[4.25]]	0.0669	0.370 ± 0.007
11CB at 1 kHz	38.2	17.3	0.1288 ± 0.0008	0.0650 ± 0.0007	3.9 ± 0.2	[[5.30]]	0.0417	0.36 ± 0.01
12CB at 1 kHz	58.4	40.3	0.190 ± 0.001	0.135 ± 0.001	4.0 ± 0.3	[[7.70]]	0.008	0.22 ± 0.01
(b) Rzoska nCB Series								
4CB at 100 kHz	47.5	22.6	0.1641 ± 0.0002	0.0820 ± 0.0002	1.15 ± 0.06	-	0.0260	0.11 ± 0.01
5CB at 10 kHz	24.6	24.6	0.0834 ± 0.0002	0.0834 ± 0.0002	1.02 ± 0.05	[[1.40]]	0.0681	0.185 ± 0.005
6CB at 10 kHz	96.0	58.4	0.3285 ± 0.0009	0.2032 ± 0.0008	2.5 ± 0.2	[[1.37]]	0.149	0.56 ± 0.03
8CB at 100 kHz	50.4	41.1	0.1702 ± 0.0004	0.1401 ± 0.0004	2.5 ± 0.1	[[1.02]]	0.1810	0.60 ± 0.02
9CB at 10 kHz	34.3	24.2	0.1129 ± 0.0002	0.0814 ± 0.0002	1.96 ± 0.05	[[1.50]]	0.1780	0.538 ± 0.008
12CB at 10 kHz	34.9	26.8	0.124 ± 0.002	0.0992 ± 0.0002	5.5 ± 0.6	[[7.70]]	0.0209	0.42 ± 0.05
(c) Rzoska nOCB Series								
6OCB at 10 kHz	21.1	13.1	0.0639 ± 0.0006	0.0408 ± 0.0006	1.1 ± 0.2	-	0.0940	0.24 ± 0.03
7OCB at 10 kHz	43.6	43.6	0.1310 ± 0.0003	0.1310 ± 0.0003	1.63 ± 0.08	-	0.1610	0.385 ± 0.008
8OCB at 10 kHz	32.5	23.6	0.0970 ± 0.0001	0.0718 ± 0.0001	1.60 ± 0.04	-	0.2130	0.517 ± 0.006
(d) Rzoska: Miscellaneous								
5CN at 10 kHz	11.4	11.4	0.0405 ± 0.0004	0.0405 ± 0.0004	1.7 ± 0.1	-	0.0105	0.112 ± 0.008
HCPP at 100 kHz	44.0	39.7	0.1390 ± 0.0002	0.1257 ± 0.0002	1.06 ± 0.05	-	0.2300	0.502 ± 0.009
9BT at 10 kHz	36.8	36.8	0.155 ± 0.004	0.1549 ± 0.0004	14 ± 1	-	0.0017	0.39 ± 0.07
10BT at 10 kHz	39.2	39.2	0.149 ± 0.003	0.149 ± 0.003	10 ± 1	-	0.0018	0.29 ± 0.04
5*CB at 1 kHz	55.7	43.7	0.237 ± 0.005	0.189 ± 0.005	3 ± 1	-	0.191	0.9 ± 0.2

[[ ]]: fixed, literature from Zink et. al. [48]

4.4.2 Selected Plots for the *n*CB Series

It is preferable to look at one homologue group in order to clearly compare the fitting parameter results. For this, the *n*CB homologue series is chosen as the majority of the samples studied used were of this series. The model (Equations 4.2, 4.5b, and 4.7) is fit for the *n*CB series as it has the isotropic-nematic phase transition through 9CB. Starting with 8CB, a smectic phase thermally forms below the nematic phase. The nematic phase becomes more thermally narrow and disappears by 10CB. Applying the model through 12CB allows for a look at what happens to the fitting parameters as the nematic phase disappears.

Two groups performed dielectric measurements for the *n*CB series. Part (a) of Tables 4.5, 4.6, and 4.7 are for Thoen et. al. (the Leuven group) [28, 37, 51]. The samples of 5CB through 12CB were looked at. Part (b) of Tables 4.5, 4.6, and 4.7 are for Rzoska et. al. (the Warsaw group) [38-46, 52]. The samples of 4, 5, 6, 8, 9, and 12CB were investigated. The results of Tables 4.5 through 4.7, parts (a) and (b) are plotted in this section.

Each group's data has its own advantage. The Leuven group systematically looked at the *n*CB series [28, 37, 51]. The numerical data were obtained directly from that group, taken at the same frequency and conditions, and measured at the same precision. The Warsaw group has a diverse selection of measuring frequencies and conditions [38-46, 52]. The data were obtained by graphically extracting the data points from published plots, leading difficulty in consistent precision.

The critical temperature T^* is plotted in Figure 4.28 for the homologous series *n*CB. As the number of carbons are added to the chain length n, the critical temperature, and the estimated transition temperature T_{IM} increase almost linearly for both groups. Between 4CB and 9CB, the phase transition from isotropic is nematic. In Figure 4.28a, there appears to be a subtle odd-even effect until 10CB is reached.

(a) Results from applying the heirarchical model to the Leuven group's data [37].

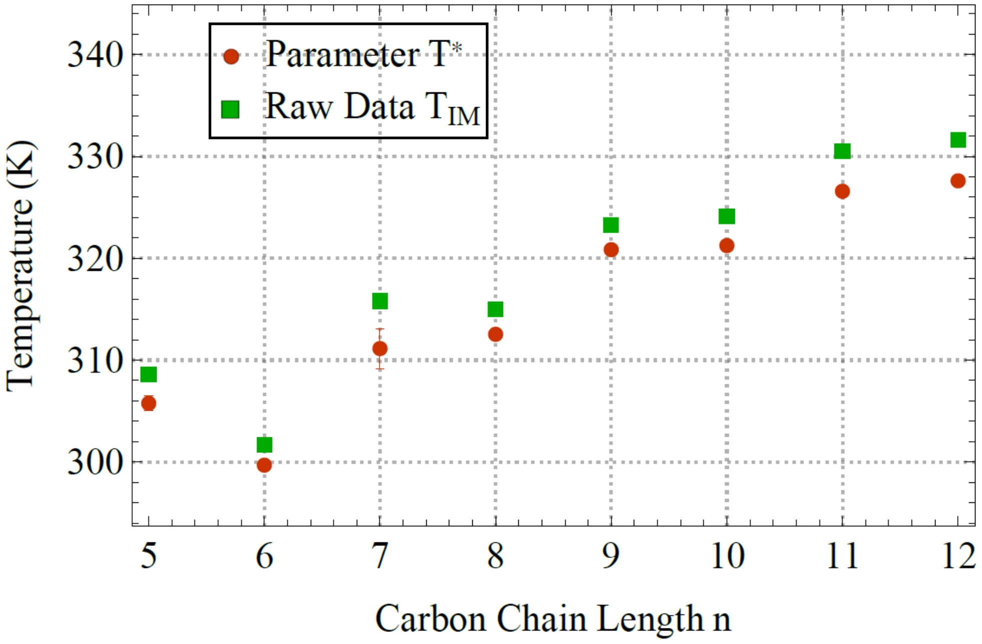

(b) Results from applying the heirarchical model to the Warsaw group's data [38-46, 52].

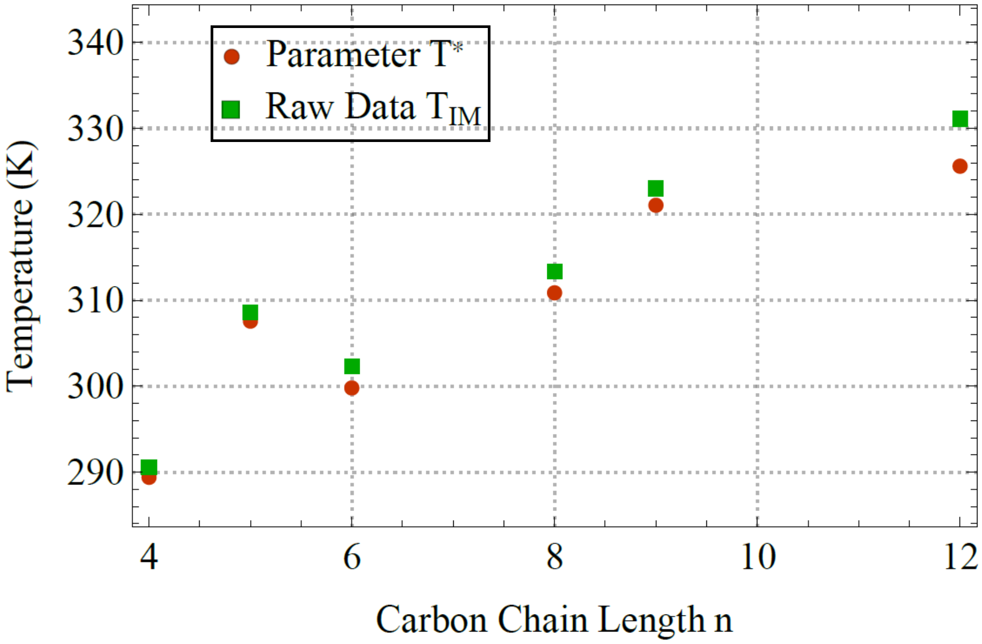

Figure 4.28: Selected results for the temperature parameter estimates of the *n*CB series.

- The values of T_{IM} are taken directly from the data (green squares).
- The critical temperature T^* is a fitting parameter from using the three-halves order expansion (see Equation 4.5b).

Figures 4.29 and 4.30 show the slope and intercept parameter estimates, respectively. Both the critical slope α and the background slope A in Figure 4.29a have a subtle odd even effect between 5CB and 9CB. Beyond 9CB, the trend versus carbon chain length appears to become more linearly decreasing. The Warsaw group slopes in Figure 4.29b have no obvious trend, due in part to being measured at different frequencies.

Figure 4.30 shows the permittivity ε_{IM} at the transition temperature, the intercept β from the three-halves expansion (see Equation 4.5b), and the background intercept B (see Equation 4.7). In part (a) (the Leuven group), all three linearly decrease with an increase in the carbon chain length. This consistency hints at consistent measuring. This is reasonable as 5CB is relatively polar while the addition of non-polar carbons dilutes this polarity.

Figure 4.30b (the Warsaw group) also shows a linear decrease in ε_{IM} with increasing carbon chain length n. However, the application of the model to their data by way of parameter results β and B hints at different conditions among each sample. The difference is the variation in frequency for all n.

The background parameter results α, A, β, and B should be compared at the same frequency. The Leuven group's results are ideal for this requirement as each sample is measured at the same frequency. For the Warsaw group, 5CB, 6CB, and 12CB were all measured at 10 kHz. The experimental goals of the Warsaw data were not necessarily focused on the nCB series. The goals ranged from super-cooling, to the mixing of two non-chiral molecules with different polarities, and to looking at lower temperature phases. An advantage of the Warsaw group's results is that they looked at quasi-critical effects leading to the empirical equation discussed in Sections 4.2.2 and 4.4.1.

(a) Results from applying the heirarchical model to the Leuven group's data [37].

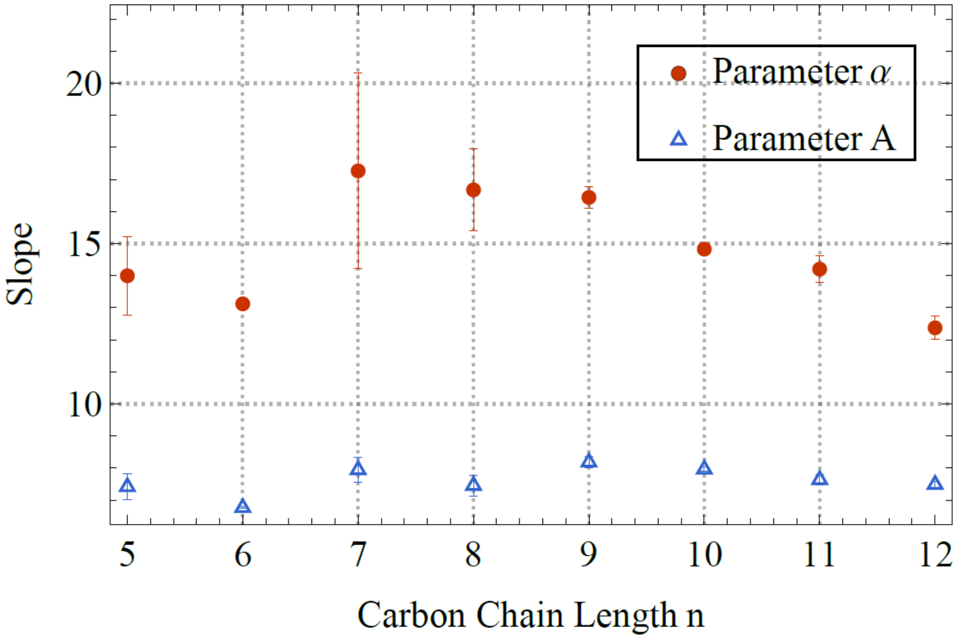

(b) Results from applying the heirarchical model to the Warsaw group's data [38-46, 52].

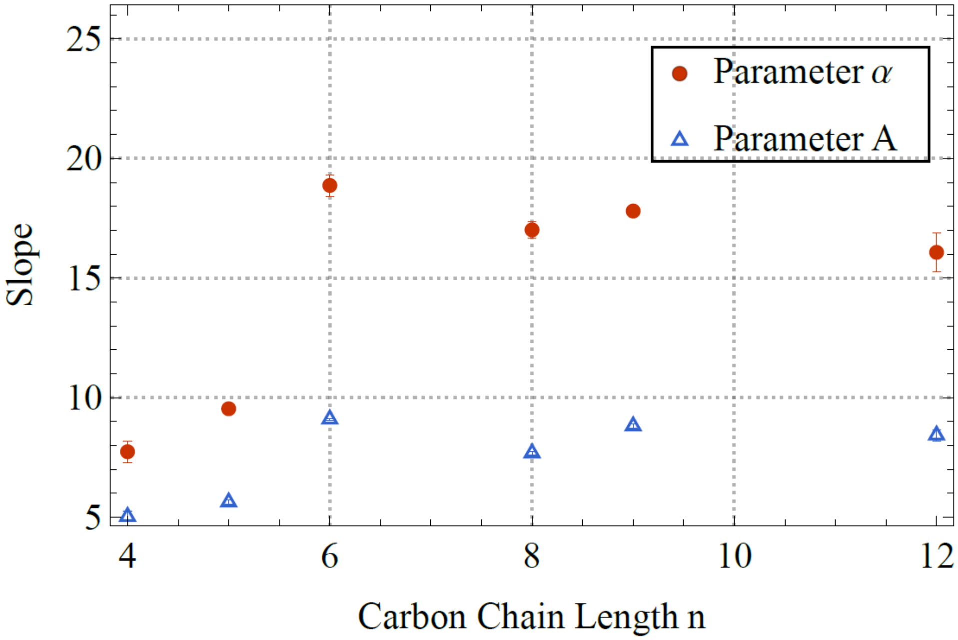

Figure 4.29: Selected results for the slope parameter estimates of the *n*CB series.

- Parameter α is a fitting parameter from the three-halves order expansion (see Equation 4.5b).
- Parameter A is the slope parameter in Equation 4.7. in the values of T_{IM} are taken directly from the data (green squares).

(a) Results from applying the heirarchical model to the Leuven group's data [37].

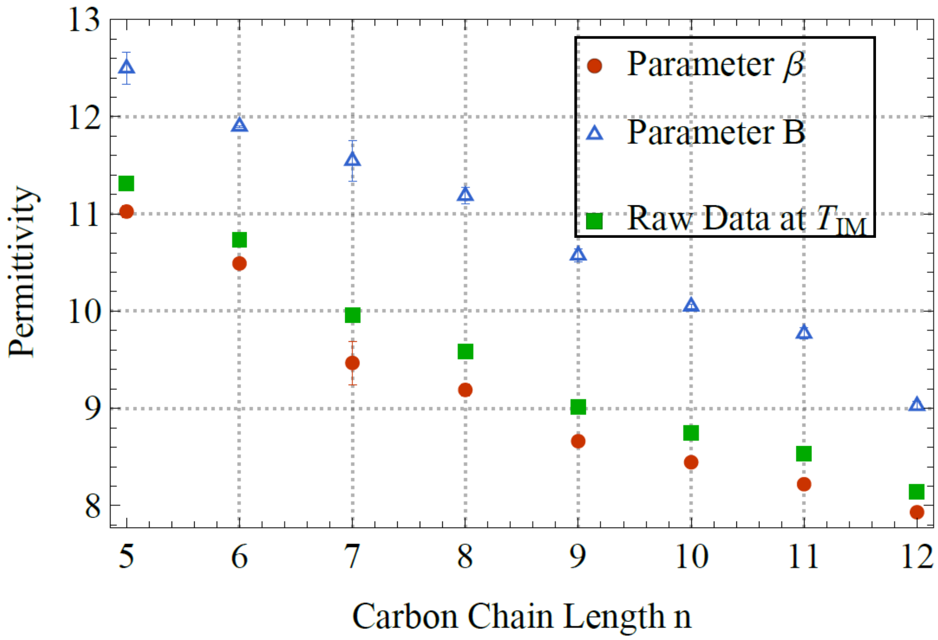

(b) Results from applying the heirarchical model to the Warsaw group's data [38-46, 52].

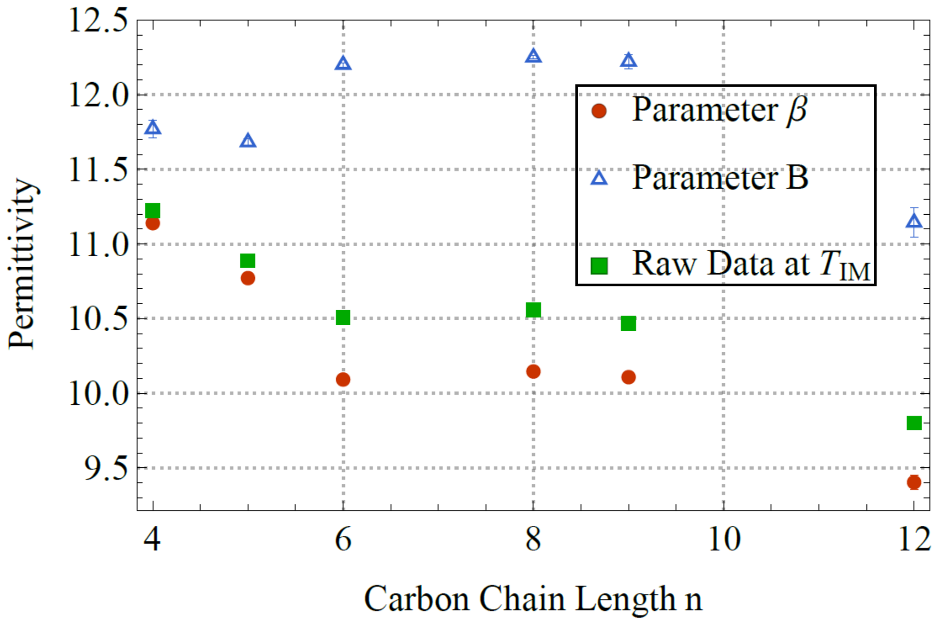

Figure 4.30: Selected results for the intercept parameter estimates of the *n*CB series.

- Parameter β is a fitting parameter from the three-halves order expansion (see Equation 4.5b).
- Parameter B is the slope parameter in Equation 4.7. The values of ε_{IM} (the green squares) are taken directly from the data.

Figure 4.31 shows the magnitude of the pretransitional curvatures represented by γ for the critical fits (see Equation 4.5b) and C for the modified full fits (see Equations 4.2 and 4.7). From the Leuven group (part (a) of Figure 4.31), both γ and C have a steep increase around carbon chain length $n = 7$. Both γ and C gradually decrease with increasing n. Although it is unclear what is happening, it is known that a smectic phase forms at a temperature below the nematic phase for 8CB. The 9CB sample has a much narrower nematic phase between the isotropic and smectic phases.

Figure 4.32a shows the calculated parameter D (see Equation 4.6a) across the entire homologous series nCB for both the Leuven and Warsaw group's data. Irrespective of frequency used, parameter D remains relatively constant with reasonable standard errors. Additionally, parameter D is near the expected order of magnitude [48, 50, 53].

Figure 4.32b shows the parameter estimates for calculated parameter g which was first shown in Equation 4.4c and Figure 4.8. Parameter γ times g competes directly with the background slope A. To within estimated error, g is around a value of 2.35 which corresponds to the quadratic contribution of the pretransitional curvature being near zero.

A positive value of parameter f allows for a single, positive solution to D (see Figure 4.8). Figure 4.32c shows the calculated parameter f (see Equation 4.4f) for the nCB series where f is mostly positive and small.

In summary, the entire nCB series returns a reasonable, positive estimate of D. Referring back to Figure 4.8, g remains above its minimum allowed value while parameter f is small and positive. A near zero value of f justifies using the three-halves expansion $\bar{\varepsilon}_{3/2}$ instead of the full second order expansion $\bar{\varepsilon}_{II}$. The consistency check of Equation 4.8 is satisfied. The model is now self-consistent.

(a) Critical fit parameter γ from the three-halves order expansion (see Equation 4.5b).

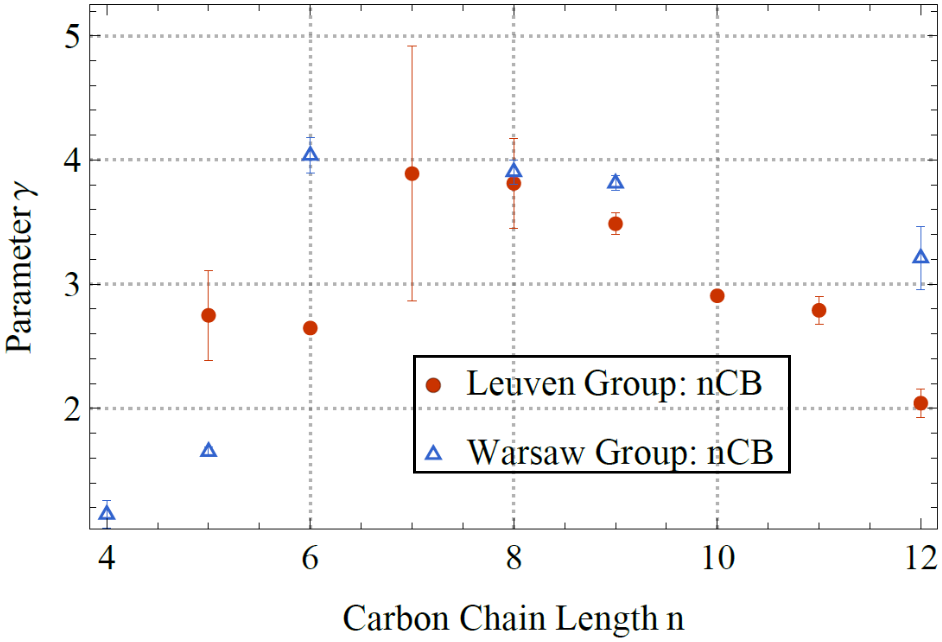

(b) Modified fit parameter C from Equation 4.7.

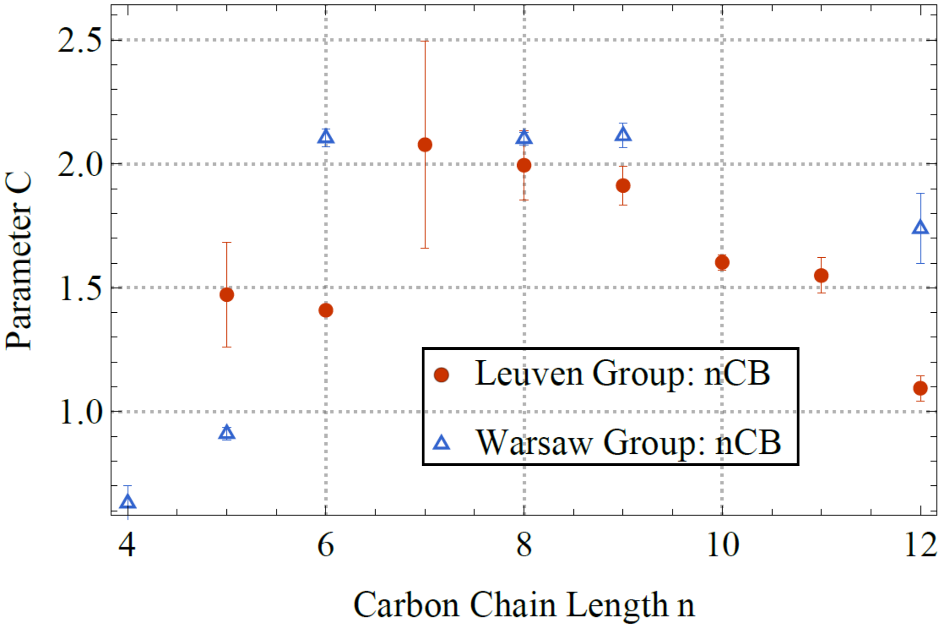

Figure 4.31: Selected estimates of the magnitude parameters γ and C of the pretransitional curvature for the *n*CB series.

Both groups are plotted together:

- Leuven data (Thoen et. al.) [37]
- Warsaw data (Rzoska et. al.) [38-46, 52]

(a) Calculated parameter D (see Equation 4.6a). The green, solid line represents the value of D when parameter f is zero.

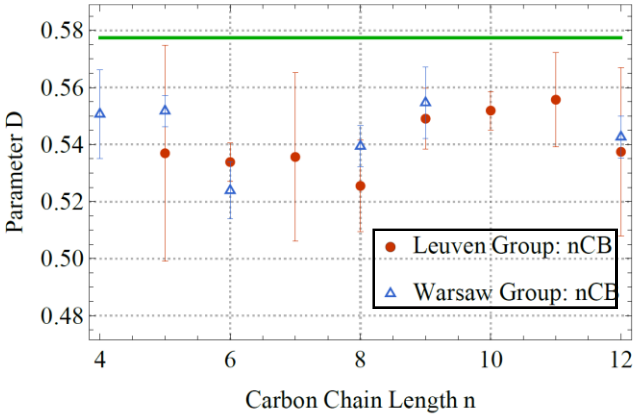

(b) Calculated parameter g (see Equation 4.4c). The product $g\gamma$ competes with the background slope A.

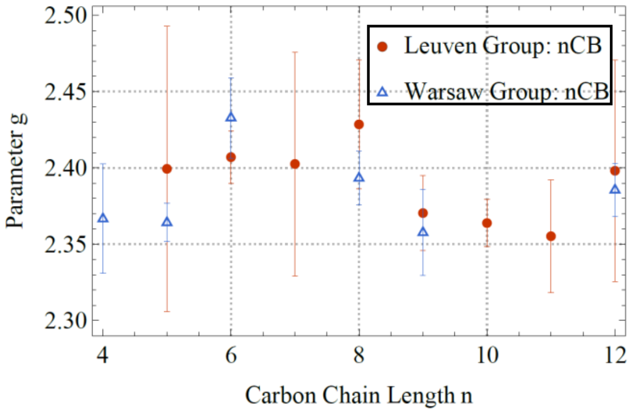

(c) Calculated parameter f (see Equation 4.4f). This parameter contributes to the pretransitional curvature.

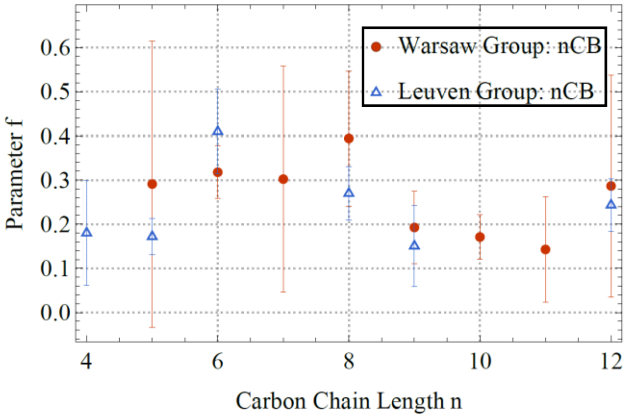

Figure 4.32: Calculated parameter estimates from the heirarchical model in Equations 4.5b and 4.7 for the nCB series.

Both groups are plotted together:

- Leuven data (Thoen et. al.) [37]
- Warsaw data (Rzoska et. al.) [38-46, 52]

CHAPTER 5 THE EFFECTS OF VARYING CHIRALITY ON THE DIELECTRIC RESPONSE OF CHOLESTERIC LIQUID CRYSTALS

Dielectric properties of achiral nematic liquid crystals have been studied extensively. With various experimental techniques (such as dynamic light scattering, heat capacity, and dielectric measurements), pretransitional anomalies in many polar nematics are observed on both sides of the nematic-isotropic phase transition [14, 26, 28, 38-46]. Chapter 4 dealt with the achiral case and applied a generalized theory to the temperature dependence of the dielectric permittivity.

Few studies have looked at the effects of chirality in a chiral nematic system [23, 54]. One dielectric study by Leys et. al. has investigated varying of chirality [23]. That study looked at mixtures of an achiral nematic 5CB (4-pentyl-cyanobiphenyl) and the chiral variant CB15 (4-(2-methylbutyl)-cyanobiphenyl) [23]. The structures of both molecules are shown in Figure 5.1.

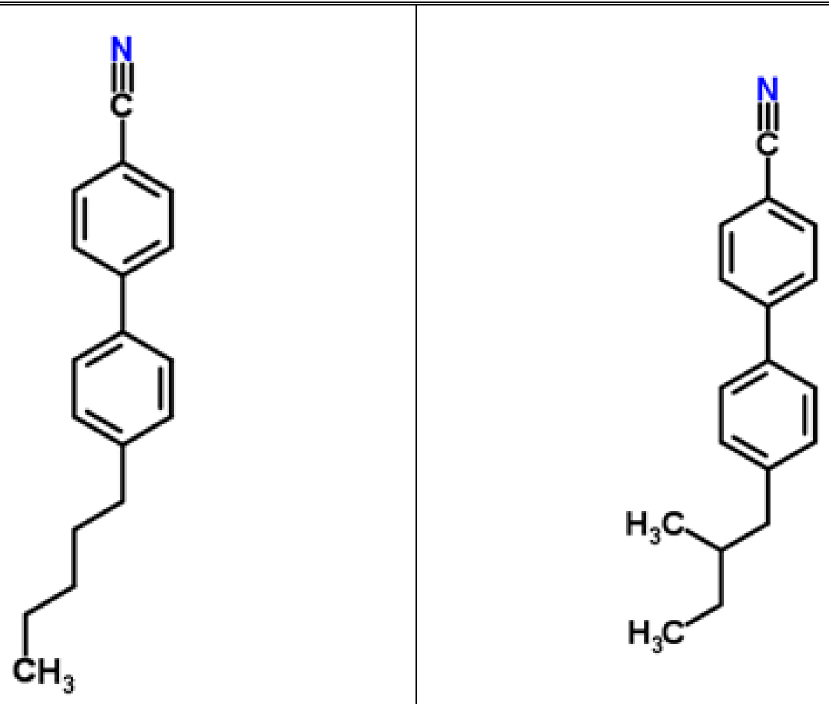

(a) 5CB [55]

(b) CB15 [56]

Figure 5.1: The molecules studied in the chirality study by Leys, Glorieux, Wübberhorst, and Thoen [23]. These chemical structure images are from the Royal Society of Chemistry's online database [55, 56].

Both molecules have the same molecular weight.

Both 5CB and CB15 possess a prominent longitudinal dipole moment and have pretransitional curvature in the isotropic phase as the mesogenic phase is approached. The 5CB-CB15 system starts with zero chirality and increases in chirality with the addition of CB15. The static dielectric permittivity was looked at for anomalous pretransitional behavior on the isotropic side of the phase transition.

The data from the study above can be seen in Figure 5.2. In addition to the data for the pure 5CB and CB15 samples, four different mixture ratios of those two samples are shown [23]. The real part ε' of the permittivity is normalized with respect to the value of the permittivity ε'_{IM} at the estimated isotropic to mesogenic phase transition temperature T_{IM}. The temperature differences are with respect to the transition temperature T_{IM}. Data below zero along the ordinate are interpreted as not contributing to the pretransitional anomaly (i.e., pretransitional curvature). Any data above zero along the ordinate is interpreted as contributing to the pretransitional curvature.

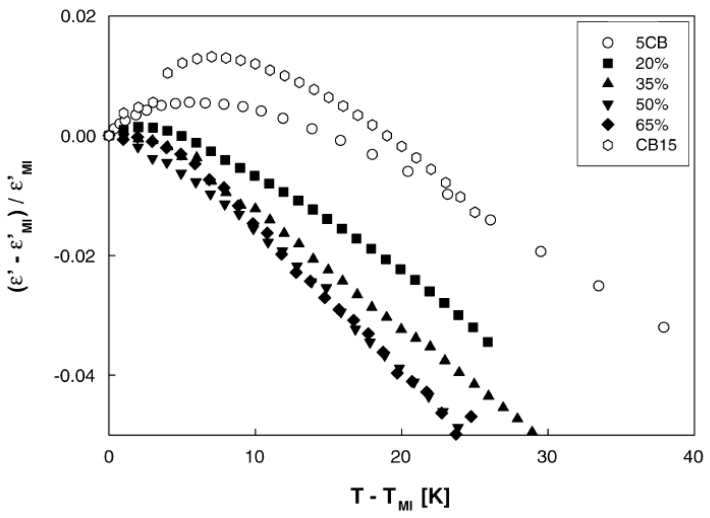

Figure 5.2: Results from the paper by Leys et. al. [23]

This is the temperature dependence of the pretransitional effects in the heating runs of 5CB with CB15 [23]. The cooling runs were stated to be similar.

As discussed in Chapter 2, one possible contribution to this curvature is the formation of anti-parallel dimers as the mesophase is approached from the isotropic side of the transition. It is of interest to see if chirality also contributes to the pre-mesophase curvature. From Figure 5.2, it can be seen that both 5CB (the least chiral of the two molecules) and CB15 (the most chiral of the two molecules) both have strong pretransitional curvature. With the addition of chirality, the pretransitional curvature appears to go away around the 50% CB15 mixture. Beyond the 50% CB15 mixture, the pretransitional curvature reappears as pure CB15 is approached. From those results, the role of chirality is ambiguous due to the relative change of the permittivity ε' not being a monotonic function of chirality.

The mixtures under investigation in this dissertation are both chiral, oppositely handed, and only one has a prominent longitudinal dipole moment (refer back to Section 3.3 for a discussion of the samples under investigation). In contrast, the 5CB-CB15 system has only one of the compounds being chiral with both have similar longitudinal dipole moments. It is a goal of this chapter to look at the dielectric response for a highly chiral system and from there vary the chirality. Three experimental approaches are presented in this chapter: the temperature dependence of the dielectric measurements at constant frequency, the frequency dependence of the dielectric measurements at constant temperature, and cross-polarized microscopic observations with no applied field. Cross-polarized microscopy is used for visual confirmation of the textures of the phases that are present and for further interpretation of the dielectric measurements.

This chapter will first focus on one of the mixtures (the 12% cholesteryl chloride mixture) as an example for common features seen in the dielectric data of all the mixtures measured. From light scattering experiments, the 12% cholesteryl chloride mixture was expected to exhibit blue phases [57, 58]. Both the temperature and frequency dependence will be discussed for this example sample.

Following the discussion of the representative sample, all of the mixture ratios will be discussed. The normalization of the permittivity data will be discussed and the estimated discontinuities at the phase transition will be addressed. The discontinuities are of particular interest due to the blue phases showing up at higher chirality (lower percentage of cholesteryl chloride). The discontinuities are indicative of an increase or decrease in chirality.

For sake of clarifying the discussion of the temperature dependence, the mixtures will be roughly divided into four composition ranges based on similar curvature at low frequency. For each range, the corresponding relaxation frequencies will be discussed in addition to the temperature dependence of the relative permittivity.

In discussing the COC-CC system, two main things were unexpected that motivated covering a broader range of mixtures than intended (the intent was 0% through 25% CC). First, the phase transitions were monotropic for percentages below 35% cholesteryl chloride. The blue phases were seen, dielectrically, on cooling. On heating, the cholesteric to isotropic phase transition was observed. Secondly, there was a significant difference between measurements done at 10 kHz and 100 kHz. This last point is indicative of a measurement taken near a relaxation peak.

5.1 The Chirality Scale Defined

As mentioned in Section 3.3, the chirality scale is made by mixing two oppositely handed molecules: cholesteryl oleyl carbonate (COC) and cholesteryl chloride (CC). The prepared compositions and the resulting uncertainties in mixing can be seen in Table 5.1. The left column of Table 5.1 lists the actual measurements used in both plotting and calculations. The right column of Table 5.1 shows what each percentage will be referred to as in the plot legends and subsequent tables.

Both molecules are highly chiral and have blue phases present between the cholesteric and isotropic phases. Consequently, it is also of interest to see how the presence of the blue phases appear over composition. This same system (COC mixed with CC) has been studied with optical observations [59]. A phase diagram as a function of composition was found; the results presented will be compared to that study. We are aware of two other dielectric studies just on COC which identify at least one blue phase [54, 60].

Table 5.1: Compositions studied. Percent composition of cholesteryl chloride mixed with cholesteryl oleyl carbonate.

Actual Value (%)	Referred to As (%)
1.503 ± 0.003	1.5
3.05 ± 0.04	3
6.081 ± 0.004	6
11.996 ± 0.005	12
15.996 ± 0.003	16
20.036 ± 0.003	20
25.000 ± 0.003	25
29.970 ± 0.003	30
35.009 ± 0.003	35
39.975 ± 0.004	40
44.977 ± 0.005	45
49.966 ± 0.005	50
54.997 ± 0.004	55
60.000 ± 0.004	60

5.2 The Dielectric Response and Microscopic Observations for a Model Mixture: 12% by Weight Cholesteryl Chloride

The blue phases are expected to appear at high chirality between the isotropic phase and the cholesteric phase. It is of interest to see how the discontinuity of the dielectric permittivity at the phase transition changes with the disappearance of the blue phases. One of the samples, pure cholesteryl oleyl carbonate, is reported to have at least one blue phase, i.e., BP III [54, 57, 58, 60]. However, cholesteryl oleyl carbonate scatters light strongly only in the ultraviolet, making it difficult to visually observe with optical cross-polarized microscopy and to compare with the dielectric results [57, 59]. From Koistinen et. al., cholesteryl chloride was added in order to shift the scattering wavelength of blue phase III into the visible [57]. The 12% cholesteryl chloride mixture with cholesteryl oleyl carbonate was used. That paper focused only on blue phase III [57].

As will be seen later in this chapter, the dielectric data presented at 10 kHz for the 1.5% through 40% cholesteryl chloride samples are qualitatively similar. From cross-polarized microscopy measurements they are expected to have blue phases [57, 59]. On cooling in the mesophase(s), the real part of the data slopes upward, reaching a maximum and then further curving downward. If dielectric measurements are able to detect any of the blue phases (which themselves are isotropic), then they would show up to within a few degrees of the isotropic to mesogenic phase transition. When blue phases were observed on cooling for the COC-CC series, a pattern was observed in the 10 kHz dielectric data. The blue phases showed up between the above mentioned maximum on cooling and the isotropic to mesogenic phase transition T_{IM}. For example, as will be seen, the 12% cholesteryl chloride's peak on cooling for the dielectric measurements was around 5.4 K below T_{IM}. From my own microscopic observations, two blue phases were definitively observed. The transition to the first one appeared through 0.4 K below T_{IM} with an increase in wavelength from yellow and stayed constant at red for an additional 0.6 K. The transition to the second blue phase lasted for a further 0.8 K with a decrease in wavelength from red and then remained a constant green for about 1 K. Below this, the color started to change blue and the cholesteric phase began to form. The cholesteric phase was observed to have fully formed between 4.7 K and 5.1 K below T_{IM}.

The 12% cholesteryl chloride sample is a model for this region. Not only does it have at least two blue phases and probably three (from both my own observations and the results reported by Koistinen et. al.), but also, as will be seen later in this chapter, the blue phases strongly scatter light in the visible range. This will allow for direct comparison of the phase sequence between cross-polarized microscopic observations and the curves seen in the dielectric data. From this it will be seen how well the blue phases are dielectrically distinguished from the cholesteric and isotropic phases.

The blue phases are not expected to be present from the 45% by weight cholesteryl chloride and above [59]. From cross-polarized microscopic measurements, I saw a cholesteric phase form directly below the isotropic beyond 30%. In this dissertation, the 35% through 60% cholesteryl chloride samples did not show obvious evidence of blue phases being present. These samples were studied so as to understand what the transition looks like without the presence of a blue phase – that is, the lower chirality limit.

5.2.1 Temperature Dependence for the Dielectric Response of 12% CC

Each mixture was cycled through heating and cooling runs at constant frequencies of 10 kHz and 100 kHz separately. At least three cycles were measured at each constant frequency. When this study began, there was a problem with noise in the apparatus at frequencies much below 100 kHz. After both grounding and shielding issues were resolved, a 10 kHz driving signal was successfully used with reliable results. It was at that point when the unexpected differences were observed between the two frequencies. This section will present first the magnitude of the results and then normalized data.

5.2.1.1 Magnitude of Response

Representative runs for the 12% cholesteryl chloride sample can be seen in Figure 5.3. It is seen that there is a significant difference in the dielectric results between the two probing frequencies. Because of this difference, both frequencies were separately used for all samples. As justified later in this chapter, the 10 kHz data are found to lie in the range of frequencies that are typically preferred for phase transition studies: avoiding both ionic conduction and any influence from relaxation processes (the plateau frequency region). The 100 kHz data show a well-defined location of the isotropic to mesogenic phase transition on both heating and cooling.

Repeatable hysteresis in the isotropic to mesogenic phase transition temperature was observed between heating and cooling. This was an artifact caused by the procedure used. For each cycle, the temperature was held constant at either end of the thermal cycle for an hour to ensure measurements were repeatable. Heating or cooling then began. The discrepancy in transition between heating and cooling was around 2 °C and was independent of frequency and composition. Because it was independent of both frequency and composition and dependent on heating versus cooling, it can be attributed to a heating or cooling lag in the experimental setup as opposed to any real effect in the samples. This does not affect the analysis since temperature differences were the primary interest.

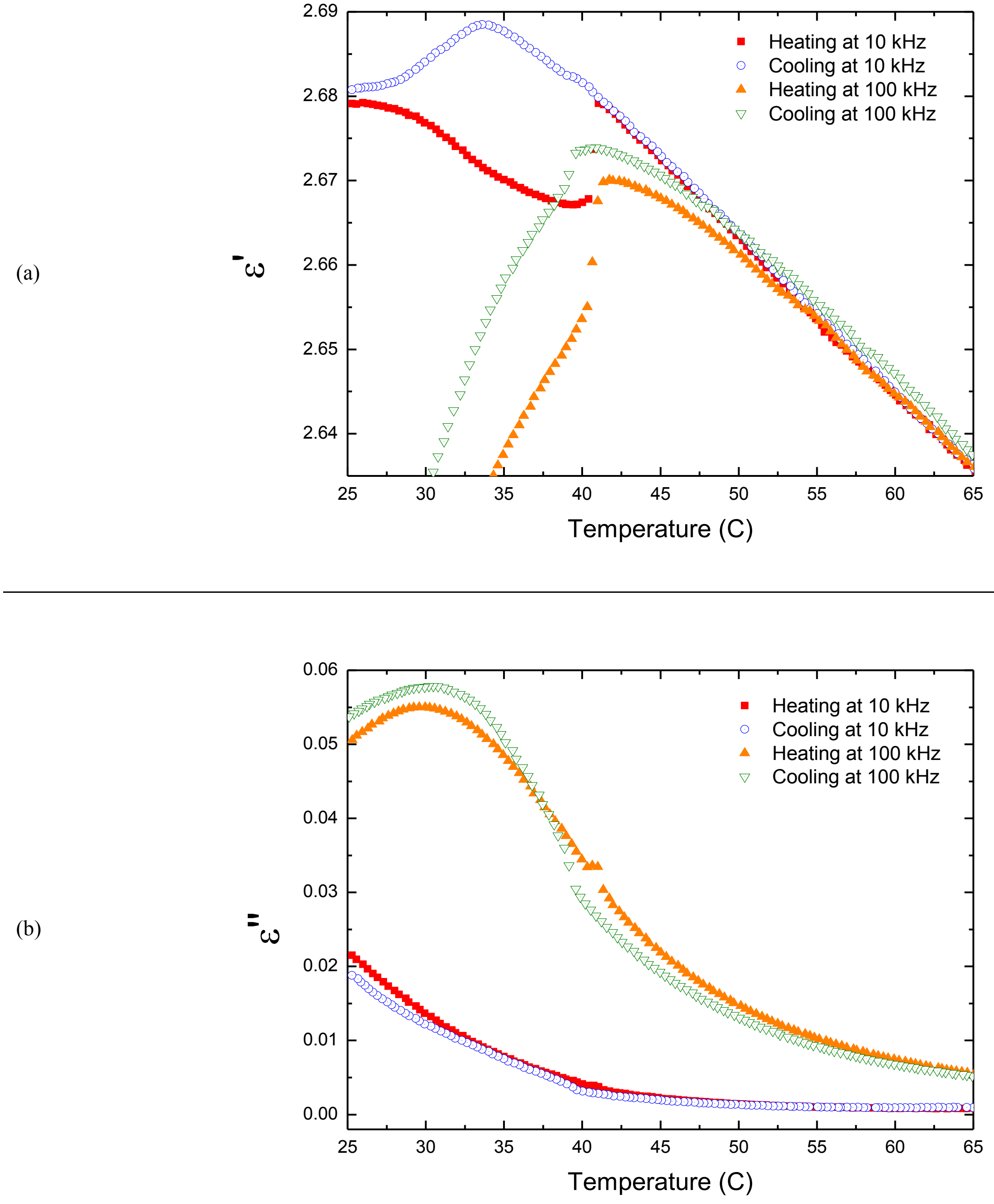

Figure 5.3: These are representative runs for the magnitude of the dielectric data collected on heating and cooling as well as at 10 kHz and then at 100 kHz.

Since this is an AC measurement, both the (a) real part ε′and (b) imaginary part ε″ are shown. Typically the imaginary part ε″ is not shown as a function of temperature in the literature as it is preferred to be close to zero.

For the real part of the permittivity at 10 kHz as seen in Figure 5.3a, the phase transition appears to have a hysteresis in the curvature of the permittivity. On heating from room temperature, the permittivity drops down followed by a large discontinuity at the mesogenic to isotropic phase transition. In the isotropic phase, the heating and cooling runs are almost identical. On cooling from the isotropic phase into the mesophase, there appears to be a negligible discontinuity in the transition. On further cooling, the real part has a kink in the data followed by further sloping upward until it reaches a peak. It continues to slope downward with decreasing temperature until it tapers off. It is important to note that these dielectric measurements are on thick, randomly aligned samples. When measuring in the mesogenic phases it is typical to use either a magnetic field or surface treatment of the electrodes to induce a particular alignment. At a given temperature, a sample would have a different behavior in the dielectric permittivity depending on whether the alignment was parallel or perpendicular to the applied, measuring field. In a randomly oriented mesophase, the measured value may or may not be the average between the perpendicular and parallel alignment.

For the real part of the permittivity at 100 kHz, the phase transition still appears to have a hysteresis in the curvature of the permittivity versus temperature. On heating, there is a slight convex curvature near the isotropic to mesogenic phase transition. The cooling run differs in that the curvature appears concave. In addition, the discontinuity at the isotropic to mesogenic phase transition is much larger on heating than on cooling. As will be seen later in Section 5.2.2, the 100 kHz measurement is very close to the relaxation frequency of the mixture in the mesophases. Near the relaxation frequency, there is an increase in the number of molecules that are unable to sufficiently respond to an applied AC field compared to a frequency that is much lower than the relaxation frequency. Within the frequency range of the relaxation peak, the ability of the molecules to form anti-parallel dimers most rapidly changes.

It is difficult to determine exactly where the phase transition is for the real part of the 10 kHz data on cooling. Because of the thermal lag in the experimental setup, the mesogenic to isotropic transition on heating cannot be used for cooling. There is no evidence that this phase transition is significantly dependent on the measuring frequency. On heating, both the 10 and 100 kHz data had phase transitions that were in agreement. Similarly, the 100 kHz data on cooling served as a way of determining where the phase transition for each sample was at 10 kHz. Also, the imaginary part of the permittivity, in Figure 5.3b, also showed a discontinuity at 10 kHz. This also served as a way of determining the phase transition temperature as the discontinuity in the real part of the permittivity data was not always obvious.

5.2.1.2 Normalization of Response

The magnitudes of the data vary widely with composition. Per composition the imaginary part $\varepsilon_{IM}^{''}$ differs by an order of magnitude between the 10 kHz and 100 kHz run, so a normalization needs to be performed in order to allow for comparison. The relative changes are also of primary interest to this dissertation. Shifting each data set by their respective estimated transition temperatures T_{IM} and the corresponding values of the real and imaginary parts of the permittivity, ε_{IM}' and $\varepsilon_{IM}^{''}$, allow for a common reference. For the temperature dependence, the estimated isotropic to mesogenic phase transition temperature T_{IM} was subtracted out. This eliminated the importance of the thermal lag between heating and cooling runs. Each cooling and heating, measured at both 10 kHz and 100 kHz, had its own estimated transition temperature T_{IM} along with the respective real and imaginary parts of the permittivity, ε_{IM}' and $\varepsilon_{IM}^{''}$. The values for the representative runs shown in Figure 5.3 can be seen in Table 5.2a. The precision over repeated runs was not as precise as a single run. The repeatability of measurements T_{IM}, ε'_{IM}, and ε''_{IM} is shown in Table 5.2b. The qualitative shape of each run compared to another run was relatively precise and reproducible.

Most of the cooling and heating runs were performed at least three times each, from which the representative data in Figure 5.3 were taken. Each run had its own T_{IM}, ε'_{IM} and ε''_{IM}. In order to obtain an estimate of the reproducibility of the magnitudes of the data, the means of T_{IM}, ε'_{IM} and ε''_{IM} were calculated with one standard deviation from the mean used as an estimate of the reproducibility of the magnitudes. Since T_{IM} appears to be frequency independent, the T_{IM} for both frequencies was averaged as one. The averages over all runs can be seen in Table 5.2b. There is a contribution to the estimate of reproducibility due to the data being recorded at approximately one-third of a degree centigrade increments. The normalization of the data shown in Figure 5.3 is seen in Figure 5.4.

Table 5.2: These are the values used to normalize the data for the 12% cholesteryl chloride sample.

These values are from the lowest temperature data point measured in the isotropic phase.

(a) A single, representative run with high precision.

ΔT_{ramp}	Frequency	T_{IM} (°C)	ε'_{IM}	ε''_{IM} (10^{-3})
Cooling	10 kHz	39.41	2.6823	3.7108
	100 kHz	39.60	2.6732	30.451
Heating	10 kHz	41.04	2.6791	3.7437
	100 kHz	41.35	2.6698	30.345

(b) The mean of all runs. A lower accuracy in the mean of the magnitudes means that, while the relative pattern of the data is highly accurate, the magnitude is not so much. The uncertainties in the temperature are well within the average temperature spacing of each data point (one-third of a degree centigrade).

ΔT_{ramp}	Frequency	T_{IM} (°C)	ε'_{IM}	ε''_{IM} (10^{-3})
Cooling	10 kHz	39.5 ± 0.1	2.681 ± 0.002	3.4 ± 0.2
	100 kHz		2.6726 ± 0.0006	30.7 ± 0.6
Heating	10 kHz	41.2 ± 0.2	2.679 ± 0.003	3.8 ± 0.2
	100 kHz		2.6702 ± 0.0005	30.6 ± 0.7

(a)

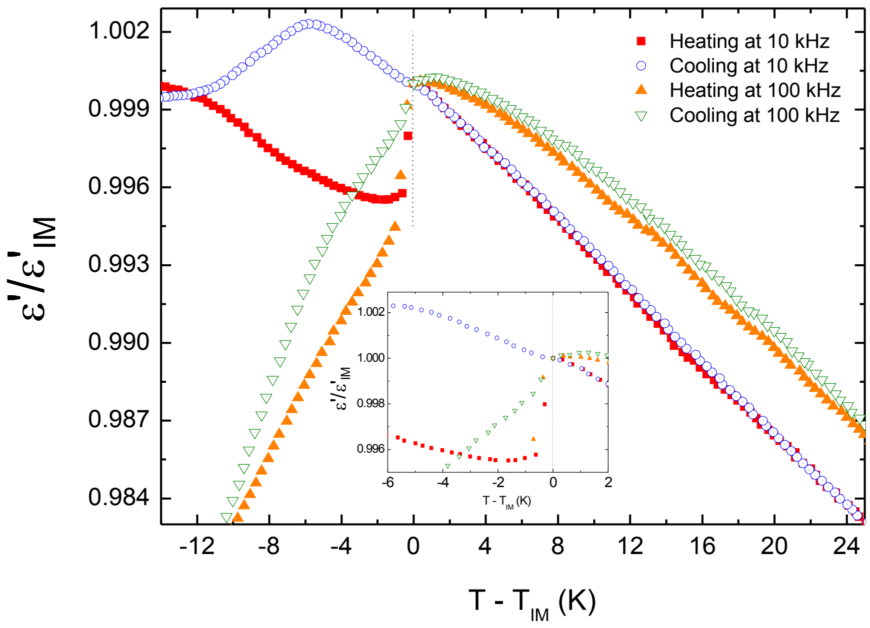

(b)

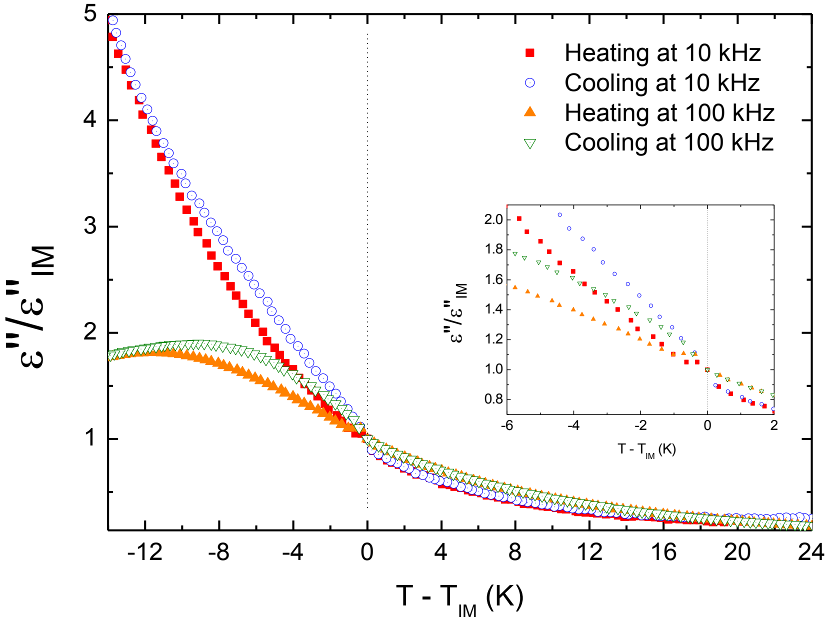

Figure 5.4: These are representative runs that have been normalized according to Table 5.2 on both heating and cooling.

Since this is an AC measurement, both the (a) real part ε' and (b) imaginary part ε'' are shown. For measurements in the static frequency range, the imaginary part ε'' is expected to be small or near zero.

Although this normalization does not change the observations noted about Figure 5.3, it will allow the comparison of all samples later in this chapter. As will be seen later, due to the addition of cholesteryl chloride (which has a prominent longitudinal dipole in comparison to pure cholesteryl oleyl chloride), the net dipole moment and permittivity of the system goes up. This makes a direct comparison of the magnitudes plotted on the same graph impractical. It will be useful to compare and plot the relative changes of each sample.

5.2.2 Frequency Dependence for the Dielectric Response of 12% CC

The theory behind dielectric relaxation as a function of frequency is well developed (see Section 2.2) [29-33]. The real and imaginary isothermal parts can be extracted out and plotted separately versus frequency. Figure 5.5 shows all of the isothermal frequency sweeps recorded for the 12% cholesteryl chloride sample. The dashed lines are fits to the data. The Cole-Cole formula in Equation 2.9 is used for fitting. These fits will be discussed in the following sections.

The dielectric response is characterized for two main frequency ranges. The first is the low frequency static region where the imaginary part ε'' is near zero (i.e., dissipation is minimized) and the relaxation process fully contributes to the real part ε' of the permittivity. The other range is near the relaxation peak where dissipative forces contribute more to ε'' and less to the real part ε'. The static region was discussed in the previous section as a function of temperature. Each phase is expected to have a different relaxation frequency. When choosing a low frequency within the static region it is important to consider how the relaxation frequency changes over the entire temperature range studied. Each temperature should have an equal contribution from the relaxation process.

The real part of the permittivity ε' in Figure 5.5a is plotted such that the data at all temperatures could be plotted on the same graph. This is done by shifting the real data along the vertical axis by the resultant fitting parameter ε_∞. The parameter ε_∞ is the value of the permittivity well above the relaxation peak. In this region the molecules have difficulty responding to the applied field. For the real part, the dielectric strength parameter $\Delta\chi_0$ is the difference between static permittivity (i.e., the lower frequency plateau, constant permittivity region with a static value of $\varepsilon_\infty - \Delta\chi_0$) and the high frequency permittivity ε_∞ (beyond the inflection point of the curve). The inflection point corresponds to where the relaxation frequency f_r lies. Also note that at the lowest frequencies measured there is some bending upward and downward in the data. For the real part, this is only expected if another relaxation process is present or if there was parasitic inductance or conductance in the system. This lowest frequency region was not fitted for the real part as it was not of interest. There is an additional parameter α that the real part depends on. However, the interpretation of α is better understood in the context of a parametric plot.

The imaginary part of the permittivity in Figure 5.5b is referred to as the dielectric loss. The data has four regions to note: low frequency ionic conduction, the static permittivity region where ε'' is minimized or zero, the relaxation process, and the higher frequency region where another relaxation process may exist. It is desired to avoid the low frequency ionic conduction. This is generally modeled by the term in Equation 3.8, $\frac{S}{\omega^n}$, where S is related to the zero frequency conductivity, n is a fitting parameter frequently taken as one and ω is the angular frequency defined in Section 2.1. When the dielectric loss bends downward and becomes negative at low frequency, that can be associated with undesirable, low frequency induction. Above the ionic conduction region (where ε'' flattens out) corresponds to the static permittivity region mentioned for the real part. It is within this frequency range that it is ideal for constant frequency, temperature sweeps. The higher range corresponds to a relaxation process. The height of this peak is related to the fitting parameter $\Delta\chi_0$. The top of the peak corresponds to the relaxation frequency f_r. At frequencies above this peak, it appears another relaxation process begins. However, the equipment was limited to a maximum frequency of 1 MHz and was not able to sufficiently probe the higher frequency process. Cole and Cole first showed that, when a relaxation process is present, parametrically plotting of the dielectric data reveals semicircles of radius R– a geometric interpretation of the data results [30]. While this eliminates an explicit dependence on frequency, it allows for three of the six fitting parameters to be well determined: the high frequency permittivity ε_∞, the dielectric strength $\Delta\chi_0$, and the depression angle related to the parameter α. From Equation 2.12a, as parameter α is reduced from one, the semicircle shifts downward resulting in a reduction of the dielectric loss. From Equation 2.12b, as parameter α is reduced from one, the radius of the semicircle increases, which depresses the dielectric loss peak.

The Cole-Cole plots for the 12% cholesteryl chloride sample can be seen in Figure 5.6. The dashed lines are parametric fits to the frequency range of the data having the relaxation process. That is, only those data determined to be part of the relaxation process were selected for fitting per temperature. The real part of the data (i.e., the horizontal axis) is shifted by the center of each semicircle so that concentric semicircles can be seen: $\varepsilon_\infty + \frac{\Delta\chi_0}{2}$.

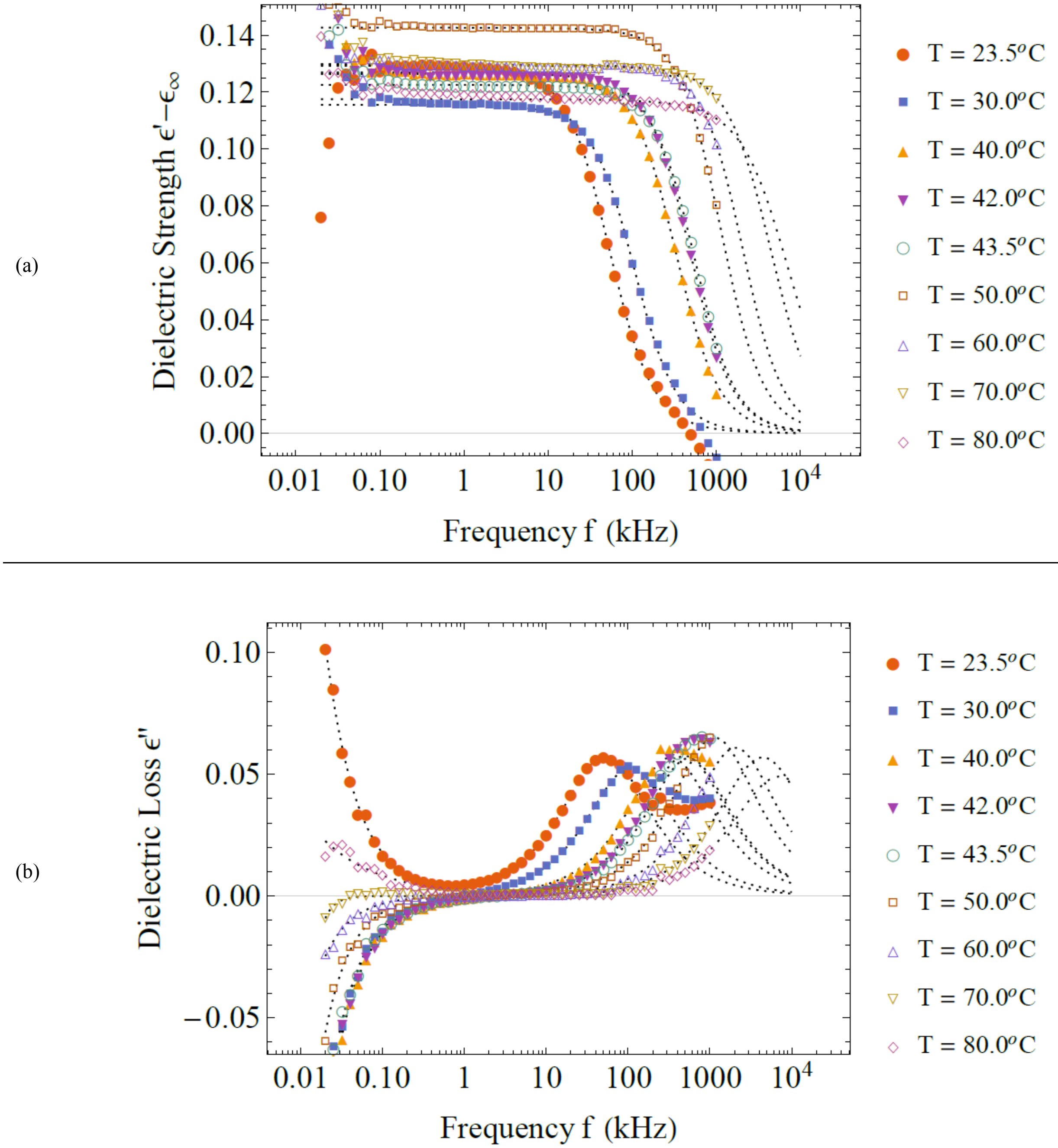

Figure 5.5: The explicit frequency dependence of the 12% CC mixture.

Data were collected from 20 Hz to 1 MHz. The dashed lines represent the fits to the data.

(a) The real part. So that the data could be plotted together, they are shifted by the high frequency limit fitting parameter ε_∞.

(b) The imaginary part. The frequency at a peak corresponds to a relaxation frequency f_r. The low frequency tail corresponds to either ionic contributions (+) or inductive contributions (-).

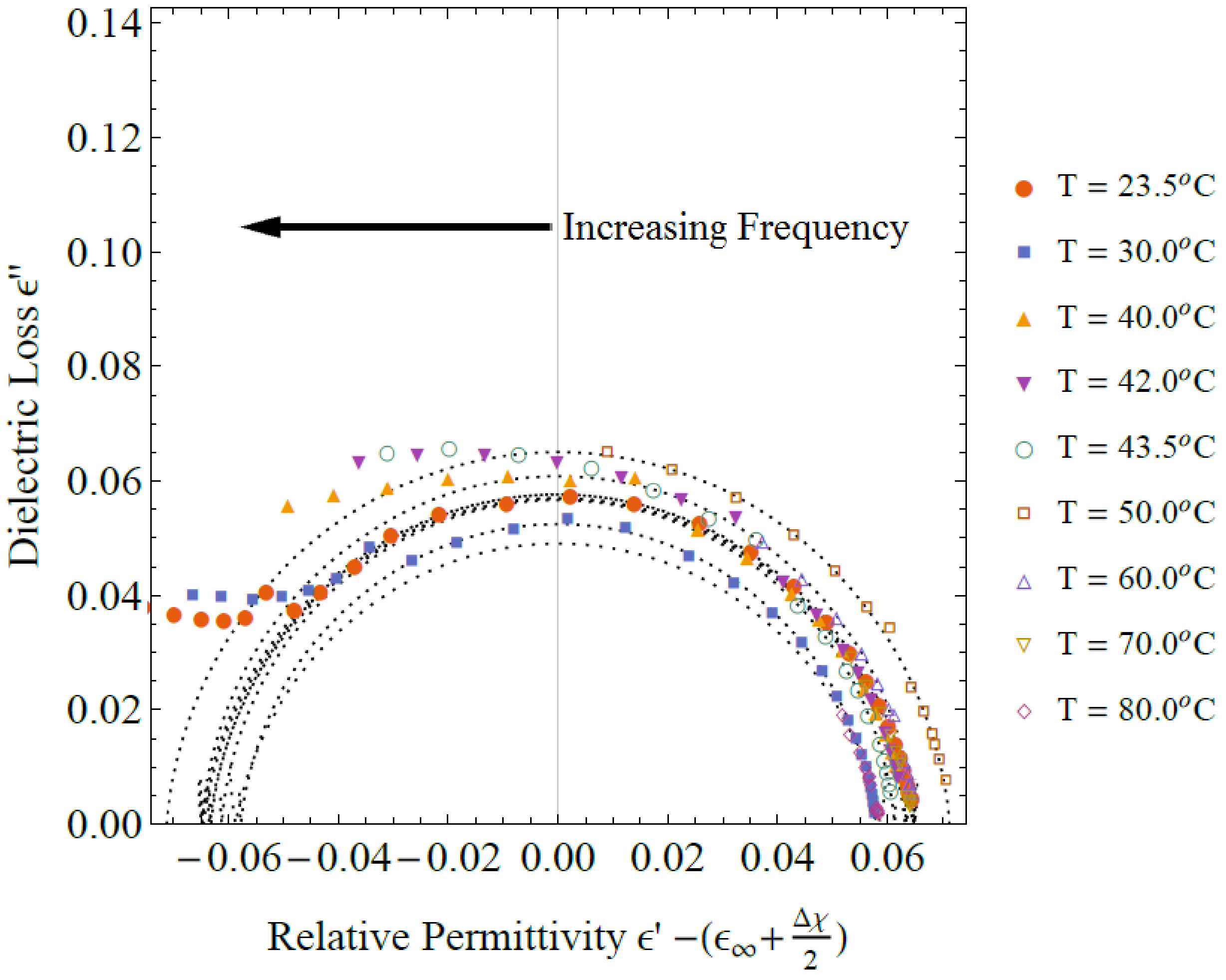

Figure 5.6: Parametric plot of all isothermal data for the 12% CC mixture.

Data were collected from 20 Hz to 1 MHz. The dashed lines represent the fits to the data such that only those data that seemed to be part of the relaxation process under investigation were used. As can be seen, there are higher frequency data points that appeared to be a part of another, higher frequency relaxation process.

5.2.2.1 Parametric Fitting Results

The fitting of relaxation data is mathematically analogous to the hierarchical model proposed in Section 4.3. In Section 4.3 a few parameters were obtained from an approximate model and then fed into the full model. This allowed for a reasonable approximation of all parameters.

For fitting a Cole-Cole relaxation process, it is useful to begin with a geometric interpretation: the semicircle introduced in Section 2.2.2. This eliminates an explicit dependence on frequency but also assumes no contributions from undesirable effects. When this is done, three of the six parameters of the model are determined: where the semicircle crosses the real axis ε_∞, the width of the semicircle $\Delta\chi_0$, and by how much it is shifted along the imaginary axis α. The downward angle φ of this shift relates to α by $\varphi = \frac{(1-\alpha)\pi}{2}$.

Table 5.3 shows the results of parametrically fitting the data at the various isotherms. In Figure 5.7, the high frequency permittivity ε_∞ shows a general increase in value as the temperature is reduced followed by a noticeable discontinuity around the phase transition. This plot shows the most reasonable of results. The parameter $\Delta\chi_0$ is the dielectric strength or width of the relaxation process. Parametrically it is the width of the semi-circle along the real axis. It does not vary much and there is scatter as a function of temperature. This is evident by looking at the third column of Table 5.3. Parameter α, seen in the fourth column of Table 5.3 reveals a near Debye type behavior over most isotherms. That is, parametrically, a Debye relaxation process shows a semicircle that is not shifted along the imaginary axis, resulting in a depression angle $\varphi = 0$ with $\alpha = 1$. More isothermal data (i.e., measure more frequencies per temperature) are needed to confirm if both $\Delta\chi_0$ and α indeed do not systematically vary as a function of temperature. The goal of the frequency dependence measurements is to find the relaxation frequency f_r as a function of temperature to check whether constant frequency data are near this or not.

Table 5.3: The fitting results of the parametric fit shown in Figure 5.6.

- High frequency permittivity ε_∞
- The dielectric strength of the relaxation process $\Delta\chi_0$
- The depression angle α

Fixed Temperature (°C)	ε_∞	$\Delta\chi_0=\varepsilon_\infty - \varepsilon_{static}$	α
$23.50_{\pm 0.06}$	$2.56666_{\pm 3*10^{-5}}$	$0.12985_{\pm 4*10^{-5}}$	$0.9238_{\pm 3*10^{-4}}$
$30.00_{\pm 0.01}$	$2.56289_{\pm 4*10^{-5}}$	$0.11555_{\pm 4*10^{-5}}$	$0.9382_{\pm 3*10^{-4}}$
$40.00_{\pm 0.01}$	$2.5571_{\pm 2*10^{-4}}$	$0.1269_{\pm 2*10^{-4}}$	$0.9302_{\pm 5*10^{-4}}$
$42.00_{\pm 0.03}$	$2.5547_{\pm 3*10^{-4}}$	$0.1264_{\pm 3*10^{-4}}$	$0.9406_{\pm 6*10^{-4}}$
$43.50_{\pm 0.02}$	$2.5556_{\pm 3*10^{-4}}$	$0.1225_{\pm 3*10^{-4}}$	$0.9498_{\pm 5*10^{-4}}$
$50.00_{\pm 0.02}$	$2.52287_{\pm 7*10^{-5}}$	$0.14266_{\pm 7*10^{-5}}$	$0.9414_{\pm 2*10^{-4}}$
$60.00_{\pm 0.05}$	$2.5157_{\pm 1*10^{-4}}$	$0.1297_{\pm 1*10^{-4}}$	$0.9594_{\pm 2*10^{-4}}$
$70.0_{\pm 0.10}$	$2.4930_{\pm 3*10^{-4}}$	$0.1292_{\pm 3*10^{-4}}$	$0.9198_{\pm 4*10^{-4}}$
$80.00_{\pm 0.07}$	$2.4850_{\pm 6*10^{-4}}$	$0.1175_{\pm 6*10^{-4}}$	$0.8856_{\pm 6*10^{-4}}$

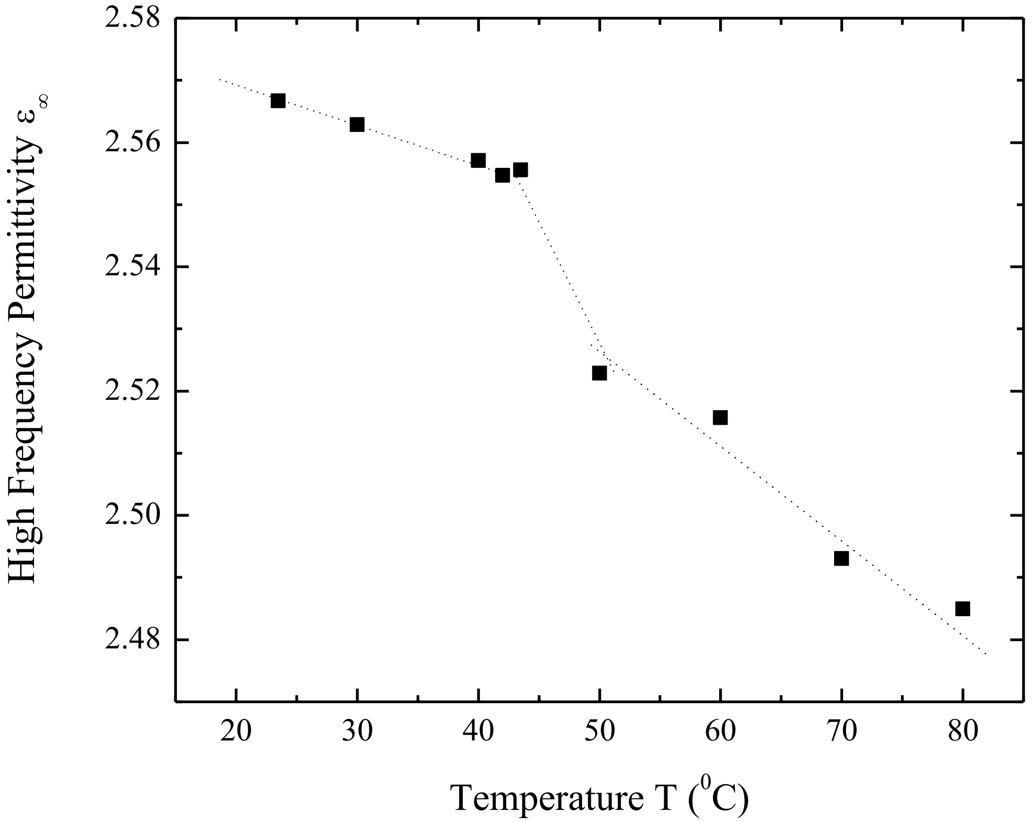

Figure 5.7: The high frequency permittivity ε_∞.

The left side of the Cole-Cole parametric plot where the permittivity theoretically crosses the real axis. The dotted line is for a guide to the reader and is not an actual fit to the data. The error bars from Table 5.3 are plotted, however they are negligible for many of the points.

5.2.2.2 Explicit Frequency Dependence Fitting Results

Parametric fitting allows for the simultaneous fitting of the real part ε' and the imaginary part ε'' around a relaxation peak at frequency f_r. After parametrically fitting the data, the results are fed into the frequency dependent models for the real and imaginary parts. Doing this reduces the real part ε' versus frequency to being dependent on a single parameter: the relaxation frequency f_r. The results of both the parametric fit and the explicit frequency dependence of the real part ε' are then used in the fit of the imaginary part ε''. This further reduces the model for the imaginary part ε'' versus frequency as a two parameter model: the low frequency ionic conductivity S and the exponent of the frequency dependence n of that low frequency behavior. In order to model the relaxation peak alone, it is sufficient to only parametrically fit the data followed by fitting the real part ε' versus frequency.

Table 5.4 shows the numerical results of the fits for the explicit frequency dependence. The relaxation frequency f_r shows a dramatic increase in the estimated standard error as f_r approaches the measuring limits of the apparatus. The low frequency parameter S is expected to represent the low frequency ionic conductivity of the sample if its sign is positive. However it is negative at many of the isothermal measurements, albeit small. This is typically associated with undesirable inductive behavior [34]. In Figure 5.5b, the static permittivity region is sufficiently wide and flat over all isotherms. It can be concluded that any low frequency inductive (or conductive) behavior is not affecting the results in the static region – namely around the 10 kHz probing frequency. Except for those isotherms where the estimated relaxation frequency exceeds the measuring capabilities of the apparatus, the exponent n of the low frequency behavior is close to a value of one at the discrete temperatures measured in figure 5.5 and 5.6.

Figure 5.8 shows the relaxation frequency versus inverse temperature. It is seen that the lowest relaxation frequency is at 53 kHz with a $\Delta\chi_0$ of 0.13. From Figure 5.5 this corresponds to 10 kHz being on the tail end of the relaxation process and 1 kHz being sufficiently beyond the relaxation curve. At higher temperatures (to within 12 °C of the phase transition; see Figure 5.3), 10 kHz is sufficiently low enough for the static permittivity measurements.

The results of the relaxation frequency versus temperature, plotted in Figure 5.8, are necessary to assess whether or not the low frequency measurements were within the static permittivity regime. That is, it is important to know if the temperature ramping measurements were in the static, plateau region of the dielectric permittivity and if the measurements were outside of the lowest frequency ionic conductivity region.

The low frequency ionic conductivity S and the low frequency index n values are seen in Table 5.4, columns three and four. For many of the measurements, parameter S was negative, meaning the imaginary part curved downward for low frequencies and probably had parasitic inductance. Looking back at Figure 5.6, the semicircles did not appear skewed; this means the undesirable low frequency behavior did not noticeably affect the relaxation curves. The fitting parameter n is near a value of one except at the isotherms of 70 °C and 80 °C. From Figure 5.5b it is seen that the low frequency tail is small at these two temperatures. So the results of S and n are not as well determined at the higher temperatures. However, for the purposes of this dissertation, it is sufficient that this low frequency region is avoided, not necessarily fully characterized. Figure 5.5b allows for a visualization of this.

The exponent β in Equation 3.8 is fixed at one for this analysis. It represents the high frequency (i.e., $f_{measured} > f_r$) linearity in the parametric relationship between ε'' and ε'. The use of $\beta \neq 1$ could not be justified due to a limited range of frequencies measured for $f_{measured} > f_r$. Without a sufficient frequency range, it is impossible to distinguish between a single skewed peak (the case where $\beta \neq 1$) and two close peaks that are superimposed on each other (where both peaks have $\beta = 1$). For most of the data sets, the maximum frequency measured $f_{measured}$ barely exceeded the fitted relaxation frequency f_r.

Table 5.4: These are the fitting results of the explicit frequency dependence of ε' and ε''after performing the parametric fits on the data shown in Figure 5.6.

The parameter estimates for ε_∞, $\Delta\chi_0$, and α are shown in Table 5.3:

- The relaxation frequency f_r
- The low frequency conductivity S
- The modification to the power of the low frequency dependence n

Fixed Temperature (°C)	Relax f_r (kHz)	Conductivity S $*10^{-3}$ (kHz^n)	Power n
23.50 ± 0.06	53 ± 1	10.28 ± 0.01	1.1119 ± $6*10^{-4}$
30.00 ± 0.01	106± 2	-8.148 ± 0.009	1.1530 ± $6*10^{-4}$
40.00 ± 0.01	332± 10	-8.860 ± 0.009	1.1622 ± $5*10^{-4}$
42.00 ± 0.03	494± 30	-8.761 ± 0.009	1.1514 ± $6*10^{-4}$
43.50 ± 0.02	555± 30	-7.178 ± 0.008	1.2260 ± $6*10^{-4}$
50.00 ± 0.02	1139± 20	-3.649 ± 0.005	1.3166 ± $8*10^{-4}$
60.00 ± 0.05	2060± 80	-1.743 ± 0.006	1.2772 ± $2*10^{-4}$
70.0 ± 0.10	4431± 500	-0.43 ± 0.03	0.0498 ± $1*10^{-4}$
80.00 ± 0.07	7033± 1000	6.282 ± 0.007	0.6165 ± $7*10^{-4}$

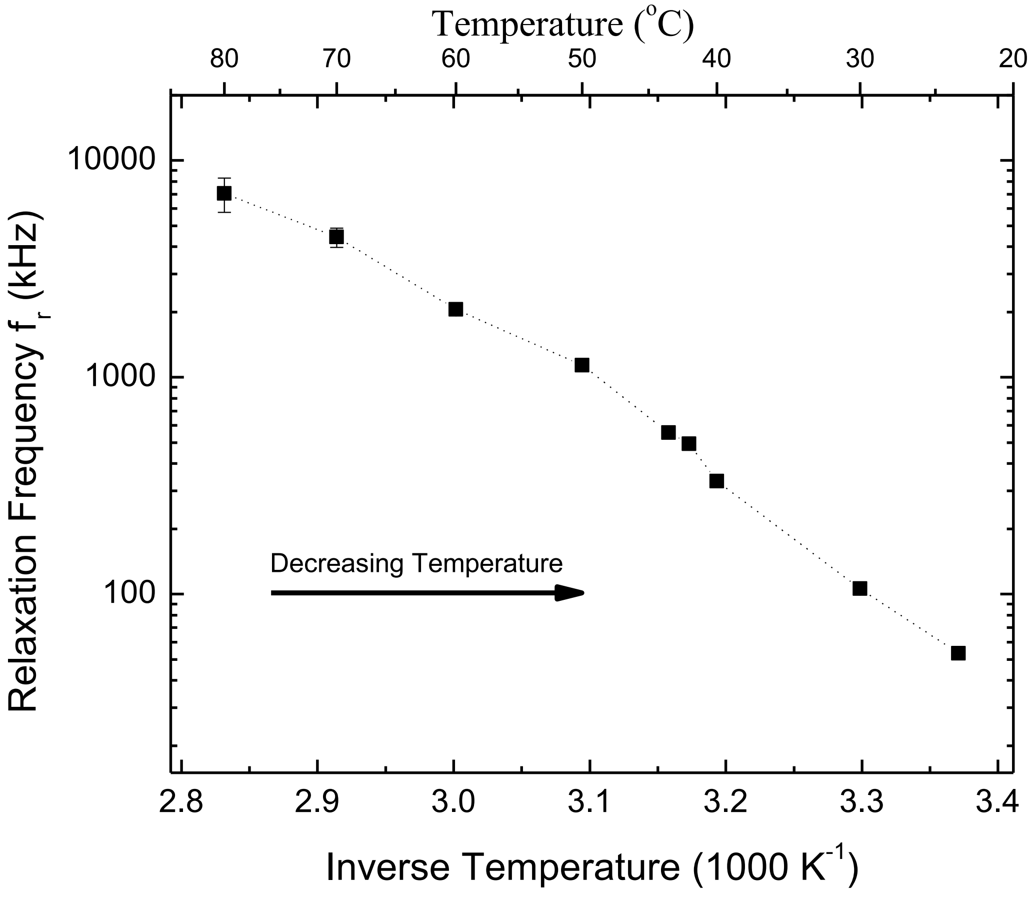

Figure 5.8: The temperature dependence of the relaxation frequency f_r for the 12% cholesteryl chloride mixture.

Parametrically, it corresponds to the peak of the semicircle. This peak is where the dielectric loss ε'' is maximum. The dotted line is for a visual guide to the reader and is not an actual fit to the data. Due to the limited number of data points, it is not obvious whether or not the three data points between $3.10 \frac{1}{\text{Mk}}$ (49.4 °C) and $3.20 \frac{1}{\text{Mk}}$ (39.4 °C) are another phase (such as a blue phase). The error bars from Table 5.4 are plotted, however they are negligible for many of the points.

5.2.3 Microscopic Observations of the 12% CC Mixture

Cross cross-polarized microscopy observations were performed in order to correlate the different characteristic regimes of the dielectric data to the textures associated with each phase for the corresponding temperature ranges. Although the dielectric and microscopic measurements were not performed simultaneously, the phase transitions were in reasonable agreement. For example, the dielectric measurements (using a thick sample) on cooling for the 12% mixture clearly showed a transition from the isotropic phase to BPIII at (39.5 ± 0.1) °C. On heating, a cholesteric to isotropic phase transition was found to be at (41.2 ± 0.2) °C. For my microscopic observations (using a thin sample on cooling), an apparent isotropic phase transition to BPII was found to be around 40.9 °C. Using the Koistinen et. al. paper as a reference (which used a thick sample), this was probably the BPIII (an isotropic phase) to BPII transition which had a BPIII that extended over a 0.6 K range [57]. Adding this range to my observed transition to BPII gives 41.5 °C. This compares well the dielectric measurement on cooling of 41.2 °C. A thick sample is needed for optical observations of BPIII.

Table 5.5 outlines the cross-polarized microscopy results for the 12% cholesteryl chloride mixture. Figure 5.8 shows selected images corresponding to Table 5.5. For this sample, the blue phases I and II were seen only under reflectance on cooling. On cooling, from the isotropic phase yellow platelets appeared within 0.2 K below the phase transition. Platelets are a characteristic texture of blue phases I and II. This corresponds to the start of the transition from BPIII to BPII. By 0.3 K below the isotropic phase the color changed to orange and the platelets increased in number and size. By 0.6 K below the transition, the orange platelets turned a dark red. These red platelets remained until 1.1 K below the isotropic phase, corresponding to BPII (when present, BPII is always at a higher temperature than BPI). At 1.2 K below the phase transition a yellow haze associated with the cholesteric phase formed with some of the red platelets turning a patch work of yellow and orange. This corresponds to the start of the transition from BPII to BPI. By 1.6 K below the isotropic phase, the red platelets changed mostly to yellow with the formation of a few green platelets. By 2.0 K below the isotropic phase all platelets were green, with some dark red patches at the periphery of the region with green platelets. The green platelets persisted until 3.0 K below the isotropic phase, corresponding to BPI. The cholesteric phase started to take form as the image turned blue at 4.5 K below the isotropic phase. During this temperature range, the cholesteric phase began to form and gradually start to dominate the image from 3.6 K below the isotropic phase until it fully occupied the view by 5.1 K below the phase transition.

Firstly, my optical observations clearly showed the presence of BPII and BPI above the cholesteric phase. Since my microscope sample slide was too thin, BPIII was not definitively observed. However, from Koistinen et. al., BPIII is known to exist between the isotropic phase and BPII for the 12% mixture over a narrow temperature range [57]. Recall from Section 1.1.2 that blue phases are cubic structures with diffuse Bragg peaks. Over the initial 0.7 K below the isotropic phase, the wavelength of the blue phase increased from yellow to red with decreasing temperature. This was followed by 0.6 K of the wavelength remaining constant at red. Then over an additional 0.6 K, the wavelength decreased from red to green. With further decreasing of the temperature, it remained green for 1.4 K until changing to blue and the cholesteric phase. This increase in the wavelength and plateau in the red is probably blue phase II (a simple cubic) as it is near the isotropic phase. Blue phase I is a body-centered cubic that typically appears between blue phase II (or BPIII, if BPII is not present) at a higher temperature and the cholesteric phase at a lower temperature. The decrease in wavelength followed by a constant green is probably blue phase I. Heating began in the cholesteric phase. By it being a uniform blue color this means that it started off planar aligned.

Secondly, from the dielectric measurements of the 12% cholesteryl chloride mixture at 10 kHz on cooling (seen in Figures 5.3 and 5.4), for the first 5.4 K below the isotropic phase the real part of the dielectric permittivity slopes upward with decreasing temperature. Within this region, the blue phases are expected to show up. From the isotropic phase, there is a slight kink in the data at the transition followed by a slight change in the slope. It is this kink that corresponds to BP III.

It is about the width reported in Koistinen et. al. for BPIII. Beyond this kink, it appears that BP I and II are dielectrically indistinguishable from each other [57]. Blue phases I and II are together dielectrically distinguishable from both the higher temperature isotropic phase and the lower temperature cholesteric phase. In order to better compare the temperature range of BPIII from dielectric measurements to Koistinen et. al., a higher density of data should be acquired for future work [57]. As for the cross-polarized microscopy observations, the camera aperture automatically adjusted to sudden lighting adjustment. In order to observe blue phase III for the optical microscopy measurements (assuming it is in the optical range of the spectrum for the 12% cholesteryl chloride sample), using a different camera setup would be helpful. Also, from Koistinen et. al., it seems a thicker sample should be used [57].

Table 5.5: Summary of cross-polarized microscopy observations for the 12% cholesteryl chloride mixture.

Temperature (°C)	Observation	Associated Phase
14.0	Texture associated with smectic.	Smectic A
23.5	Uniform color, Blue; Planar alignment	N*
40.9	Isotropic	BPIII [57]
40.8	Yellow platelets form	BPII forming
40.7	Orange platelets form	
40.6 to 39.9	Platelets turn Red, stay Red	BPII
39.8	Parts turn Orange and Yellow	BPI forming
39.4	Yellow and Orange	
39.2	Green and Yellow	
39.0 to 37.2	Turns Green, stays Green	BPI
37.1 to 36.6	Green changes to Blue-Green	N* Forming
36.5	Blue platelets with large cholesteric patches	
35.9	Cholesteric fully formed	N*

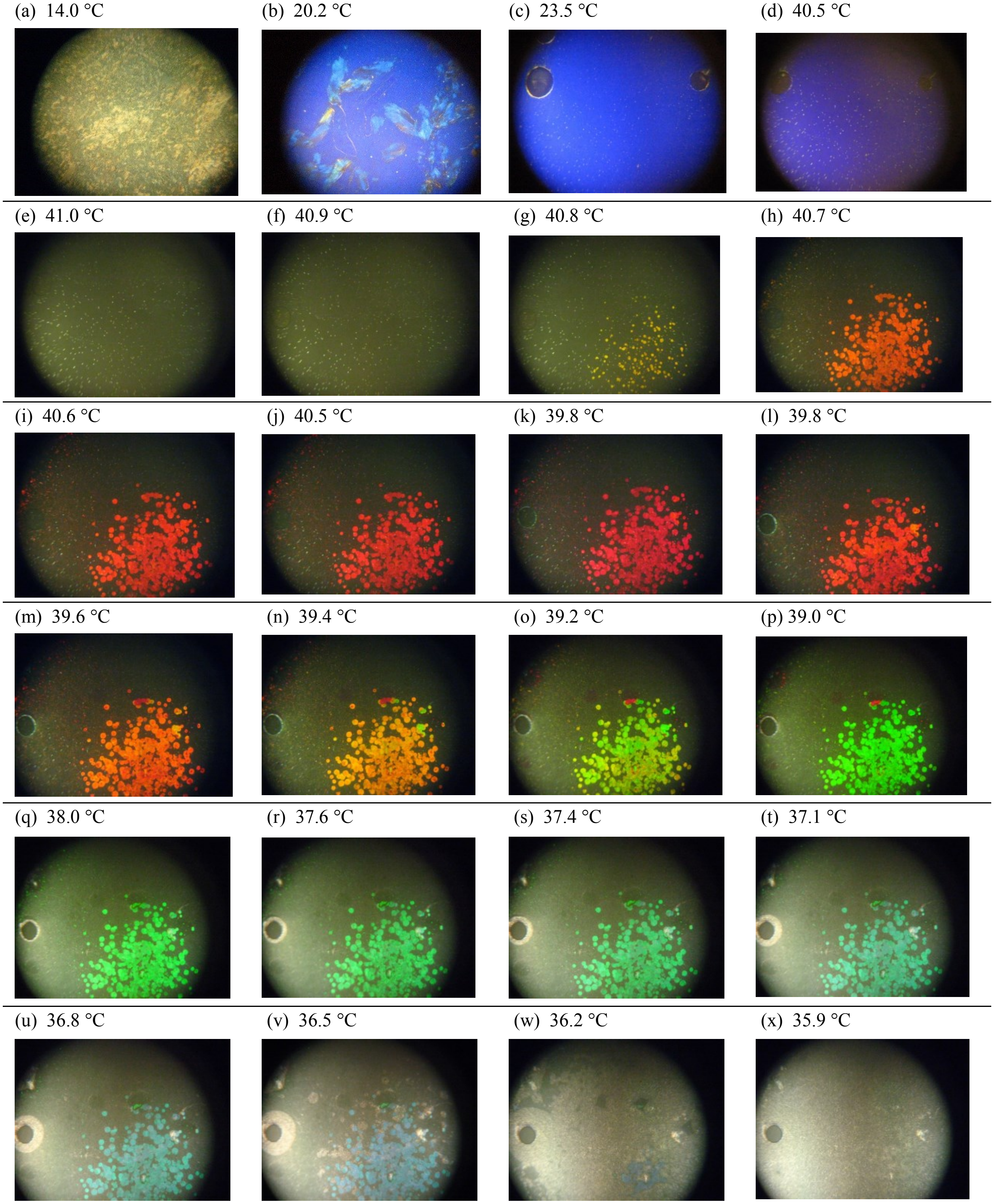
(a) 14.0 °C
(b) 20.2 °C
(c) 23.5 °C
(d) 40.5 °C
(e) 41.0 °C
(f) 40.9 °C
(g) 40.8 °C
(h) 40.7 °C
(i) 40.6 °C
(j) 40.5 °C
(k) 39.8 °C
(l) 39.8 °C
(m) 39.6 °C
(n) 39.4 °C
(o) 39.2 °C
(p) 39.0 °C
(q) 38.0 °C
(r) 37.6 °C
(s) 37.4 °C
(t) 37.1 °C
(u) 36.8 °C
(v) 36.5 °C
(w) 36.2 °C
(x) 35.9 °C

Figure 5.9: Optical cross-polarized microscopy images for the representative 12% cholesteryl chloride mixture.

All images are captured under reflectance. Indices (a) and (b) are from a different run in which the sample was cooled below room temperature looking for a smectic phase. The dark circle is an air bubble. The white dots observed at 40.8 °C and above were present for all mixtures. The white dots did not show up when the crossed polarizers were removed.

5.3 The Dielectric Response and Microscopic Observations for All Investigated COC-CC Mixtures

Mixtures of cholesteryl chloride with cholesteryl oleyl carbonate were made between 0% and 60% cholesteryl chloride. The mixtures were studied to see how the blue phases evolve as a function of composition. Blue phases are expected to be present between the 0% and 40% cholesteryl chloride mixtures [59]. As such, the 12% mixture was looked at in the previous section as an example that includes dielectric features common to those mixtures having blue phases. The optical results from McKinnon et. al. of the isotropic to mesophase transition versus composition can be seen in Figure 5.10 [59]. Intermediate compositions of cholesteryl chloride with cholesteryl oleyl carbonate approach the low chirality limit where blue phases are not present.

The dielectric measuring process and data acquisition for the heating and cooling runs were performed the same way as with the 12% cholesteryl chloride mixture discussed previously in both Sections 3.2 and 5.2. The only exception in data acquisition was for the number of data points collected every degree centigrade. The 3%, 6%, and 12% mixtures were the first samples to be dielectrically measured in this study – the data were recorded every third of a degree centigrade. Considering the error bars on the temperatures in Table 5.2b, it was an initial concern that recording more data points per temperature would result in noisy data. The 20% and 30% cholesteryl chloride mixtures were then measured – the data were recorded every fourth of a degree. It was realized that as composition was increased, the temperature range of the blue phases decreased. More data points per degree centigrade were necessary. The remaining mixtures, including a repeat of pure cholesteryl oleyl carbonate, were measured every fifth of a degree for the dielectric temperature cycling.

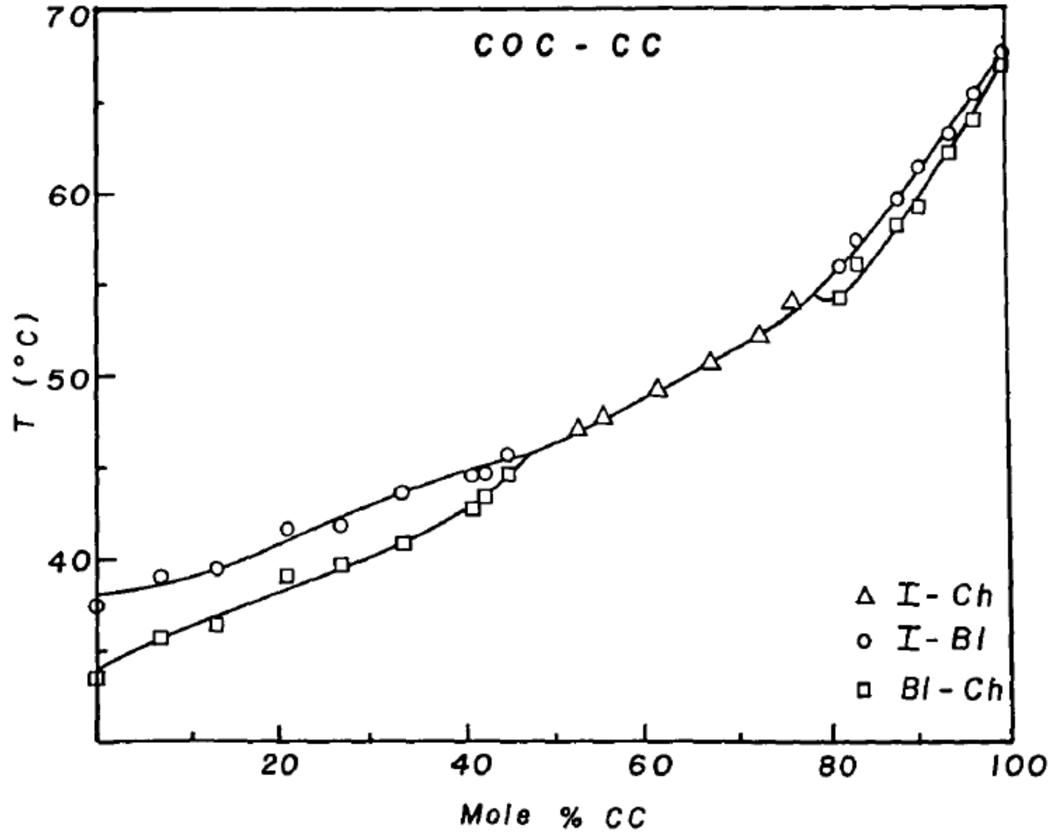

Figure 5.10: Phase diagram from the paper by P. H. Keyes, A. J. Nicastro and E. M. McKinnon [59].

This is the estimate of the phase transitions from optical measurements. When this paper was published, it was not yet well established that there was more than one blue phase.

5.3.1 Normalization of the Temperature Dependence

The same normalization procedure as with the 12% cholesteryl chloride composition was performed for all compositions. The normalization was done with respect to the isotropic to mesogenic phase transition. The transition temperature T_{IM} for each composition needed to be found for both heating and cooling run. The value of T_{IM} was subtracted out from all temperatures. The respective real and imaginary parts of the permittivity, ε'_{IM} and ε''_{IM}, are then determined. The permittivity values were divided by their respective ε'_{IM} and ε''_{IM} values.

5.3.1.1 The Isotropic to Mesogenic Phase Transition Temperature T_{IM}

The mean values for the estimated transition temperatures from the isotropic to mesogenic phase T_{IM} are shown for all compositions studied in Table 5.6. As mentioned earlier, each heating and cooling cycle was performed multiple times. The values reported are the averages over all runs with one standard deviation from the mean reported as the uncertainty. The uncertainty is a measure of the repeatability of the magnitudes; the precision of an individual run was high with the relative shapes being consistent. The values in Table 5.6 are plotted in Figure 5.11.

Both heating and cooling run transition temperatures follow an approximately linear trend versus composition. A proportional increase in T_{IM} with the addition of cholesteryl chloride to cholesteryl oleyl carbonate is expected. That is, cholesteryl oleyl carbonate has a much lower isotropic to mesogenic phase transition than cholesteryl chloride. Pure cholesteryl oleyl carbonate has an isotropic transition temperature that is around 38 °C. As discussed in Section 3.3, cholesteryl chloride has a monotropic phase sequence, where the transition temperature T_{IM} on heating is at 98 °C (crystal to isotropic) and on cooling is at 72 °C (isotropic to blue phase). The slopes of both the heating and cooling runs can are shown in Figure 5.11.

Table 5.6: The average estimated transition temperature T_{IM} for the heating and cooling runs.

The isotropic to mesogenic phase transition temperature did not appear to be dependent on the frequency. Each is a combined mean of the 10 kHz and 100 kHz runs. One standard deviation from this mean is reported as the uncertainty. The difference between the heating and cooling runs for all compositions was relatively constant: $T_{IM}^{Heating} - T_{IM}^{Cooling} = (1.9 \pm 0.3)$ °C.

Composition (% CC)	T_{IM} (°C) on Heating	T_{IM} (°C) on Cooling
0	39.3 ± 0.1	37.4 ± 0.1
1.5	39.9 ± 0.1	37.9 ± 0.1
3	40.8 ± 0.4	39.2 ± 0.2
6	41.2 ± 0.3	39.3 ± 0.1
12	41.2 ± 0.2	39.5 ± 0.1
16	42.5 ± 0.2	40.8 ± 0.1
20	43.7 ± 0.1	41.8 ± 0.1
25	45.1 ± 0.1	43.07 ± 0.05
30	46.5 ± 0.2	44.4 ± 0.1
35	48.1 ± 0.1	45.9 ± 0.1
40	47.6 ± 0.1	45.97 ± 0.04
45	50.3 ± 0.1	47.8 ± 0.1
50	51.6 ± 0.1	49.6 ± 0.1
55	52.6 ± 0.5	50.1 ± 0.5
60	53.3 ± 0.1	51.6 ± 0.2

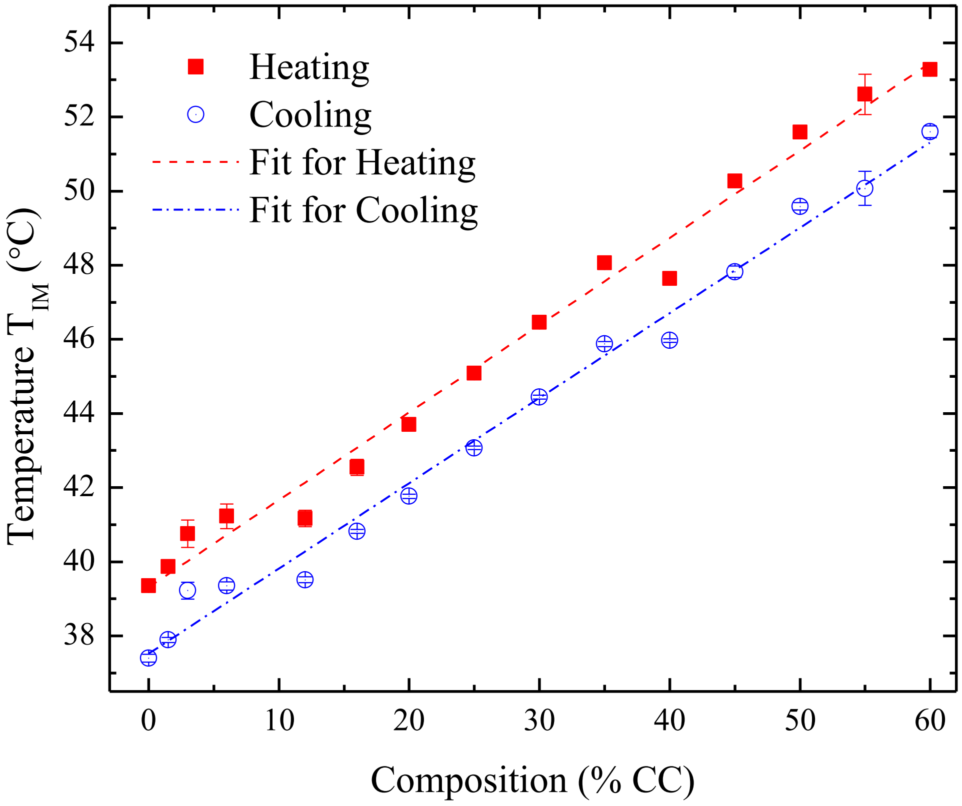

Figure 5.11: The average estimated transition temperatures T_{IM} for the dielectric heating and cooling runs from Table 5.6 for all compositions.

The error bars from Table 5.6 are included in the plot. They are relatively small for most mixtures. Both types of runs appear to be linear with some scatter. A linear fit was performed for each type of run (not graphically shown). The linear fitting results of both the heating and cooling runs as a function of composition are given:

	Slope $\left(\frac{℃}{\%CC}\right)$	Intercept (℃)
Heating	0.236 ± 0.002	39.3 ± 0.6
Cooling	0.230 ± 0.002	37.5 ± 0.5

5.3.1.2 The Real Part ε'_{IM} of the Permittivity at the Transition Temperature T_{IM}

As mentioned in Section 3.3, cholesteryl chloride has a significant longitudinal dipole moment, which is a major contributor to the value of the real part of dielectric permittivity ε'. Cholesteryl oleyl carbonate does not have a significant longitudinal dipole moment. It is expected that, as cholesteryl chloride is added, the net dipole moment and real part of the permittivity ε' will increase.

The mean values of the real part of the permittivity at the transition isotropic to mesogenic phase transition ε'_{IM} are shown for all compositions in Table 5.7 and plotted in Figure 5.12. The values reported are the averages over all runs with one standard deviation from the mean reported as the uncertainty. All runs (on both heating and cooling, and at 10 kHz and 100 kHz) follow an approximately linear trend as a function of composition. Also, unlike the phase transition temperature T_{IM}, the permittivity ε'_{IM} at the phase transition is not heavily dependent on heating versus cooling. It is not clear whether the scatter in the data over composition is due to random error, to systematic errors, or to whether or not the data can be broken up into smaller regions. The slope of the line as a function of composition is seen in Figure 5.12.

Table 5.7: The average real part of the permittivity at the transition ε'_{IM}.

This corresponds to the estimated transition temperatures T_{IM} from Table 5.6 for the heating and cooling runs at both 10 kHz and 100 kHz. Within error all four values per composition were relatively close.

Composition (% CC)	ε'_{IM} on Heating		ε'_{IM} on Cooling	
	10 kHz	100 kHz	10 kHz	100 kHz
0	2.607 ± 0.002	2.5986 ± 0.0007	2.606 ± 0.001	2.598 ± 0.001
1.5	2.5324 ± 0.0006	2.522 ± 0.001	2.5334 ± 0.001	2.523 ± 0.002
3	2.5468 ± 0.0006	2.539 ± 0.001	2.5460 ± 0.001	2.5376 ± 0.0004
6	2.671 ± 0.001	2.6640 ± 0.0005	2.6726 ± 0.001	2.6661 ± 0.0003
12	2.679 ± 0.003	2.6702 ± 0.0004	2.681 ± 0.001	2.6726 ± 0.0006
16	2.7136 ± 0.0006	2.7019 ± 0.0003	2.7143 ± 0.001	2.7028 ± 0.0002
20	2.885 ± 0.001	2.876 ± 0.002	2.8888 ± 0.001	2.879 ± 0.002
25	2.837 ± 0.003	2.816 ± 0.003	2.837 ± 0.001	2.815 ± 0.004
30	3.032 ± 0.001	3.0085 ± 0.0005	3.034 ± 0.001	3.011 ± 0.001
35	3.075 ± 0.003	3.054 ± 0.001	3.076 ± 0.001	3.0557 ± 0.0005
40	3.155 ± 0.001	3.142 ± 0.001	3.158 ± 0.001	3.146 ± 0.003
45	3.2467 ± 0.0006	3.235 ± 0.001	3.2485 ± 0.001	3.236 ± 0.001
50	3.383 ± 0.001	3.354 ± 0.001	3.3833 ± 0.001	3.3537 ± 0.0003
55	3.3521 ± 0.0006	3.333 ± 0.001	3.3544 ± 0.001	3.3343 ± 0.0005
60	3.420 ± 0.002	3.3976 ± 0.0005	3.4228 ± 0.001	3.3996 ± 0.0006

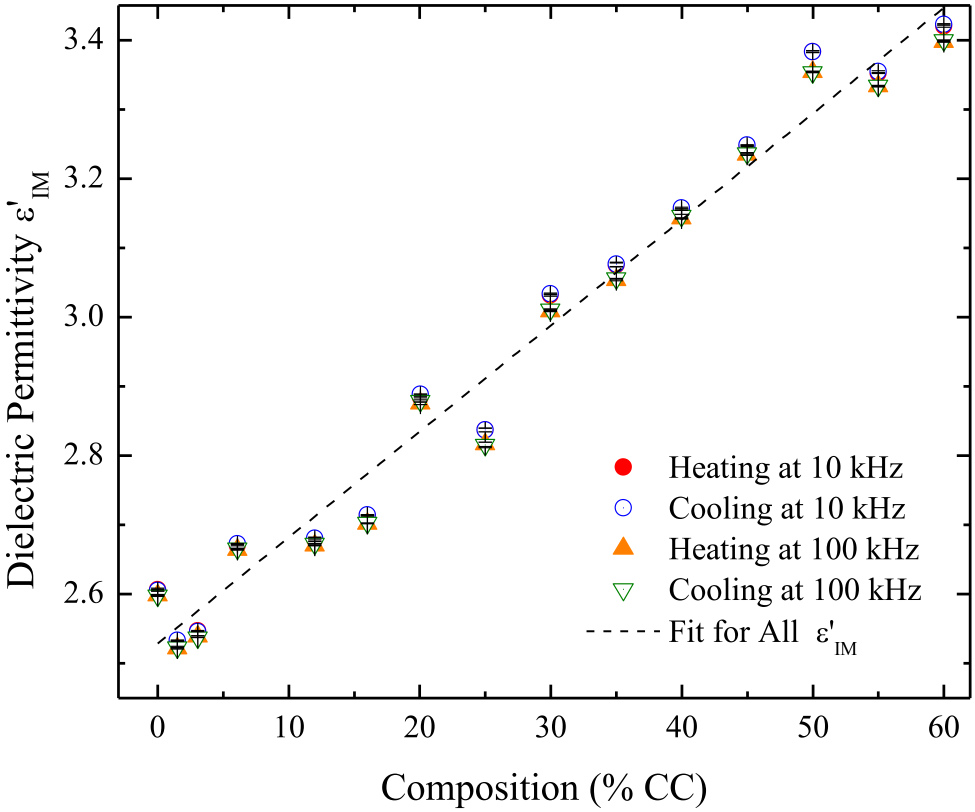

Figure 5.12: The average real part of the permittivity transition ε'_{IM}.

This corresponds to the estimated transition temperatures T_{IM} from Table 5.6 for the heating and cooling runs at both 10 kHz and 100 kHz. For a single composition (look at Figure 5.3a of the 12% composition for example), the heating and cooling values appear quite different between the 10 kHz and 100 kHz runs. When plotted as a function of composition, these differences appear negligible. The relationship between ε'_{IM} and composition appears linear over both heating and cooling runs as well as 10 kHz versus 100 kHz. A combined fit was found:

- The overall slope is $(0.01530 \pm 10^{-5})\ \frac{1}{\%\mathrm{CC}}$.
- The intercept is 2.53 ± 0.05.

5.3.1.3 The Dielectric Loss ε''_{IM} of the Permittivity at the Transition Temperature T_{IM}

The dielectric loss (also referred to as the imaginary part of the permittivity) is a measure of the energy dissipation when a field is applied. The addition of cholesteryl chloride means the addition of longitudinal dipoles. More dipoles mean that there are more constituents to stir back and forth in response to an applied field. As discussed earlier, as the applied frequency nears the relaxation frequency, maximal dissipation occurs.

The mean values of the dielectric loss ε''_{IM} that correspond to the above mentioned isotropic to mesogenic phase transition temperatures are shown for all compositions in Table 5.8 and plotted in Figure 5.13. The values reported are the averages over all runs with one standard deviation from the mean reported as the uncertainty. Unlike the real part, there is a distinct difference between the 10 kHz and 100 kHz measurements. For most of the compositions near the isotropic to mesogenic phase transition, 10 kHz is in the frequency range of lowest dissipation (i.e., far from the relaxation peak). This is also referred to as the frequency plateau or static permittivity region. In the static permittivity region the molecules are able to sufficiently respond and realign in response to an applied field.

Table 5.8: The average imaginary part of the permittivity transition ε''_{IM}.

This corresponds to the estimated transition temperatures T_{IM} from Table 5.6 for heating and cooling runs at both 10 kHz and 100 kHz. The two frequencies gave two distinct behaviors. For a single frequency measurement, both heating and cooling runs were relatively similar at a fixed frequency.

Composition (% CC)	$\varepsilon''_{IM} \times 10^{-3}$ on Heating		$\varepsilon''_{IM} \times 10^{-3}$ on Cooling	
	10 kHz	100 kHz	10 kHz	100 kHz
0	1.56 ± 0.03	5.50 ± 0.04	1.61 ± 0.03	5.52 ± 0.03
1.5	0.92 ± 0.04	9.50 ± 0.06	0.93 ± 0.04	9.57 ± 0.05
3	1.94 ± 0.04	13.200 ± 0.004	1.686 ± 0.004	12.95 ± 0.03
6	3.1 ± 0.1	20.11 ± 0.02	2.805 ± 0.004	19.96 ± 0.04
12	3.8 ± 0.2	30.6 ± 0.7	3.4 ± 0.2	30.7 ± 0.6
16	4.6 ± 0.2	39.4 ± 0.4	3.96 ± 0.09	39.7 ± 0.5
20	5.5 ± 0.2	45.0 ± 0.6	5.46 ± 0.07	45.2 ± 0.4
25	5.64 ± 0.07	54.5 ± 0.3	5.7 ± 0.1	54.7 ± 0.3
30	12.3 ± 0.2	61.6 ± 0.6	12.4 ± 0.2	63.1 ± 0.3
35	7.2 ± 0.1	68.4 ± 0.4	7.5 ± 0.2	69.1 ± 0.5
40	8.2 ± 0.2	73 ± 3	8.3 ± 0.1	70.0 ± 0.9
45	8.4 ± 0.1	76.2 ± 0.5	8.9 ± 0.2	77.3 ± 0.9
50	20 ± 3	86 ± 1	17.2 ± 0.5	88 ± 1
55	9.5 ± 0.1	83.2 ± 0.9	10.2 ± 0.6	88 ± 1
60	14.9 ± 0.7	85.9 ± 0.6	15.0 ± 0.3	87.1 ± 0.8

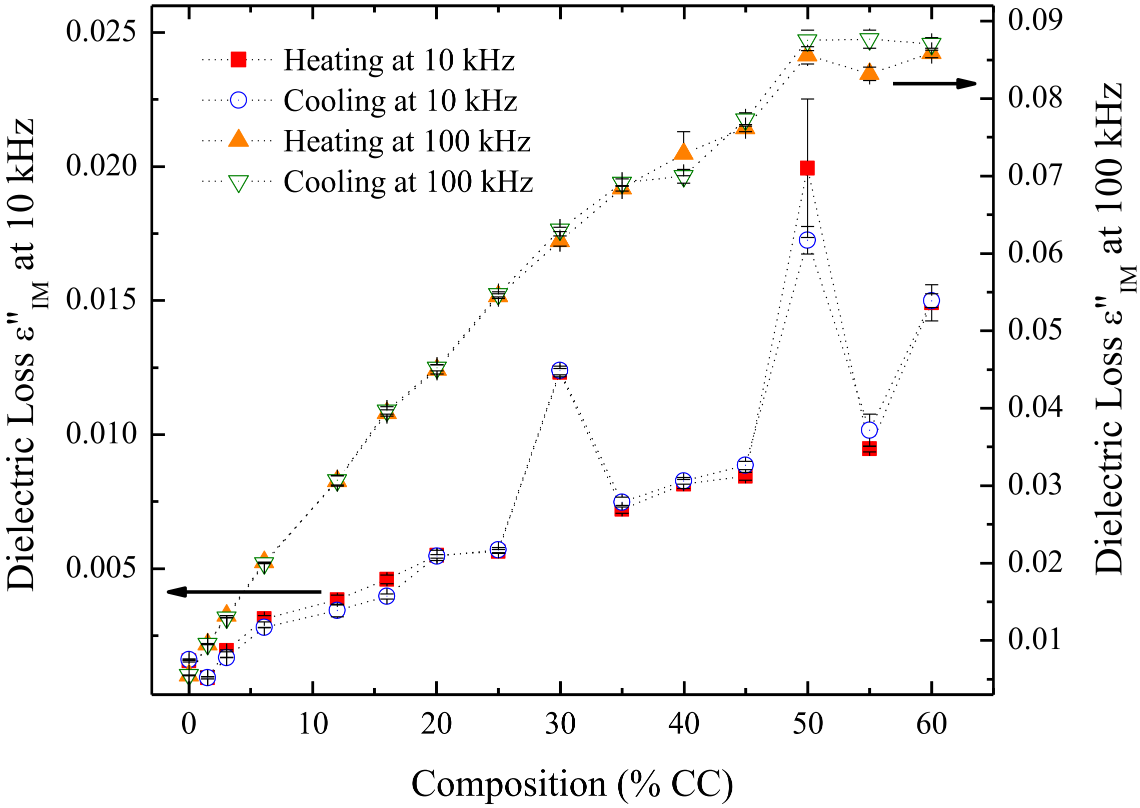

Figure 5.13: The imaginary part of the permittivity at the transition ε''_{IM}.

This corresponds to the estimated transition temperature T_{IM} from Table 5.6 for the heating and cooling runs at both 10 kHz and 100 kHz. The dotted lines are for reference only and are not fits.

When plotted as a function of composition, both the 10 kHz and 100 kHz runs are non-linear over the compositions measured. As more longitudinal dipoles are added (i.e., higher concentration of cholesteryl chloride in cholesteryl oleyl carbonate), there are more constituents that respond by oscillating back and forth. This results in more thermal dissipation. The 10 kHz measurements are in a regime of lowest dissipation (i.e., the frequency plateau).

At 10 kHz a spike in the dissipation occurs at both 30% and 50% cholesteryl chloride. At 50% cholesteryl chloride, the blue phases are gone, the cholesteric phase is narrow, and two smectic phases appear. Both above and below 50% cholesteryl chloride, the chiral nematic phase is relatively wide. Based on McKinnon et. al., the blue phases are expected to dissapear by 45% CC [59]. However, no blue phases were observed under the microscope above 25%. If a blue phase exists above 25% CC, then it most likely has a Bragg reflection that lies within the IR.

5.3.2 Permittivity Discontinuity at the Isotropic-Mesophase Transition

As discussed in Section 1.2.2.3, a phase transition can be classified as either first or second order. A first order transition, the order parameter ε' versus temperature (discussed in Section 1.2.2.3), shows a discontinuity in the data between where one phase ends and another begins. In the limit of low chirality, cholesteric liquid crystals are approximately nematic, which have a first order transition.

The discontinuities of both the real part and imaginary part of the permittivity, respectively $\Delta\varepsilon'$ and $\Delta\varepsilon''$, are estimated by taking the difference between the estimated lowest temperature value, ε'_{IM} or ε''_{IM}, of the permittivity in the isotropic phase and the highest temperature value, $\varepsilon'_{Mesophase}$ or $\varepsilon''_{Mesophase}$, of the permittivity in the mesophase. In the previous section the lowest temperature data point in the isotropic phase was given by the simultaneous values of ε'_{IM}, ε''_{IM}, and T_{IM}. A corresponding set of values were used as the highest temperature data point in the mesophase that followed the isotropic phase. The estimated discontinuity $\Delta\varepsilon'$ for the real part of the permittivity is shown in Figure 5.14 versus composition. The estimated discontinuity $\Delta\varepsilon''$ for the dielectric loss is shown in Figure 5.15.

On cooling in Figure 5.14, the 10 kHz measurements of the real part $\Delta\varepsilon'$ have no discontinuity in the isotropic to mesogenic transition for the cholesteryl oleyl carbonate rich mixtures. The transition on cooling is monotropic and shows an isotropic to blue phase transition between the cholesteric and isotropic phase from the 0% through 20% mixtures. This will be discussed in detail Section 5.3.3. As the 40% mixture is approached there is a noticeable change in $\Delta\varepsilon'$. The mixtures up to 40% are of the most interest because they were reported to have at least one blue phase [59]. As will be seen in Section 5.3.3, at least two blue phases were visually confirmed up to the 20% mixture. If a blue phase exists above 25%, it would be seen in the infrared (which is beyond the capability of the measuring apparatus used). Between the 40% and 60% mixtures, an isotropic to cholesteric phase transition was confirmed both dielectrically and visually. The 100 kHz measurements seemed to have an increasing discontinuity from 0% to the 30% mixture. This may be due to each increase in composition happens to also be closer to resonance, which was around 100 kHz.

On heating in Figure 5.14, both the 10 kHz and 100 kHz measurements show a noticeable discontinuity $\Delta\varepsilon'$ for the mesogenic to isotropic phase transition. The transition on heating is cholesteric to isotropic for all mixtures. The increase in discontinuity for heating measurements are showing a decrease in chirality with the possible loss of a blue phase.

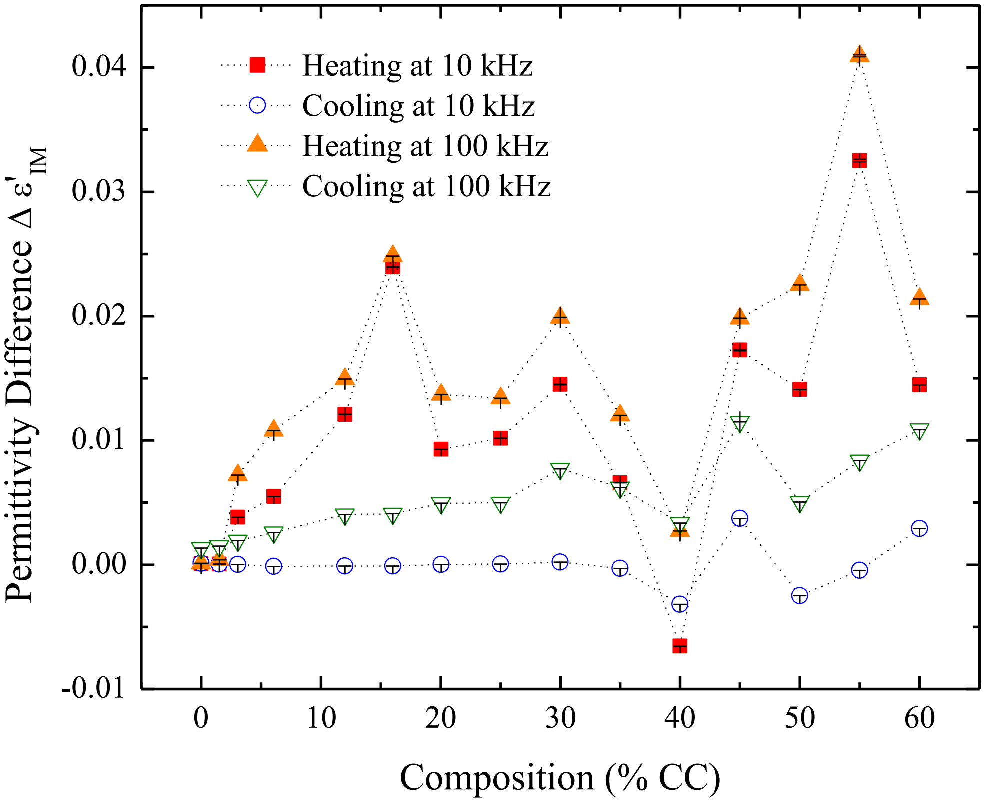

Figure 5.14: This is the estimated discontinuity of the real part of the permittivity at the phase transition.

The estimated discontinuity is $\Delta\varepsilon' = \varepsilon'_{IM} - \varepsilon'_{Mesophase}$ of the real part ε' of the permittivity at the phase transition. The value $\varepsilon''_{Mesophase}$ represents an arbitrary value of the dielectric loss ε'' in any mesogenic phase. The dotted lines are for reference only and are not fits. After the value of ε'_{IM} corresponding to the transition temperature T_{IM} was found, the value below the isotropic phase in the mesophase was chosen:

- For the cooling runs at 10 kHz, the choice generally corresponded to the neighboring data point immediately below ε'_{IM}.
- For the heating runs at 10 kHz as well as all 100 kHz runs, the value chosen in the mesophase, may have been up to two data points removed from ε'_{IM}. That is, looking at Figure 5.4a for the 12% mixture, it is seen that at least one data point immediately below ε'_{IM} occurs within the temperature range at which the transition is still occurring.

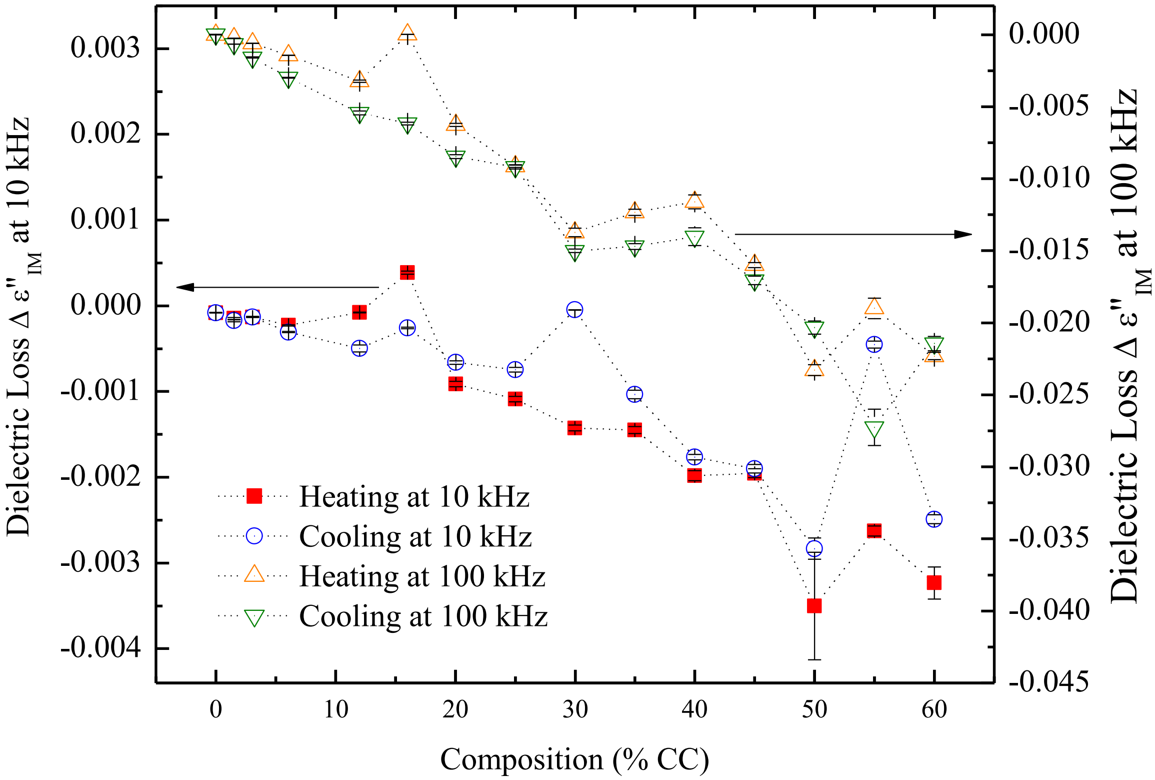

Figure 5.15: The estimated discontinuity of the dielectric loss at the phase transition.

The discontinuity is defined as $\Delta\varepsilon'' = \varepsilon''_{IM} - \varepsilon''_{Mesophase}$. The value $\varepsilon''_{Mesophase}$ represents an arbitrary value of the dielectric loss ε'' in any mesogenic phase. The dotted lines are for reference only and are not fits. After the value of ε''_{IM} was found, the value below the isotropic phase in the mesophase was determined by the corresponding real part $\varepsilon'_{Mesophase}$ discussed in Figure 5.14. At both measuring frequencies as well as on heating and cooling the discontinuity increases. Some of the peaks seen in Figure 5.14 can be seen here. On heating at both 10 kHz and 100 kHz, there is an obvious spike in the discontinuity $\Delta\varepsilon''$ at the 16% composition. On cooling, there is an obvious spike at the 30% composition.

5.3.3 Temperature and Frequency Dependence: Dividing the Data into Four Composition Regions

Section 5.3.3 aims to set the context of the argument with respect to the phase sequence of each sample. The optical microscopy results set this context as they are a direct confirmation of a change in a phase. Each subsection of 5.3.3.1 through 5.3.3.4 will first discuss the optical microscopy results. The frequency and thermal response of the dielectric permittivity will then be discussed. The frequency response is important for determining how near or far a measurement is from a relaxation peak at frequency f_r. The thermal response at two different frequencies will allow for a comparison of how each phase behaves.

Fifteen different mixtures of cholesteryl oleyl carbonate with cholesteryl chloride were studied. Data collection followed the same pattern as for the 12% mixture which was discussed in Section 5.2. Both dielectric and cross-polarized microscopy data were collected.

The amount of data collected was too much to clearly show in only a few graphs. For clarity, the data are split into four manageable regions of three to five mixtures each. For each region, the following will be discussed in order: cross-polarized microscopy observations, frequency dependence, the high frequency (100 kHz) temperature measurements, and the low frequency (10 kHz) temperature measurements.

The discontinuity $\Delta\varepsilon'$ discussed in Section 5.3.2 and presented in Figure 5.14 serves as a reasonable guide to splitting up the data. Region I consists of the 0% through 6% cholesteryl chloride mixtures. Region II consists of the 12% through 30% cholesteryl chloride mixtures in which there is a peak in $\Delta\varepsilon'$ (see Figure 5.14) at the 16% mixture on heating at 10 kHz. Regions III and IV equally consist of the remaining six compositions studied from 35% through 60% cholesteryl chloride. For Region III, there is an extremum at 40% for $\Delta\varepsilon'$ (Figure 5.14) and an discontinuity at 40% for $\Delta\varepsilon''$ (Figure 5.15).

Regions I and II are of primary interest to this dissertation. Not only were blue phases seen in my own measurements, but also they were reported in another study for the range of those regions [59]. Regions III and IV were studied to understand what the phase transition looks like for samples without a blue phase. Additionally, the 55% mixture in Region IV unexpectedly had a narrow cholesteric phase with a thermally wide smectic phase below that.

The cross-polarized microscopy observations helped inform what phases were seen dielectrically. In order to serve as a guide for the discussion in the subsections that follow, the resultant phase diagram from my optical microscopy observations is shown in Figure 5.16. The textures (the resultant photograph taken with cross-polarized microscopy at a given frequency and temperature) associated with a given phase are well known [61]. The identification of those textured from cross-polarized microscopy was assisted with Ingo Dierking's book on liquid crystalline textures [61]. It is beneficial to view the microscopic observations in color.

(a) Phase Diagram on Heating

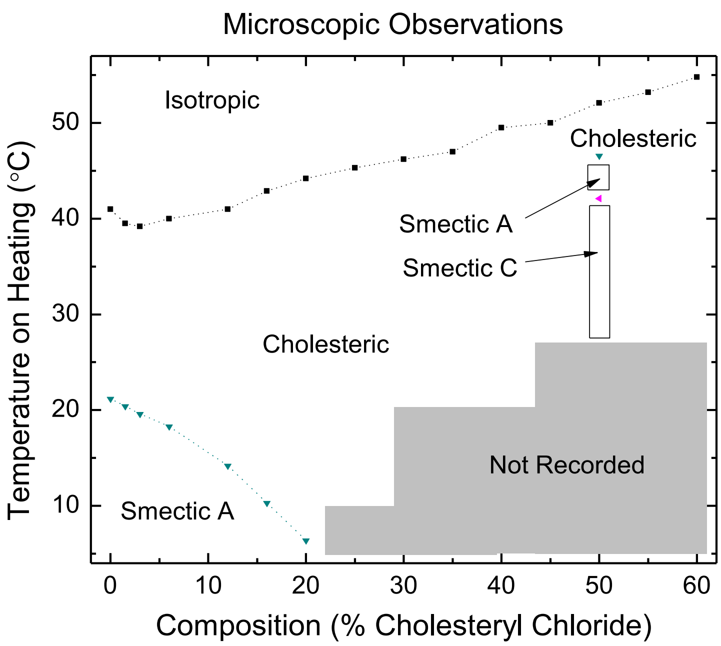

(b) Phase Diagram on Cooling

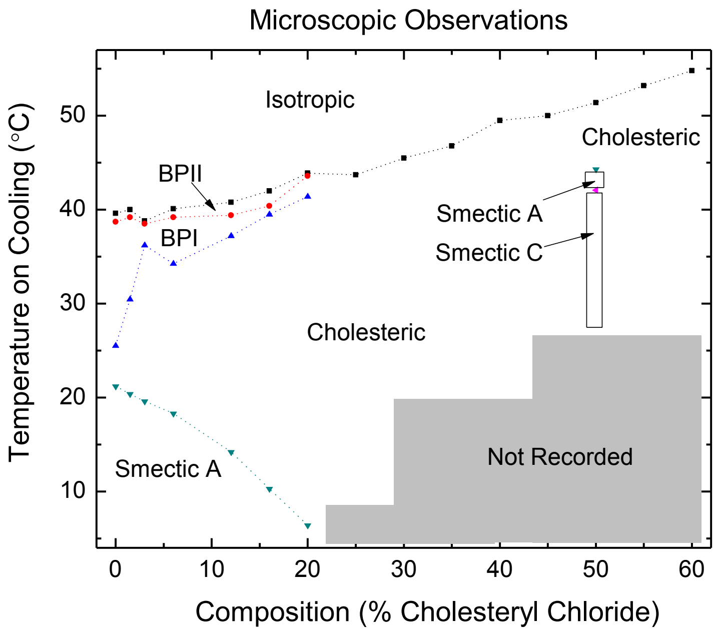

Figure 5.16: Phase diagram from the optical cross-polarized microscopy observations.

The phase diagram from all microscopic observations. As will be seen per region, some of the phases have temperature ranges of coexistence. For clarity, the coexistence regions are not shown in these phase diagram. For the cases of phase coexistence, the onset of the phase is reported as either the phase transition or the point at which one phase dominates over the other in the photographs (which ever was clearer).

5.3.3.1 Region I Results: 0, 1.5, 3, 6% Cholesteryl Chloride

Region I mixtures are highly chiral, meaning they have blue phases which are of primary interest in this dissertation. Figures 5.17 through 5.20 show the optical cross-polarized microscopy images at select temperatures taken for each mixture.

Unmixed cholesteryl oleyl carbonate is the starting point. It is an overall interest to see how its phases evolve as a function of chirality when cholesteryl chloride is increasingly added. Cross-polarized microscopy results are seen for cholesteryl oleyl carbonate in Figure 5.17 with its phase sequence summarized in Table 5.9a. It has a smectic phase around room temperature and below. Figures 5.17c through 5.17f shows the smectic phase winding into a cholesteric phase on heating. At least a blue phase I or II was seen. Cholesteryl oleyl carbonate also has a blue phase III [57]. However, its reflection is in the ultraviolet which are not easily accessible with the setup.

All of Region I has a similar phase sequence to cholesteryl oleyl carbonate. The phase sequences for the 1.5% through 6% mixtures are seen in Figures 5.17 through Figure 5.20 and are summarized in Table 5.9. It is seen, in Table 5.14, that all of Region I is monotropic for the blue phases. Blue phases I and II appear only on cooling. The smectic and cholesteric phases are not monotropic.

The selective reflections of the blue phases and cholesteric phase for Region I follow a pattern. On increasing composition (i.e., decreasing chirality), the selective reflections of the blue phases change. Blue phase II has a selective reflection that increases in wavelength from violet to green. Blue phase I has a selective reflection that increases in wavelength from cyan to yellow. The cholesteric phase (i.e., N*) on increasing composition (whenever it became planar aligned) appears to go from violet to blue. In all cases, an unaligned cholesteric phase appears yellow or tan.

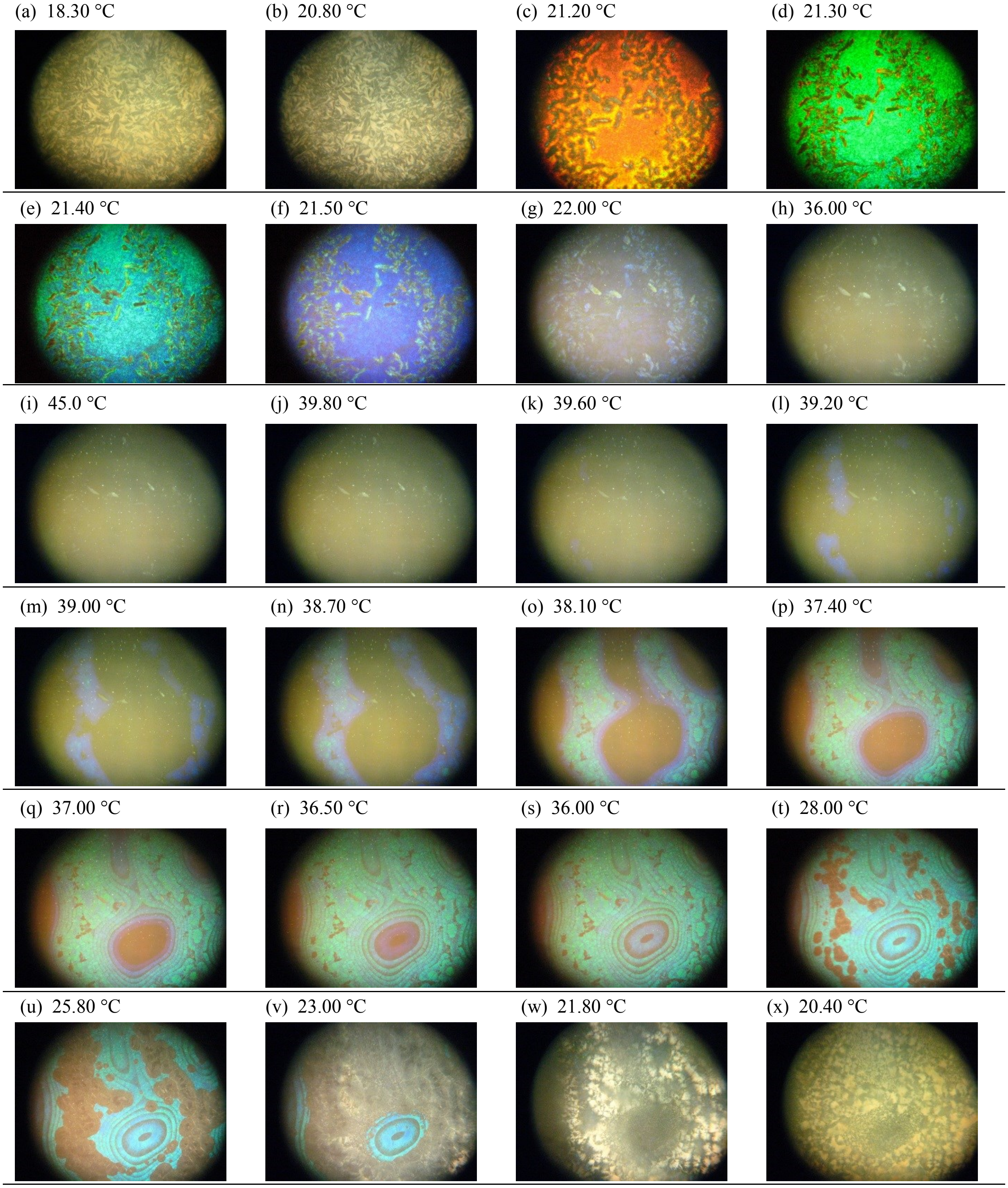

(a) 18.30 °C
(b) 20.80 °C
(c) 21.20 °C
(d) 21.30 °C
(e) 21.40 °C
(f) 21.50 °C
(g) 22.00 °C
(h) 36.00 °C
(i) 45.0 °C
(j) 39.80 °C
(k) 39.60 °C
(l) 39.20 °C
(m) 39.00 °C
(n) 38.70 °C
(o) 38.10 °C
(p) 37.40 °C
(q) 37.00 °C
(r) 36.50 °C
(s) 36.00 °C
(t) 28.00 °C
(u) 25.80 °C
(v) 23.00 °C
(w) 21.80 °C
(x) 20.40 °C

Figure 5.17: Region I optical cross-polarized microscopy images for cholesteryl oleyl carbonate.

Selected images captured under reflectance. Indices (a) through (i) are on heating. Indices (j) through (x) are on cooling. Prior to cooling, the sample was heated a few degrees into the isotropic phase, index (i). The temperature rate did not exceed 0.2 K per minute for temperature changes above room temperature (above 21 °C). The white dots observed in the isotropic phase are dust on the slide and cover slip.

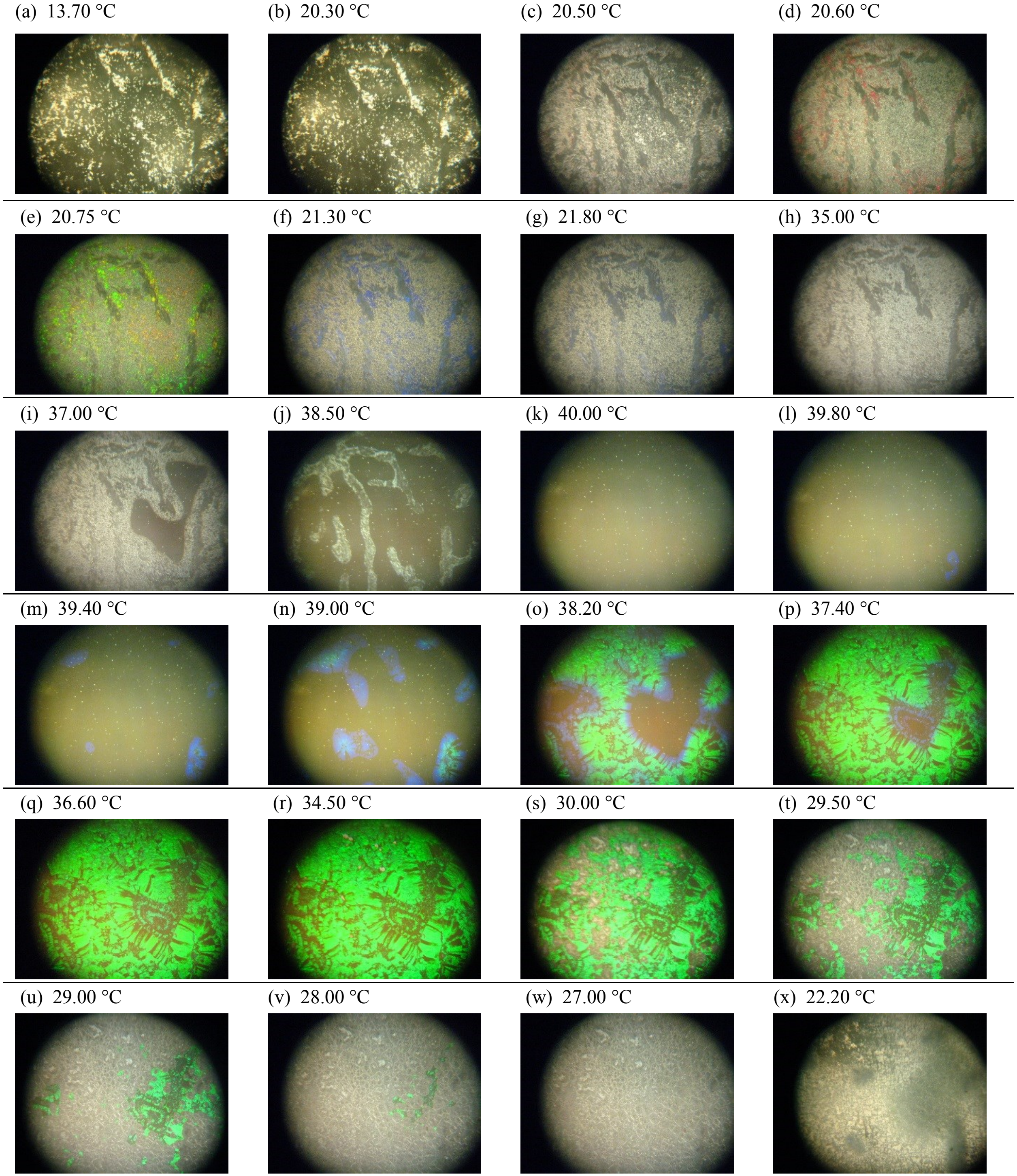

(a) 13.70 °C
(b) 20.30 °C
(c) 20.50 °C
(d) 20.60 °C
(e) 20.75 °C
(f) 21.30 °C
(g) 21.80 °C
(h) 35.00 °C
(i) 37.00 °C
(j) 38.50 °C
(k) 40.00 °C
(l) 39.80 °C
(m) 39.40 °C
(n) 39.00 °C
(o) 38.20 °C
(p) 37.40 °C
(q) 36.60 °C
(r) 34.50 °C
(s) 30.00 °C
(t) 29.50 °C
(u) 29.00 °C
(v) 28.00 °C
(w) 27.00 °C
(x) 22.20 °C

Figure 5.18: Region I optical cross-polarized microscopy images for the mixture 1.5% cholesteryl chloride at select temperautres.

Selected images captured with cross-polarized microscopy under reflectance. Indices (a) through (k) are on heating. Indices (l) through (x) are on cooling. Prior to cooling the sample was heated a few degrees into the isotropic phase. The temperature rate did not exceed 0.2 K per minute for temperature changes above room temperature (above 21 °C). The white dots observed in the isotropic phase are dust on the slide and cover slip.

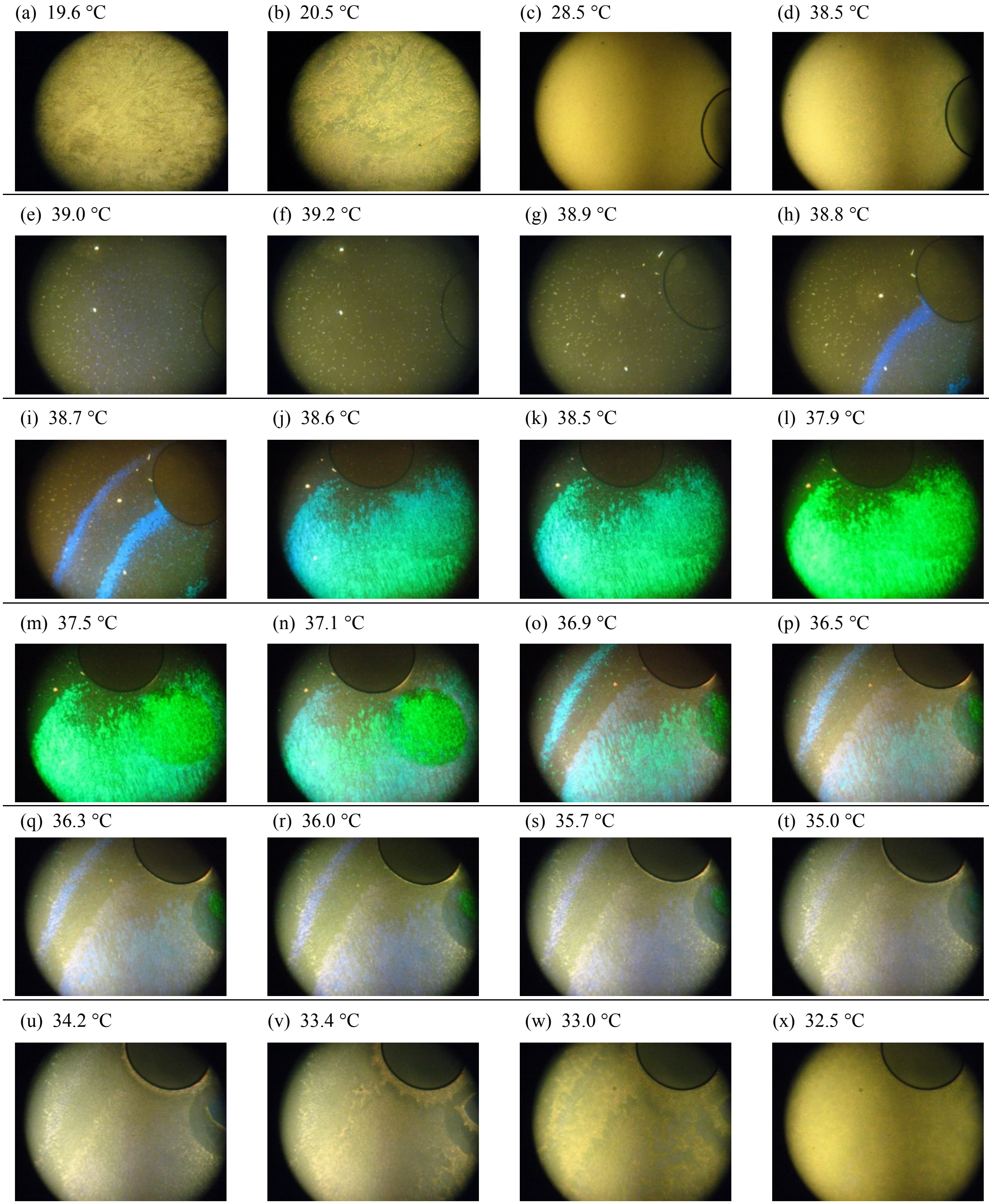

(a) 19.6 °C (b) 20.5 °C (c) 28.5 °C (d) 38.5 °C

(e) 39.0 °C (f) 39.2 °C (g) 38.9 °C (h) 38.8 °C

(i) 38.7 °C (j) 38.6 °C (k) 38.5 °C (l) 37.9 °C

(m) 37.5 °C (n) 37.1 °C (o) 36.9 °C (p) 36.5 °C

(q) 36.3 °C (r) 36.0 °C (s) 35.7 °C (t) 35.0 °C

(u) 34.2 °C (v) 33.4 °C (w) 33.0 °C (x) 32.5 °C

Figure 5.19: Region I optical cross-polarized microscopy images for the mixture 3% cholesteryl chloride at select temperautres.

Selected images captured with cross-polarized microscopy under reflectance. Indices (a) and (b) are from a different cooling/heating run that went below room temperature. Indices (c) through (f) are on heating. Indices (g) through (x) are on cooling. The white dots observed in the isotropic phase are dust on the slide and cover slip. Index (c) is interpreted as the cholesteric phase spontaneously planar aligning prior to the transition into the isotropic phase.

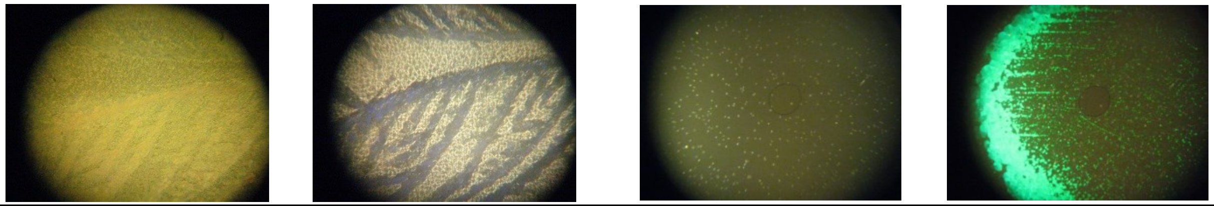
(a) 15.9 °C (b) 21.8 °C (c) 40.2 °C (d) 40.1 °C

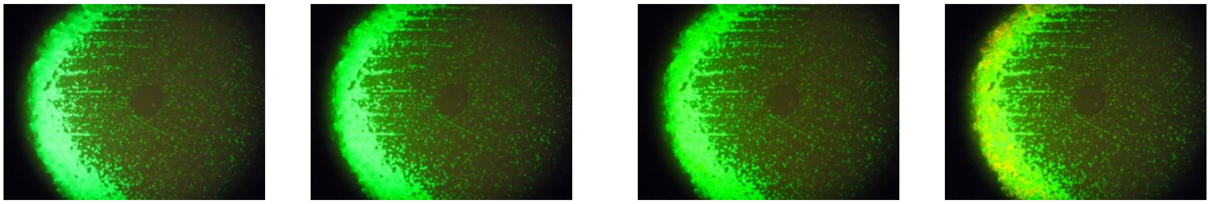
(e) 40.0 °C (f) 39.9 °C (g) 39.7 °C (h) 39.5 °C

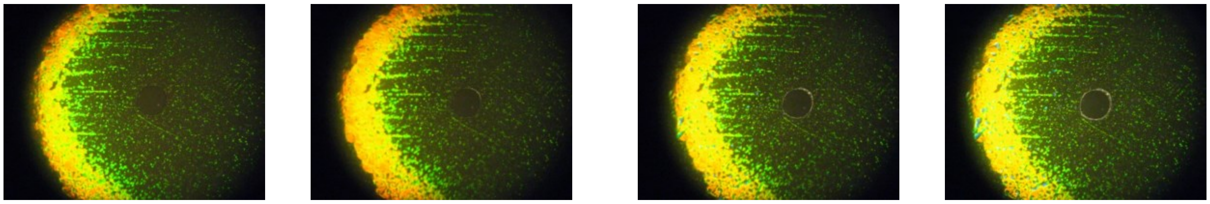
(i) 39.3 °C (j) 39.1 °C (k) 37.1 °C (l) 36.7 °C

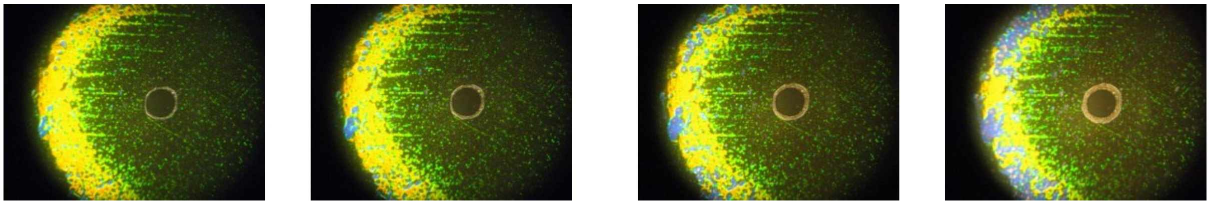
(m) 36.3 °C (n) 35.9 °C (o) 35.5 °C (p) 35.0 °C

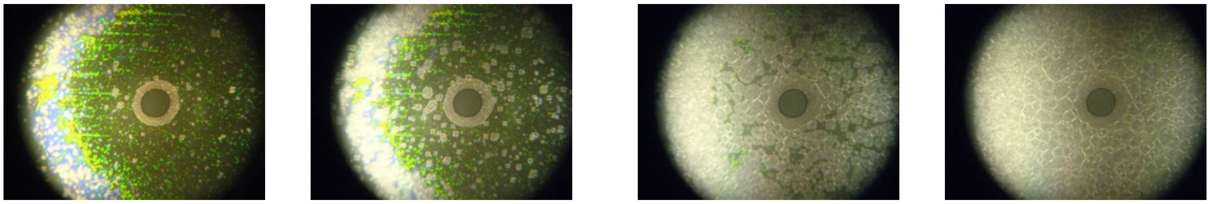
(q) 34.5 °C (r) 34.0 °C (s) 33.0 °C (t) 32.0 °C

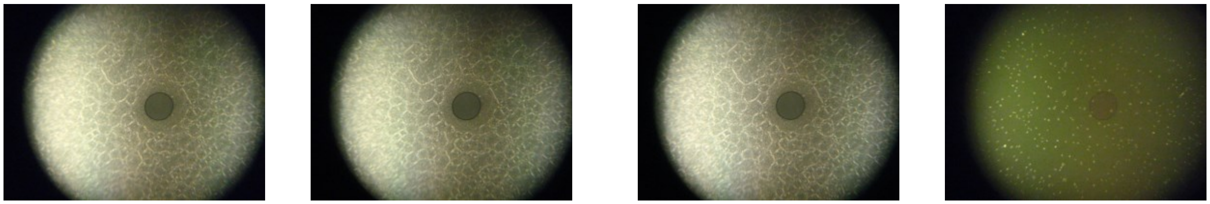
(u) 34.0 °C (v) 36.0 °C (w) 38.0 °C (x) 40.0 °C

Figure 5.20: Region I optical cross-polarized microscopy images for mixture 6% cholesteryl chloride at select temperatures.

Selected images captured with cross-polarized microscopy under reflectance. Indices (a) and (b) are from a different heating/cooling run where the sample was cooled below room temperature. The sample was heated into the isotropic phase prior to taking any photographs after (b). Indices (c) through (t) are on cooling. Indices (u) through (x) are on heating. The white dots observed in the isotropic phase are dust on the slide and cover slip.

Table 5.9: Region I observed phase sequences from optical cross-polarized microscopy.

Blue phases were observed for all of these mixtures on cooling. The color of the associated blue phases is included. For the cholesteric (N*) phase, the color is included on heating since that is where it was observed (i.e., the sample spontaneously planar aligned). On cooling it was randomly aligned.

All of Region I has a smectic phase. Due to the lack of temperature control below 20.0 °C on cooling, the same SmA transition temperature is reported for both cooling and heating for the (d) 3% and (e) 6% mixtures.

(a) 0% mixture	Heating	$\mathrm{SmA} \xrightarrow{21.2\,^\circ\mathrm{C}} \underset{\mathrm{UV?}}{\mathrm{N}^*} \xrightarrow{41.0\,^\circ\mathrm{C}} \mathrm{Isotropic}$
	Cooling	$\mathrm{SmA} \xleftarrow{21.2\,^\circ\mathrm{C}} \mathrm{N}^* \xleftarrow{28.0\,^\circ\mathrm{C}} \vert \quad \vert \xleftarrow{36.5\,^\circ\mathrm{C}} \underset{\mathrm{Violet}}{\mathrm{BPII}} \xleftarrow{39.6\,^\circ\mathrm{C}} \mathrm{Isotropic}$ $\vert \xleftarrow{23.0\,^\circ\mathrm{C}} \underset{\mathrm{Cyan}}{\mathrm{BPI\ ?}} \xleftarrow{38.7\,^\circ\mathrm{C}} \vert$
(b) 1.5% mixture	Heating	$\mathrm{SmA} \xrightarrow{20.4\,^\circ\mathrm{C}} \underset{\mathrm{UV?}}{\mathrm{N}^*} \xrightarrow{39.5\,^\circ\mathrm{C}} \vert$ $\vert \xrightarrow{37.0\,^\circ\mathrm{C}} \mathrm{Isotropic}$
	Cooling	$\mathrm{SmA} \xleftarrow{20.4\,^\circ\mathrm{C}} \mathrm{N}^* \xleftarrow{33.4\,^\circ\mathrm{C}} \vert \quad \vert \xleftarrow{37.5\,^\circ\mathrm{C}} \underset{\mathrm{Blue}}{\mathrm{BPII}} \xleftarrow{40\,^\circ\mathrm{C}} \mathrm{Isotropic}$ $\vert \xleftarrow{27.5\,^\circ\mathrm{C}} \underset{\mathrm{Green}}{\mathrm{BPI}} \xleftarrow{39.2\,^\circ\mathrm{C}} \vert$
(c) 3% mixture	Heating	$SmA \xrightarrow{19.6\,^\circ\mathrm{C}} \underset{\mathrm{Violet}}{\mathrm{N}^*} \xrightarrow{39.0\,^\circ\mathrm{C}} \underset{\mathrm{Violet}}{\mathrm{BPI}} \xrightarrow{39.2\,^\circ\mathrm{C}} \mathrm{Isotropic}$
	Cooling	$\vert \xleftarrow{35.7\,^\circ\mathrm{C}} \underset{\mathrm{Green}}{\mathrm{BPI}} \xleftarrow{38.5\,^\circ\mathrm{C}} \underset{\mathrm{Blue}}{\mathrm{BPII}} \xleftarrow{38.8\,^\circ\mathrm{C}} \mathrm{Isotropic}$ $\mathrm{SmA} \xleftarrow{19.6\,^\circ\mathrm{C}} \mathrm{N}^* \xleftarrow{36.7\,^\circ\mathrm{C}} \vert$
(d) 6% mixture	Heating	$SmA \xrightarrow{18.3\,^\circ\mathrm{C}} \underset{\mathrm{Blue}}{\mathrm{N}^*} \xrightarrow{40.0\,^\circ\mathrm{C}} \mathrm{Isotropic}$
	Cooling	$\vert \xleftarrow{33.0\,^\circ\mathrm{C}} \underset{\mathrm{Green}}{\mathrm{BPII}} \xleftarrow{40.1\,^\circ\mathrm{C}} \mathrm{Isotropic}$ $\vert \xleftarrow{33.0\,^\circ\mathrm{C}} \underset{\mathrm{Yellow}}{\mathrm{BPI}} \xleftarrow{39.2\,^\circ\mathrm{C}} \vert$ $\mathrm{SmA} \xleftarrow{18.3\,^\circ\mathrm{C}} \mathrm{N}^* \xleftarrow{35.5\,^\circ\mathrm{C}} \vert$

The purpose of looking at the frequency response of each mixture was to determine the relaxation frequencies f_r as a function of temperature. This was motivated by the striking difference between the 10 kHz and 100 kHz thermal cycling measurements. It was of interest to see if the 100 kHz probe frequency measurements for thermal cycling were near a relaxation process f_r or in the plateau region (that is, the low frequency region).

Figure 5.21 shows the relaxation frequency at discrete temperatures for Region I. Above the mesogenic to isotropic transition temperature T_{IM} (in Figure 5.21, measurements to the left), all of the mixtures have relaxation processes that are well above 100 kHz. Near and below the transition temperature T_{IM}, all of Region I has a relaxation process f_r near 100 kHz. As discussed in Section 5.2.2 for the representative 12% mixture, the 10 kHz probe measurement was more appropriate for studying the temperature dependence of the static dielectric permittivity. For a given constant frequency measurement, it is important that all temperature measurements are in the plateau frequency region.

The 100 kHz thermal cycling measurements are seen in Figure 5.22. Despite being near the relaxation processes of Region I, there are three useful features to note for both the heating and cooling runs. First, in the isotropic phase, there is a pretransitional curvature near T_{IM} as discussed in Chapters 2 and 4. It is not clear if the pretransitional curvature observed is due to the same mechanism as in Chapter 4. Secondly, the discontinuity from the isotropic phase into the mesophase (or vice versa on heating) is exaggerated in comparison to the 10 kHz measurements seen in Figure 5.23. The transition temperature T_{IM} does not have a frequency dependence. The 100 kHz probe measurements (near a relaxation process) serve as a way of determining where the phase transition is at for the 10 kHz measurements in Figure 5.23 (especially for the cooling runs where a discontinuity is not noticeable). Thirdly, the mesophase measurements fan out versus composition. The slope for each compositions mesophase increases with increasing composition in Region I, distinguishing one phase from another. The 100 kHz measurements serve as a check on the mixture process (so long as they are near the relaxation frequency).

The 10 kHz thermal cycling measurements are seen in Figure 5.23. The pretransitional curvature in the isotropic phase leading to T_{IM} is noticeably absent. This leads to concluding that the mechanism for the curvature in the isotropic phase for the 100 kHz measurement is a frequency dependent viscosity effect while the effect discussed in Section 2.3 and all of Chapter 4 is due to antiparallel dimer formation.

In comparison to the 100 kHz measurements, the mesophase region at 10 kHz (i.e., below T_{IM}) is feature rich. On heating a noticeable first order discontinuity is seen between the cholesteric phase and the isotropic phase. On cooling, as shown in Table 5.9, blue phases are seen between the isotropic and cholesteric phases. As shown in Figures 5.3a for the 12% mixture, as well as for all of Region I in Figure 5.23, the peak on cooling is the mesophase temperature range that corresponds to when the cholesteric phase is fully formed. Between that peak and isotropic phase corresponds to the blue phases. Although not seen under the microscope, I suspect blue phase III corresponds to the almost flat, narrow temperature range below the isotropic phase. Blue phases I and II are not distinguishable with dielectric measurements. Based on microscopic observations this could be due to at least two factors: coexistence of the two blue phases occurring for Region I mixtures, and both are cubic structures which to first approximation are isotropic.

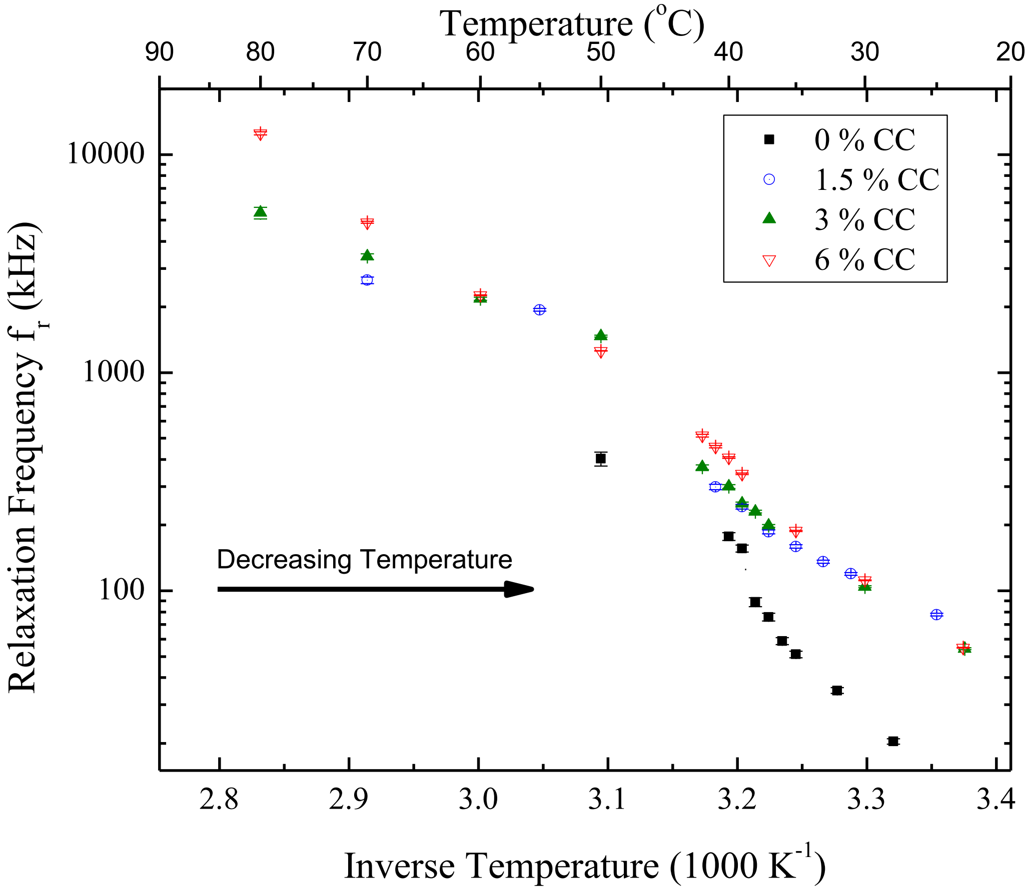

Figure 5.21: Region I temperature dependence of the relaxation frequency f_r.

The frequency f_r is a fitting parameter discussed for the 12% mixture above. Parametrically, it corresponds to the peak of the semicircle discussed in Figure 5.6b. For Region I, the most striking change in the slope of the data is between the 0% and 1.5% cholesteryl chloride mixture. The other three had very similar relaxation processes, with the probe frequency of 10 kHz being sufficiently within the plateau frequency region (i.e., sufficiently outside of the relaxation semicircle).

(a) Heating runs of ε' with an inset of ε''

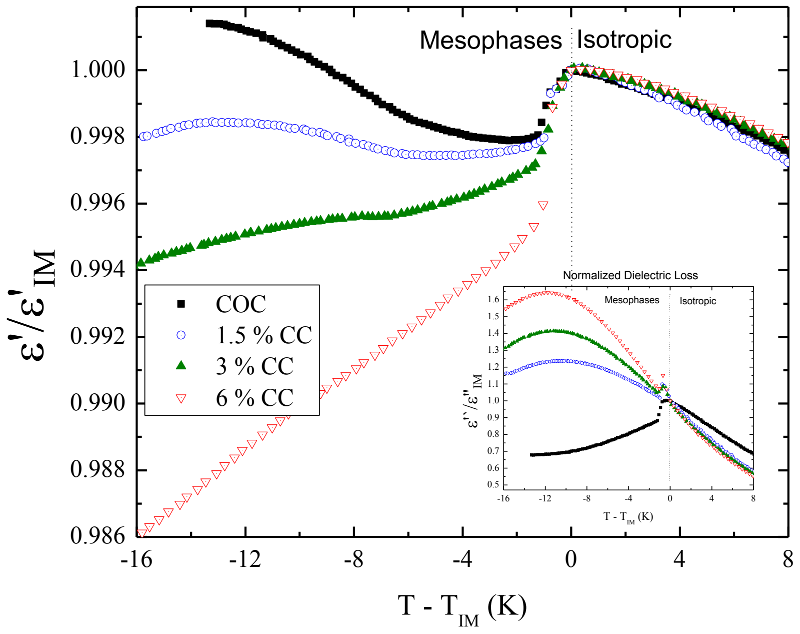

(b) Cooling runs of ε' with an inset of ε''

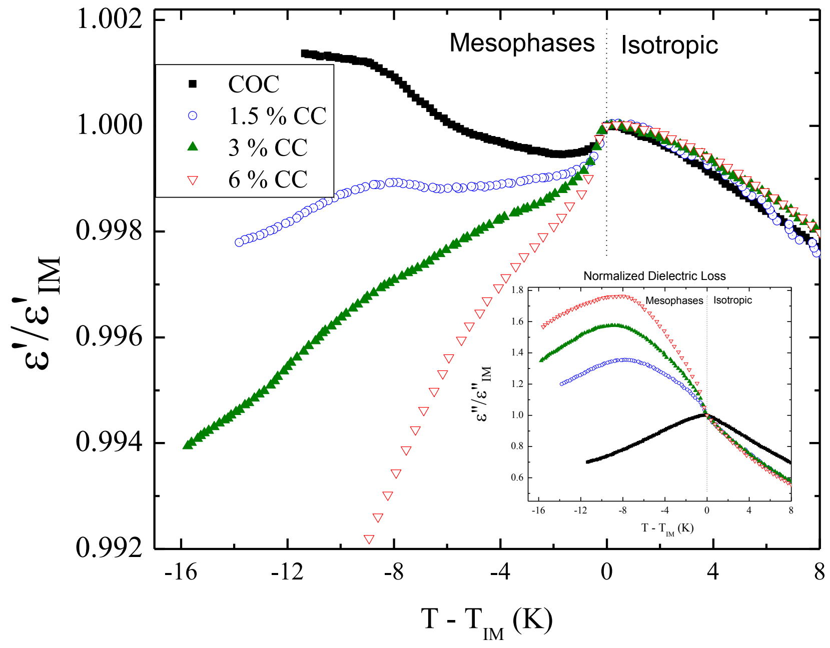

Figure 5.22: Region I permittivity at 100 kHz. At this frequency, a regular pattern of the slope is formed.

(a) Heating runs of ε' with an inset of ε''

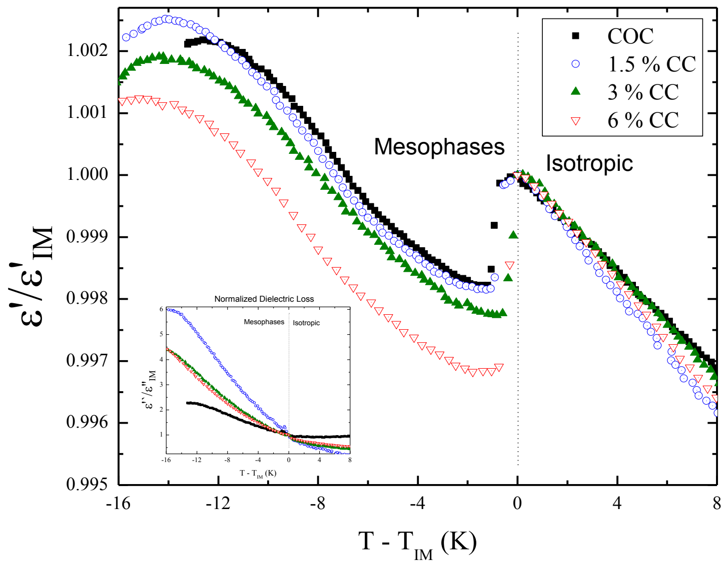

(b) Cooling runs of ε' with an inset of ε''

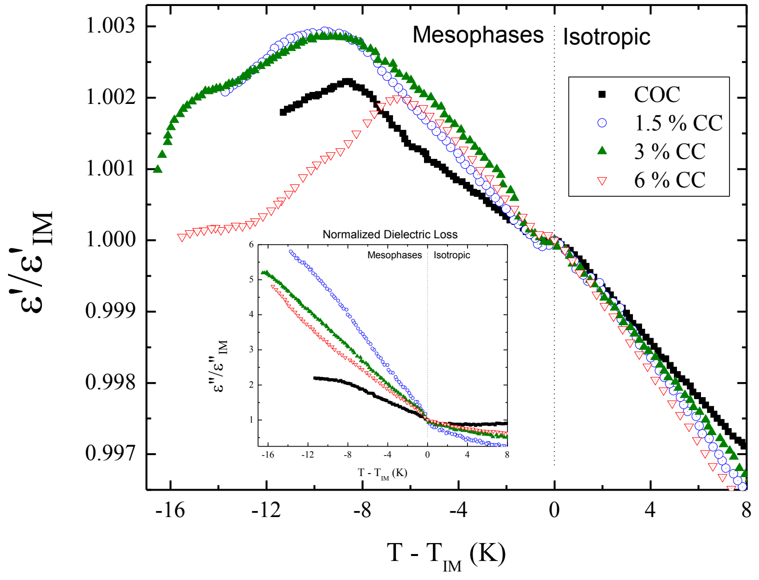

Figure 5.23: Region I permittivity at 10 kHz.

Heating and cooling runs are different. The heating runs in part (a) shows a large discontinuity before entering the isotropic phase. A few data points on heating have a different slope right before entering the highest temperature isotropic phase. There may be a blue phase on heating in the isotropic phase. The cooling runs in part (b) show the possibility of more than one blue phase. Optical microscopy observations corroborate this. Additionally, on increasing chirality, there is a contraction of the width in the mesophase peak.

5.3.3.2 Region II Results: 12, 16, 20, 25, 30% Cholesteryl Chloride

Region II mixtures are also expected to be highly chiral but less chiral than Region I [59]. Figures 5.9 and 5.24 through 5.27 show the cross-polarized microscopy images at select temperatures for each mixture in Region II. Table 5.10 shows the corresponding sequence of phases.

In Figure 5.14, a peak in the discontinuity $\Delta\varepsilon'$ is seen at the 16% mixture. This probably corresponds to a loss of one of the blue phases. The 12%, 16%, and 20% mixtures have monotropic blue phases. The 12% mixture was discussed in Section 5.2.3 with microscopy results shown in Figure 5.9. In addition to blue phase I and II seen in Figure 5.24, the 12% mixture has a blue phase III [57]. The 16% mixture (seen in Figure 5.25) also has a blue phase I and II while the 20% only has a blue phase I (seen in Figure 5.26). Since blue phase III is not directly observed in these measurements, it is probably only blue phase II that is disappearing after the 16% mixture. It is known that blue phase II exists over a limited range of intermediate chirality [3]. At the highest and lowest chirality thresholds (where blue phases can exist), blue phases I and III are allowed to be present [3].

The selective reflections of the blue phases and cholesteric phase in the 12%, 16%, and 20% mixtures continue the same pattern from Region I. On increasing composition, the selective reflection of blue phase II increases from green to red and then disappears by the 20% mixture. Blue phase I has a selective reflection that increases from green to red and disappears by the 25% mixture. The cholesteric phase has a selective reflection that increases from blue for the 12% mixture (Figure 5.9), green at 16% (Figure 5.24), orange at 20% (Figure 5.25), to red at 25% (Figure 5.26).

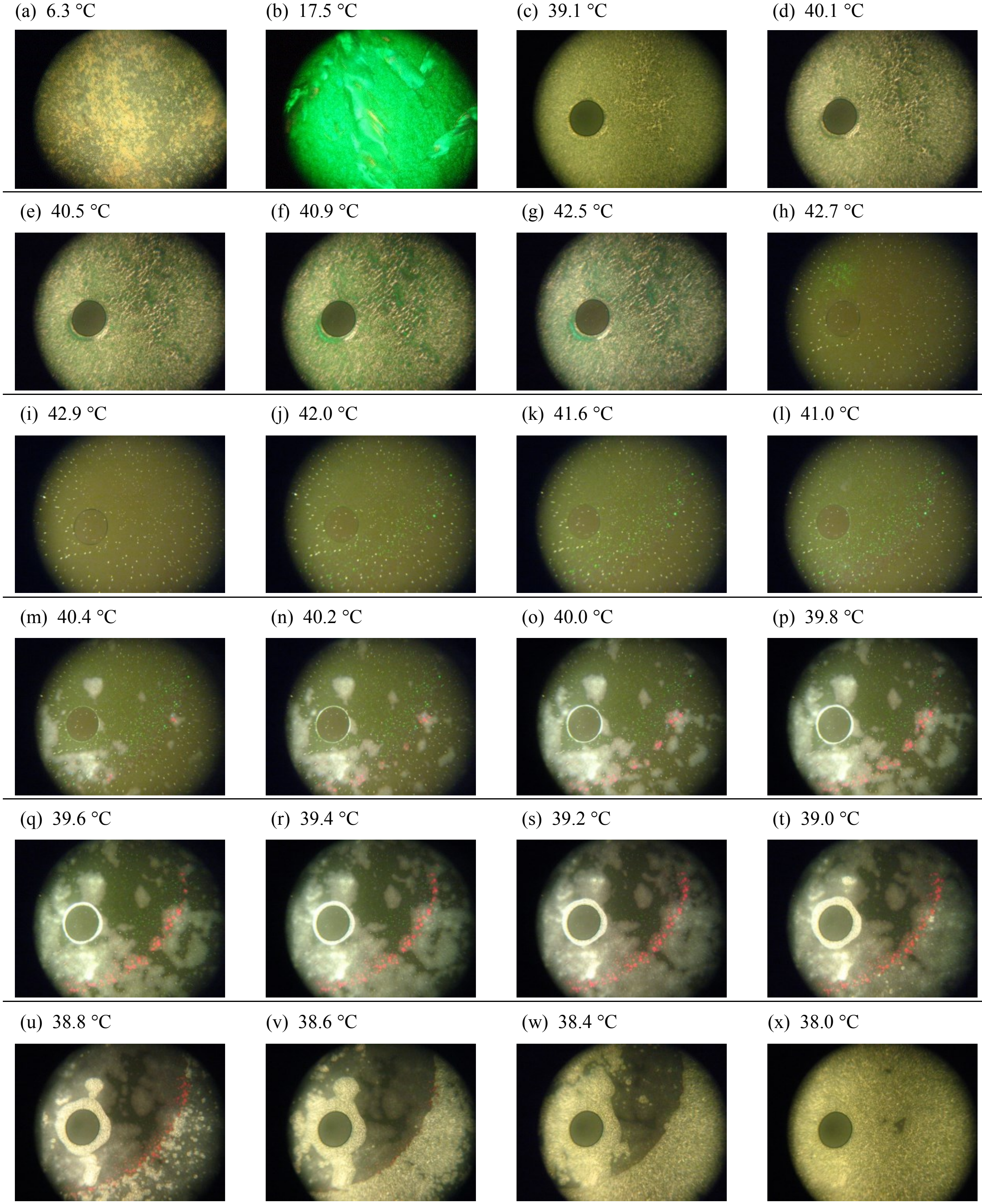

(a) 6.3 °C
(b) 17.5 °C
(c) 39.1 °C
(d) 40.1 °C
(e) 40.5 °C
(f) 40.9 °C
(g) 42.5 °C
(h) 42.7 °C
(i) 42.9 °C
(j) 42.0 °C
(k) 41.6 °C
(l) 41.0 °C
(m) 40.4 °C
(n) 40.2 °C
(o) 40.0 °C
(p) 39.8 °C
(q) 39.6 °C
(r) 39.4 °C
(s) 39.2 °C
(t) 39.0 °C
(u) 38.8 °C
(v) 38.6 °C
(w) 38.4 °C
(x) 38.0 °C

Figure 5.24: Region II optical cross-polarized microscopy images for the 16% cholesteryl chloride mixture at selected temperatures.

Selected images captured with cross-polarized microscopy under reflectance. Indices (a) and (b) are from a different run where the sample was cooled below room temperature. Indices (c) through (i) are on heating. Indices (j) through (x) are on cooling. The white dots observed in the isotropic phase are dust on the slide and cover slip.

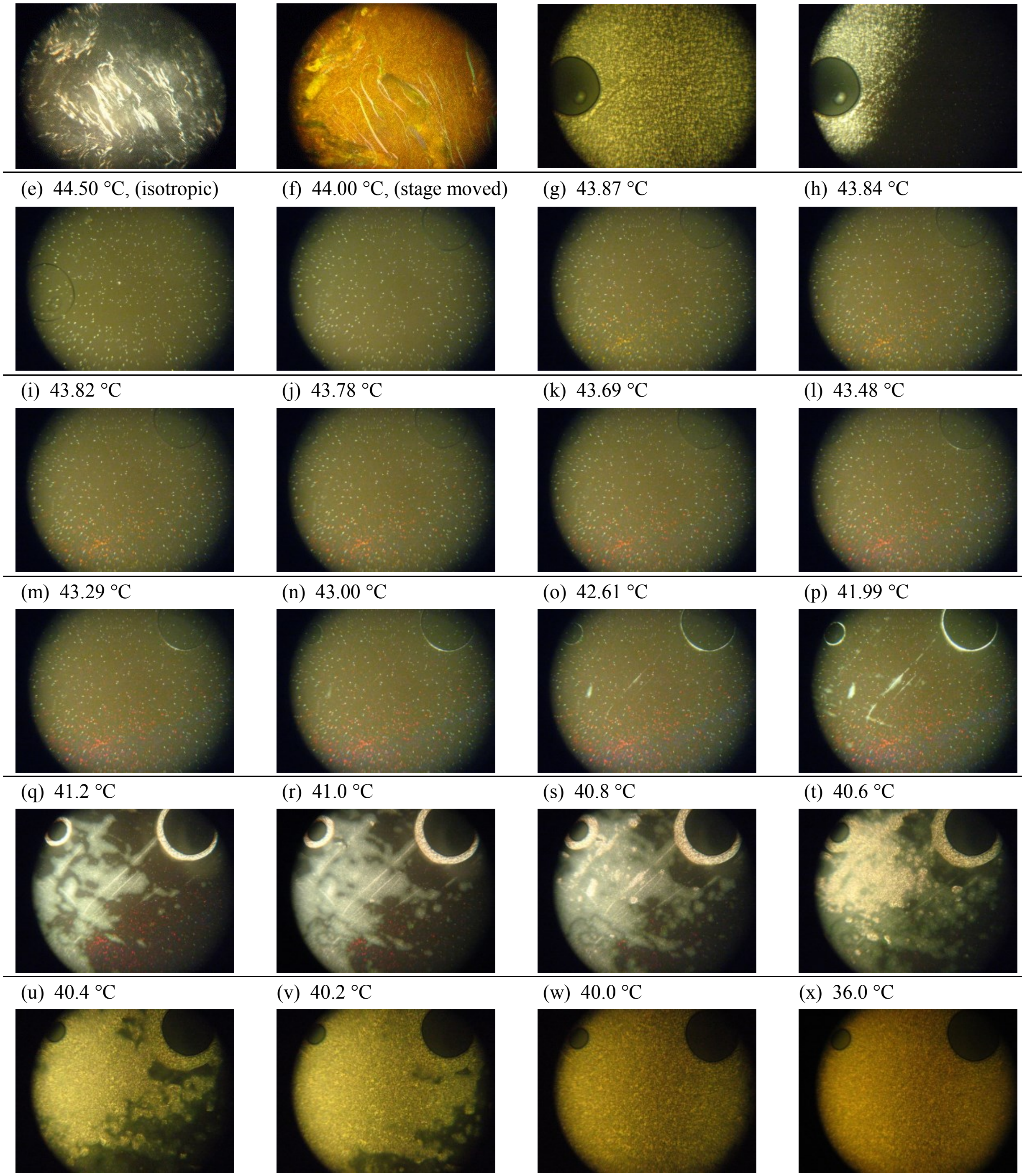

(a) 6.2 °C (b) 14.9 °C (c) 43.80 °C (d) 44.10 °C

(e) 44.50 °C, (isotropic) (f) 44.00 °C, (stage moved) (g) 43.87 °C (h) 43.84 °C

(i) 43.82 °C (j) 43.78 °C (k) 43.69 °C (l) 43.48 °C

(m) 43.29 °C (n) 43.00 °C (o) 42.61 °C (p) 41.99 °C

(q) 41.2 °C (r) 41.0 °C (s) 40.8 °C (t) 40.6 °C

(u) 40.4 °C (v) 40.2 °C (w) 40.0 °C (x) 36.0 °C

Figure 5.25: Region II optical cross-polarized microscopy images for the 20% cholesteryl chloride mixture at selected temperatures.

Images captured under reflectance. Indices (a) and (b) are from a different run where the sample was cooled below room temperature. Indices (c) through (e) are on heating. Indices (f) through (x) are on cooling. The white dots observed in the isotropic phase are dust on the slide and cover slip.

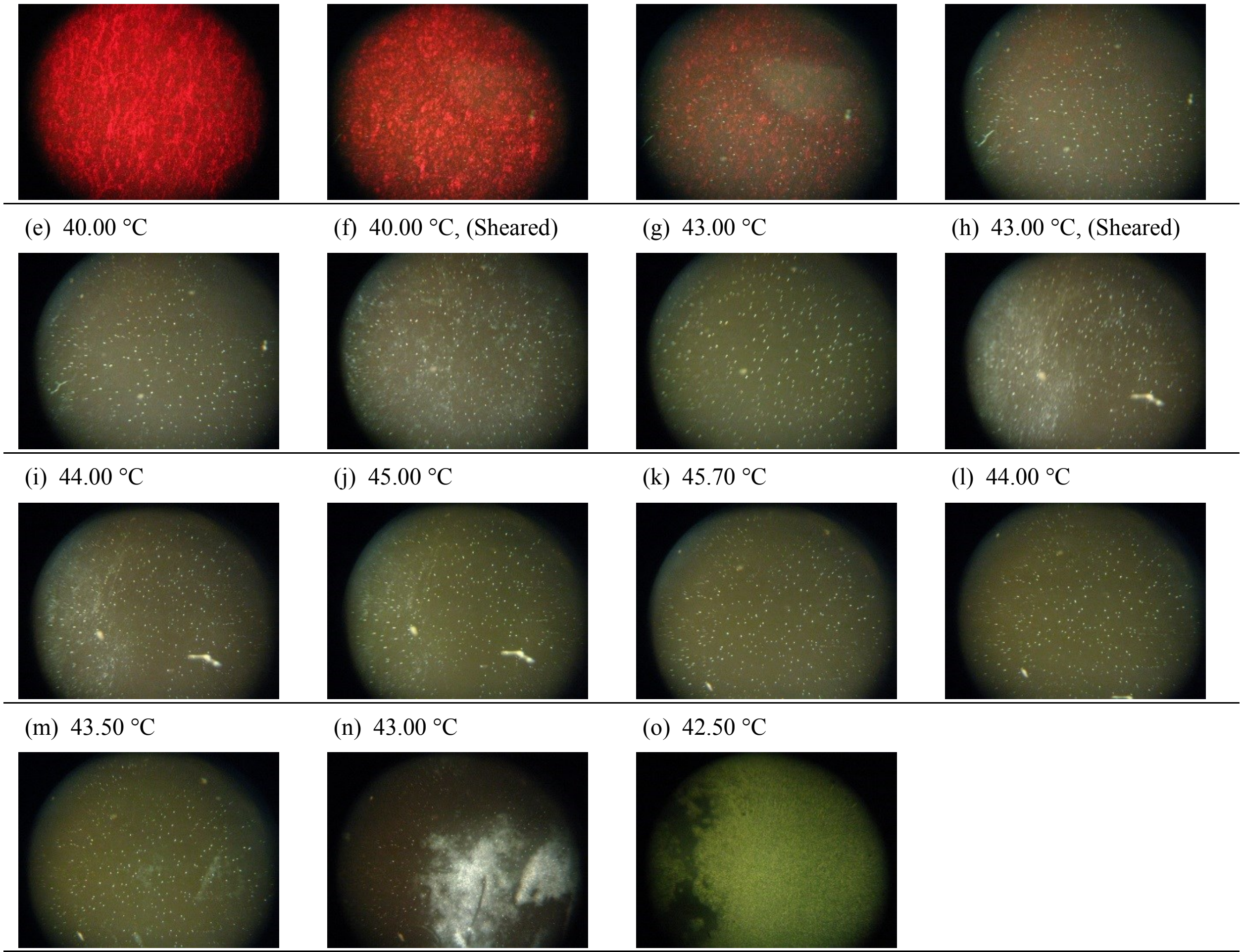

(a) 19.80 °C
(b) 27.50 °C
(c) 30.00 °C
(d) 35.00 °C
(e) 40.00 °C
(f) 40.00 °C, (Sheared)
(g) 43.00 °C
(h) 43.00 °C, (Sheared)
(i) 44.00 °C
(j) 45.00 °C
(k) 45.70 °C
(l) 44.00 °C
(m) 43.50 °C
(n) 43.00 °C
(o) 42.50 °C

Figure 5.26: Region II optical cross-polarized microscopy images for the 25% cholesteryl chloride mixture at selected temperautres**.**

Images captured under reflectance. Indices (a) through (k) are on heating. Indices (l) through (x) are on cooling. The temperature rate did not exceed 0.2 K per minute for temperature changes above room temperature (above 21 °C). The white dots observed in the isotropic phase are dust on the slide and cover slip. For index (k), the stage was bumped slightly so the image location is different. Prior to image (l), the system was heated to 44 °C.

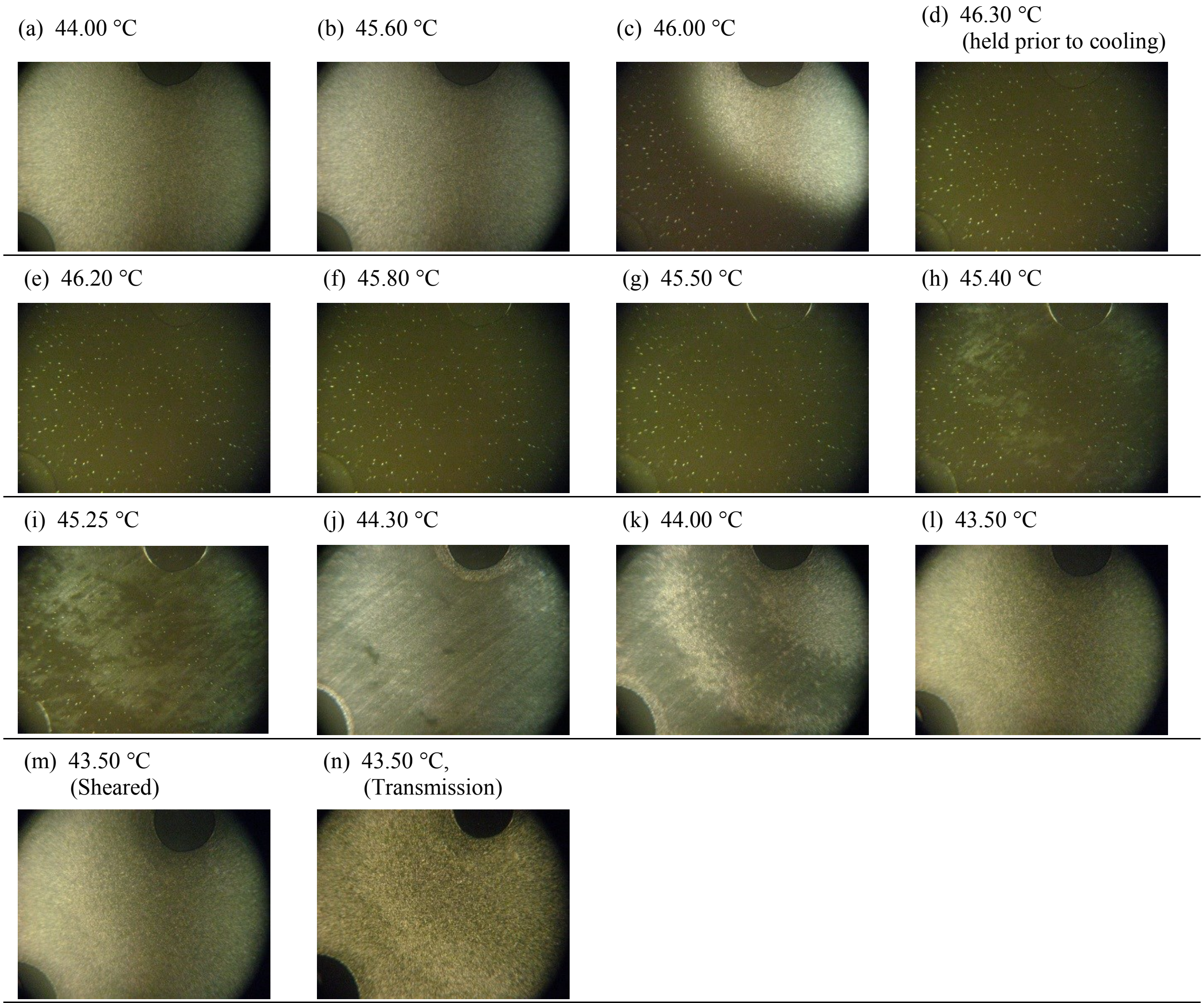

(a) 44.00 °C

(b) 45.60 °C

(c) 46.00 °C

(d) 46.30 °C
(held prior to cooling)

(e) 46.20 °C

(f) 45.80 °C

(g) 45.50 °C

(h) 45.40 °C

(i) 45.25 °C

(j) 44.30 °C

(k) 44.00 °C

(l) 43.50 °C

(m) 43.50 °C
(Sheared)

(n) 43.50 °C,
(Transmission)

Figure 5.27: Region II optical cross-polarized microscopy images for the 30% cholesteryl chloride mixture at selected temperatures.

All images are on reflectance unless otherwise noted. Indices (a) through (d) are on heating. Indices (e) through (n) are on cooling. The temperature rate did not exceed 0.2 K per minute for temperature changes above room temperature (above 21 °C). The white dots observed in the isotropic phase are dust on the slide and cover slip. For index (d), the temperature was held for 10 minutes prior to cooling. After index (l), the sample was sheared to see if the samples alignment changed.

Table 5.10: Region II phase sequences from optical cross-polarized microscopy for the 12% through 30% cholesteryl chloride mixtures.

Blue phases and a smectic phase were observed for (a) the 12%, (b) the 16%, and (c) the 20% mixtures. The color for the associated blue phases are included. Neither blue phases nor smectic phases were observed in (d) the 25% mixture and (e) the 30% mixture down to 6 °C.

For the 25% and 30% mixtures are increasingly less chiral then the previous mixtures. This means that, for the cholesteric phase, the wavelength of the selective reflectance is increasing. Since the 25% mixture has an aligned cholesteric that is red, it stands to reason that the 30% is in the infrared.

Due to the limited temperature control on cooling below 20.0 °C, the same SmA transition temperature is reported for both cooling and heating for the (d) 3% and (e) 6% mixtures. The lowest attainable temperature for the experimental setup ranged between 5.5 °C and 12 °C.

(a) 12% mixture	Heating	$SmA \xrightarrow{14.2\,^{\circ}\mathrm{C}} \underset{\text{Blue}}{\mathrm{N}^*} \xrightarrow{41.0\,^{\circ}\mathrm{C}} \text{Isotropic}$
	Cooling	$\vert \xleftarrow{36.5\,^{\circ}\mathrm{C}} \underset{\text{Green}}{\text{BPI}} \xleftarrow{39.4\,^{\circ}\mathrm{C}} \underset{\text{Red}}{\text{BPII}} \xleftarrow{40.8\,^{\circ}\mathrm{C}} \text{Isotropic}$ $\text{SmA} \xleftarrow{14.2\,^{\circ}\mathrm{C}} \mathrm{N}^* \xleftarrow{37.6\,^{\circ}\mathrm{C}} \vert$
(b) 16% mixture	Heating	$\text{SmA} \xrightarrow{10.3\,^{\circ}\mathrm{C}} \underset{\text{Green}}{\mathrm{N}^*} \xrightarrow{42.9\,^{\circ}\mathrm{C}} \text{Isotropic}$
	Cooling	$\vert \xleftarrow{38.6\,^{\circ}\mathrm{C}} \underset{\text{Green}}{\text{BPII}} \xleftarrow{42.5\,^{\circ}\mathrm{C}} \text{Isotropic}$ $\vert \xleftarrow{38.6\,^{\circ}\mathrm{C}} \underset{\text{Red}}{\text{BPI}} \xleftarrow{40.4\,^{\circ}\mathrm{C}} \vert$ $\text{SmA} \xleftarrow{10.3\,^{\circ}\mathrm{C}} \mathrm{N}^* \xleftarrow{40.4\,^{\circ}\mathrm{C}} \vert$
(c) 20% mixture	Heating	$SmA \xrightarrow{6.4\,^{\circ}\mathrm{C}} \underset{\text{Orange}}{\mathrm{N}^*} \xrightarrow{44.2\,^{\circ}\mathrm{C}} \text{Isotropic}$
	Cooling	$\vert \xleftarrow{40.6\,^{\circ}\mathrm{C}} \underset{\text{Red}}{\text{BPI}} \xleftarrow{43.9\,^{\circ}\mathrm{C}} \text{Isotropic}$ $\text{SmA} \xleftarrow{6.4\,^{\circ}\mathrm{C}} \mathrm{N}^* \xleftarrow{41.8\,^{\circ}\mathrm{C}} \vert$
(d) 25% mixture	Heating	$\underset{\text{Red}}{\mathrm{N}^*} \xrightarrow{45.3\,^{\circ}\mathrm{C}} \text{Isotropic}$
	Cooling	$\mathrm{N}^* \xleftarrow{43.7\,^{\circ}\mathrm{C}} \text{Isotropic}$
(e) 30% mixture	Heating	$\underset{\text{IR?}}{\mathrm{N}^*} \xrightarrow{46.2\,^{\circ}\mathrm{C}} \text{Isotropic}$
	Cooling	$\mathrm{N}^* \xleftarrow{45.5\,^{\circ}\mathrm{C}} \text{Isotropic}$

The 25% and 30% mixtures were different. Blue phases I and II were not seen at the 25% mixture and above. Only an isotropic-cholesteric phase transition was observed. Based on the literature, it is possible that blue phase III still exists up to 30%, although it was not observed in any of my measurements [59].

Figure 5.28 follows the same frequency dependence trend as Region I, seen in Figure 5.21. For measurements in the isotropic phase, Region II has relaxation processes that are well above 100 kHz. In the mesophases, all of the relaxation processes are near 100 kHz for the temperature range studied.

The 100 kHz thermal cycling measurements are seen in Figure 5.29. As in Region I the mesophases fan out as composition is increased. However, the 16% mixture on heating noticeably stands out. Also, the dielectric measurements of the 25% and 30% mixtures runs appear almost identical when normalized. Differences are observed by looking at the magnitudes of transition temperatures T_{IM} (see Table 5.6), the permittivity ε'_{IM} (see Table 5.7), and the 10 kHz measurements (see Figure 5.30).

The 10 kHz thermal cycling measurements are seen in Figure 5.30. The heating and cooling runs follow the same pattern as in Region I with the exception of the 16% mixture having a large relative discontinuity. Also, on cooling, note the peak in the mesophase. The temperature width between the peak and the isotropic to mesogenic phase transition temperature T_{IM} decreases with increasing composition. That is to say, the temperature range of the blue phases decreases. The one exception is the 16% mixture. From Figure 5.14, the discontinuity $\Delta\varepsilon'$ on heating for the 16% mixture is higher relative to the adjacent compositions. On cooling at 10 kHz, the range between the isotropic phase and the peak in the mesophase dramatically narrows. A blue phase is lost and the chirality decreases.

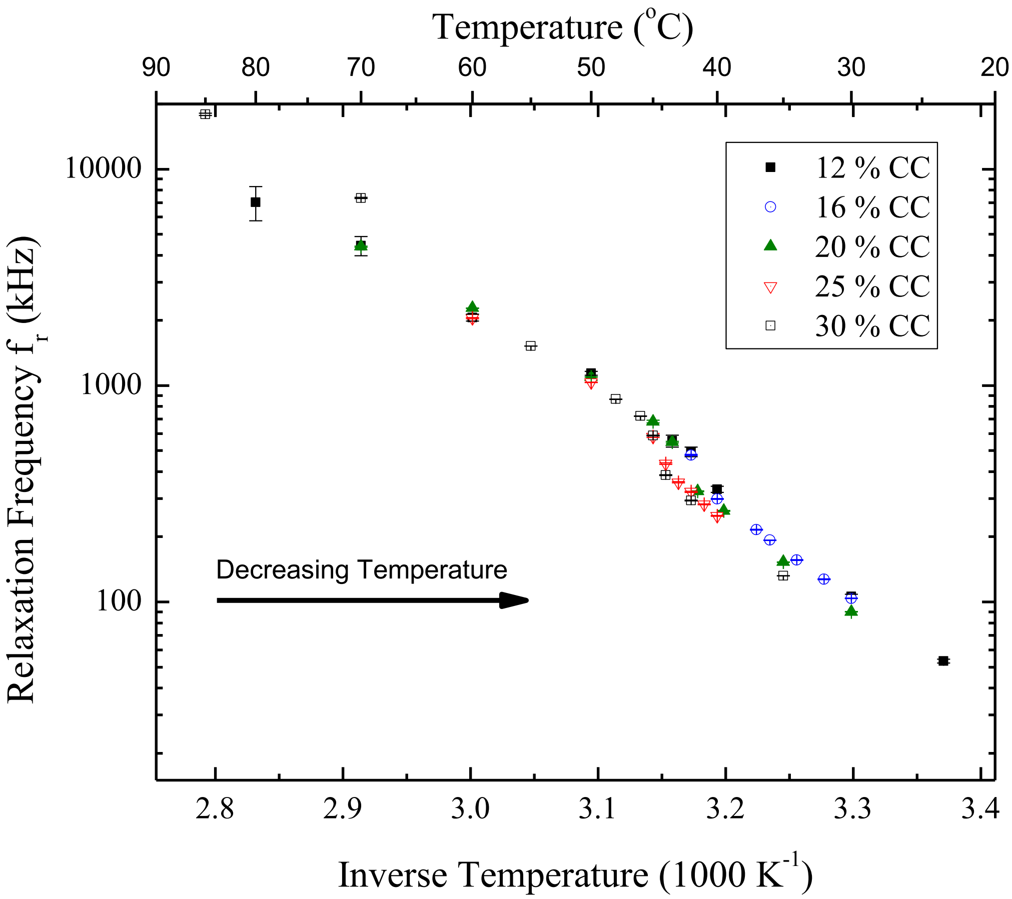

Figure 5.28: Region II temperature dependence of the relaxation frequency.

The relaxation frequency f_r is a fitting parameter that was discussed for the 12% mixture above. Parametrically, it corresponds to the peak of the semicircle shown in Figure 5.6 for the 12% mixture.

For Region II, the relaxation processes are nearly identical. Only the phase transition temperature f_r seems to change. The lowest temperature relaxation process had a frequency of 53.3 kHz. However, most temperatures of interest (i.e., near the blue phases and transition to/from the isotropic phase) were above 30 °C. By 30 °C the relaxation process was near 90.0 kHz. Near the phase transitions, the relaxation frequencies ranged from 282.5 kHz to 385.6 kHz. The probing frequency of 100 kHz was well within a relaxation processes. From the raw data (not shown), there is a hint of a higher frequency relaxation process above the measuring capabilities of the instrument (i.e., $f > 1$ MHz).

The relaxation frequency increases with increasing temperature. For both the mesophases and the isotropic phase, the processes appear mostly Arrhenius. Arrhenius behavior means that, on a log versus inverse temperature plot, the data form straight lines. This corresponds to a single relaxation process.

(a) Heating runs of ε' with an inset of ε''

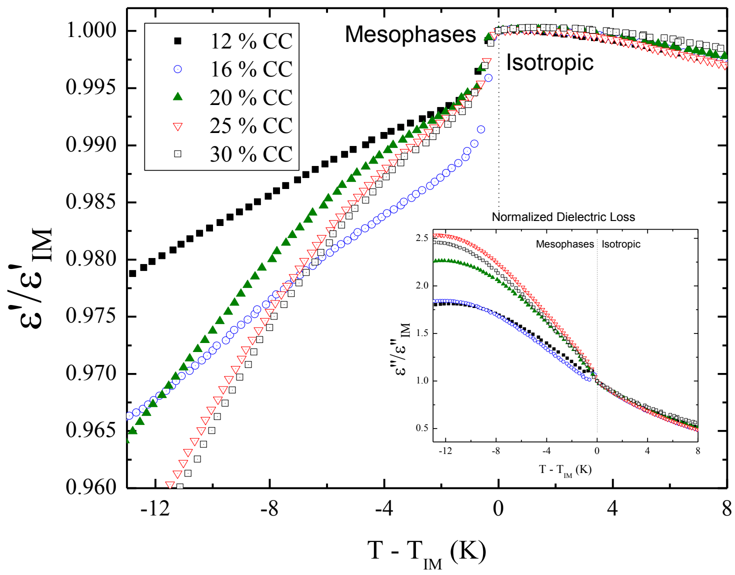

(b) Cooling runs of ε' with an inset of ε''

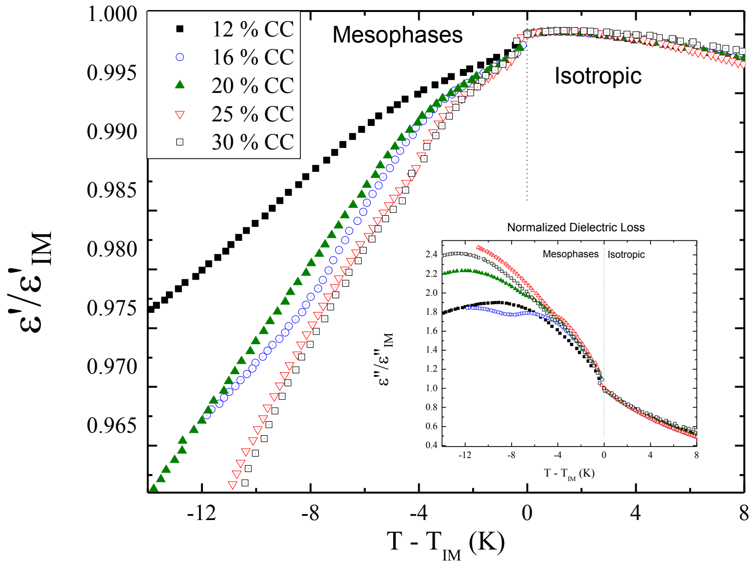

Figure 5.29: Region II permittivity at 100 kHz.

On both heating and cooling, the 12% and 16% mixtures continue the fanning out pattern (with a decreasing slope on increasing percent composition) seen in Figure 5.22. However, by the 20% mixture, the relative slope abruptly increases and then decreases at 25%. This abrupt change beyond the 16% mixture could be due to a combination of both a decrease in chirality and the loss of preferential allignment in the dielectric cell.

(a) Heating of ε' with an inset of ε''

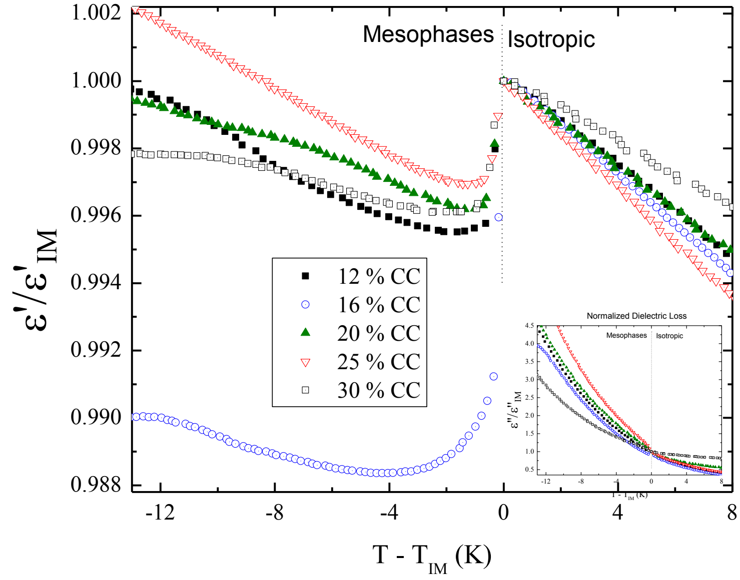

(b) Cooling of ε' with an inset of ε''

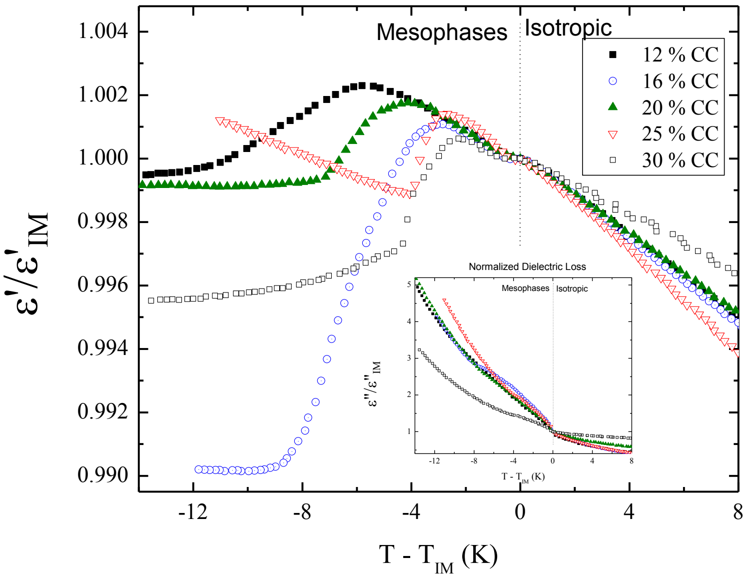

Figure 5.30: Region II permittivity at 10 kHz.

On heating in part (a) the 12% and 16% mixtures continue the pattern of increasing discontinuity $\Delta\varepsilon'$ with increasing percent composition from Region I seen in Figure 5.23a. Beyond the 16% mixture, $\Delta\varepsilon'$ begins to decrease. This abrupt change beyond the 16% mixture could be due to a combination of both a decrease in chirality and a loss of a blue phase. The cooling run in part (b) continues the trend from Region I seen in Figure 5.23b in which the width of the mesophase peak decreases on decreasing chirality. This hump which is decreasing in width in the mesophase region is at least one blue phase.

5.3.3.3 Region III Results: 35, 40, 45% Cholesteryl Chloride

Based on McKinnon et. al. (see Figure 5.10), Region III mixtures are expected to mark the range in which the blue phases disappear, leaving a less chiral system with only an isotropic to cholesteric phase transition [59]. The cross-polarized microscopy observations seen in Figure 5.31 only show a cholesteric to isotropic phase transition on both heating and cooling. The phase sequence for Region III is shown in Table 5.11.

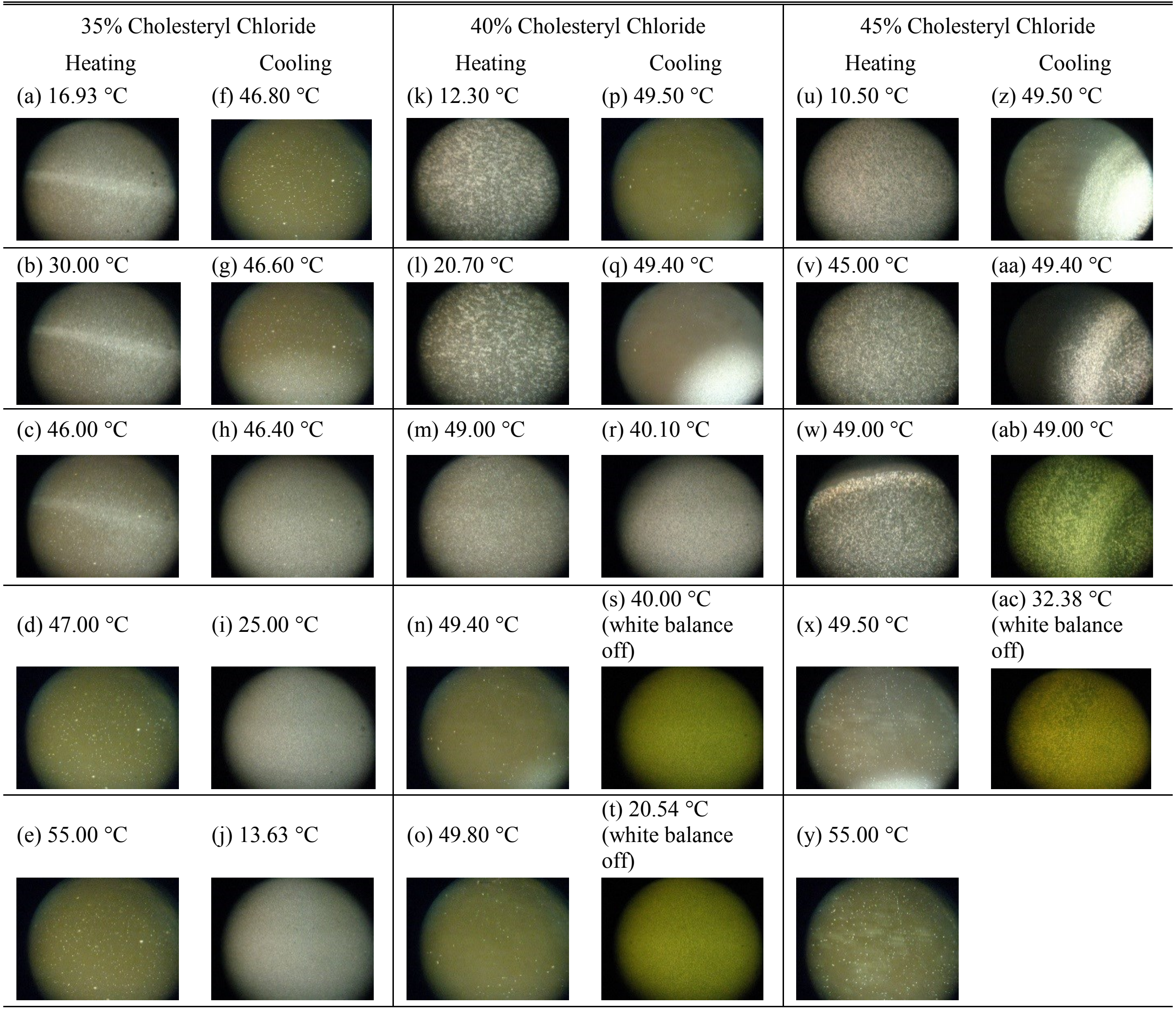

35% Cholesteryl Chloride		40% Cholesteryl Chloride		45% Cholesteryl Chloride	
Heating	Cooling	Heating	Cooling	Heating	Cooling
(a) 16.93 °C	(f) 46.80 °C	(k) 12.30 °C	(p) 49.50 °C	(u) 10.50 °C	(z) 49.50 °C
(b) 30.00 °C	(g) 46.60 °C	(l) 20.70 °C	(q) 49.40 °C	(v) 45.00 °C	(aa) 49.40 °C
(c) 46.00 °C	(h) 46.40 °C	(m) 49.00 °C	(r) 40.10 °C	(w) 49.00 °C	(ab) 49.00 °C
(d) 47.00 °C	(i) 25.00 °C	(n) 49.40 °C	(s) 40.00 °C (white balance off)	(x) 49.50 °C	(ac) 32.38 °C (white balance off)
(e) 55.00 °C	(j) 13.63 °C	(o) 49.80 °C	(t) 20.54 °C (white balance off)	(y) 55.00 °C	

Figure 5.31: Region III optical microscopy images for the 35%, 40%, and 45% cholesteryl chloride mixtures at selected temperatures.

Images shown are under reflectance as transmission microscopy results gave no new information. For all three samples heating was performed from below room temperature prior to cooling. The temperature rate did not exceed 0.2 K per minute for temperature changes above room temperature (above 21 °C). The white dots observed in the isotropic phase are dust on the slide and cover slip.

Table 5.11: Region III transition temperatures between the isotropic and cholesteric phases for the 35%, 40%, and 45% cholesteryl chloride mixtures.

Neither blue phases nor smectic phases were observed for room temperature and above. The only phase transition observed was cholesteric to isotropic.

Composition	Heating	Cooling
35%	47.0 °C	46.8 °C
40%	49.5 °C	49.5 °C
45%	50.0 °C	50.0 °C

If a blue phase does exist for the 35%, 40%, or 45% mixtures, either then it is very narrow or it has a Bragg peak in the infrared that is beyond the capability of the measuring apparatus used. A Bragg peak in the infrared can be supported by extrapolating the wavelength shift of the blue phase Bragg peaks observed for 0% through 20% cholesteryl chloride (refer to the phase sequences shown in Tables 5.9 and 5.10).

Along with the microscopic observations, Region III mixtures have almost the same relaxation frequency dependence, seen in Figure 5.32. However, in comparison to Regions I and II, the relaxation frequency around the isotropic to cholesteric phase transition is higher than 100 kHz. In Figure 5.33, the 100 kHz thermal cycling measurements are almost identical with the main difference being the discontinuity at the phase transition.

The differences amongst the three are seen in the 10 kHz thermal cycling measurements, seen in Figure 5.34. On heating and cooling, the 35% and 45% mixtures have very similar temperature dependence. However, again on both heating and cooling, the 40% composition is drastically different below the isotropic phase. As seen in Figure 5.14, there is a dramatic change in the discontinuity $\Delta\varepsilon'$ of the isotropic to mesogenic phase transition. Mixtures between 45% and 80% are expected to be the least chiral with somewhere lying within that range being mostly achiral nematic [59].

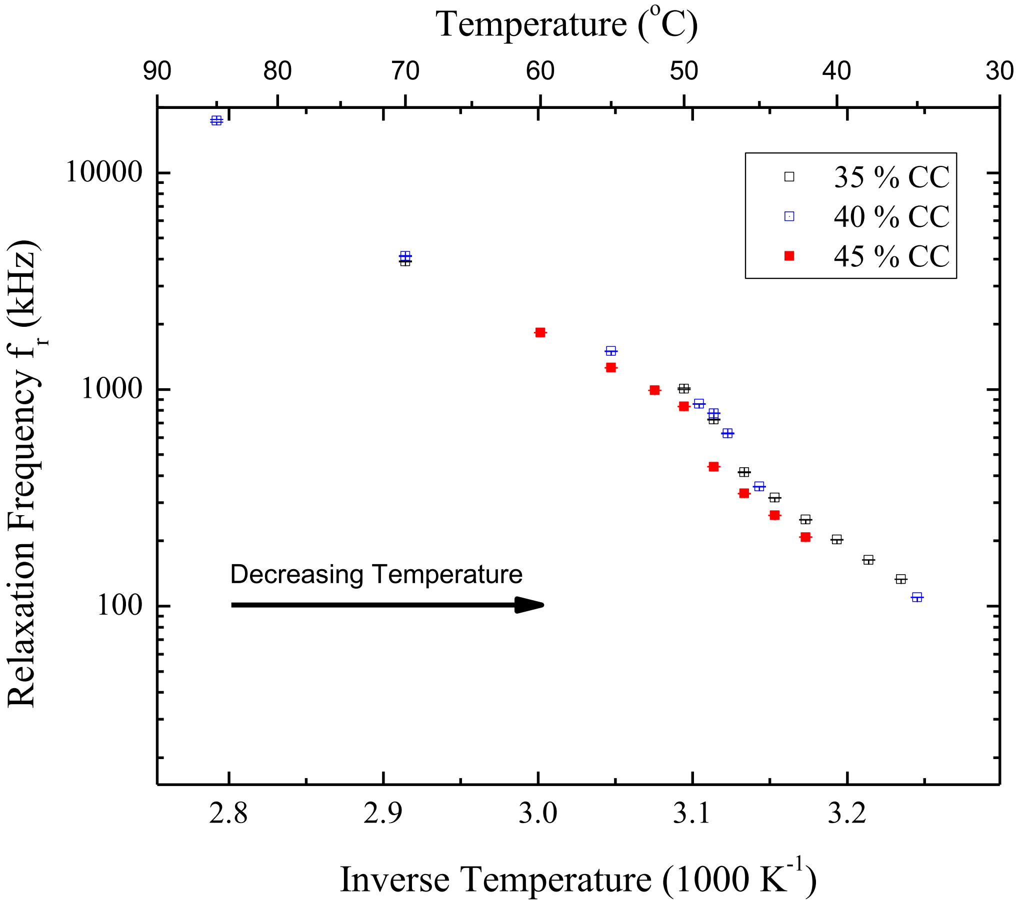

Figure 5.32: Region III temperature dependence of the relaxation frequency.

The relaxation frequency f_r is a fitting parameter that was discussed for the 12% mixture above. Parametrically, it corresponds to the peak of the semicircle discussed in Figure 5.6 for the 12% mixture. Standard errors are shown.

For Region III, as with Region II, the relaxation processes are nearly identical. Only the phase transition temperature f_r seems to noticeably change. With that said, the resolution of the discrete temperature (i.e., equilibrium) data is too low to definitively see subtle changes. However, the span of temperatures measured allows for a reasonable estimate of the range of low frequencies to use. From the thermal runs, the only non-smooth behavior expected is at the isotropic to mesogenic phase transition where an appreciable discontinuity is present.

The relaxation frequency increases with increasing temperature. For both the mesophases and the isotropic phase, the processes appear mostly Arrhenius, with a single prominent relaxation curve over the frequency range measured. The lowest temperature relaxation process had a frequency of 109.7 kHz. At the highest temperature measured (i.e., 90 °C), the fitted relaxation process had a frequency f_r that is well above the measuring capabilities of the instrument used (i.e., $f_{instrument\_max}$ = 1 MHz): 17.38 MHz. Near the transition, the fitted relaxation process had a frequency f_r at 990.4 kHz. Near the phase transition, both probing frequencies (i.e., 10 kHz and 100 kHz) appeared outside of the relaxation process. In the isotropic phase, the highest temperature permittivity measured is the same for both frequencies. However, only the 10 kHz measurements were consistently in the plateau frequency region for all temperatures measured.

(a) Heating runs of ε' with an inset of ε''

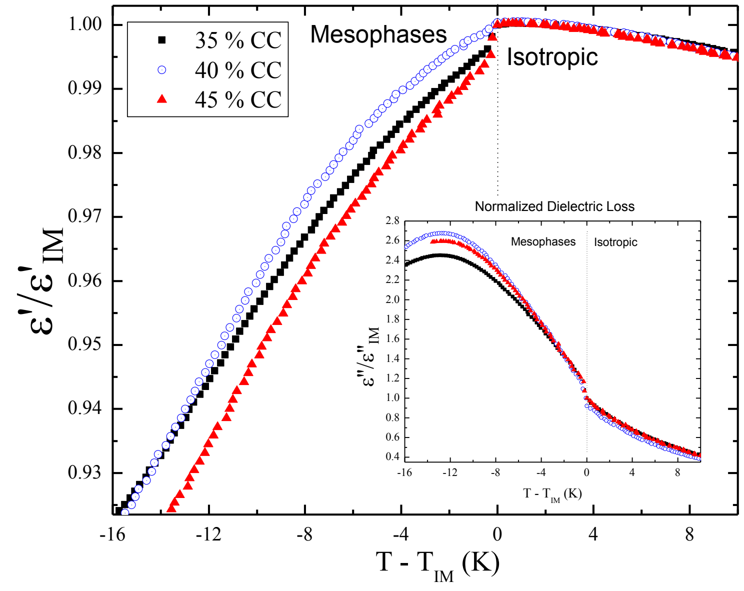

(b) Cooling runs of ε' with an inset of ε''

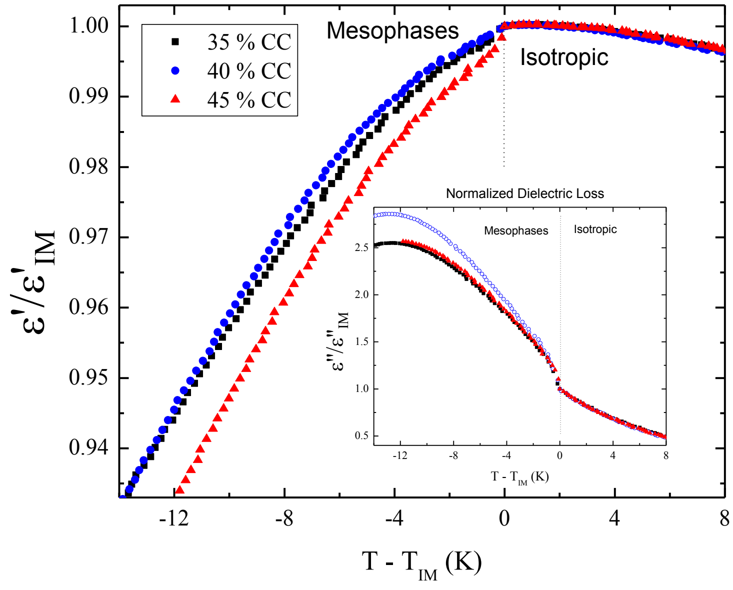

Figure 5.33: Region III permittivity at 100 kHz.

At this frequency, there is no significant relative difference among 35%, 40%, and 45% mixtures aside from the discontinuity from the isotropic phase. Additionally, unlike Regions I and II, there is no significant relative difference between heating and cooling among Region III mixtures.

(a) Heating of ε' with an inset of ε''

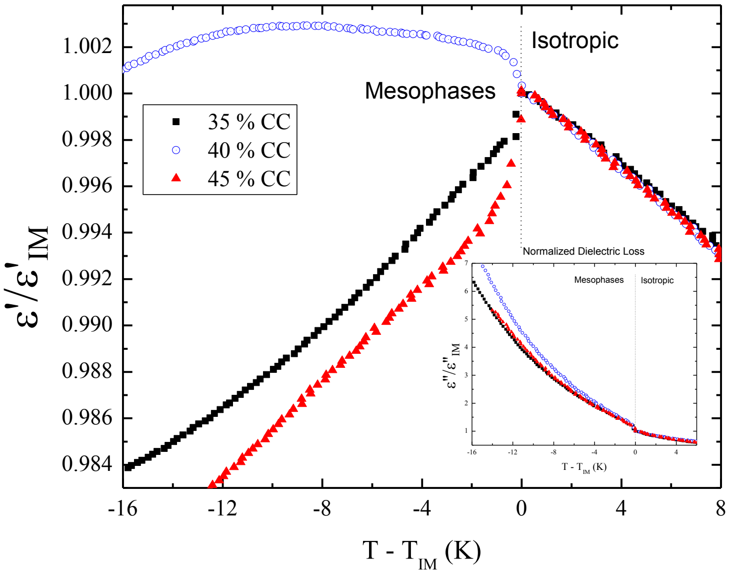

(b) Cooling of ε' with an inset of ε''

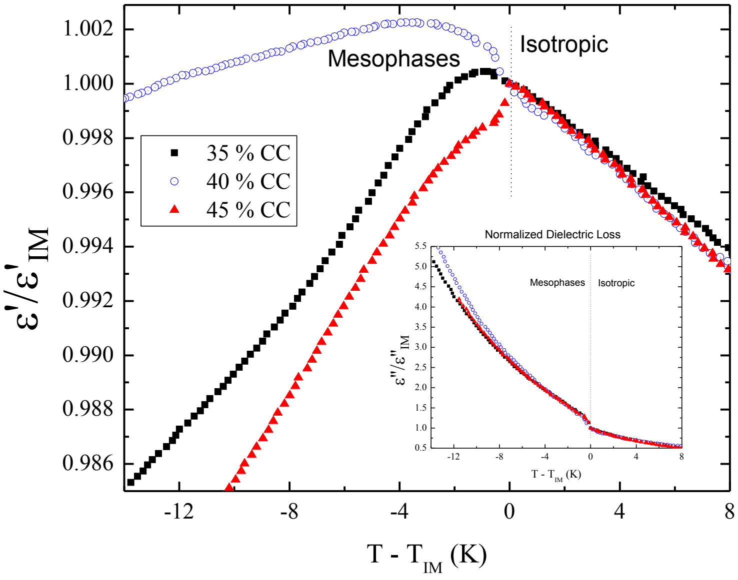

Figure 5.34: Region III permittivity at 10 kHz.

In contrast with Regions I and II, there is no significant relative difference between heating and cooling among Region III mixtures. In contrast to the 100 kHz measurements, there is an obvious difference. The 35% to 45% mixtures have a significant difference in the mesophase slope and hump. By 45%, the hump is gone.

5.3.3.4 Region IV Results: 50, 55, 60% Cholesteryl Chloride

The initial interest of this chapter was the range of percentages in which blue phases exist for two different chirality ranges: 0% to 40% CC and 80% to 100% CC (see Figure 5.10) [59]. The cholesteryl chloride rich mixtures (Regions I and II) are of opposite chirality to that of the cholesteryl chloride rich compounds. Refer back to Figure 1.4 for the chemical structures of cholesteryl oleyl carbonate and cholesteryl chloride.

Region IV mixtures approach a lower chiral nematic behavior. It was of interest to see if Region IV would exhibit appreciable pretransitional curvature as the samples looked at in Chapter 4. Due to unexpected issues with the 70% and above mixtures, the presented mixtures end with Region IV at 60% cholesteryl chloride. In Section 3.3, it was discussed that the cholesteryl chloride rich mixtures were not stable and eventually decomposed under dielectric measurements.

Region IV mixtures motivated a further investigation in the microscopic observation for a smectic phase. As expected, no blue phase was observed in Region IV [59]. The observed phase sequences for Region IV are seen in Table 5.12. The 50% mixture showed an unexpected smectic phase that was relatively close (6 °C below the isotropic phase transition into cholesteric) to the isotropic phase. See Figure 5.16 for the phase diagram that summarizes the observed phase transitions. The microscopic observations for the 50% mixture can be seen in Figure 5.35. Figure 5.36 shows the observed microscopic observations for the 55% and 60% mixtures in which only an cholesteric to isotropic phase transition was observed to within 20 °C below the isotropic to cholesteric phase transition.

Table 5.12: Region IV phase sequences from optical cross-polarized microscopy for the 50%, 55%, and 60% cholesteryl chloride mixtures.

These are the observed phase sequences from cross-polarized microscopy. For (b) the 55% mixture and (c) the 60% mixture, neither blue phases nor smectic phases were observed in the visible between room temperature and above. Interestingly, unlike the mixtures between 25% and 60%, (a) the 50% mixture has two smectic phases that are closer to the isotropic phase relative to pure cholesteryl oleyl carbonate.

(a)	50% mixture	Heating	$\mathrm{Sm_C} \xrightarrow{42.1\ ^\circ\mathrm{C}} \mathrm{Sm_A} \xrightarrow{46.4\ ^\circ\mathrm{C}} \mathrm{N^*} \xrightarrow{52.1\ ^\circ\mathrm{C}} \mathrm{Isotropic}$
		Cooling	$\mathrm{Sm_C} \xleftarrow{40.7\ ^\circ\mathrm{C}} \mathrm{Sm_A} \xleftarrow{44.3\ ^\circ\mathrm{C}} \mathrm{N^*} \xleftarrow{51.4\ ^\circ\mathrm{C}} \mathrm{Isotropic}$
(b)	55% mixture	Heating and Cooling	$\mathrm{N^*} \xleftrightarrow{53.2\ ^\circ\mathrm{C}} \mathrm{Isotropic}$
(c)	60% mixture	Heating and Cooling	$\mathrm{N^*} \xleftrightarrow{54.8\ ^\circ\mathrm{C}} \mathrm{Isotropic}$

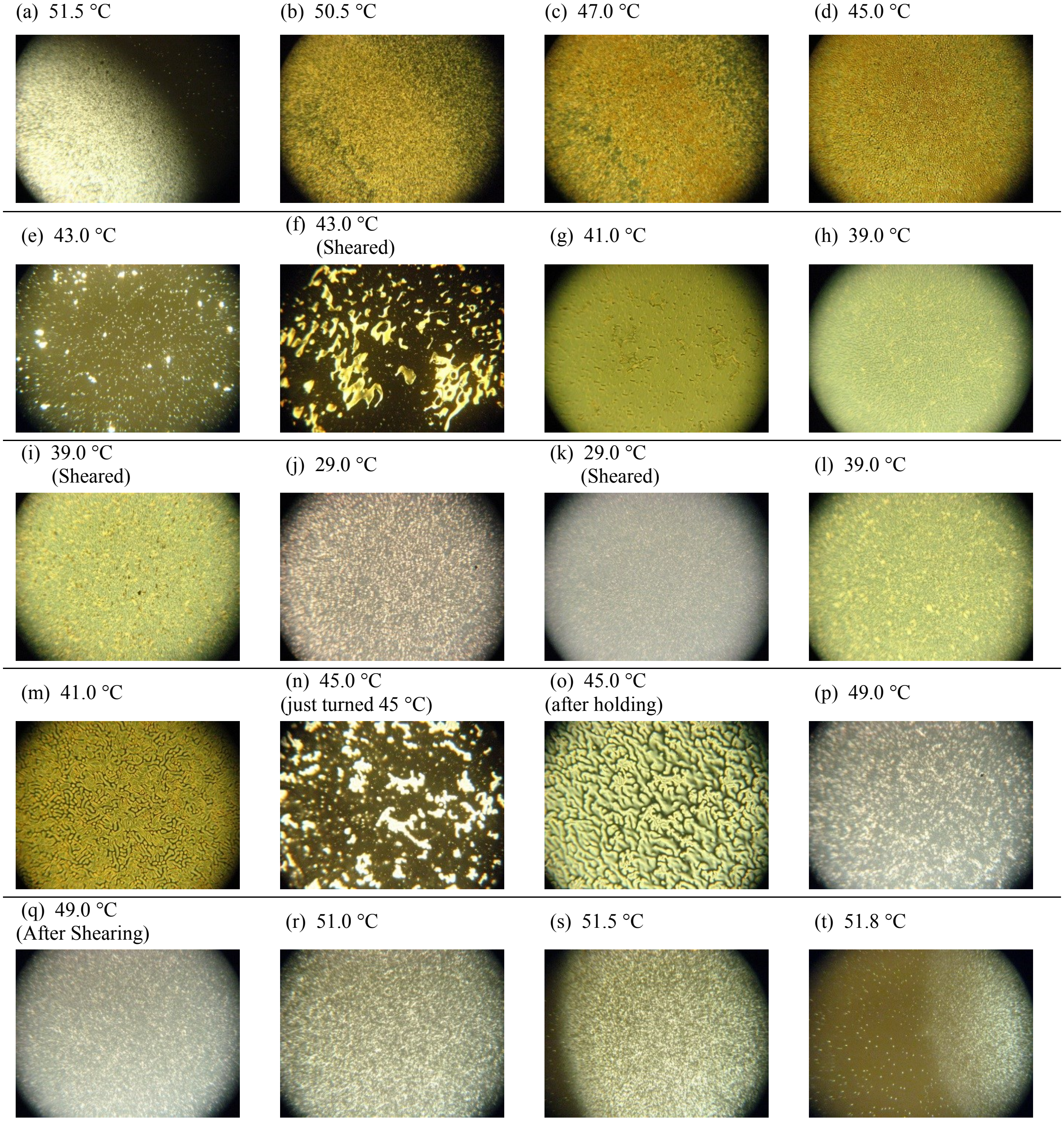

(a) 51.5 °C
(b) 50.5 °C
(c) 47.0 °C
(d) 45.0 °C
(e) 43.0 °C
(f) 43.0 °C (Sheared)
(g) 41.0 °C
(h) 39.0 °C
(i) 39.0 °C (Sheared)
(j) 29.0 °C
(k) 29.0 °C (Sheared)
(l) 39.0 °C
(m) 41.0 °C
(n) 45.0 °C (just turned 45 °C)
(o) 45.0 °C (after holding)
(p) 49.0 °C
(q) 49.0 °C (After Shearing)
(r) 51.0 °C
(s) 51.5 °C
(t) 51.8 °C

Figure 5.35: Region IV optical microscopy images for the 50% cholesteryl chloride mixture at select temperatures.

Images captured under transmission. Reflectance, unlike for Regions I through III, did not give clear images of the textures. The sample was initially heated into the isotropic phase. Indices (a) through (k) are on cooling. Indices (k) through (t) are on heating. The white dots observed in the isotropic phase are dust on the slide and cover slip. Index (e) sheared in (f) is indicative of a smectic A phase, where the background appears isotropic when it is planar aligned. Upon shearing the observed texture appears. Based on the phase sequence, index (g) and lower temperatures are in the smectic C phase.

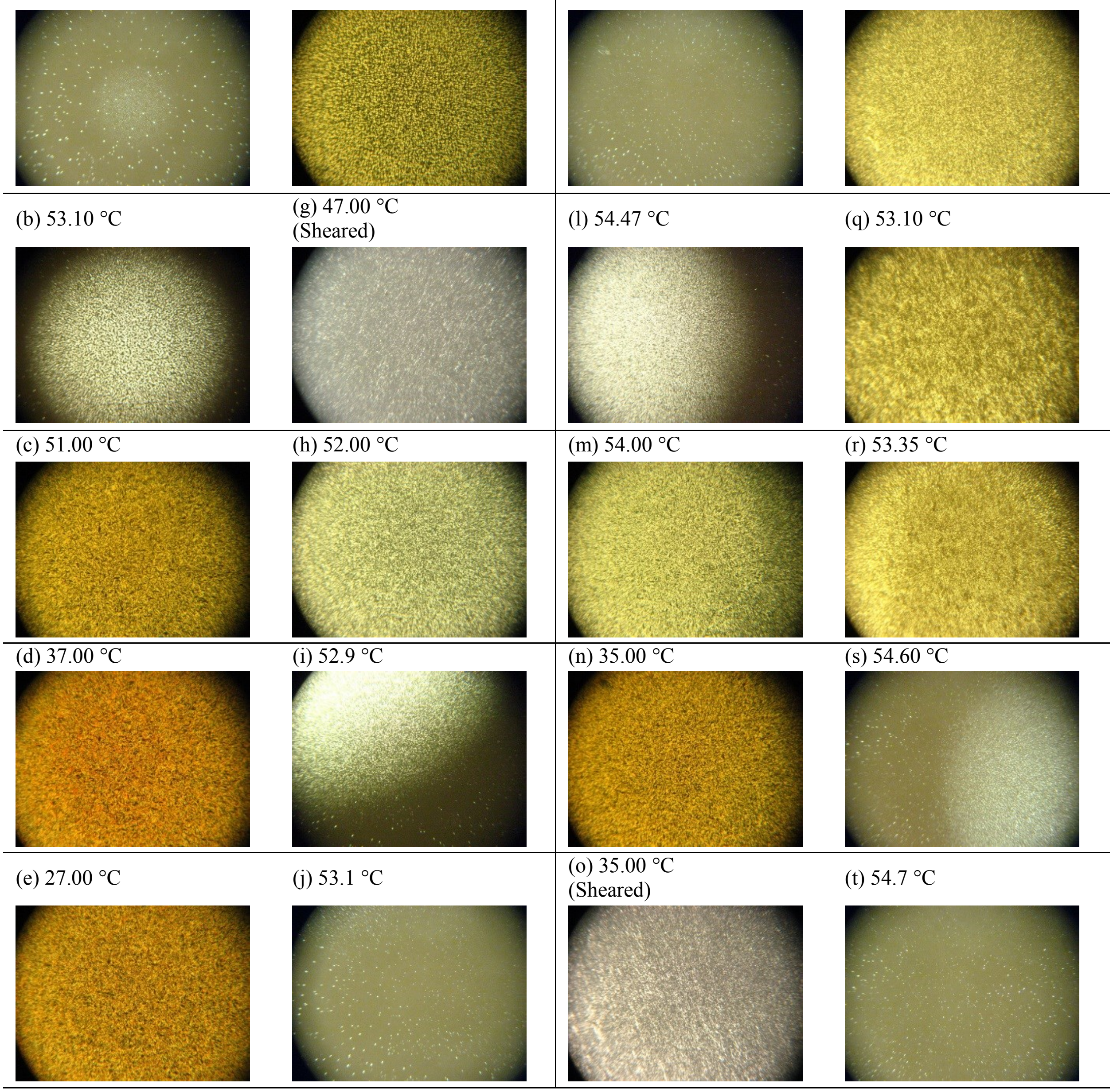

55% Cholesteryl Chloride

60% Cholesteryl Chloride

Cooling

Heating

Cooling

Heating

(a) 52.15 °C

(f) 47.00 °C

(k) 54.8 °C

(p) 40.00 °C

(b) 53.10 °C

(g) 47.00 °C
(Sheared)

(l) 54.47 °C

(q) 53.10 °C

(c) 51.00 °C

(h) 52.00 °C

(m) 54.00 °C

(r) 53.35 °C

(d) 37.00 °C

(i) 52.9 °C

(n) 35.00 °C

(s) 54.60 °C

(e) 27.00 °C

(j) 53.1 °C

(o) 35.00 °C
(Sheared)

(t) 54.7 °C

Figure 5.36: Region IV optical microscopy images for the 55% and 60% cholesteryl chloride mixtures at select temperatures.

Selected images captured under transmission. Neither blue phases nor smectic phases were observed on reflectance and transmission. Transmission for Region IV mixtures gave more detailed textures for phase identification [61]. Between each temperature, the magnitude of the heating or cooling rates were at most 0.2 °C /min. Indices (a) through (j) are for the 55% mixture. Indices (k) through (t) are for the 60% mixture. The temperature rate did not exceed 0.2 K per minute for temperature changes above room temperature (above 21 °C)

Region IV mixtures have almost the same temperature dependence for the relaxation frequency f_r. This is seen in Figure 5.37. As with the other regions, the relaxation frequency around each mixtures isotropic-mesogenic phase transition increases with composition. This means that as composition is increased, the 10 and 100 kHz data would be expected to be closer to the plateau, static permittivity range of frequencies.

The 100 kHz thermal cycling measurements are seen in Figure 5.38. As with Region III, the normalized relative dielectric response for Region IV is similar for all three mixtures. The major difference among Region III mixtures at 100 kHz is the discontinuity at the isotropic to cholesteric phase transition.

The 10 kHz thermal cycling measurements are seen in Figure 5.39. All three mixtures are strikingly different from each other on both heating (Figure 5.39a) and cooling (Figure 5.39b). This is evident in the phase sequences shown in Table 5.12.

The phase behavior of the 50% mixture is interesting in its variety. On both heating and cooling, the dielectric behavior at 10 kHz (Figure 5.39) shows multiple peaks below the isotropic phase. On cooling (Figure 5.39b), the dielectric peak that is -7 °C from the isotropic to cholesteric transition matches the transition observed below the cholesteric phase observed under the microscope at -7.1 °C from the isotropic to cholesteric transition (see Figure 5.35e). The dielectric peak at -10 °C from the isotropic to cholesteric transition matches the transition observed under the microscope at -7.1 °C from the isotropic phase (see Figure 5.35, parts (g) and (h)). The textures observed below the cholesteric phase under the microscope matched closely to the examples given of Smectic A and C, respectively, in the book by Ingo Dierking [61]. The dielectric peak to microscopy observation textures was similar on heating.

The 55% and 60% mixtures at 10 kHz on cooling have a dielectric response (Figure 5.39b) that continuously decreases at least -12 °C from the isotropic phase. Compared to Figure 5.36 from the optical microscopy observations, this corresponds to the cholesteric phase. Based on the pattern observed thus far on cooling at 10 kHz, when a phase begins to transition to another phase, the dielectric data begin to change the sign of the slope.

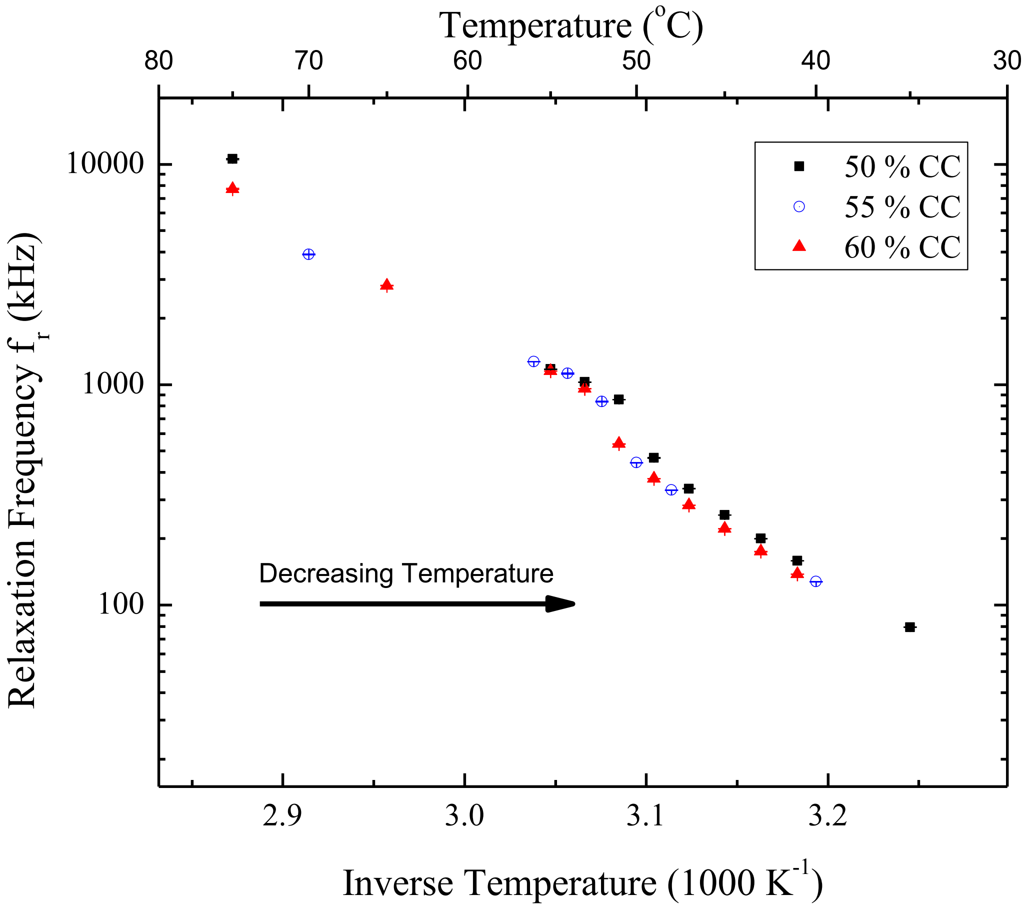

Figure 5.37: Region IV temperature dependence of the relaxation frequency.

The relaxation frequency f_r is a fitting parameter that was discussed for the 12% mixture in Section 5.2.2. Parametrically, it corresponds to the peak of the semicircle discussed in Figure 5.6 for the 12% mixture. Standard errors are shown.

For Region III, as with Region II, the relaxation processes are nearly identical to each other. With increasing composition, the relaxation frequencies shift up such that 100 kHz is closer to the plateau frequency region.

(a) Heating of ε' with an inset of ε''

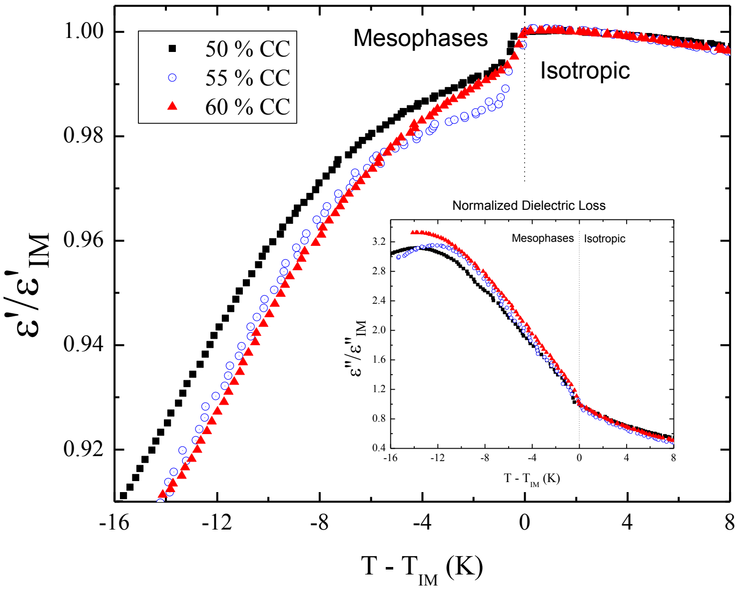

(b) Cooling of ε' with an inset of ε''

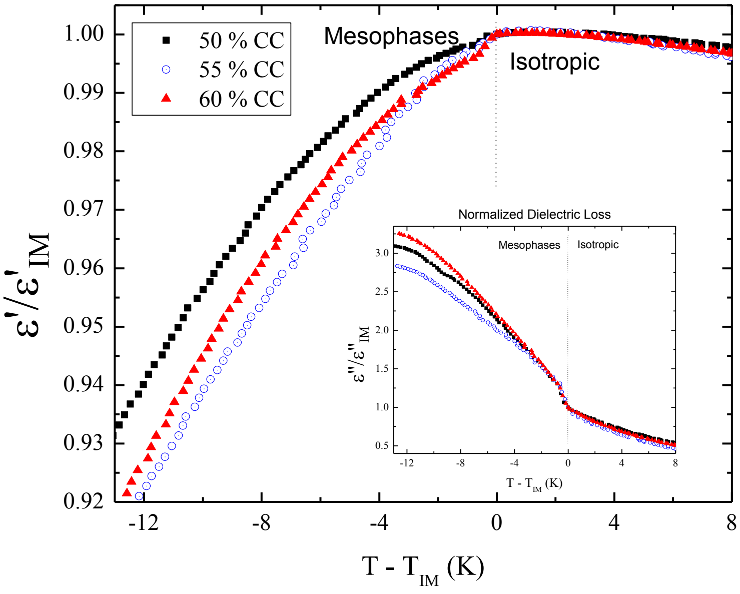

Figure 5.38: Region IV permittivity at 100 kHz.

At this frequency, the mesophase measurements are still near the relaxation frequencies of each mesophase. This results in the monotonic drop in the permittivity. Despite the differences among the phase sequences among Region IV mixtures, all have nearly identical relative temperature dependencies.

(a) Heating of ε' with an inset of ε''

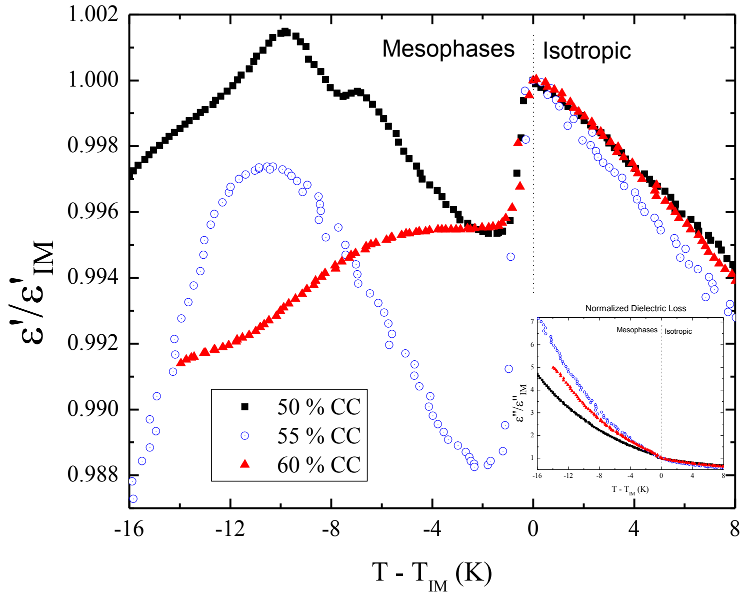

(b) Cooling of ε' with an inset of ε''

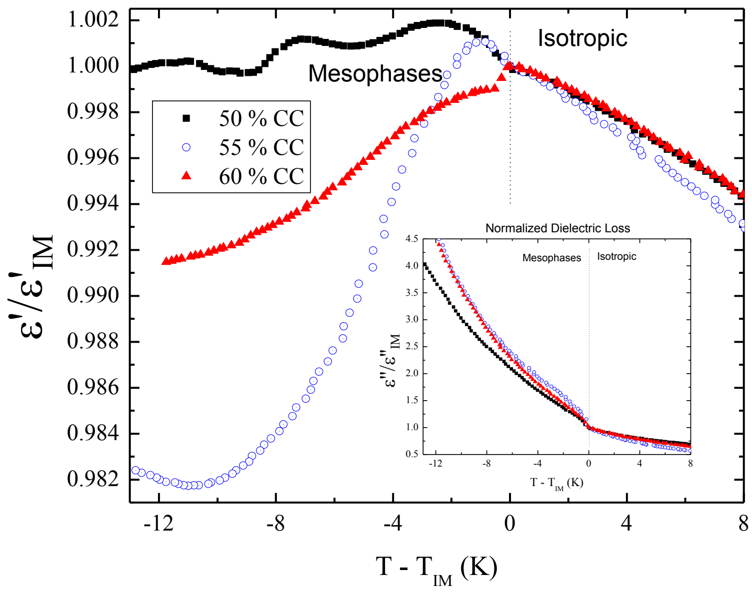

Figure 5.39: Region IV permittivity at 10 kHz.

At this frequency, the differences among the three mixtures are apparent. The 55% and 60% mixtures each have a relatively constant slope which corresponds roughly the microscopic observations in which only one phase transition was observed.

5.4 Conclusions

5.4.1 Comparison of Phase Diagrams

Figure 5.40 shows a phase diagram generated from the dielectric measurements on cooling at 10 kHz in part (a). Part (b) of Figure 5.40 presents the zoomed-in version of Figure 5.16b at the same scale as Figure 5.40a.

The transition temperatures T_{IM} from the familiar high temperature isotropic phase and the lower mesophases are estimated from the 100 kHz data when no obvious discontinuity appears for the 10 kHz measurements. The mesophase to mesophase transitions were estimated by looking at the peaks observed relative to T_{IM} on cooling at 10 kHz for the 0% through 30% mixtures. The samples were not aligned. The presumed smectic phases and indeterminate region estimates may be incorrect.

The resultant phase diagrams in Figure 5.40 are now compared to the one produced by McKinnon et. al., shown in Figure 5.10, which served as a guide in this dissertation [59]. Two important differences are noted. First, they estimate a narrower temperature range of blue phases between the isotropic and cholesteric phases. Second, their measurements were only taken near the isotropic to cholesteric (or blue phase) transitions. Both of my dielectric measurements and optical microscopy results which explored a broad range of temperatures (shown in Figure 5.40) show a smectic phase for the 50% mixture close to the isotropic phase. The cholesteric phase at the 50% mixture has a narrow temperature range. The 45% and 55% mixtures do not show a smectic. Although their cholesteryl chloride and cholesteryl oleyl carbonate could have been of either different batches or different purities, the observation of a smectic phase so close to the isotropic phase was unexpected.

Figure 5.40b shows the optical microscopy phase diagram of Figure 5.16b zoomed in to the same scale as the dielectric phase diagram of Figure 5.40a. The isotropic to mesophase transition temperature estimates T_{IM} match relatively well between parts (a) and (b). The transition temperature estimates between blue phases I and II do not match well below the 12% mixture. A higher temperature resolution is needed due to the small discontinuities between blue phases. However, due to the experimental limitations this was not achieved.

Although the smectic phases were not of interest to this dissertation, it was surprising to see two smectic phases form for the 50% composition within 5 K of the isotropic to cholesteric transition. The optical microscopy results in Figure 5.40b confirm that the indeterminate region for the dielectric estimates is in fact a continuation of the smectic C phase. Smectic phases require alignment for dielectric studies in order to obtain reliable results.

(a) Dielectric phase diagram on cooling at 10 kHz. For smectic phases A and C as well as the indeterminate region, definitive results require sample alignment. The samples were not aligned by any external field beyond the applied AC field.

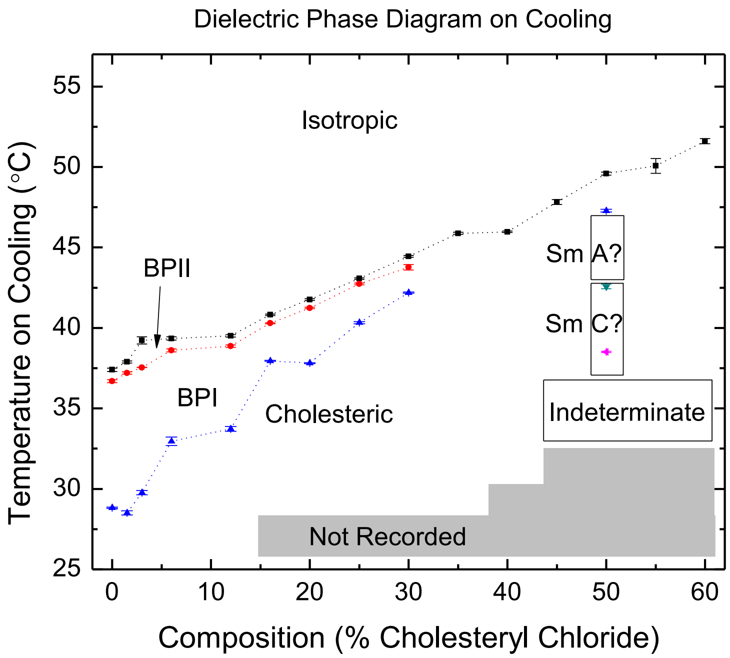

(b) Results from cross-polarized microscopy. Values given are from when the phase fully formed.

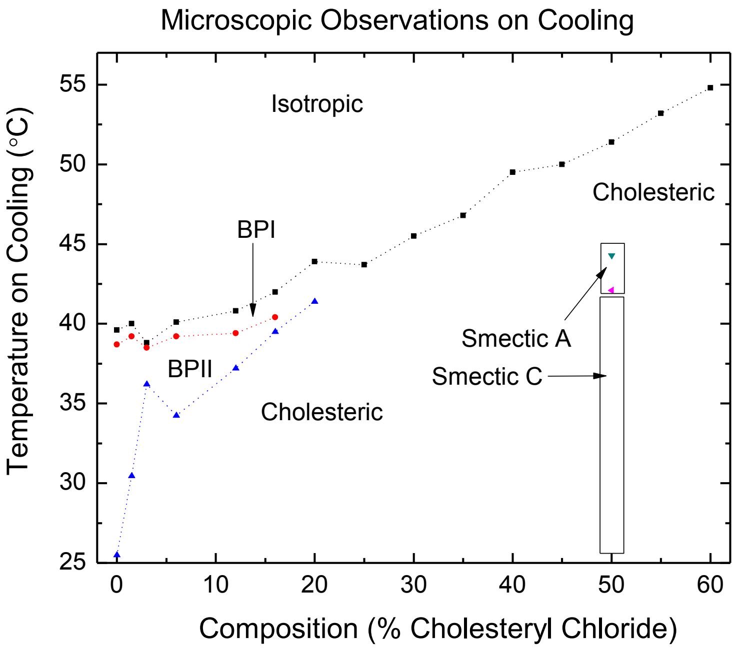

Figure 5.40: Proposed phase diagram based on dielectric measurements. Measurements on cooling.

5.4.2 A Second Study in Varying Chirality

This chapter constitutes a second study in the effects of varying chirality on dielectric measurements. As mentioned in the introduction to this chapter, one other study has investigated the effects of varying chirality by looking at mixtures of two similar molecules, except that one is the chiral variant of the other (see Figure 5.2 for their results) [36]. Both molecules had prominent dipole moments and exhibited pretransitional curvature that was of interest. The phase sequence for Leys et. al. was the same on heating as cooling [36]. This chapter took a slightly different approach in that both molecules were of opposite chirality.

The phase sequence of my mixtures was monotropic for the low compositions. This was neither predicted nor expected. On heating, a cholesteric to isotropic transition was observed for all mixtures. It was on cooling that the blue phases were present. Figure 5.4a clearly shows this difference in the dielectric measurements of a representative mixture. For the 25% and below mixtures of cholesteryl oleyl carbonate with cholesteryl chloride, a broad bump in the dielectric data appears for the 10 kHz cooling runs at temperatures below the isotropic phase. For the 12% mixture, this corresponds to 5 K below the phase transition. From the optical microscopy observations (see Figure 5.9), the dielectric peak of this bump corresponded to when the cholesteric phase almost fully formed. The temperature range between this peak and the isotropic phase at 10 kHz on cooling corresponded to the full development of the cholesteric phase with respect to the microscopy observations. This temperature range decreased with increasing amounts of cholesteryl chloride (that is, decreasing chirality). Although optical microscopy results showed no blue phase at 25% through 35%, this bump appeared in the dielectric data through the 35% mixture. This leads to the conclusion that a blue phase exists through the 35%, however based on the progression of colors of the blue phase between 0% and 20%, these must lie within the infrared.

The progression of the temperature range of this bump can be seen on cooling at 10 kHz in Regions I, II, and III (Figures 5.23b, 5.30b, and 5.34b, respectively).

Although unexpected, the monotropic phase sequences below the 35% mixture allowed for the observation of the cholesteric to isotropic phase on heating and the isotropic to blue phase on cooling. From Figure 5.14 on heating, the discontinuity changes in accordance with Brazovskii and Dimitriev [62, 63]. On cooling in Figure 5.14, the discontinuity is relatively small below 35% cholesteryl chloride, and with the disappearance of the blue phases above the 40% composition the discontinuity at the transition increases.

There was a striking difference between the 10 kHz measurements and the 100 kHz measurements. The low frequency measurements gave information on the dielectric behavior of the phase transitions (see Figures 5.23, 5.30, 5.34, and 5.39). While the high frequency measurements definitively showed the isotropic to mesophase transition, the shape of the curve was almost linear in the mesophase but with a different slope negative to that of the isotropic phase (see Figures 5.22, 5.29, 5.33, and 5.38).

Also, at the high frequency measurements (see Figures 5.22, 5.29, 5.33, and 5.38), the mesophase slopes fanned out as a function of chirality. A look at the frequency domain allows for a better understanding of this. First, the relaxation frequencies are shown for Regions I, II, III, and IV (see Figures 5.21, 5.28, 5.32, and 5.37). Most of the mesophase measurements have relaxation frequencies that are near 100 kHz. Secondly, a look at the representative 12% mixtures frequency plots (see Figures 5.5 and 5.6) reveals three potential issues to be aware of that were discussed in Section 2.2. In Figure 5.6b, the dielectric loss shows low frequency interference below 1 kHz. For a positive value this is attributed to ionic conductivity, for a negative value this is attributed inductive interference [34]. The 10 kHz measurements are mostly safe, in that they are far from either extreme condition (low frequency interference, and higher frequency relaxation peak). The fanning out of the 100 kHz measurements (see Figures 5.22, 5.29, 5.33, and 5.38) may be, in part, due to a relaxation peak being approached near 100 kHz on increasing composition.

5.4.3 A Comparison Theoretical Predictions

Figure 5.41 is a schematic of a theoretical prediction that describes the formation of the blue phases with respect to the discontinuity of the transition. The schematic uses a generic representation of the discontinuity in the form of the difference between the transition temperature T_{IM} (estimated from the data) and the critical temperature T^* (a fitting parameter discussed in Chapter 4). An equivalent discontinuity, specific to this dissertation, is the permittivity $\Delta\varepsilon'$ and $\Delta\varepsilon''$ (Figures 5.14 and 5.15, respectively).

As chirality is gradually increased from a low chirality, a transition from the high temperature isotropic phase to the cholesteric phase is usually observed as shown by the green, thick solid line in Figure 5.41. Brazovskii and Dimitriev predicted that as the chirality is increased for the cholesteric phase, the transition should become second order, represented by the green, thick line in Figure 5.41 [62, 63].

Brazovskii and Dimitriev further predicted that the second order transition between high temperature isotropic phase to the cholesteric is never reached [62, 63]. As shown by the black, thick dash-dotted line in Figure 5.41, the transition from isotropic to cholesteric is interrupted by the formation of a new phase. This new phase takes better advantage of the cubic term in the free energy expansion discussed in both Section 1.2.2.1 and Figure 1.6. At high chirality, a lower free energy minimum is allowed. The black, thick line also shows that the transition with the high temperature phase ends at a critical point [62, 63].

The new transition from the high temperature phase represented by the black, thick solid line in Figure 5.41 is for an isotropic to isotropic phase. In contrast, the transition represented by the green, thick, solid line in Figure 5.41 is for an isotropic to anisotropic transition. Such a transition is first order.

The new phase that forms has, instead of the single helical periodicity of a cholesteric phase, three dimensions of helical periodicity. This three dimensions of periodicity gives it a cubic structure. Cubic structures are treated as being isotropic, whereas the high temperature isotropic phase is amorphous.

Since Brazovskii and Dimitriev's theoretical framework was published, it is now known that there are three of these phases, the so called blue phases I, II and III. The thin, red lines in Figure 5.41 shows a schematic of these three phases between the high temperature isotropic and the cholesteric phase. Not all three are necessarily present together for all phase sequences. I remind the reader from Section 1.2.2.1, blue phases I and II are cubic isotropic (simple and body-centered, respectively). Blue phase III is an amorphous isotropic. The transition between the isotropic phase and any one of the blue phases is between two dielectrically isotropic phases.

Figure 4.15 shows heating runs at both measuring frequencies. The discontinuity is generally larger for higher compositions which corresponds to regions of lower chirality where the structure of the cholesteric phase, N^*, has a globally minimum free energy. Brazovskii and Dimitriev's conclusions are supported by my data of the estimated discontinuities $\Delta\varepsilon'$ and $\Delta\varepsilon''$ (Figures 5.14 and 5.15, respectively) where the magnitude of each is generally increasing. The temperature dependence within each phase can of course be different via changes in slope and so forth. This results in a smaller discontinuity than between any isotropic phase and the anisotropic cholesteric phase.

At a high enough chirality there is a transition between two amorphous isotropic phases: blue phase III and the familiar high temperature isotropic phase. At some critical point on the chirality scale a critical point is reached. There is no transition beyond the critical point between blue phase III and the high temperature isotropic phase.

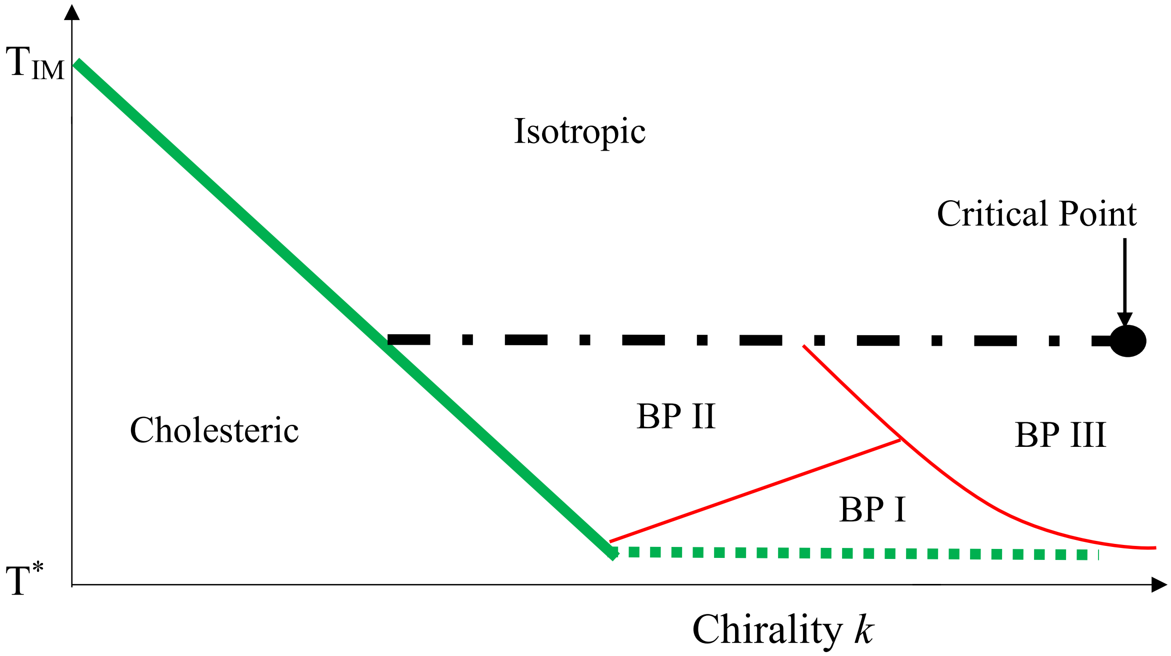

Figure 5.41: A schematic of the predictions of Brazovskii and Dimitriev where the difference between *Tc* and *T** represents the discontinuity in the phase transition.

- Thick, green lines (both solid and dotted) – Expected behavior between the isotropic and cholesteric phase. The solid line is the actual behavior.
- Black, thick, dash-dot line – the predicted development of a new phase ending at a critical point (the thick black dot).
- Red, thin, solid lines – Beyond the predition of Brazovskii and Dimitriev, the one phase is actually three distinct phases that develop between the isotropic and cholesteric phases at high enough chiralities. As discussed in this chapter, those phaes are blue phases I, II, and III.

CHAPTER 6 CONCLUDING THOUGHTS AND FUTURE WORK

This dissertation set out to study the dielectric properties of nematic liquid crystals in both the achiral and chiral limits. A model was developed for the achiral limit to describe pretransitional curvature in the dielectric permittivity on the isotropic side of the transition that had not been previously described by theory. With the addition of chirality, new phases eventually develop called blue phases which were studied with dielectric measurements. Additionally, cross-polarized microscopy was utilized to corroborate which phases were seen under the dielectric measurements.

6.1 Achiral Nematics

The generalization of the order parameter in Section 2.3.2 has led to a successful macroscopic description of the pretransitional curvature. The initial form of the model shown Equation 4.2 ran into fitting difficulties in the form of either a double minimum in chi-square space or a single minimum with unrealistic standard errors. This was overcome by looking at a second order expansion and observing the relationships among the fitting parameters. An expansion to the three-halves order was found to best describe the data when looked at under range shrinking. Because it was desired to extract original parameters *C* and *D*, Equation 4.2 eventually transformed into a hierarchical fitting process that overcame any ambiguities in the parameter estimates.

As discussed in Section 4.4.2, two groups performed dielectric measurements on the *n*CB series. From the fitting parameter results versus carbon chain length *n*, it is seen that the hierarchical fitting approach not only describes an individual molecules dielectric behavior well in the isotropic phase, but also well over a series of molecules.

For future work, this model can be extended to the nematic side of the phase transition. The theoretical framework for the nematic side is similar to what was setup for the isotropic side in Section 2.3.2, Equations 2.17 through 2.26. Unlike the isotropic side of the transition, $\langle Q_{\alpha\beta} \rangle$ is not equal to zero.

6.2 Chiral Nematics

As discussed in Section 5.4.2, this is the second study to look at the effect of varying chirality on dielectric measurements. Two main topics motivated this section. First, it was of interest if the pretransitional curvature in the isotropic phase varied with composition. Second, it was of interest how well the dielectric signature of blue phases I, II, and III differed from the high temperature isotropic phase.

While pretransitional curvature appeared at 100 kHz, in the low frequency plateau measurements (recall in Section 2.2 that this is a measurement away from a relaxation peak) no obvious pretransitional curvature was seen. Without that, it is difficult to attest whether or not chirality is playing any role in counteracting anti-parallel dipole formation.

Despite the negative result on pretransitional curvature, the transition sequences were unexpectedly monotropic. On heating at the highest of chiralities (0% through 35% mixtures), only the cholesteric to isotropic phase transition was observed. This was verified under cross-polarized microscopy where the observed textures were referenced to a book on liquid crystalline textures. As mentioned in Section 5.4.3, this led to a direct confirmation of a theoretical prediction on how the discontinuity from cholesteric to isotropic changes as a function of changing chirality.

Future work can be divided into two categories. Cholesteryl chloride spontaneously decomposed. A very narrow cholesteric phase followed by a very wide smectic phase was unexpectedly present for the 50% sample.

First, any future work using cholesteryl chloride needs to investigate first why the high composition cholesteryl chloride mixtures spontaneously crystalize and decompose under an applied AC field. From optical microscopy observations (with no applied field) it was observed that cholesteryl chloride spontaneously crystalizes. However, repeated thermal cycling for optical observations did not destroy the sample. When the same thermal cycling is repeated inside of the capacitor setup at an applied AC field, the sample decomposes.

Second, the 50% mixture had unexpected smectic A and C phases near the isotropic phase, where near means within 10 K, as shown in Figures 5.16 and 5.40. No smectic phase was observed for the 25% through 45% mixtures and for the 50% and 60% mixtures. Additional work can be done to find the phase boundaries of the smectic phases.

REFERENCES

1. *Phases of Matter*. (The National Aeronautics and Space Administration's Glenn Research Center, http://www.grc.nasa.gov/WWW/k-12/airplane/state.html, 2014).

2. P. J. Collings, *Liquid Crystals: Nature's Delicate Phase of Matter*, 2 ed. (Princeton University Press, Princeton, 2002).

3. P. G. deGennes, *The Physics of Liquid Crystals*. (Oxford University Press, Oxford, 1993).

4. *Chemical Structure of 6CB*. (Royal Society of Chemistry, http://www.chemspider.com/Chemical-Structure.35514.html, 2016).

5. *Chemical Structure of 8CB*. (Royal Society of Chemistry, http://www.chemspider.com/Chemical-Structure.94149.html, 2016).

6. P. J. Collings and J. S. Patel, (Oxford University Press, New York, 1997).

7. S. Meiboom and M. Sammon, Physical Review Letters **44** (886) (1980).

8. S. Chandrasekhar, *Liquid Crystals*, 2 ed. (Cambridge University Press, Cambridge, 1993).

9. M. B. Bowling, P. J. Collings, C. J. Booth and J. W. Goodby, Physical Review E **48** (1993).

10. P. J. Collings and M. Hird, *Introduction to Liquid Crystals: Chemistry and Physics*. (Taylor & Francis, Philadelphia, 1997).

11. G. Vertogen and W. H. d. Jeu, *Thermotropic Liquid Crystals, Fundamentals*. (Springer-Verlag, New York, 1988).

12. R. N. Kleinman, D. J. Bishop, R. Pindak and P. Taborek, Physical Review Letters **53** (1984).

13. J. Thoen, Physical Review A **37** (5) (1988).

14. E. Karatairi, B. Rožič, Z. Kutnjak, V. Tzitzios, G. Nounesis, G. Cordoyiannis, J. Thoen, C. Glorieux and S. Kralj, Physical Review E **81** (041703) (2010).

15. *Chemical Structure of Cholesteryl Chloride*. (Sigma-Aldrich, http://www.sigmaaldrich.com/catalog/product/aldrich/c76604, 2016).

16. *Chemical Structure of Cholesteryl Nonanoate*. (Royal Society of Chemistry, http://www.chemspider.com/Chemical-Structure.83818.html, 2016).

17. *Chemical Structure of Cholesteryl Oleyl Carbonate*. (Sigma-Aldrich, http://www.sigmaaldrich.com/catalog/product/aldrich/151157, 2016).

18. *Chemical Structure of CE8*. (The ChemicalBook http://www.chemicalbook.com/ProductChemicalPropertiesCB9934713_EN.htm, 2016).

19. F. Grandjean, C.R. Acad. Sci. **164**, 280-283 (1917).

20. V. N. Tsvetkov, Acta Physicochimica U.R.S.S. **16**, 132-147 (1942).

21. I. W. Hamley, *Introduction to Soft Matter*, Revised ed. (John Wiley & Sons, West Sussex, 2007).

22. L. D. Landau and E. M. Lifshitz, *Statistical Physics*, 3 ed. (Reed Educational and Professional Publishing LTD, 1980).

23. J. Leys, C. Glorieux, M. Wübbenhorst and J. Thoen, Liquid Crystals **34** (6), 749-759 (2007).

24. L. D. Landau and E. M. Lifshitz, *Electrodynamics of Continuous Media*, 2 ed. (Elsevier Butterworth Heinemann, 1984).

25. J. P. F. Lagerwell, presented at the International Liquid Crystal Conference, Keystone, Colorado, 2006 (unpublished).

26. J. P. F. Lagerwell, Chalmers University of Technology
Göteborg University, 2000.

27. W. H. d. Jeu, *Physical Properties of Liquid Crystalline Materials*. (Gordon and Breach Science Publishers, 1980).

28. J. Thoen and T. K. Bose, in *Handbook of Low and High Dielectric Constant Materials and Their Applications*, edited by H. S. Nalwa (Academic Press, San Diego, 1999), Vol. 1, pp. 501-561.

29. P. Debye, *Polar Molecules*. (Chemical Catalogue Co., New York, 1929).

30. K. S. Cole and R. H. Cole, J. Chem. Phys. **9** (341) (1941).

31. D. W. Davidson and R. H. Cole, J. Chem. Phys. (20) (1952).

32. R. H. Cole, J. Chem. Phys. **9** (493) (1955).

33. S. Havriliak and S. Negami, J. Polymer **8**, 161-210 (1967).

34. Agilent Technologies Inc.

35. S. Yagihara, M. Oyama, A. Inoue, M. Asano, S. Sudo and N. Shinyashiki, IOP Meas. Sci. Technol. **18** (983) (2007).

36. G. Sinha, J. Leys, C. Glorieux and J. Thoen, Physical Review E **72** (051710) (2005).

37. T. K. Bose and J. Thoen, (1988).

38. A. Drozd-Rzoska, S. J. Rzoska, S. Pawhus and J. Ziolo, Physical Review E **72** (2005).

39. A. Drozd-Rzoska, S. Pawhus and S. J. Rzoska, Physical Review E **64** (2001).

40. A. Drozd-Rzoska, S. J. Rzoska and J. Ziolo, Physical Review E **54** (1996).

41. A. Drozd-Rzoska, S. J. Rzoska and J. Ziolo, Physical Review E **61** (2000).

42. A. Drozd-Rzoska, S. J. Rzoska and K. Czupryñski, Physical Review E **61** (2000).

43. M. Ginovska, H. Kresse, D. Bauman, G. Czechowski and J. Jadzyn, Physical Review E **69** (2004).

44. S. J. Rzoska, M. Paluch, S. Pawlus, A. Drozd-Rzoska, J. Ziolo, J. Jadzyn, K. Czuprynski and R. Dabrowski, Physical Review E **68** (2003).

45. S. J. Rzoska, J. Ziolo, W. Sułkowski, J. Jadżyn and G. Czechowski, Physical Review E **64** (2001).

46. A. Drozd-Rzoska, Physical Review E **59** (1999).

47. P. H. Keyes, (Soon).

48. H. Zink and W. H. d. Jeu, **124**, 287-304 (1985).

49. D. A. Belsley, E. Kuh and R. E. Welsch, *Regression diagnostics : identifying influential data and sources of collinearity*. (Wiley, Hoboken, N.J., 2004).

50. A. C. Atkinson, *Plots, transformations, and regressions : an introduction to graphical methods of diagnostic regression analysis*. (Clarendon Press, New York, 1985).

51. S. o. Thoen, Leuven, 198x.

52. S. J. Rzoska, A. Drozd-Rzoska, B. K. Mukherjee, D. O. Lopez and J. C. Martinez-Garcia, Journal of Physics Condensed Matter **25** (2013).

53. T. Snijders and R. Bosker, *Multilevel Analysis: An Introduction to Basic and Advanced Multilevel Modeling*, 2 ed. (Sage, Los Angeles).

54. S. Pawlus, M. Zasada and S. J. Rzoska, Z. Naturforsch **57 a**, 126-128 (2002).

55. *Chemical Structure of 5CB*. (Royal Society of Chemistry, http://www.chemspider.com/Chemical-Structure.83347.html, 2016).

56. *Chemical Structure CB15*. (Royal Society of Chemistry, http://www.chemspider.com/Chemical-Structure.3163234.html, 2015).

57. E. P. Koistinen and P. H. Keyes, Physical Review Letters **74** (22) (1995).

58. Z. H. Wang and P. H. Keyes, Physical Review E **54** (4) (1996).

59. P. H. Keyes, A. J. Nicastro and E. M. McKinnon, Mol. Cryst. Liq. Cryst. **67**, 59-68 (1981).

60. R. Manohar, M. Gupta and J. P. Shukla, Journal of Physics and Chemistry of Solids **61**, 1465-1473 (2000).

61. I. Dierking, *Textures of Liquid Crystals*. (Wiley-VCH Verlag GmbH & Co. KGaA, Weinheim, 1993).

62. S. A. Brazovskii and S. G. Dmitriev, Sov. Phys. JETP **42** (3), 497-502 (1975).

63. S. A. Brazovskii and V. M. Filev, Sov. Phys. JETP **48** (1978).

ABSTRACT

DIELECTRIC ANOMALIES OF BOTH CHIRAL AND ACHIRAL NEMATOGENS NEAR THE ISOTROPIC TO MESOGENIC PHASE TRANSITION

by

GARRETT J. GODFREY

August 2016

Advisor: Dr. Paul H. Keyes

Major: Physics

Degree: Doctor of Philosophy

The dielectric properties of nematic liquid crystals were studied in both the achiral and chiral limits. For achiral nematics, the literature documents that pretransitional curvature occurs for polar molecules on both sides of the nematic and isotropic phase transition. This curvature is due to anti-parallel dimer formation. However, past models have failed to quantitatively describe pretransitional curvature. Through a generalization of the order parameter, a macroscopic model has been developed to mathematically describe the pretransitional curvature on the isotropic side of the transition. The new model was fitted to dielectric data from the literature. Meaningful parameter estimates were extracted.

The dielectric response of chiral nematic systems has not been well studied in the literature. A system with tunable chirality was dielectrically studied by mixing two highly chiral liquid crystals: cholesteryl oleyl carbonate (left handed) and cholesteryl chloride (right handed). An apparatus was designed and built to systematically measure the dielectric response of the mixtures. Optical cross-polarized microscopy was used to identify the transition temperatures of each phase. The transition temperatures were then correlated with the dielectric response.

The initial intentions of studying chiral systems was two-fold: to see how chirality played a role in the pretransitional curvature, and to see if the blue phases were dielectrically distinguishable. While the initial intentions were null and indecisive, respectively, interesting results were obtained. First, the phase transitions were monotropic for the highest chirality mixtures. Second, the estimated discontinuity at the isotropic to mesogenic transition followed theoretical predictions that had not been tested for dielectric measurements.

AUTOBIOGRAPHICAL STATEMENT

Education

- Doctor of Philosophy in Physics: August 2016: Wayne State University, Detroit, MI
- Master of Science in Physics: May 2012: Wayne State University, Detroit, MI
- Bachelor of Science in Physics: August 2008: Wayne State University, Detroit, MI 48201, USA

Publications

- Laser-induced breakdown spectroscopy at a water/gas interface: A study of bath gas-dependent molecular species, M Adamson, A Padmanabhan, **GJ Godfrey**, SJ Rehse, Spectrochimica Acta Part B: Atomic Spectroscopy 62 (12), 1348-1360, 2007
- Investigation of non-linear effects of coupling materials in sonic IR imaging, X Han, Y Song, **G Godfrey**, The 15th International Symposium on: Smart Structures and Materials & Nondestructive Evaluation and Health Monitoring, International Society for Optics and Photonics, 69320N-69320N-6, 2008
- What Role A Coupling Material Could Play In Sonic IR Imaging, YY Song, **G Godfrey**, X Han, Review of Progress in Quantitative Nondestructive Evaluation: Proceedings of the 35th Annual Review of Progress in Quantitative Nondestructive Evaluation, Vol 1096 Issue 1, p 511-517, AIP, 2009